Nucleon Electromagnetic Structure Studies in the Spacelike and Timelike Regions

Dissertation
zur Erlangung des Grades
„ Doktor der Naturwissenschaften “

am Fachbereich Physik, Mathematik und Informatik
der Johannes Gutenberg-Universität Mainz

vorgelegt von

Julia Guttmann

geboren in Bochum

Mainz, 2013

Tag der mündlichen Prüfung: 23. Juli 2013
D77 (Dissertation Universität Mainz)

Abstract

The thesis investigates the nucleon structure probed by the electromagnetic interaction. One of the most basic observables, reflecting the electromagnetic structure of the nucleon, are the form factors, which have been studied by means of elastic electron-proton scattering with ever increasing precision for several decades. In the timelike region, corresponding with the proton-antiproton annihilation into a electron-positron pair, the present experimental information is much less accurate. However, in the near future high-precision form factor measurements are planned.

About 50 years after the first pioneering measurements of the electromagnetic form factors, polarization experiments stirred up the field since the results were found to be in striking contradiction to the findings of previous form factor investigations from unpolarized measurements. Triggered by the conflicting results, a whole new field studying the influence of two-photon exchange corrections to elastic electron-proton scattering emerged, which appeared as the most likely explanation of the discrepancy.

The main part of this thesis deals with theoretical studies of two-photon exchange, which is investigated particularly with regard to form factor measurements in the spacelike as well as in the timelike region. An extraction of the two-photon amplitudes in the spacelike region through a combined analysis using the results of unpolarized cross section measurements and polarization experiments is presented. Furthermore, predictions of the two-photon exchange effects on the e^+p/e^-p cross section ratio are given for several new experiments, which are currently ongoing.

The two-photon exchange corrections are also investigated in the timelike region in the process $p\bar{p} \to e^+e^-$ by means of two factorization approaches. These corrections are found to be smaller than those obtained for the spacelike scattering process. The influence of the two-photon exchange corrections on cross section measurements as well as asymmetries, which allow a direct access of the two-photon exchange contribution, is discussed. Furthermore, one of the factorization approaches is applied for investigating the two-boson exchange effects in parity-violating electron-proton scattering.

In the last part of the underlying work, the process $p\bar{p} \to \pi^0 e^+e^-$ is analyzed with the aim of determining the form factors in the so-called unphysical, timelike region below the two-nucleon production threshold. For this purpose, a phenomenological model is used, which provides a good description of the available data of the real photoproduction process $p\bar{p} \to \pi^0\gamma$.

Zusammenfasssung

Die vorliegende Dissertation untersucht die Struktur des Nukleons mittels elektromagnetischer Wechselwirkung. Formfaktoren sind mit die elementarsten Observablen, welche die elektromagnetische Struktur des Nukleons widerspiegeln, und werden seit mehreren Jahrzehnten mit Hilfe elastischer Elektron-Proton-Streuung mit steigender Genauigkeit bestimmt. Der zeitartige Bereich, welcher der Proton-Antiproton-Vernichtung in ein Elektron-Positronpaar entspricht, ist bislang experimentell weniger gut erforscht. Allerdings sind in naher Zukunft Messungen der Formfaktoren mit hoher Präzision geplant.

Ungefähr 50 Jahre nach den ersten bahnbrechenden Messungen der elektromagnetischen Formfaktoren sorgten Polarisationsexperimente für Aufsehen, deren Ergebnisse in großem Widerspruch zu den bisherigen Resultaten der Formfaktoruntersuchungen standen. Ausgelöst durch diese widersprüchlichen Ergebnisse entstand ein neues Arbeitsfeld, welches Zwei-Photon-Austauschkorrekturen zur elastischen Elektron-Proton-Streuung untersucht, die als wahrscheinlichste Erklärung der Diskrepanz gelten.

Der Hauptteil der vorliegenden Arbeit beschäftigt sich mit theoretischen Studien des Zwei-Photon-Austausches, der insbesondere mit Hinblick auf Messungen der Formfaktoren sowohl im raumartigen als auch zeitartigen Bereich untersucht wird. Eine kombinierte Analyse der Daten aus unpolarisierten Wirkungsquerschnittsmessungen und Polarisationsexperimenten erlaubt eine Bestimmung der Zwei-Photon-Amplituden im raumartigen Bereich. Eine Vorhersage für den Einfluss des Zwei-Photon-Austausches auf das Verhältnis der e^+p und e^-p Wirkungsquerschnitte kann somit präsentiert werden, das momentan an verschiedenen Experimenten untersucht wird.

Die Zwei-Photon-Austauschkorrekturen werden zudem im zeitartigen Bereich für den Prozess $p\bar{p} \to e^+e^-$ mittels zweier Faktorisierungsansätze untersucht. Die auf diese Weise erhaltenen Korrekturen sind kleiner als jene, die für den raumartigen Streuprozess ermittelt wurden. Der Einfluss dieser Zwei-Photon-Austauschkorrekturen auf Messungen des Wirkungsquerschnittes sowie Asymmetrien, welche einen direkten Zugang zu Beiträgen des Zwei-Photon-Austausches ermöglichen, wird diskutiert. Außerdem wird einer der Faktorisierungsansätze zur Untersuchung von Effekten des Zwei-Boson-Austausches in paritätsverletzender Elektron-Proton-Streuung angewandt.

Im letzten Teil der vorliegenden Dissertation wird der Prozess $p\bar{p} \to \pi^0 e^+e^-$ mit dem Ziel die elektromagnetischen Formfaktoren im sogenannten unphysikalischen, zeitartigen Bereich unterhalb der Produktionsschwelle eines Nukleonpaares zu bestimmen, analysiert. Hierfür wird ein phänomenologisches Modell verwendet, welches eine gute Beschreibung der vorhandenen Daten für den Prozess der reellen Photoproduktion $p\bar{p} \to \pi^0\gamma$ liefert.

Contents

1 Introduction **1**

2 Electromagnetic Form Factors of the Nucleon **7**
2.1 Properties of Electromagnetic Form Factors 7
2.2 Form Factor Investigation using Elastic Electron-Proton Scattering 11
2.2.1 Rosenbluth Separation 12
2.2.2 Polarization Transfer Measurements 14
2.2.3 Discussion of the Discrepancy 15
2.3 Electromagnetic Form Factors in the Timelike Region 17
2.3.1 Accessing Form Factors in the Timelike Region 18
2.3.2 Electromagnetic Form Factors in the Unphysical Region 22
2.4 Form Factor Models 23

3 Two-Photon Exchange in Elastic Electron-Proton Scattering **27**
3.1 Electron-Proton Scattering beyond the Born Approximation 27
3.2 Model Calculations of Two-Photon Exchange 30
3.3 Observables related to Two-Photon Exchange 33
3.3.1 Comparison of Positron-Proton and Electron-Proton Scattering 33
3.3.2 Beam-Normal and Target-Normal Spin Asymmetries 34
3.4 Determination of Two-Photon Amplitudes from ep-Scattering Data 35
3.4.1 Measurement of Effects beyond the Born Approximation in Polarization Transfer Observables 35
3.4.2 Phenomenological Extraction of Two-Photon Exchange Amplitudes from ep-Scattering Data 37
3.4.3 Positron-Proton versus Electron-Proton Scattering 43
3.5 Conclusions 44

4 Two-Photon Exchange in the Timelike Region **45**
4.1 Timelike Two-Photon Exchange: General Formalism 46
4.2 Timelike Two-Photon Exchange Corrections at Large q^2: pQCD Result 49
4.2.1 Nucleon Distribution Amplitudes and pQCD Factorization Approach . 49
4.2.2 Timelike Two-Photon Exchange within a pQCD Factorization Approach 53
4.2.3 Results 61
4.3 Partonic Calculation of Timelike Two-Photon Exchange: GDA Approach . . . 66
4.3.1 Generalized Distribution Amplitudes 66
4.3.2 Timelike Two-Photon Exchange within a GDA based Approach 68
4.3.3 Results 73
4.4 Conclusions 75

5 Two-Boson Exchange in Parity-Violating Electron-Proton Scattering 79
5.1 Parity-Violating Electron-Proton Scattering . . . 79
5.2 Two-Boson-Exchange Effects in Parity-Violating ep-Scattering . . . 84
5.2.1 General Formalism . . . 84
5.2.2 Two-Boson Exchange within a perturbative QCD Factorization Approach 87
5.3 Conclusions . . . 93

6 Nucleon Form Factors in the Unphysical Region 95
6.1 Probing Nucleon Form Factors in the Unphysical Region . . . 96
6.1.1 Timelike Pion Electroproduction . . . 96
6.1.2 Real Photoproduction . . . 98
6.2 Regge Theory . . . 100
6.3 Real Photoproduction within a Regge Framework . . . 104
6.4 Timelike Pion Photoproduction within a Regge Framework . . . 111
6.4.1 General Analysis of the Annihilation Cross Section . . . 111
6.4.2 Results within a Regge Framework . . . 114
6.5 Conclusions . . . 118

7 Conclusions and Outlook 119

Appendix 121

A Notations and Conventions 123
A.1 Lorentz Vectors . . . 123
A.2 Light-Cone Coordinates . . . 123
A.3 Pauli and Dirac Matrices . . . 124
A.4 Dirac Spinors . . . 125

B Amplitudes within a pQCD Factorization Approach 129
B.1 Results of Two-Photon Exchange Contributions . . . 129
B.2 Results of γZ-Exchange Contributions . . . 130

C Form Factor Parametrization 135
C.1 Electromagnetic Nucleon Form Factors . . . 135
C.2 Axial Nucleon Form Factor . . . 137

List of Acronyms 137

Bibliography 141

Chapter 1

Introduction

The idea of discrete constituents building up all matter arose already thousands of years ago. Democritus proposed the philosophical concept that all matter is composed of indivisible building blocks, called $\alpha\tau o\mu o\varsigma$. This basic idea has been recovered in the 18th and 19th century. At that time, all materials had been found to be made of certain components, the atoms, which were thought to be fundamental. However, the discovery of the electron and nucleus, as well as its constituents, the proton and neutron, revealed the subatomic structure and disproved the atoms' indivisibility.

No evidence of the electron being a composite particle has been found until today. By contrast, since the measurement of the proton magnetic moment [1], which differs significantly from the expected value of a pointlike elementary particle, the question of the building blocks of the proton and neutron has emerged. A complete description of the proton and neutron internal structure is still an unsolved problem of hadron and particle physics.

Today the Standard Model of particle physics, as the theory of fundamental particles and their interactions, describes the composition of matter and successfully explains a large variety of phenomena of particle and hadron physics. Recently, the observation of a new boson at the Large Hadron Collider [2,3] is supposed to be the discovery of the last missing particle of the Standard Model, the Higgs boson.

There are four fundamental forces in nature, the strong force, the weak force, the electromagnetic force and gravity, where the latter one is not included in the Standard Model. The fundamental constituents can be classified into two categories according to how they interact, the leptons and the quarks, which appear in three generations (or families) each containing two particles. For each of these particles a corresponding antiparticle exists. The interaction between the particles is mediated via the so-called gauge bosons, to which the particles can couple if they carry the charge of the appropriate interaction. The Higgs boson is essential in order to explain the masses of the particles, which are generated via the interaction with the Higgs field. Leptons interact weakly, given by the exchange of the weak gauge bosons $W^{\pm}$ and Z, and, in the case of charged leptons, also electromagnetically. By carrying an electric charge, the particles can interact via couplings to the photon, the transmitter of the electromagnetic interaction. Besides a weak and electric charge, the quarks carry an additional charge, known as color, which enables them to couple to gluons, the gauge bosons mediating the strong force. The particles of the Standard Model are summarized in Fig. 1.1.

The electromagnetic force is well described within a quantum field theory known as Quantum Electrodynamics (QED), whose predictions have been tested experimentally with extremely high accuracy. One can take advantage of the smallness of the electromagnetic coupling, $\alpha_{\mathrm{em}} \sim 1/137$, which enables a perturbative treatment of electromagnetic processes as an expansion in terms of increasing powers of α_{em}. QED and the weak interaction can be unified to the electroweak gauge theory.

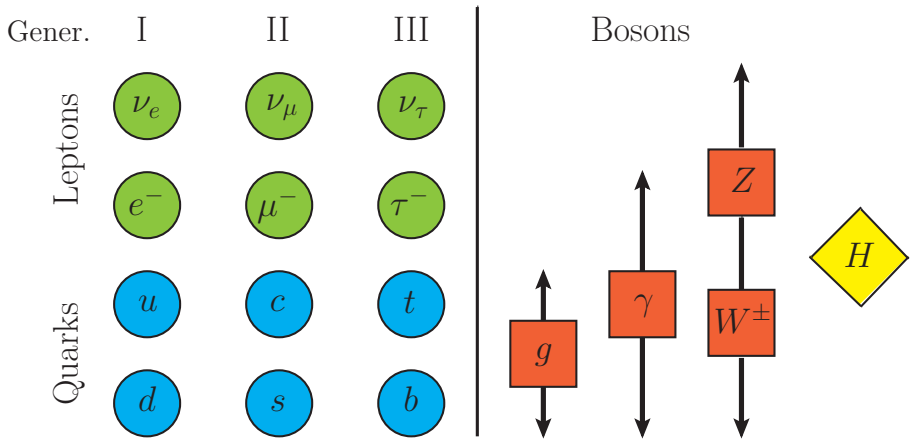

Figure 1.1: Particles of the Standard Model: The uncharged leptons (ν_e, ν_μ, ν_τ), the charged leptons (e^-, μ^-, τ^-) and the quarks (u, d, c, s, t, b), which are arranged in three generations, as well as the gauge bosons of the weak (Z, $W^\pm$), electromagnetic (γ) and the strong interaction (g), and the Higgs boson (H).

The theory of strong interactions, Quantum Chromodynamics (QCD), describes the interaction between quarks and gluons. The proton and neutron themselves, which are denoted as nucleons, are no elementary particles, just like all other observable strongly interacting particles, called hadrons. Understanding the structure of the nucleon as a complex system built up of strongly interacting particles is one of the main tasks of hadron physics. At present, the concept of the nucleon is seen as a system containing three valence quarks and an arbitrary number of quark-antiquark pairs and gluons.

The investigation of the nucleon structure is complicated due to two remarkable features of QCD. The first one, denoted as color confinement, manifests itself by the impossibility to observe colored quarks and gluons as free particles. Therefore, the nucleon structure cannot be investigated simply by a decomposition into its constituent parts. Instead, indirect measurements have to be performed, which allow conclusions regarding the underlying properties of the nucleon. The second phenomenon, called asymptotic freedom, characterizes the running of the strong coupling α_S, which decreases for increasing energies and even disappears, if the energy tends to infinity. The asymptotic freedom has been proved in [4,5], rewarded by the Nobel prize in 2004. A perturbative treatment of QCD at lower energies is not applicable so far due to large values of α_S. A non-perturbative access is given by lattice gauge theories, where QCD is studied on a space-time, which is discretized into a finite lattice and evaluated numerically [6]. Nevertheless, no analytical solutions of QCD at lower energies are known so far.

Besides numerical simulations using lattice QCD, approaches to deal with processes involving strongly interacting particles, such as nucleons, at intermediate and low energies are necessary. Anyhow, many reactions can be calculated at least in part by means of perturbative QCD (pQCD). This concept, known as QCD factorization, is based on the separation of the process into a part, for which a perturbative treatment is applicable, and a non-perturbative contribution, which has to be handled phenomenologically. In order to deal with hadronic reactions, such factorization approaches will be applied in the course of this thesis.

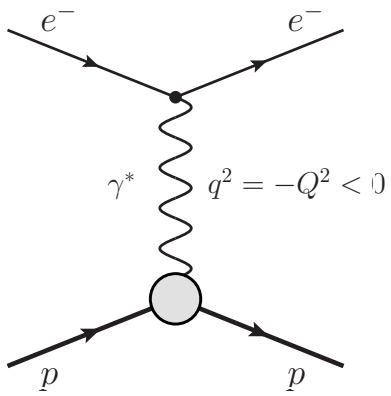

Figure 1.2: Elastic electron-proton scattering in the Born approximation

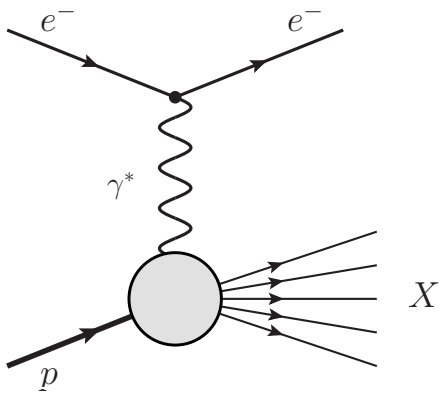

Figure 1.3: Deep inelastic scattering in the Born approximation

Despite the fact that the constituents of the nucleon cannot be observed directly, there are several possibilities for probing properties of the proton and neutron. An excellent tool to investigate the structure of the nucleon is electron scattering. Since the interplay between the electron and the transferred photon is well described within QED, the electromagnetic interaction provides a well known probe. Hence, one is able to infer information on the nucleon composition from the results of scattering experiments. The leading-order contribution to elastic electron-proton scattering arises from the exchange of a single photon between the electron and proton, which is known as the Born approximation and is depicted in Fig. 1.2.

A milestone in the exploration of the sub-nuclear structure was reached in the 1950s by Hofstadter and collaborators using elastic electron-proton scattering [7]. These experiments allowed for the first time to determine the so-called electromagnetic form factors of the nucleon, which provided a considerable insight into the underlying structure of the nucleon, for which Hofstadter was awarded the Nobel prize in 1961. Electromagnetic form factors are the most basic observables reflecting the composite nature of the nucleon, giving rise to the distribution of the charge and magnetic moments inside the proton and neutron. This structure is parametrized in terms of two form factors, denoted as G_E and G_M, which are functions of the momentum transfer squared Q^2, which is mediated via the photon between the electron and the proton. This was the starting point for a large number of experiments, which have measured the elastic electron-proton scattering cross section with increasing precision over a wide kinematical range in order to extract the electromagnetic form factors.

If electrons with higher energies scatter off nucleons, the probability of an inelastic reaction is increasing, where instead of a single proton several particles are produced in the final state. The high-energy scattering process known as deep inelastic scattering, $e^- + p \to e^- + X$, is presented in Fig. 1.3, where X stands for a not further specified hadronic final state. Measurements of such deep inelastic processes have started in the 1960s, leading to significant observations concerning the interiors of the proton. The results of these experiments can be explained within the parton model, which assumes that during the short interaction time the scattering is performed at quasi-free pointlike objects inside the nucleon, denoted as partons [8]. This was the first convincing evidence for the existence of pointlike nucleon constituents, which later have been identified as quarks. These investigations have been awarded with the Nobel prize in 1990. Within QCD factorization, the deep-inelastic scattering cross section

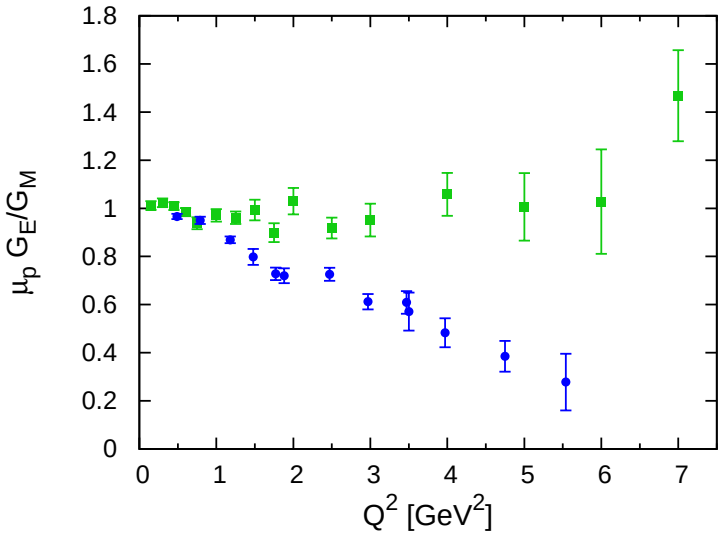

Figure 1.4: Form factor ratio $\mu_p G_E/G_M$ (with the magnetic moment of the proton μ_p) extracted in electron-proton scattering. The green data correspond to the results of Ref. [10] via unpolarized measurements, the blue data points indicate the findings of Refs. [9, 11] from polarization experiments.

is given as a convolution of the lepton-quark scattering cross section and a non-perturbative contribution denoted as parton distribution functions, containing information on the partonic nucleon structure.

About 50 years after the pioneering experiments of Hofstadter et al. [7], form factor investigation through polarization measurements became feasible, giving rise to additional and independent experimental observables. However, the results of the form factors extracted from polarization experiments are in striking contradiction to the findings of the unpolarized cross section measurements [9]. To illustrate this discrepancy, in Fig. 1.4 the results of the form factor ratio G_E/G_M as found in the experiments of Refs. [9–11] are shown, where the green data points indicate the results of the unpolarized measurement [10] and the findings of the polarization experiments [9,11] are represented by the blue data points. The noticeable difference between the two experimental methods is clearly seen.

These conflicting results led to intense studies, from both experimental and theoretical sides, attempting to explain and reconcile both experimental methods. Since our understanding of the electromagnetic structure of the nucleon is related to the knowledge of the electromagnetic form factors, it is of great importance to understand the discrepancy in order to find a reliable picture of the electromagnetic form factors of the proton. Due to the fact that all these measurements have been analyzed using the Born approximation, considerable doubt on the validity of this approximation arose.

Theoretical studies indicated that a possible explanation of the inconsistent results can be provided by two-photon exchange processes, which are next-to-leading order corrections to the Born approximation. In the analysis of cross section and polarization measurements, effects of the exchange of two or more photons have been neglected. Such contributions are suppressed by at least an additional factor α_{em} compared to the leading terms, giving rise to corrections of order of a few percent. Nevertheless, it has been shown that these corrections

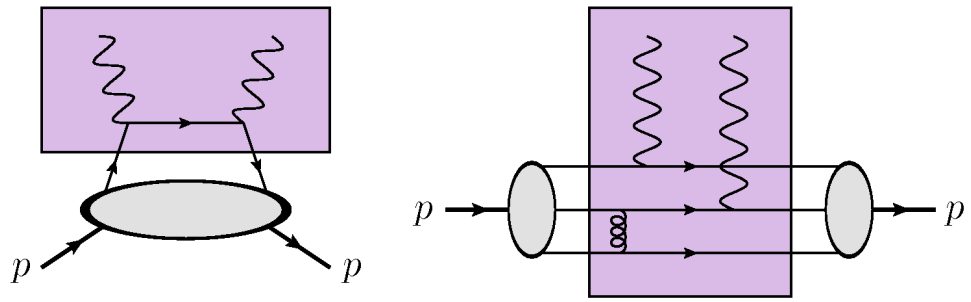

Figure 1.5: Sketch of factorization approaches used in this thesis. Left panel: factorization within the framework of GPDs. Right panel: factorization within a hard scattering perturbative QCD approach. The purple regions are associated with the partonic subprocesses, which are directly calculable, while the gray blobs indicate the non-perturbative contributions.

can impact the form factor extraction from the unpolarized cross section measurements significantly.

Elastic scattering reactions allow only to reveal the form factor structure in the spacelike region, corresponding to the region where the momentum transfer $q^2 = -Q^2$ of the photon is negative. The timelike region of positive momentum transfer q^2 can be examined with the crossed processes, as proton-antiproton annihilation into a lepton-antilepton pair or the vice versa reaction of the annihilation of a lepton-antilepton pair into a nucleon and antinucleon. A consistent description of the nucleon electromagnetic structure can only be achieved through detailed knowledge of the form factors over the complete kinematical range. So far, in the timelike regime only few data of the form factors with less precision exist. New experiments are planned to probe the form factors to high accuracy in the timelike region. With regard to such accurate experiments one has to be aware of two-photon exchange contributions, which apparently have noticeable effects on the extraction on spacelike form factors.

The main part of this thesis deals with two-photon exchange corrections, which are studied in the spacelike as well as in the timelike regions of momentum transfer. For this purpose, factorization approaches are applied for calculating the two-photon contributions to timelike annihilation processes. Like the decomposition of the deep inelastic scattering cross section, the considered factorization descriptions state, that in high energy processes the nucleons behave like a set of free partons. The cross section is then calculated from the cross section of the process at parton level and the distribution functions for finding the corresponding parton state in the hadrons. These functions are non-perturbative objects, which are independent of the explicit form of the partonic subprocess. This remarkable property allows to apply factorization models to two-photon exchange reactions, which have been probed in other processes.

The basic concepts of the two factorization approaches, which are discussed in this thesis, are sketched in Fig. 1.5. The purple regions indicate the processes at the parton-level, which are calculable within pQCD, while the gray blobs represent the non-perturbative parts. The first approach, illustrated in the left panel of Fig. 1.5, gives rise to the concept of the so-called generalized parton distributions (GPDs), which e.g. have been discussed extensively for the

process of deeply virtual Compton scattering. A single quark state of the involved hadrons participates in the partonic subprocess, which is embedded into the nucleons as described by the GPDs. The second approach, presented by the graph in the right panel of Fig. 1.5, is based on hard scattering perturbative QCD factorization, which at parton level implies a process with three active valence quarks. The non-perturbative contribution is given by the Distribution Amplitudes (DAs) of the nucleon, describing how the momenta of the nucleons are shared between the constituents.

With the aforementioned processes it is not possible to reach the complete allowed kinematical range of the form factors. The so-called unphysical region of momentum transfer, which is the timelike region below the production threshold of two nucleons, cannot be accessed. A part of the thesis focuses on the analysis of the process $p\bar{p} \to \pi^0 e^+ e^-$ as a means to provide constraints on timelike nucleon form factors, particularly in the unphysical region.

Outline

This thesis is organized as follows:

In Chapter 2 an introduction to the electromagnetic form factors in the spacelike and timelike regions is given.

Chapter 3 deals with the two-photon exchange effects in the elastic electron-proton scattering process. The general formalism of two-photon exchange is introduced and the results of several model calculations are briefly discussed. In the second part of the chapter a phenomenological determination of the two-photon exchange corrections is presented. Using the available cross section and polarization data, an extraction of the two-photon amplitudes is provided and predictions for experiments, which are presently underway, are given. The results of this work appeared in Ref. [12].

In Chapter 4 the two-photon exchange in the timelike region for the annihilation reaction $p\bar{p} \to e^+ e^-$ is studied. For the calculation of the two-photon exchange contribution to the cross section of the process, two different approaches are taken into account, both based on factorization principles, in oder to deal with the hadronic interactions. This work has in part been published in Ref. [13].

In Chapter 5 one of the approaches used in the previous chapter is applied for the investigation of the two-boson exchange contribution in parity-violating elastic electron-proton scattering. Besides the exchange of a photon, the Standard Model provides the possibility that electron-proton scattering is performed by the exchange of a Z boson. This Z boson exchange, even though it is suppressed at lower energies, manifests itself in a parity-violating contribution to the cross section, which can be affected by two-boson exchange contributions as well, namely two-photon or Z-photon exchange corrections.

Chapter 6 is devoted to the process $p\bar{p} \to \pi^0 e^+ e^-$, with particular focus on the possibility to determine the nucleon electromagnetic form factors in the unphysical region. The annihilation reaction is analyzed within a phenomenological model, allowing for predictions for forthcoming experiments. Since no data of this reaction has been taken so far, the model is first tested for the reaction $p\bar{p} \to \pi^0 \gamma$. The results of this work can be found in Ref. [14].

Finally, a summary of the results and an outlook is given in Chapter 7.

Chapter 2

Electromagnetic Form Factors of the Nucleon

Understanding the internal structure of the nucleon as a composite system, built up of quarks and gluons, is one of the most important unsolved problems in hadron physics.

Since the observation of the magnetic moment of the proton [1], which was found to be 2.8 times larger than the expected value for a fundamental pointlike particle, it is known that the proton is not an elementary particle but made of more fundamental constituents.

Starting in the 1950s, the structure of the nucleon has been studied by means of the electromagnetic interaction. The results of these measurements can be expressed in terms of the electromagnetic form factors of the nucleon, which are functions describing the internal structure as it is seen by the electromagnetic probe. For the first time, a measurement of the electromagnetic form factors has been performed by Hofstadter et al. [7] using elastic electron scattering off nucleons, which is still used for investigating the nucleon structure nowadays.

In this chapter the basic properties of the electromagnetic form factors as well as the results of the dedicated experiments are reviewed.

2.1 Properties of Electromagnetic Form Factors

In contrast to elementary particles like the electron, the nucleon has an extended structure, which can be explored in electromagnetic processes like elastic electron-proton (ep-) scattering. In the leading-order approximation of elastic electron-proton scattering, the Born approximation, the electromagnetic interaction is mediated by the exchange of a single photon. The corresponding leading-order Feynman diagram is shown in Fig. 1.2.

The electron-photon interaction is fully described by the theory of electromagnetic interactions and can be calculated directly within QED. Therefore electron-scattering provides a clear probe to study properties of composite systems. In contrast to the electron-photon vertex, the proton-virtual-photon interaction, encoding information about the extended spatial distribution in the nucleon, cannot be calculated from first principles due to the unknown interplay between the nucleon and photon. However, any deviation between the measurements of the reaction and the results expected for scattering of two fundamental pointlike particles is caused by the composite nature of the proton. These deviations can be described in terms of the electromagnetic form factors of the proton.

To study the scattering process in terms of proton form factors, we first consider the electromagnetic current of a pointlike Dirac particle with charge q_e (for the electron $q_e = -e$, with $e > 0$) which is given by:

$$\left\langle l(k')\middle|j^{\mu}_{\mathrm{em}}(0)\middle|l(k)\right\rangle = q_e\,\bar{u}_l(k')\gamma^{\mu}u_l(k), \tag{2.1}$$

where j^μ_{em} is the electromagnetic current operator and k (k') is the four-momentum of the initial (final) particle. $u_l(k)$ and $\bar{u}_l(k')$ represent the Dirac spinors of the incoming and outgoing particles, which appear in the plane-wave solutions of the Dirac equation. This current is conserved, i.e. $\partial_\mu j^\mu_{\text{em}} = 0$, giving rise to

$$q_\mu \big\langle l(k') \big| j^\mu_{\text{em}}(0) \big| l(k) \big\rangle = 0, \tag{2.2}$$

where $q = k - k'$ is the momentum of the transmitted virtual photon. The Lorentz invariant four-momentum transfer is defined as

$$Q^2 = -q^2 = -(k - k')^2 > 0. \tag{2.3}$$

In contrast to j^μ_{em}, the matrix element of the electromagnetic current operator of the nucleon, J^μ_{em}, as a system of strong interaction particles, cannot be calculated from first principles. Therefore, J^μ_{em} has to be parametrized by the most general structure Γ^μ,

$$\big\langle N(p') \big| J^\mu_{\text{em}}(0) \big| N(p) \big\rangle = e \bar{N}(p')\, \Gamma^\mu\, N(p), \tag{2.4}$$

reflecting the electromagnetic properties of the nucleon, with the Dirac spinors $N(p)$ and $\bar{N}(p')$ of the proton in the initial and final state, respectively.

However, Γ^μ is restricted by Lorentz invariance, parity and charge conservation. The first condition implies that J^μ_{em} has to transform in an analogous manner as j^μ_{em}, which is a Lorentz four-vector, depending only on p and p' or $q = p' - p$. This allows to decompose the hadronic current in terms of Dirac bilinears, which fulfill the given transformation properties. Parity and charge conservation constrain the number of the allowed contributions. In addition, the current J^μ_{em} has to satisfy the conservation of the electromagnetic current. Consequently, the most general decomposition of Γ^μ can be reduced to two independent Lorentz structures, which are introduced in combination with two form factors. Hence, the nucleon electromagnetic current can be expressed as

$$\big\langle N(p') \big| J^\mu_{em}(0) \big| N(p) \big\rangle = e \bar{N}(p') \left[F_1(Q^2)\, \gamma^\mu + F_2(Q^2)\, \frac{i}{2m_N} \sigma^{\mu\nu} q_\nu \right] N(p), \tag{2.5}$$

with the nucleon mass m_N and $\sigma^{\mu\nu} = \frac{i}{2}[\gamma^\mu, \gamma^\nu]$. The form factors F_1 and F_2 are scalar functions of the momentum transfer $Q^2 = -q^2$, the only independent kinematic scalar quantity constructed from p, p' and q for $p^2 = p'^2 = m_N^2$. F_1 and F_2 are known as Dirac form factor (F_1) and Pauli form factor (F_2). Eq. (2.5) describes the parametrization of both currents, the proton as well as the neutron electromagnetic current.

The form factors are defined over the complete range of momentum transfer $-\infty < q^2 < \infty$. In the spacelike region of negative momentum transfer with $q^2 = -Q^2 < 0$, the form factors can be investigated in scattering processes. The corresponding crossed annihilation processes allow to access the form factors in the timelike region ($q^2 > 0$). Section 2.3 deals with the form factors in the timelike regime, whereas this section focuses on the spacelike form factors.

The electromagnetic current operator is a hermitian operator. For spacelike momentum transfer, $q^2 < 0$, this fact gives rise to

$$\big\langle N(p') \big| J^\mu_{\text{em}}(0) \big| N(p) \big\rangle^* = \big\langle N(p) \big| J^{\mu\,\dagger}_{\text{em}}(0) \big| N(p') \big\rangle = \big\langle N(p) \big| J^\mu_{\text{em}}(0) \big| N(p') \big\rangle. \tag{2.6}$$

With

$$\begin{aligned}\langle N(p')|J^{\mu}_{\rm em}(0)|N(p)\rangle^{*} &= e\bar{N}(p)\left[F_1^{*}(Q^2)\,\gamma^{\mu} - F_2^{*}(Q^2)\,\frac{i}{2m_N}\sigma^{\mu\nu}(p'-p)_{\nu}\right]N(p'),\\ \langle N(p)|J^{\mu}_{\rm em}(0)|N(p')\rangle &= e\bar{N}(p)\left[F_1(Q^2)\,\gamma^{\mu} + F_2(Q^2)\,\frac{i}{2m_N}\sigma^{\mu\nu}(p-p')_{\nu}\right]N(p'),\end{aligned} \tag{2.7}$$

one can conclude, that the spacelike form factors must be purely real functions, whereas the timelike form factors have to be treated as complex functions in general.

If Q^2 tends to zero, the photon can only probe the static properties of the nucleon. Therefore the form factors are normalized to the charge and the magnetic moment of the proton and neutron, as

$$\begin{aligned}F_1^p(0) &= 1, \qquad F_2^p(0) = \mu_p - 1 = \kappa_p,\\ F_1^n(0) &= 0, \qquad F_2^n(0) = \mu_n = \kappa_n,\end{aligned} \tag{2.8}$$

where F_i^p and F_i^n are associated with the form factors of the proton and neutron, respectively. $\kappa_{p,n}$ is the anomalous magnetic moment of the corresponding nucleon, given by $\kappa_p = 1.79$ and $\kappa_n = -1.91$.

In some cases it is useful to consider the isoscalar (F_i^S) and isovector (F_i^V) description of the form factors indicating the isospin symmetry properties of the proton and neutron. These factors are defined as

$$F_i^S = \frac{1}{2}\left(F_i^p + F_i^n\right), \qquad F_i^V = \frac{1}{2}\left(F_i^p - F_i^n\right). \tag{2.9}$$

In order to express observables, it is often convenient to use the Sachs form factors G_E and G_M instead of F_1 and F_2, given by the linear combinations

$$\begin{aligned}G_E(Q^2) &= F_1(Q^2) - \tau F_2(Q^2),\\ G_M(Q^2) &= F_1(Q^2) + F_2(Q^2)\,,\end{aligned} \tag{2.10}$$

where τ is defined by $\tau = {}^{-q^2}/_{4m_N^2} = {}^{Q^2}/_{4m_N^2}$. The Sachs form factors are referred to as the electric (G_E) and magnetic form factor (G_M) of the associated nucleon.

In the limit $Q^2 \to 0$ the form factors G_E and G_M have the static values of charge and of the magnetic moments $\mu_{p,n}$ of the proton and neutron, respectively:

$$\begin{aligned}G_{E_p}(0) &= 1, \qquad G_{M_p}(0) = \mu_p = 2.79\\ G_{E_n}(0) &= 0, \qquad G_{M_n}(0) = \mu_n = -1.91.\end{aligned} \tag{2.11}$$

In a particular Lorentz frame, the so-called Breit frame, G_E can be related to the Fourier transform of the spatial charge distribution of the nucleon and G_M to the distributions of the magnetic moments. In this frame, the three-momentum of the initial nucleon is given by -$\vec{q}/2$, while the outgoing nucleon carries $\vec{q}/2$. Since no energy in transferred, the four-momentum of the photon reads $q = (0, \vec{q})$. This leads to a hadronic electromagnetic current of the form

$$\begin{aligned}\left\langle N\left(\vec{q}/2\right)\right| J^0_{\rm em}(0)\left|N\left(-\vec{q}/2\right)\right\rangle &= 2e\,m_N\,G_E(\vec{q}^{\,2}),\\ \left\langle N\left(\vec{q}/2\right)\right| \vec{J}_{\rm em}(0)\left|N\left(-\vec{q}/2\right)\right\rangle &= {\rm i}e\,\chi^{\dagger}_{s'}\left(\vec{\sigma}\times\vec{q}\right)\chi_s\,G_M(\vec{q}^{\,2}).\end{aligned} \tag{2.12}$$

where $\vec{\sigma}$ refers to the Pauli matrices and χ to the Pauli spinors, given in Appendix A, with the helicity of the initial (final) state nucleon λ_p ($\lambda_{p'}$). Accordingly, in analogy to nonrelativistic physics, $G_E(\vec{q})$ measures the Fourier transform of the electric charge distribution $\rho_E(\vec{r})$ and $G_M(\vec{q})$ the Fourier transform of the distribution of the magnetization $\rho_M(\vec{r})$. However, each value of Q^2 requires a particular Breit frame and $\rho_{E,M}(\vec{r})$ are no observables.

The slopes of the form factors in the limit $Q^2 \to 0$ are defined as the electric and magnetic charge radii of the nucleon:

$$< r_E^2 >= -6 \left. \frac{dG_E(Q^2)}{dQ^2} \right|_{Q^2=0}, \qquad < r_M^2 >= \frac{-6}{G_M(0)} \left. \frac{dG_M(Q^2)}{dQ^2} \right|_{Q^2=0}. \tag{2.13}$$

If the momentum transfer tends to infinity, the form factors can be calculated in the framework of perturbative QCD, since the (vanishingly) small coupling constant α_S of the strong interaction allows for a perturbative treatment. Within these calculations, a scaling behavior of the form factors has been derived, giving [15]

$$\begin{aligned} F_1\,(Q^2) &\sim \frac{1}{Q^4}, \qquad & F_2\,(Q^2) &\sim \frac{1}{Q^6}, \\ G_M(Q^2) &\sim \frac{1}{Q^4}, \qquad & G_E(Q^2) &\sim \frac{1}{Q^4}, \end{aligned} \tag{2.14}$$

which are expected to be valid at a sufficiently high momentum transfer.

Alternatively, one can define a set of quark flavor form factors $F_{1,2}^q$ and $G_{E,M}^q$, with $q = u, d, s$ to describe the electromagnetic distribution of each quark flavor inside the nucleon. Contributions of quarks heavier than the strange quark have been neglected, since these are expected to be small. The hadronic current can be rewritten as

$$\begin{aligned} \left\langle N(p') \middle| J^\mu_{\text{em}}(0) \middle| N(p) \right\rangle &= \left\langle N(p') \middle| \sum_{q=u,d,s} Q_q\, \bar{q} \gamma^\mu q \middle| N(p) \right\rangle \\ &= e\, N(p') \left\{ \sum_{q=u,d,s} Q_q \left[F_1^q \gamma^\mu + F_2^q \frac{\mathrm{i}}{2m_N} \sigma^{\mu\nu} q_\nu \right] \right\} N(p) \end{aligned} \tag{2.15}$$

where Q_q is the charge fraction of the quarks, with $Q_u = 2/3$ and $Q_{d,s} = -1/3$. At the quark level, the electromagnetic form factors can be decomposed as

$$\begin{aligned} F_{1,2}^{p,n}(Q^2) &= \sum_{q=u,d,s} Q_q\, F_{1,2}^{q\;p,n}\,(Q^2), \\ G_{E,M}^{p,n}(Q^2) &= \sum_{q=u,d,s} Q_q\, G_{E,M}^{q\;p,n}\,(Q^2), \end{aligned} \tag{2.16}$$

such that $G_{E,M}^{qp}$ ($G_{E,M}^{qn}$) refers to the contribution from different quark flavors q to the form factor of the proton (neutron). Using isospin symmetry, giving rise to $G_E^{up} = G_E^{dn}$, $G_E^{dp} = G_E^{un}$ and $G_E^{sp} = G_E^{sn}$, enables to express the proton and neutron form factors in terms of the quark distributions inside the proton:

$$\begin{aligned} G_{E,M}^p &= \frac{2}{3} G_{E,M}^u(Q^2) - \frac{1}{3} G_{E,M}^d(Q^2) - \frac{1}{3} G_{E,M}^s(Q^2), \\ G_{E,M}^n &= \frac{2}{3} G_{E,M}^d(Q^2) - \frac{1}{3} G_{E,M}^u(Q^2) - \frac{1}{3} G_{E,M}^s(Q^2), \end{aligned} \tag{2.17}$$

where $G_{E,M}^u$, $G_{E,M}^d$ and $G_{E,M}^s$ are the contributions of the u, d and s quarks in the proton. If not mentioned explicitly, omitting the index p, n of the quark form factors refers to the flavor form factors of the proton. Flavor separation of the form factors can be achieved by probing different hadrons.

2.2 Form Factor Investigation using Elastic Electron-Proton Scattering

The elastic scattering process

$$e^-(k) + p(p) \to e^-(k') + p(p') \tag{2.18}$$

in the Born approximation can be described in a frame-independent way by means of the Lorentz-invariant Mandelstam variables. For the given process, they are defined as

$$\begin{aligned} s &= (p+k)^2 = (p'+k')^2, \\ t &= (p'-p)^2 = (k-k')^2 = -Q^2, \\ u &= (p-k')^2 = (p'-k)^2, \end{aligned} \tag{2.19}$$

satisfying the relation

$$s + t + u = \sum_i m_i^2 = 2m_N^2 + 2m_e^2, \tag{2.20}$$

where $\sum_i m_i^2$ corresponds to the sum of the squared masses of all external particles of the process and m_e is the electron mass.

In most cases, it is a good approximation to neglect the mass of the electron in the calculations, as it is much smaller compared to the nucleon mass and the momentum transfer of the process, $m_e^2 \ll m_N^2, Q^2$. If not mentioned otherwise, the formulas have been evaluated in the ultrarelativistic limit for the electron, in which we can take $m_e = 0$.

The invariant amplitude of the scattering process is given by the matrix elements of the leptonic and the hadronic electromagnetic currents connected with a photon propagator:

$$\mathrm{i}\,\mathcal{M} \;=\; e^2\,\bar{u}_l(k')\,\gamma^\nu\,u_l(k)\left(-\frac{\mathrm{i}g_{\nu\mu}}{q^2}\right)\bar{N}(p')\,\Gamma^\mu\,N(p). \tag{2.21}$$

The scattering process is normally discussed in the laboratory frame, presented in Fig. 2.1, where the initial nucleon is at rest and the four-momentum of the incoming electron is given by $k = (E, \vec{k}\,)$, where $\vec{k}$ is conventionally chosen to be in the z-direction. The momentum transfer can be expressed as

$$Q^2 = 2EE'\left(1 - \cos\theta_{\mathrm{lab}}\right), \tag{2.22}$$

where θ_{lab} is the scattering angle of the electron in the laboratory frame and E and E' are the energies of the initial and final electrons, respectively.

The differential cross section can be obtained in the laboratory frame as

$$\left(\frac{d\sigma}{d\Omega}\right)_{\mathrm{lab}} = \left(\frac{1}{4\pi\,m_N\,Q^2}\frac{E'}{E}\right)^2 \overline{|\mathcal{M}|}^{\,2} \tag{2.23}$$

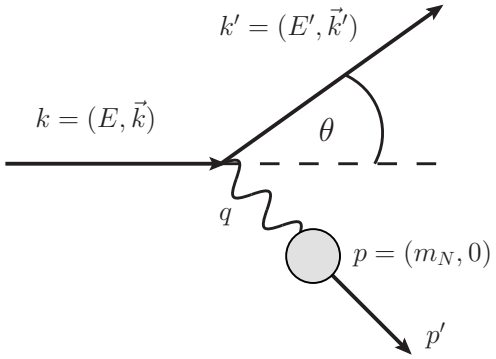

Figure 2.1: Kinematics for elastic *ep*-scattering in the laboratory frame.

with the leptonic solid angle $d\Omega$. The expression $\overline{|\mathcal{M}|}^2$ denotes the spin-averaged squared matrix element of Eq. (2.21).

At present, the most important facilities for form factor investigation using *ep*-scattering are the Mainz Microtron (MAMI), covering the the region of low Q^2, and the Continuous Electron Beam Accelerator Facility (CEBAF) at the Thomas Jefferson National Accelerator Facility (JLab) for the range of higher momentum transfer.

2.2.1 Rosenbluth Separation

Starting with the pioneering work of Hofstadter [7] in the 1950s, the electromagnetic form factors have been investigated in a large number of experiments using the Rosenbluth separation technique. This method allows to extract both form factors, G_E and G_M, from the unpolarized elastic scattering cross section.

The cross section depends on two kinematical variables, typically taken to be the momentum transfer Q^2 (or τ) and the polarization of the virtual photon ε, which is related to the scattering angle θ_{lab} by

$$\varepsilon = \left(1 + 2(1+\tau)\tan^2\left(\frac{\theta_{\text{lab}}}{2}\right)\right)^{-1}. \tag{2.24}$$

In the one-photon exchange approximation, the differential cross section of the reaction can be written in terms of the cross section for scattering off a pointlike particle, the Mott cross section $(d\sigma/d\Omega)_{\text{Mott}}$, and the electric and magnetic form factors:

$$\frac{d\sigma}{d\Omega} = \left(\frac{d\sigma}{d\Omega}\right)_{\text{Mott}} \frac{1}{1+\tau}\left(G_E^2 + \frac{\tau}{\varepsilon}G_M^2\right), \tag{2.25}$$

where $d\sigma/d\Omega$ is the measured cross section. Equation (2.25) is known as the Rosenbluth formula [16]. The Mott cross section is given by:

$$\left(\frac{d\sigma}{d\Omega}\right)_{\text{Mott}} = \frac{\alpha_{\text{em}}^2 \cos^2\left(\frac{\theta_{\text{lab}}}{2}\right)}{4E^2 \sin^4\left(\frac{\theta_{\text{lab}}}{2}\right)} \frac{E}{E'} \tag{2.26}$$

with the fine structure constant $\alpha_{\text{em}} = e^2/4\pi \sim 1/137$.

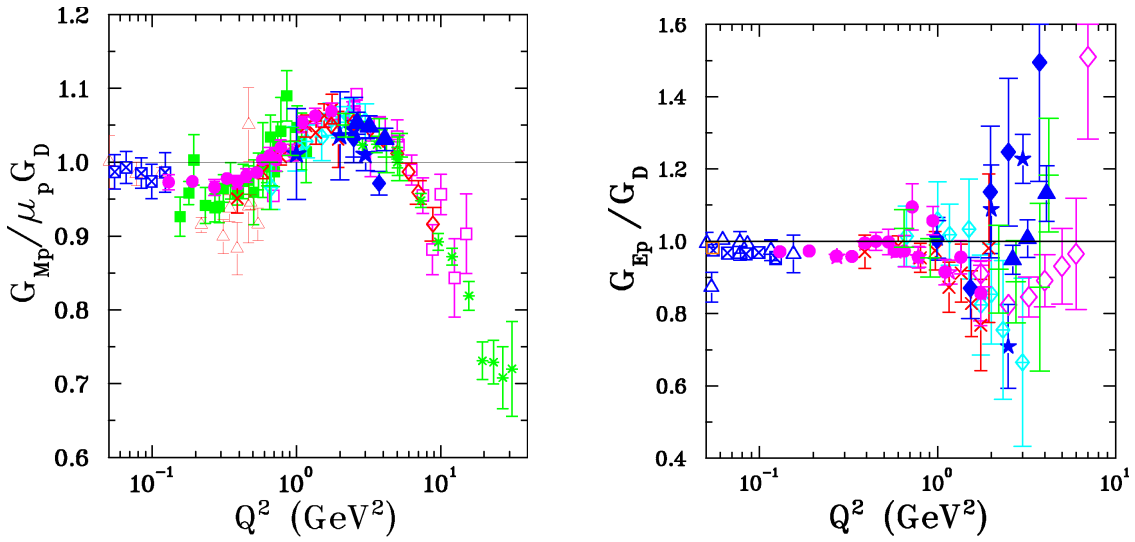

Figure 2.2: Overview of form factor results obtained by Rosenbluth extraction: $G_M/\mu_p G_D$ (left panel) and G_E/G_D (right panel). The figure is adapted from [17].

Besides, it is convenient to define the reduced cross section σ_R:

$$\begin{aligned} \sigma_R &= \frac{\varepsilon(1+\tau)}{\tau}\left(\frac{d\sigma}{d\Omega}\right) \Big/ \left(\frac{d\sigma}{d\Omega}\right)_{\text{Mott}} \\ &= G_M^2 + \frac{\varepsilon}{\tau} G_E^2. \end{aligned} \tag{2.27}$$

Since the form factors G_E and G_M are functions of Q^2 only, measuring the cross section for different values of ε, while keeping Q^2 fixed, allows access to both form factors from the ε dependence of σ_R. A linear fit of σ_R to ε gives G_E from the slope of the ε dependence of the cross section and G_M from the intercept at $\varepsilon = 0$. This so-called Rosenbluth extraction of the form factors requires that the energy of the initial electron and the scattering angle are adjusted in a way that Q^2 is constant while varying the photon polarization ε.

The findings of the Rosenbluth experiments are, that both G_E and G_M follow the form of an approximate dipole form factor G_D:

$$\begin{aligned} G_E(Q^2) &\simeq \frac{G_M(Q^2)}{\mu_p} \simeq G_D(Q^2), \\ \text{with} \quad G_D(Q^2) &= \frac{1}{\left(1 + \frac{Q^2}{0.71\,\text{GeV}^2}\right)^2}. \end{aligned} \tag{2.28}$$

The approximate dipole behavior implies that the form factor ratio can be found as

$$\frac{\mu_p G_E(Q^2)}{G_M(Q^2)} \simeq 1. \tag{2.29}$$

The results of the experiments are collected in Fig 2.2, where the form factors have been divided by the standard dipole G_D. One notices the increasing uncertainties on the extracted

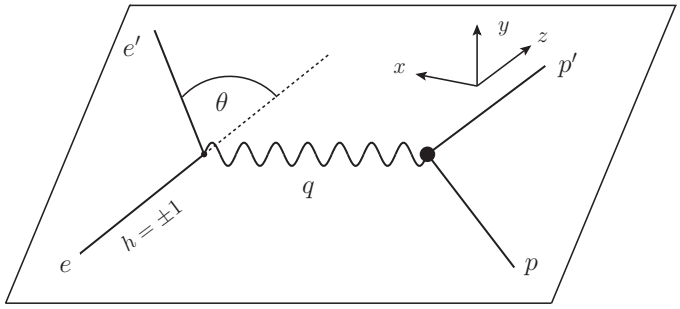

Figure 2.3: Kinematics for polarization transfer from a longitudinally polarized electron on an unpolarized proton in the Born approximation.

values of G_E for large momentum transfer, starting at $Q^2 \sim 1$ GeV^2. As one can see from Eq. (2.27), at large Q^2 ($\tau \gg 1$) the reduced cross section is dominated by the contribution of the magnetic form factor G_M, whereas the contribution of G_E is suppressed with $1/Q^2$. This fact makes an extraction of G_E from the measured cross section increasingly more difficult in the larger Q^2 range, resulting in the rising error bars at larger Q^2, as it is seen in Fig. 2.2.

Besides the reduction of the G_E contribution at larger Q^2 due to the factor $1/\tau$ in Eq. (2.27), the relation $G_M^2 \sim \mu_p^2 G_E^2$ implies an additional suppression factor of ~ 8 independent of Q^2.

2.2.2 Polarization Transfer Measurements

An alternative experimental technique to access the electromagnetic form factors in elastic *ep*-scattering became practical in the late 1990's, the double polarization measurement. This method allows for an investigation of the form factors by scattering a longitudinally polarized electron beam from an unpolarized proton target and measuring the polarization of the recoiling proton,

$$\vec{e}(k) + p(p) \rightarrow e(k') + \vec{p}(p'), \tag{2.30}$$

which will be referred to as polarization transfer method, or equivalently by using a polarized electron beam and a polarized proton target.

The kinematics of the reaction of Eq. (2.30) in the Born approximation is sketched in Fig. 2.3.

In the Born approximation, two non-zero polarization components of the recoiling proton appear, the longitudinal (P_l) and the transverse (P_t) component:

$$\begin{aligned} P_l &= \sqrt{1-\varepsilon^2}(2h)\,\frac{G_M^2}{\sigma_R}, \\ P_t &= -\sqrt{\frac{2\varepsilon(1-\varepsilon)}{\tau}}(2h)\,\frac{G_E G_M}{\sigma_R}, \end{aligned} \tag{2.31}$$

where h is the helicity of the incident electron.

Therefore, the ratio of the polarization components can be related to the ratio of the

electric to magnetic proton form factors:

$$\frac{P_t}{P_l} = -\sqrt{\frac{2\varepsilon}{\tau(1+\varepsilon)}}\frac{G_E}{G_M}. \tag{2.32}$$

The advantage of using the polarization transfer method in order to access G_E/G_M is that for a given Q^2 only one single measurement is necessary, if both polarization components can be measured simultaneously. In the ratio, the electron beam polarization drops out. These facts reduce systematic errors emerging through the variation of the beam energy or scattering angle.

The results of the form factor ratio measurements using the polarization transfer method are at variance with the Rosenbluth extraction of G_E/G_M. This ratio was found to be nearly linear, decreasing with increasing Q^2, in contrast to the well known scaling-behavior of $\mu_p G_E/G_M \sim 1$ determined by the Rosenbluth separation technique. Therefore, as a good approximation the polarization results can be described by a straight line. A linear fit to the results of these experiments leads to [11]

$$\frac{\mu_p G_E(Q^2)}{G_M(Q^2)} = 1 - 0.13\left(\frac{Q^2}{\mathrm{GeV}^2} - 0.04\right), \tag{2.33}$$

demonstrating the remarkable different Q^2 dependence of the form factor ratio, presented in Fig. 2.4.

2.2.3 Discussion of the Discrepancy

The contradicting results of the Rosenbluth and polarization experiments have triggered a lot of effort in order to understand and resolve the discrepancy. In Fig 2.4 the results of the extracted ratio $\mu_p\, G_E/G_M$ of both experimental methods are shown. The deviation between the two techniques starts at values of about $Q^2 \sim 1$ GeV^2 growing with the momentum transfer.

First, it was assumed that the discrepancy arises from uncertainties in the Rosenbluth extraction of the proton form factors, which at high Q^2 is very sensitive to even small corrections due to the small contribution of G_E to the cross section. A global reanalysis of the world cross section data [19] shows that the data from previous Rosenbluth measurements are consistent with each other. It was found, that the discrepancy is not caused by problems in one or two single experimental setups and that the Rosenbluth data cannot be brought into agreement with the results of the polarization transfer method by adjusting the data within the normalization uncertainties.

Furthermore, new data of a high-precision Rosenbluth measurement of G_E/G_M became available [20], in which the final proton instead of the electron has been detected, confirming the results of previous measurements. This detection procedure reduces the systematic uncertainties due to a weaker dependence of the cross section on beam energy and scattering angle.

In addition, the studies focused on the calculation of radiative corrections, which are QED corrections to first order of α_{em} to ep-scattering, caused by the exchange of a second virtual photon or the emission of a real bremsstrahlung photon. The leading-order corrections are illustrated in Fig. 2.5, where the corrections on the electron side (diagrams a-d), which are independent of the nucleon structure, are shown on the left side and the Feynman graphs

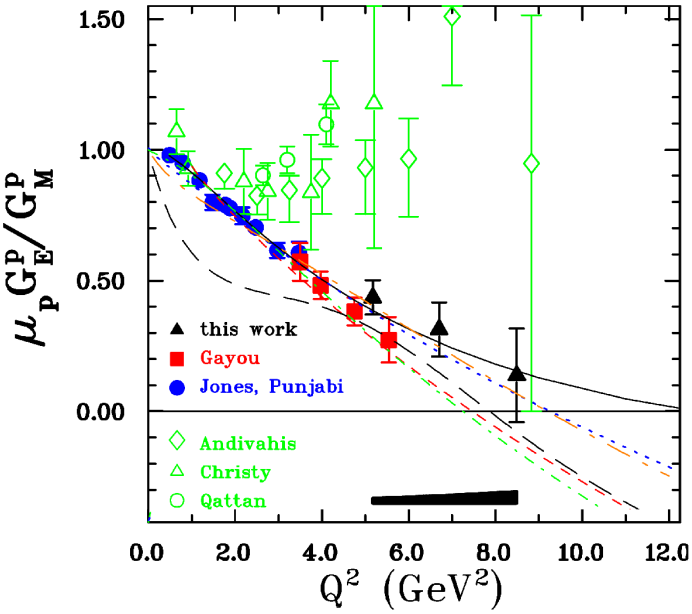

Figure 2.4: Ratio of the electric to magnetic proton form factors as a function of Q^2. The green data points indicate the results of the Rosenbluth extraction. The blue circles, red squares and black triangles are the results of the polarization experiments. The figure is adapted from Ref. [18].

on the right side (diagrams e-h) correspond to the nucleon structure dependent corrections. To obtain results with high accuracy, the measured cross sections need to be corrected for radiative corrections, effecting the cross section typically in the range of 10%-30%. Since these corrections are ε dependent, they can change the slope of the Rosenbluth plot and consequently influence the results of the extracted form factors. Polarization observables, as being ratios of cross sections are less sensitive to radiative corrections, especially the ratio G_E/G_M extracted from polarization transfer measurements, which is a ratio of polarization observables.

Radiative corrections have been applied in the analysis of the cross sections mostly using the standard formalism of Mo and Tsai [21,22]. In these calculations any effect of the proton structure has been neglected, hence only the electron corrections and the corrections on the nucleon side in the soft photon approximation, i.e. when the additional virtual photon carries a vanishing small momentum, have been taken into account and several approximations have been used for the computation. Improvements of the radiative corrections have been performed in Refs. [23–26], such as including hadron structure effects and removing some other assumptions, nevertheless without achieving a reconciliation of both methods. However, it has been shown, that the corrections required to bring the results into agreement are at the level of a few percent of the cross section [19].

One process which has not been included in all previous calculations of radiative corrections is two-photon exchange (Fig. 2.5 h)) in the case that both photons carry non-vanishing virtualities, i.e. both photons are semi-hard or hard. In Ref. [27] it has been shown that taking these corrections into account may lead to significant ε dependent contributions to

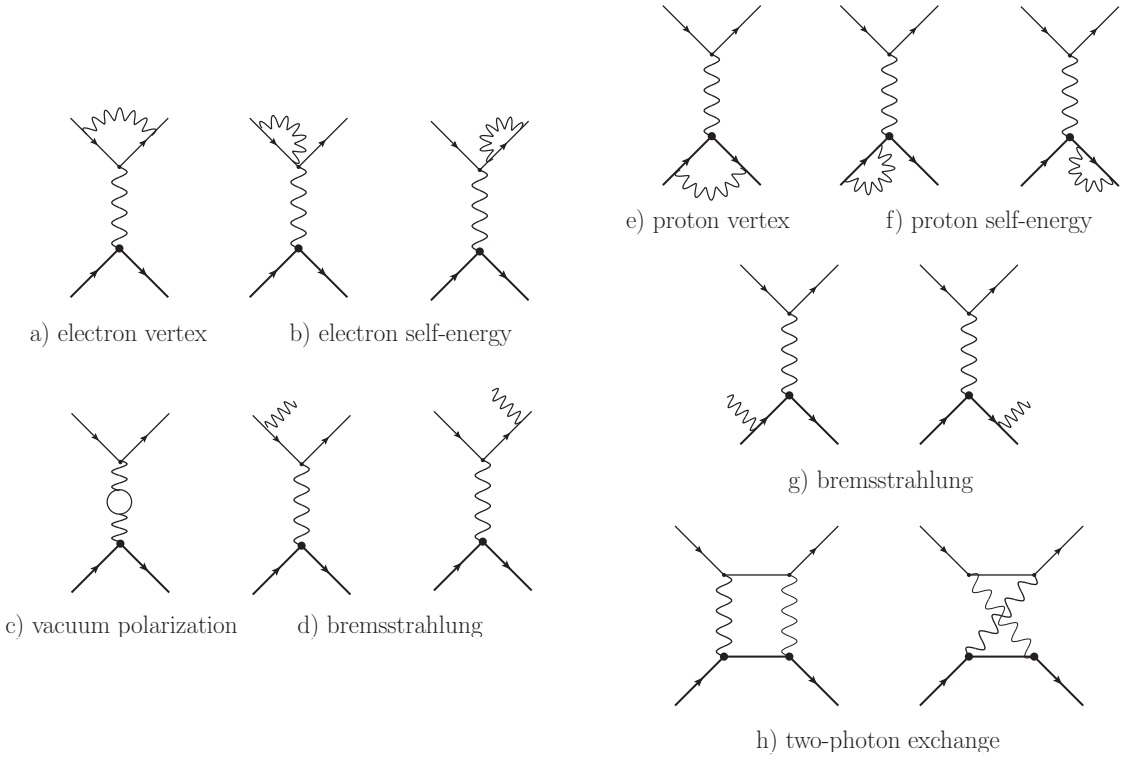

Figure 2.5: Lowest-order radiative corrections for elastic *ep*-scattering: diagrams left (a-d) show the correction graphs for the electron side, diagrams one the right side (e-h) are graphs depending on the hadron structure.

the cross section and provide a possible explanation of the form factor results.

In recent years, two-photon exchange has been studied extensively, from both experimental as well as theoretical side. The following two chapters of this thesis deal with two-photon exchange processes, which will be discussed in the spacelike as well as in the timelike regions of momentum transfer.

2.3 Electromagnetic Form Factors in the Timelike Region

In order to obtain a complete description of the electromagnetic structure of the nucleon, the investigation of the form factors over the full range of momentum transfer is necessary.

The measurements of the nucleon form factors at spacelike momentum transfers, by means of elastic electron proton scattering, are complemented by measurements in the timelike region, through the corresponding crossed processes $p\,\bar{p} \to e^+\,e^-$ or $e^+\,e^- \to p\,\bar{p}$, which allow to access the form factors in the timelike region, starting from the threshold $q^2_{\rm thr} = 4m^2_N$. These processes are related via the crossing symmetry.

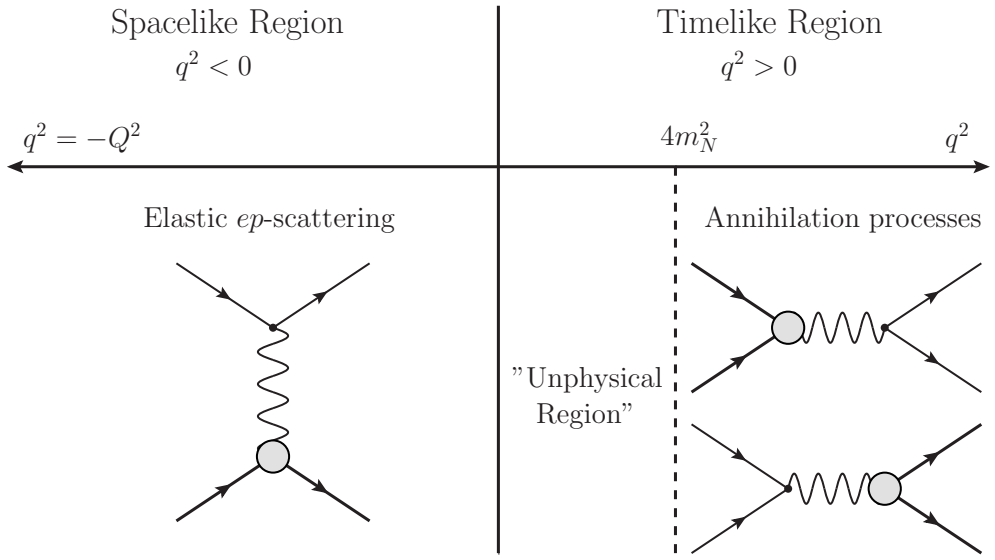

Figure 2.6: Spacelike and timelike regions and the appropriate processes, which can be used to study electromagnetic form factors. In the spacelike region, with momentum transfer $q^2 = -Q^2 < 0$, the form factors can be investigated by means of scattering reactions. For the timelike region, defined by $q^2 > 0$, annihilation processes can be used to access the form factors in the range $q^2 \geq q_{\text{thr}} = 4m_N^2$.

2.3.1 Accessing Form Factors in the Timelike Region

The annihilation reaction $p\,\bar{p} \to e^+\,e^-$ and the time-reserved process $e^+\,e^- \to p\,\bar{p}$ offer the possibility to study the proton electromagnetic form factors in the timelike region. In the Born approximation the interaction is mediated through the exchange of one virtual photon with positive momentum transfer $q^2 > 4m_N^2$, depicted in Fig 2.7.

For investigating the process

$$p(p_1) + \bar{p}(p_2) \to e^-(k_1) + e^+(k_2) \tag{2.34}$$

one can take advantage of the crossing relations, connecting the elastic ep-scattering amplitude with the amplitude of the annihilation process. The crossing symmetry of the spacelike

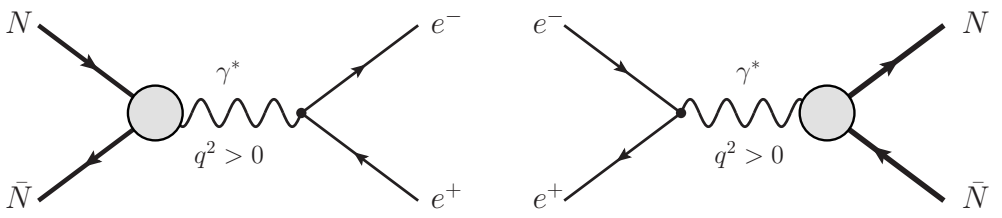

Figure 2.7: The timelike processes $N\bar{N} \to e^-e^+$ and $e^-e^+ \to N\bar{N}$ in Born approximation

and timelike momenta can be found as

$$\begin{aligned} p &\longleftrightarrow \quad p_1, \qquad p' \longleftrightarrow -p_2, \\ k &\longleftrightarrow -k_2, \qquad k' \longleftrightarrow \quad k_1. \end{aligned} \tag{2.35}$$

Introducing the Mandelstam variables of the reaction Eq. (2.34),

$$\begin{aligned} s &= q^2 = (p_1 + p_2)^2 = (k_1 + k_2)^2, \\ t &= (p_1 - k_2)^2 = (p_2 - k_1)^2, \\ u &= (p_1 - k_1)^2 = (p_2 - k_2)^2, \end{aligned} \tag{2.36}$$

enables us to find the following relations with the Mandelstam variables of the spacelike scattering process:

$$\begin{aligned} & \text{timelike} && \text{spacelike} \\ s = q^2 &= (p_1 + p_2)^2 && \longleftrightarrow \quad (p - p')^2 = -Q^2, \\ t &= (p_1 - k_2)^2 && \longleftrightarrow \quad (p + k)^2 = s, \\ u &= (p_1 - k_1)^2 && \longleftrightarrow \quad (p - k')^2 = u, \end{aligned} \tag{2.37}$$

with the variables of the timelike (spacelike) on the left-hand side (right-hand side).

Assuming one-photon exchange, the matrix element of the process can in an analogous manner be expressed by two form factors, e.g. the timelike Dirac form factor $F_1(q^2)$ and Pauli form factor $F_2(q^2)$:

$$i\mathcal{M} \;=\; e^2 \left[\bar{u}(k_1)\gamma^\nu v(k_2)\right] \frac{-ig_{\nu\mu}}{q^2} \left[\bar{N}(p_2)\left(F_1\gamma^\mu - \frac{i}{2m_N}F_2\sigma^{\mu\nu}q_\nu\right)N(p_1)\right], \tag{2.38}$$

where $N(p_1)$ and $\bar{N}(p_2)$ stand for the Dirac spinors of the incoming proton and antiproton, respectively.

Accordingly, one can introduce the timelike electric and magnetic form factors G_E and G_M:

$$\begin{aligned} G_E(q^2) &= F_1(q^2) + \tau F_2(q^2), \\ G_M(q^2) &= F_1(q^2) + F_2(q^2), \end{aligned} \tag{2.39}$$

with $\tau = q^2/4m_N^2$.

In contrast to the spacelike form factors, the form factors in the timelike region are in general complex functions of the momentum transfer q^2.

It is often convenient to study the process $p\bar{p} \to e^+e^-$ in the center-of-mass (c.m.) frame of the reaction. In this reference frame the 3-momenta of the incoming nucleons have opposite direction, the proton conventionally chosen to be in the z-direction, which yields

$$\begin{aligned} p_1 &= \frac{\sqrt{s}}{2}\left(1, 0, 0, \frac{\sqrt{\tau - 1}}{\tau}\right), \\ p_2 &= \frac{\sqrt{s}}{2}\left(1, 0, 0, -\frac{\sqrt{\tau - 1}}{\tau}\right), \end{aligned} \tag{2.40}$$

where $\sqrt{s}$ is the c.m. energy. Identifying the reaction plane with the x-z-plane, allows one to express the momenta of the leptons as

$$\begin{aligned} k_1 &= \frac{\sqrt{s}}{2}\big(1,\ \ \sin\theta\,,\ 0\,,\ \ \cos\theta\,\big), \\ k_2 &= \frac{\sqrt{s}}{2}\big(1,-\sin\theta,\,0\,,-\cos\theta\big), \end{aligned} \tag{2.41}$$

where θ is the c.m. scattering angle of the electron with respect to the proton.

In the ultrarelativistic limit of vanishing lepton masses, the unpolarized differential cross section in the c.m. frame using the Born approximation can be found as,

$$\left(\frac{d\sigma}{d\cos\theta}\right)_{1\gamma} = \frac{\alpha_{\rm em}^2\pi}{8m_N^2\sqrt{\tau(\tau-1)}}\left\{\left|G_M(q^2)\right|^2(1+\cos^2\theta) + \frac{1}{\tau}\left|G_E(q^2)\right|^2\sin^2\theta\right\}, \tag{2.42}$$

depending on the c.m. scattering angle, q^2 and the moduli of the form factors, $|G_M(q^2)|$ and $|G_E(q^2)|$. An individual extraction of $|G_E|$ and $|G_M|$ can be achieved through a measurement of the cross section over a wide range of $\cos\theta$ at fixed q^2.

The total cross section in the 1γ-approximation is obtained by integrating Eq. (2.42) over the c.m. scattering angle, which yields

$$\begin{aligned} \sigma &= \frac{\pi\alpha_{\rm em}}{3m_N^2\sqrt{\tau(\tau-1)}}\left[|G_M(q^2)|^2 + \frac{1}{2\tau}|G_E(q^2)|^2\right] \\ &= \frac{\pi\alpha_{\rm em}}{3m_N^2\sqrt{\tau(\tau-1)}}\left[1+\frac{1}{2\tau}\right]\left|G_{\rm eff}(q^2)\right|^2, \end{aligned} \tag{2.43}$$

where an effective form factor has been introduced, which characterizes the deviation between the total cross section and the cross section one would obtain for an annihilation process with only pointlike particles participating. In terms of $|G_E|$ and $|G_M|$, the effective form factor is given by

$$G_{\rm eff}(q^2) = \sqrt{\frac{2\tau|G_M(q^2)|^2 + |G_E|^2}{2\tau+1}}. \tag{2.44}$$

Most experiments were able to extract the effective form factor from the measured cross section, but not $|G_E|$ and $|G_M|$ separately through a measurement of the angular dependence. Consequently, a statement regarding the individual form factors can only be made by means of assumptions, which link one form factor to the other. Often, the assumptions $|G_E| = |G_M|$ or $G_E = 0$ are used. In Fig. 2.8 the world data set on the effective form factor $G_{\rm eff}$ extracted from different experiments using $p\bar{p} \to e^+e^-$, $e^+e^- \to p\bar{p}$ and $e^+e^- \to p\,\bar{p}\,\gamma$ can be found as a function of q^2. In all cases, the assumption $|G_E| = |G_M|$ has been used to analyze the data, which results in $|G_M| = G_{\rm eff}$.

Only two experiments have performed an individual determination of both form factors, the PS170 experiment at LEAR [29], and the BaBar experiment at SLAC [30,31], where in the latter experiment the form factors have been extracted through the initial state radiation reaction $e^+e^- \to p\,\bar{p}\,\gamma$. The results of the ratio $|G_E/G_M|$, which are presented in Fig. 2.9, include large uncertainties and are not consistent with each other, clearly calling for future experiments.

New measurements of the timelike form factors are planned by the PANDA experiment at the Facility for Antiproton and Ion Research (FAIR) [32] and the BES-III experiment at the

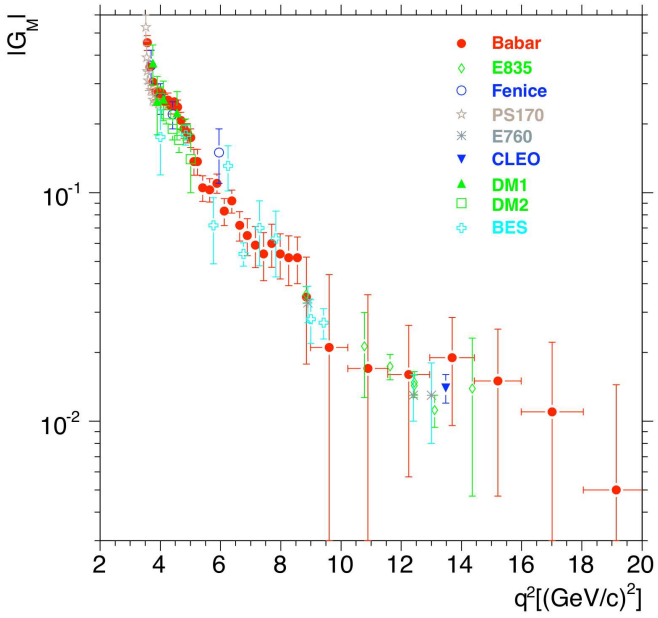

Figure 2.8: Results of the effective form factor measured by various experiments as a function of q^2. The figure is adapted from Ref. [28]. In the analysis the assumption $|G_M| = |G_E| = G_{\text{eff}}$ has been made.

Beijing Electron Positron Collider II (BEPC-II). They will explore the at present still largely uncharted timelike region in much greater detail, bringing values of about $s = 30$ GeV^2 into reach. Those experiments, which also attempt to measure $|G_E|$ and $|G_M|$ separately with high precision, will improve the knowledge of the electromagnetic form factors in the timelike region and complement our picture of the nucleon.

By measuring the unpolarized cross section Eq. (2.42) of the aforementioned annihilation processes, only the moduli of the electromagnetic form factors can be investigated, whereas the phases of the form factors can only be accessed by taking additional observables into account, in particular polarization observables. Due to the complex structure of the nucleon form factors, further polarization observables emerge in the timelike region. For instance, the single-spin asymmetry (SSA), when either the proton or the antiproton is polarized perpendicular to the scattering plane and does not require polarization of the leptons in the final state. The SSA is defined as

$$A_y = \frac{d\sigma^{\uparrow} - d\sigma^{\downarrow}}{d\sigma^{\uparrow} + d\sigma^{\downarrow}}, \tag{2.45}$$

where $d\sigma^{\uparrow}$ ($d\sigma^{\downarrow}$) denotes the cross section for an incoming nucleon with positive (negative) perpendicular polarization. In the case of a polarized proton the asymmetry in the 1γ-approximation reads

$$\begin{aligned} A_y &= -\frac{2\sin\theta\cos\theta\,\mathrm{Im}\,[G_E G_M^*]}{\sqrt{\tau}\,\mathcal{D}} \\ &= -\frac{2\sin\theta\cos\theta\,|G_E||G_M|\sin(\phi_E - \phi_M)}{\sqrt{\tau}\,\mathcal{D}}, \end{aligned} \tag{2.46}$$

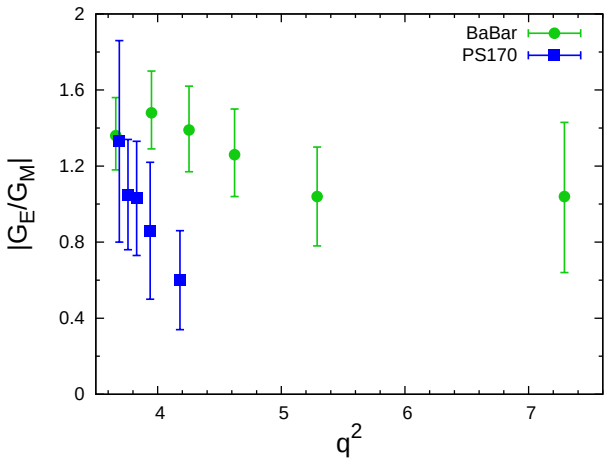

Figure 2.9: Results of the (timelike) form factor ratio $|G_E|/|G_M|$ as a function of q^2: Green circles display the data of the BaBar experiment [31], blue triangles refer to the results of the PS170 experiment [29].

where ϕ_E and ϕ_M correspond to the phases of the electric and magnetic form factors, respectively, and $\mathcal{D}$ is given by

$$\mathcal{D} = |G_M|^2(1+\cos^2\theta) + \frac{1}{\tau}|G_E|. \tag{2.47}$$

Hence, measurements of both, the angular distribution of the unpolarized cross section and the SSA, can be used to get information on the moduli of the electromagnetic form factors as well as their relative phases.

2.3.2 Electromagnetic Form Factors in the Unphysical Region

The timelike region below the $(p+\bar{p})$-threshold, associated with a momentum transfer of $0 < q^2 < 4m_N^2$, is known as the unphysical region, since these values of momentum transfer cannot be accessed by annihilation processes as $p\bar{p} \to e^+e^-$ or $e^+e^- \to p\bar{p}$. Anyhow, it is worth to explore the form factors in that kinematical range, which presumably contains important information concerning the link between the spacelike and timelike regimes. In Fig. 2.10 a comparison of spacelike and timelike form factor data is shown. The gray colored band indicates the unphysical timelike region. Information on the form factors in that kinematical range will certainly improve our understanding of the internal nucleon structure.

Several models predict large contributions of vector meson resonances in the unphysical region, which likewise impact the form factor behavior in the above-threshold region as well as in the spacelike regime. A measurement of the form factor offers the opportunity to constrain and disentangle such models.

Furthermore, the threshold behavior of the nucleon form factors at $q^2 \sim 4m_N^2$ raised attention due to the unexpected sharp rising of the cross section, when approaching the near-threshold region. The enhancement of the cross section entails a strong momentum transfer dependence of the timelike form factors in the q^2 region close to $4m_N^2$, which has not been explained so far.

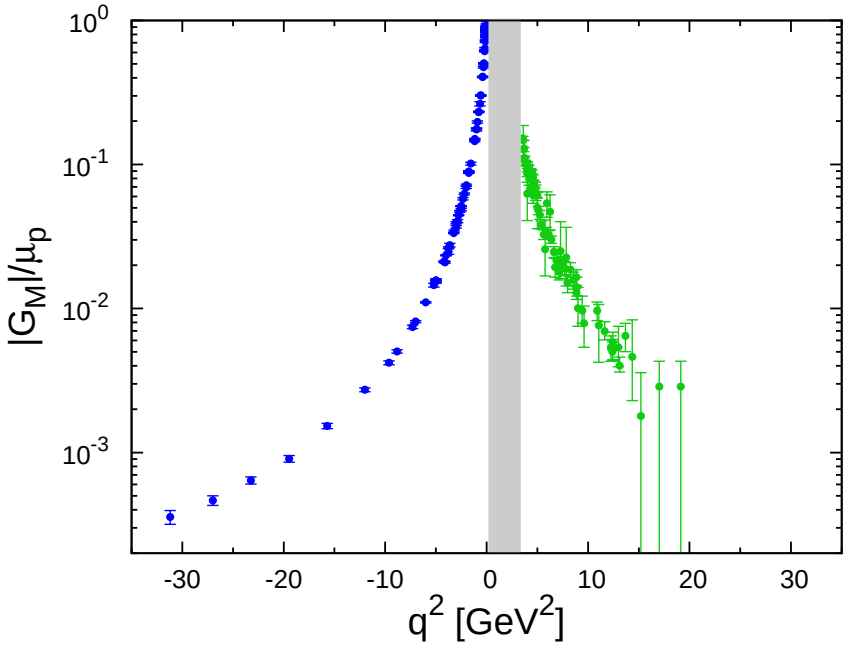

Figure 2.10: Comparison of spacelike and timelike data of the form factors $|G_M|/\mu_p$. The blue data points correspond to G_M/μ_p extracted from Rosenbluth measurements, taken from Refs. [10, 20, 33–38]. The green data points indicate the extracted effective form factor G_{eff}/μ_p in the timelike region measured in the annihilation reactions $p\bar{p} \to e^-e^-$, $e^+e^- \to p\bar{p}$ and $e^+e^- \to p\bar{p}\gamma$. The data is adapted from Refs. [29, 31, 39–44]. The gray shaded area represents the unphysical region $0 < q^2 < 4m_N^2$.

Despite all this, no data of the form factors in the unphysical regions exist so far. But, as a possible way to access the form factors below the threshold, an investigation of the reaction $\bar{p}p \to \pi^0 e^+e^-$ has been proposed in Ref. [45] and of the process $\bar{p}d \to e^+e^-n$ in Ref. [46]. An analysis of the former process with regard to the determination of the form factors will be given in Chapter 6.

2.4 Form Factor Models

In order to calculate observables concerning the electromagnetic structure of the nucleon, parametrizations of the electromagnetic form factors are required. Due to the numerous data sets in the spacelike region, parametrizations based upon fits to the data are commonly used for spacelike form factors, such as the dipole parametrization presented in Eq. (2.28), or an expression of the ratio G_E/G_M as found by fitting the polarization transfer data, e.g. the linear fit given by Eq. (2.33). For instance, one can parametrize G_M by the results obtained in the Rosenbluth separation, for which the extraction is expected to be more accurate than the one of the electric form factors, and G_E is then expressed by the parametrization of G_M and the form factor ratio found in polarization transfer measurements.

Other form factor parametrizations rest upon model descriptions, which attempt to explain the properties of the nucleon form factors. The earliest models of the nucleon form factors

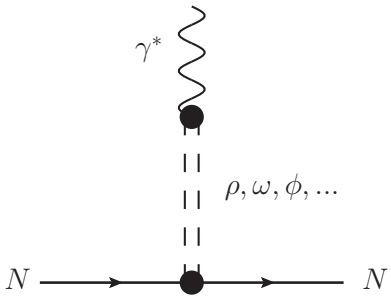

Figure 2.11: VMD coupling of the photon to the nucleon.

are based on vector meson dominance (VMD), corresponding to a photon interacting with the nucleon through the exchange of the lowest lying vector mesons, as shown in Fig (2.11).

In Ref. [47] a VMD based model of the proton and neutron form factors has been presented, where the photon couples to both, an intrinsic structure, given by an intrinsic form factor, and a meson cloud, described within the VMD framework. A form factor model for both spacelike as well as timelike electromagnetic form factors has been presented in Ref. [48], by generalizing the findings of Ref. [47] and including new data for fitting the free parameters of the model. This model is mostly used as parametrization of the timelike electromagnetic nucleon form factor in the calculations presented in this thesis.

The spacelike form factor parametrization of Ref. [48] is given by:

$$\begin{aligned}
F_1^S(q^2) &= \frac{1}{2}\, g(q^2) \left[(1 - \beta_\omega - \beta_\phi) - \beta_\omega \frac{m_\omega^2}{q^2 - m_\omega^2} - \beta_\phi \frac{m_\phi^2}{q^2 - m_\phi^2} \right], \\
F_1^V(q^2) &= \frac{1}{2}\, g(q^2) \left[1 - \beta_\rho - \beta_\rho \frac{m_\rho^2}{q^2 - m_\rho^2} \right], \\
F_2^S(q^2) &= \frac{1}{2}\, g(q^2) \left[(0.12 + \alpha_\phi) \frac{m_\omega^2}{q^2 - m_\omega^2} - \alpha_\phi \frac{m_\phi^2}{q^2 - m_\phi^2} \right], \\
F_2^V(q^2) &= \frac{1}{2}\, g(q^2) \left[-\, 3.706 \frac{m_\rho^2}{q^2 - m_\rho^2} \right],
\end{aligned} \tag{2.48}$$

where

$$g(q^2) = \frac{1}{(1 - \gamma q^2)^2} \tag{2.49}$$

is the intrinsic form factor, characterizing the size of the constituent quarks inside the nucleon. The masses of the vector mesons are $m_\omega = 0.783$ GeV, $m_\phi = 1.019$ GeV and $m_\rho = 0.776$ GeV and the free parameters are obtained by fitting the spacelike data. To take the non-negligible width of the ρ meson into account, the propagator has been replaced as

$$\frac{m_\rho^2}{q^2 - m_\rho^2} \;\rightarrow\; \frac{m_\rho^2 + 8\Gamma_\rho m_\pi/\pi}{q^2 - m_\rho^2 + (q^2 - 4m_\pi^2)\,\Gamma_\rho \alpha(Q^2)/m_\pi}. \tag{2.50}$$

This model has been extended to the timelike region using $Q^2 \rightarrow -q^2$. In addition a phase

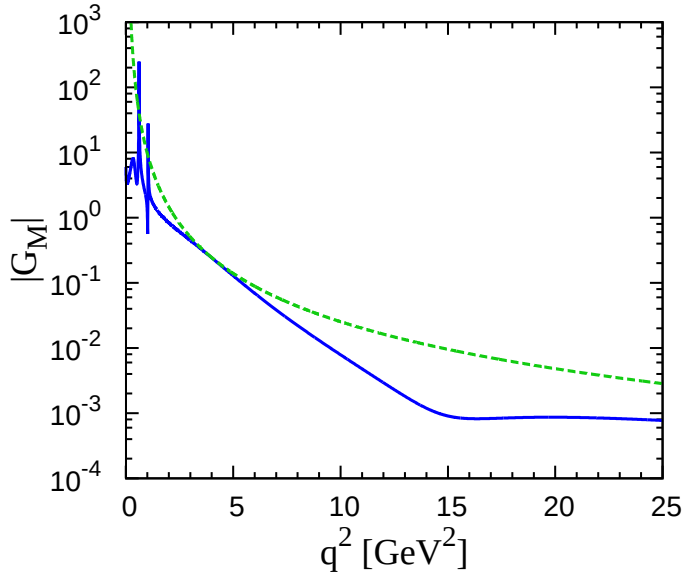

Figure 2.12: Timelike form factor models: blue solid curve: VMD model; green dashed curve: pQCD based model according to Eq. (2.53).

has been introduced to the intrinsic timelike form factors:

$$g(q^2) = \frac{1}{(1 - e^{i\theta}\gamma q^2)^2}, \tag{2.51}$$

where the phase θ is obtained from a fit to the timelike data. Furthermore, the pole of the ρ meson has been modified as

$$\frac{m_\rho^2}{q^2 - m_\rho^2} \;\rightarrow\; \frac{m_\rho^2 + 8\Gamma_\rho m_\pi/\pi}{q^2 - m_\rho^2 + (q^2 - 4m_\pi^2)\Gamma_\rho \alpha(q^2)/m_\pi - \mathrm{i}\Gamma_\rho 4 m_\pi \beta(q^2)}. \tag{2.52}$$

Such a model predicts a resonance structure of the form factors in the unphysical region, due to the interaction of the vector mesons.

Another model, which is also used to parametrize the timelike electromagnetic form factors, is based on the predicted pQCD behavior of the form factors. This model is given by an analytical continuation of the dipole parametrization of the spacelike form factors. The moduli of the form factors are

$$|G_{E,M}| = \frac{\mathcal{B}}{q^4 \left(\ln^2 \frac{q^2}{\Lambda^2} + \pi^2\right)}, \tag{2.53}$$

with $\Lambda = 0.3$ GeV. The parameter $\mathcal{B}$ is a free parameter, in Ref. [49] it was found to be $\mathcal{B} = 56.3$ GeV^2 for the proton and $\mathcal{B} = 77.15$ GeV^2 for the neutron.

In Fig. 2.12 both models, the VMD model and the model based on pQCD behavior are shown for timelike momentum transfers. One can clearly see the predicted resonance structure of the VMD model in the unphysical region arising from the poles of the ρ, ω and ϕ mesons, whereas the pQCD based model gives a smooth behavior of $|G_M|$, steeply rising for $q^2 \to 0$.

Chapter 3

Two-Photon Exchange in Elastic Electron-Proton Scattering

Triggered by the discrepancy between data of unpolarized Rosenbluth measurements and of polarization experiments, in recent years a whole new field studying the influence of two-photon exchange corrections to elastic electron-nucleon scattering emerged, from both experimental and theoretical sides. In this chapter the effects of two-photon (2γ-) exchange in elastic ep-scattering are presented. The general formalism of 2γ-exchange in terms of three generalized (2γ-) form factors is introduced and a brief discussion of existing model calculations as well as observables which are directly related to 2γ-exchange effects is given.

Subsequently, a phenomenological determination of the 2γ-amplitudes from elastic ep-scattering data is presented. Motivated by new high-precision measurements of polarization observables in ep-scattering performed at JLab/Hall C [50], the available cross section and polarization data are used to provide an extraction of the two-photon exchange amplitudes. Furthermore, predictions for the e^+p/e^-p cross section ratio, which is presently under investigation in several experimental setups, are given.

3.1 Electron-Proton Scattering beyond the Born Approximation

In order to calculate the two-photon exchange in elastic electron-proton scattering, we consider the process

$$p(p, \lambda_p) + e^-(k, h) \;\rightarrow\; p(p', \lambda_{p'}) + e^-(k', h'), \tag{3.1}$$

where p (p') and k (k') are the momenta of the initial (final) proton and electron, respectively, and λ_p ($\lambda_{p'}$), h (h') are the corresponding helicities. The 2γ-exchange process is described by the direct and crossed box diagrams presented in Fig. 3.1, where the gray blobs indicate the unknown hadronic interaction of the 2γ-exchange reaction.

For this purpose, we introduce the 4-vectors

$$P^\mu = \frac{1}{2}(p^\mu + p'^\mu), \quad K^\mu = \frac{1}{2}(k^\mu + k'^\mu), \quad Q^\mu = p'^\mu - p^\mu. \tag{3.2}$$

The scattering process can be described by two independent variables, which are chosen to be

$$\nu = K \cdot P, \qquad Q^2 = -q^2 = -(p' - p)^2. \tag{3.3}$$

The invariant Mandelstam variables are defined as

$$s = (p + k)^2, \qquad t = (p' - p)^2 = -Q^2, \qquad u = (p - k')^2, \tag{3.4}$$

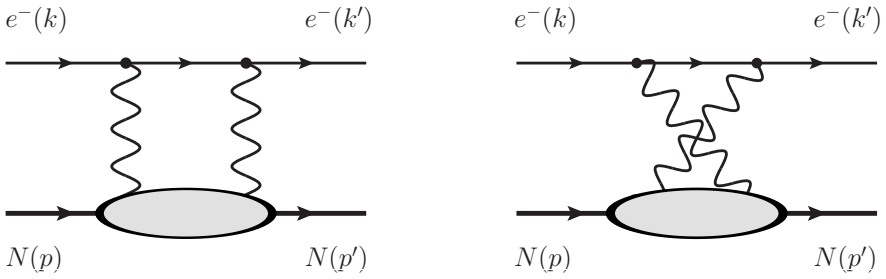

Figure 3.1: Direct and crossed box diagrams of two-photon exchange in elastic electron-proton scattering

giving rise to

$$\nu \;=\; \frac{1}{4}\left(s+u-2m_N^2\right). \tag{3.5}$$

The general concept of two-photon exchange as explanation for the discrepancy between Rosenbluth measurements and polarization experiments has been discussed in Ref. [27]. It has been shown, that taking Lorentz invariance, parity conservation, and charge conjugation into account, the general form of the two-photon exchange diagrams can be written in terms of an effective current-current interaction with one additional structure beyond those that gave G_E and G_M. This expression can be derived starting with the most general expansion of the amplitude $\mathcal{M}$ of elastic *ep*-scattering, permitting the exchange of more than a single photon

$$\mathcal{M} \;=\; e^2\,\bar{u}_l(k')\,\Gamma_{e\,\mu}\,u_l(k)\,\bar{N}(p')\,\Gamma_N^{\mu}\,N(p), \tag{3.6}$$

where the general Lorentz structures Γ_N^{μ} and Γ_e^{μ}, with respect to a set of Dirac bilinears and to the vector basis defined by P^{μ}, K^{μ}, Q^{μ} and $L^{\mu} = \varepsilon^{\mu\nu\rho\sigma}P_{\nu}K_{\rho}Q_{\sigma}$, can be written as

$$\begin{aligned}\Gamma_N^{\mu} &= a_1 1 + b_1\gamma_5 + c_1\gamma^{\mu}K_{\mu} + d_1\gamma_5\gamma^{\mu}K_{\mu}\\ \Gamma_e^{\mu} &= a_2 1 + b_2\gamma_5 + c_2\gamma^{\mu}P_{\mu} + d_2\gamma_5\gamma^{\mu}P_{\mu}.\end{aligned} \tag{3.7}$$

All other structures either do not contribution or can be reduced to the structures above by means of the Dirac equation. Therefore, the matrix can be expanded in terms of 16 Lorentz structures. Taking parity conservation into account reduces the number to 8, since terms containing only one γ_5 are not invariant under parity transformations. In addition, two structures, namely $\bar{u}_l\,\gamma_5\,u_l\,\bar{N}\,\gamma_5\,\gamma^{\mu}K_{\mu}\,N$ and $\bar{u}_l\,\gamma_5\,\gamma_{\mu}P^{\mu}\,u_l\,\bar{N}\,\gamma_5\,N$, are not invariant under CPT transformations , which leads to 6 remaining amplitudes:

$$\begin{aligned}&\bar{u}_l(k')u_l(k)\,\bar{N}(p')N(p), \quad \bar{u}_l(k')u_l(k)\,\bar{N}(p')\gamma^{\mu}K_{\mu}N(p),\\ &\bar{u}_l(k')\,\gamma_{\mu}P^{\mu}\,u_l(k)\,\bar{N}(p')N(p), \quad \bar{u}_l(k')\,\gamma_{\mu}P^{\mu}\,u_l(k)\,\bar{N}(p')\,\gamma^{\nu}K_{\nu}\,N(p),\\ &\bar{u}_l(k')\,\gamma_5\,u_l(k)\,\bar{N}(p')\,\gamma_5\,N(p), \quad \bar{u}_l(k')\,\gamma_5\gamma_{\mu}P^{\mu}\,u_l(k)\,\bar{N}(p')\,\gamma_5\gamma^{\nu}K_{\nu}\,N(p).\end{aligned} \tag{3.8}$$

In the limit of vanishing electron masses, $m_e \to 0$, the helicity of the leptons is conserved, which implies invariance under the chirality transformation $u_l(k) \to \gamma_5 u_l(k)$ and $\bar{u}_l(k') \to$

$-\bar{u}_l(k')\gamma_5$. Structures, which change sign under these transformations, describe a helicity-flip of the electron and are suppressed by a factor m_e. Consequently, we can neglect any structure given in Eq. (3.8), which contains either $\bar{u}_l(k')u_l(k)$ or $\bar{u}_l(k')\,\gamma_5\,u_l(k)$, when assuming $m_e = 0$.

Hence, the scattering process beyond the Born approximation, in the ultra-relativistic limit, can be described by three independent amplitudes. By means of the Dirac equation and elementary relations between the Dirac matrices, the most general matrix element of elastic electron-nucleon scattering can be expressed as [27]:

$$\mathcal{M} = \frac{e^2}{Q^2}\bar{u}_l(k')\gamma_\mu u_l(k)\,\bar{N}(p')\left\{\tilde{G}_M(Q^2,\nu)\gamma^\mu - \tilde{F}_2(Q^2,\nu)\frac{P^\mu}{m_N} + \tilde{F}_3(Q^2,\nu)\frac{\not{K}P^\mu}{m_N^2}\right\}N(p). \tag{3.9}$$

The three generalized form factors $\tilde{G}_M$, $\tilde{F}_2$ and $\tilde{F}_3$ are complex functions of two variables, e.g. Q^2 and ν. Several equivalent representations of Eq. (3.9) exist. In some cases an axial parametrization of the matrix element has been used to calculate the 2γ-exchange processes, where $\tilde{F}_3$ is replaced by an axial-like term $\tilde{G}_A$, using the relation

$$\begin{aligned}\bar{u}_l(k')\not{P}u_l(k)\,\bar{N}(p')\not{K}N(p) \;&=\; \frac{s-u}{4}\,\bar{u}_l(k')\gamma_\mu u_l(k)\,\bar{N}(p')\gamma^\mu N(p)\\ &+\; \frac{t}{4}\,u_l(k')\gamma_\mu\gamma_5 u_l(k)\,\bar{N}(p')\gamma^\mu\gamma_5 N(p).\end{aligned} \tag{3.10}$$

In the following, the representation of Eq. (3.9) will be used. The expressions for the axial-vector expansion of the scattering amplitude can be obtained through a simple transformation of the three generalized form factors.

We also introduce the "electric" amplitude $\tilde{G}_E$, defined as

$$\tilde{G}_E = \tilde{G}_M - (1+\tau)\tilde{F}_2, \tag{3.11}$$

which is commonly used to characterize 2γ-exchange.

To identify the effects caused by multi-photon exchange, the amplitudes $\tilde{G}_M$ and $\tilde{G}_E$ can be written as a decomposition of the usual proton form factor and a form factor which originates from processes including the exchange of at least two photons. The additional third amplitude, $\tilde{F}_3$, vanishes in the one-photon approximation:

$$\begin{aligned}\tilde{G}_M(Q^2,\nu) \;&=\; G_M(Q^2) + \delta\tilde{G}_M(Q^2,\nu)\\ \tilde{G}_E(Q^2,\nu) \;&=\; G_E(Q^2) + \delta\tilde{G}_E(Q^2,\nu)\\ \tilde{F}_3(Q^2,\nu) \;&=\; \delta\tilde{F}_3(Q^2,\nu)\end{aligned} \tag{3.12}$$

The complex amplitudes $\delta\tilde{G}_M$, $\delta\tilde{G}_E$ and $\delta\tilde{F}_3$ are suppressed by α_{em} compared to the electromagnetic form factors G_E and G_M. Using Eq. (3.12), the squared matrix element of the elastic scattering process can be expanded with respect to α_{em}:

$$|\mathcal{M}|^2 = |\mathcal{M}_{1\gamma}|^2 + 2\mathrm{Re}[\mathcal{M}_{1\gamma}^*\mathcal{M}_{2\gamma}] + \mathcal{O}(\alpha_{\mathrm{em}}^2), \tag{3.13}$$

with the electric charge appearing in Eq. (3.9) taken out. The amplitude $\mathcal{M}_{1\gamma}$ is the amplitude of the process in Born approximation and $\mathcal{M}_{2\gamma}$ stands for the amplitude describing 2γ-exchange, which is suppressed by an additional factor α_{em} relative to $\mathcal{M}_{1\gamma}$. Consequently,

the leading order correction to the squared matrix element is given by the real part of the interference of 1γ- and 2γ-exchange processes, $2\mathrm{Re}[\mathcal{M}_{1\gamma}^{*}\mathcal{M}_{2\gamma}]$, which is of order α_{em} compared to the Born contribution. Higher order corrections in α_{em}, e.g. terms $\propto |\mathcal{M}_{2\gamma}|^2$ or contributions caused by the exchange of three or more photons, are neglected in the following calculations.

The reduced cross section including the two-photon exchange corrections calculated up to first order corrections in α_{em} becomes

$$\sigma_R = G_M^2 + \frac{\varepsilon}{\tau} G_E^2 + 2 G_M \mathrm{Re}\left(\delta\tilde{G}_M + \varepsilon \frac{\nu}{m_N^2}\tilde{F}_3\right) + 2\frac{\varepsilon}{\tau} G_E \mathrm{Re}\left(\delta\tilde{G}_E + \frac{\nu}{m_N^2}\tilde{F}_3\right), \quad (3.14)$$

where the first two terms are the reduced cross section in Born approximation given by Eq. (2.27) and the second part is the interference term $\propto 2\mathrm{Re}[\mathcal{M}_{1\gamma}^{*}\mathcal{M}_{2\gamma}]$.

The transverse and longitudinal polarization components can be found as

$$\begin{aligned} P_t &= -2h\frac{1}{\sigma_R}\sqrt{\frac{2\varepsilon(1-\varepsilon)}{\tau}}\left\{G_E G_M + G_M \mathrm{Re}\left(\delta\tilde{G}_E + \frac{\nu}{m_N^2}\tilde{F}_3\right) + G_E \mathrm{Re}\,\delta\tilde{G}_M\right\}, \\ P_l &= 2h\frac{1}{\sigma_R}\sqrt{1-\varepsilon^2}\left\{G_M^2 + 2G_M \mathrm{Re}\left(\delta\tilde{G}_M + \frac{\varepsilon}{1+\varepsilon}\frac{\nu}{m_N^2}\tilde{F}_3\right)\right\}, \end{aligned} \quad (3.15)$$

corresponding to a polarization ratio P_t/P_l:

$$\frac{P_t}{P_t} = -\sqrt{\frac{2\varepsilon}{\tau(1+\varepsilon)}}\frac{G_E}{G_M}\left\{1 - \mathrm{Re}\frac{\delta\tilde{G}_M}{G_M} + \mathrm{Re}\frac{\delta G_E}{G_E} + \frac{\nu}{m_N^2}\mathrm{Re}\tilde{F}_3\left(\frac{1}{G_E} - \frac{2\varepsilon}{1+\varepsilon}\frac{1}{G_M}\right)\right\}. \quad (3.16)$$

In Born approximation, these corrections vanish and the well known expressions for these observables, Eqs. (2.31) and (2.32), are recovered.

The expressions of the observables including the 2γ contributions presented in this section are model-independent. However, the 2γ-amplitudes $\delta\tilde{G}_M$, $\delta\tilde{G}_E$ and $\tilde{F}_3$ cannot be calculated from first principles due to the unknown hadronic interaction. Therefore, different approaches have been used in order to obtain quantitative results for the corrections. Some of these approaches will be discussed in the following.

3.2 Model Calculations of Two-Photon Exchange

Since the form factor discrepancy has been confirmed, several model approaches have been applied to calculate 2γ-exchange corrections to the elastic scattering process, where a few of these approaches will be reviewed in this section.

In the analysis of Ref. [27], it has been demonstrated, that two-photon exchange contributions are able to change the Rosenbluth extraction of G_E in a significant way, affecting the polarization transfer measurements only minimally. The 2γ-exchange corrections to the cross section, as one might expect from perturbation theory, could at large momentum transfer be comparable in size to the term containing G_E^2 in the Rosenbluth cross section and consequently could have a large impact on the extraction of G_E. Furthermore, ε-dependent corrections to the G_M^2 term can appear as well. These results obviously call for further precise calculations.

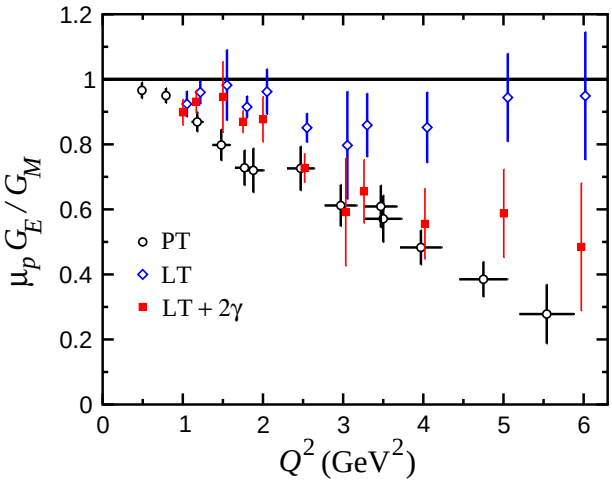

Figure 3.2: Extracted ratio $\mu_p G_E/G_M$ including 2γ-exchange calculated within a hadronic approach using a single nucleon as the hadron intermediate state. Black circles (PT): results of G_E/G_M from polarization experiments; blue diamond (LT): results of G_E/G_M from Rosenbluth experiments; red squares (Lt + 2γ): G_E/G_M from Rosenbluth experiments including the 2γ-corrections. Figure adapted from Ref. [51].

A model calculation of the direct and crossed box diagram of 2γ-exchange within a hadronic approach has been done in Refs. [51–54], using nucleons and resonances as intermediate states to describe the hadronic vertices. In the first calculations [51, 52] only the elastic nucleon intermediate state has been used. The analysis has been extended by first including the $\Delta(1232)$ resonance in the calculation of the 2γ-exchange corrections [53] and later by a larger set of spin-$1/2$ and spin-$3/2$ resonances as intermediate states [54]. The results of two-photon exchange contributions using an elastic nucleon intermediate state are shown in Fig. 3.2. The authors of Refs. [51,52] found, that the elastic nucleon contributions have a large effect on the results of the Rosenbluth extraction and are able to resolve the discrepancy partially. The effect of the Δ and higher mass resonances were found to be small, cancelling the 2γ-exchange contribution of the nucleon intermediate state in part. The hadronic model is limited to low Q^2, where the contributions of the excited intermediate states should be small.

In order to estimate the 2γ-exchange contribution at larger Q^2, a partonic calculation was performed in Refs. [55,56], by relating the so-called generalized parton distributions (GPDs) of the proton to the 2γ-exchange diagrams. Within this factorization approach the amplitude of the process is given as a convolution of a hard subprocess and a soft non-perturbative part, which can be parametrized by the GPDs. The corresponding Feynman diagram in the so-called handbag factorization is illustrated in Fig. 3.3, where in the hard subprocess, indicated by the hard scattering amplitude H, the lepton scatters off one massless quark in the nucleon:

$$e^-(k) + q(p_q) \to e^-(k') + q(p'_q). \tag{3.17}$$

The two-photon contribution to the elastic cross section can be obtained by calculating the 2γ-exchange direct and crossed box diagrams of the electron-quark scattering process.

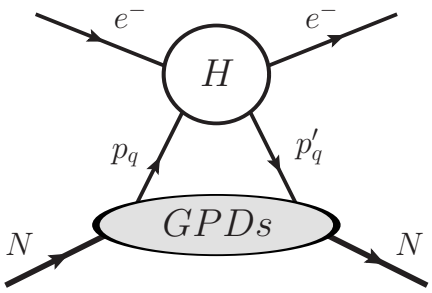

Figure 3.3: Handbag factorization approximation of elastic electron-nucleon scattering: in the hard partonic subprocess H the electron scatters off one single quark in the nucleon. The soft process is parametrized by the GPDs of the nucleon, presented by the lower blob.

Accordingly, the quarks are embedded in the nucleon as described by the GPDs of the proton. This approach is valid at larger values of momentum transfer Q^2 and center-of-mass energy s, with Q^2, $s \gg m_N^2$.

The effect of the hard two-photon corrections on the form factor ratio extracted from unpolarized Rosenbluth measurements is shown in Fig. 3.4. In the Q^2 range of 2-3 GeV^2 the Rosenbluth results including the 2γ-corrections agree with the results from polarization experiments. However, at larger Q^2 the corrections can partially reconcile both methods. The size of the corrections to the polarization results is small and within their experimental uncertainties, thus they are not presented in Fig. 3.4.

In Refs. [57, 58], two-photon exchange has been studied at high Q^2 in the framework of perturbative QCD using the concept of hadron distribution amplitudes (DAs). The amplitude of the process appears as a convolution of a non-perturbative contribution parametrized through the proton DA and a hard kernel H, which can be calculated within perturbative QCD. In the leading-order contribution to the 2γ-exchange, as shown in Fig. 3.5, all three valence quarks participate in the subprocess. The two exchanged photons, which must have large virtualities, couple to different quarks and the third quark interacts via the exchange of a hard gluon. In the calculation of Ref. [57] two different models of DAs have been taken into account. The authors found a 2γ-effect of a few percent, depending on the model for the DAs.

Two-photon exchange effects have been studied in Ref. [59] using the dispersion relation technique for the nucleon form factors. Assuming, that the 2γ-exchange is responsible for the difference between the two methods and that the effect on the polarization ratio is negligible, the dispersion results were found to be in agreement with previous model calculations [51,56]. In Ref. [60] the two-photon exchange amplitude has been computed in the framework of dispersion relations for nucleon intermediate states using on-shell nucleon form factors. The obtained effects are similar to those found within a hadronic approach [51], especially in the smaller Q^2 region.

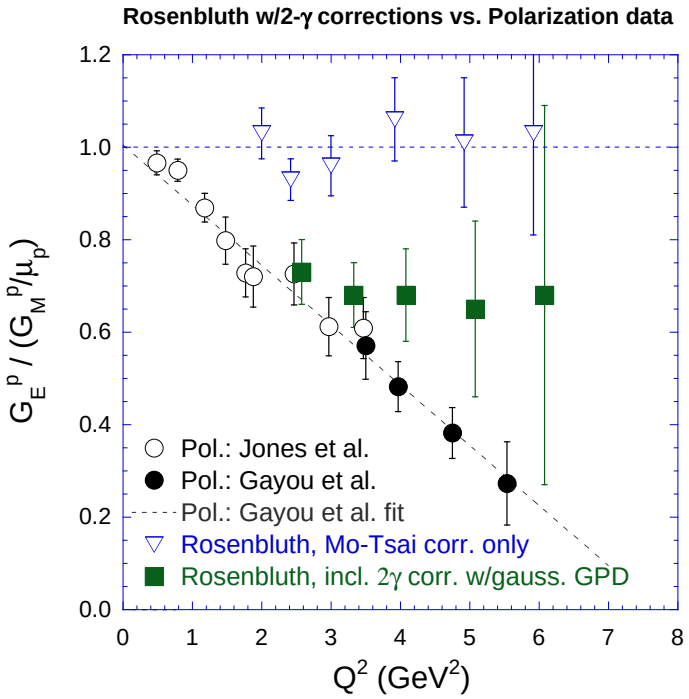

Figure 3.4: Rosenbluth extraction of the form factor ratio R including two-photon exchange corrections obtained by a GPD based partonic approach. The results of the Rosenbluth determination of G_E/G_M including the 2γ-corrections are presented by the filled squares. The polarization data are indicated by the circles and the Rosenbluth extraction without two-photon corrections by blue triangles. The figure is taken from Ref. [56].

3.3 Observables related to Two-Photon Exchange

Besides searching for effects beyond the Born approximation in the Rosenbluth cross sections and polarization transfer experiments, two-photon exchange can be probed using observables which are directly connected with the 2γ-amplitudes. The comparison of positron-proton and electron-proton scattering cross sections allows to access the real part of the 2γ-amplitudes, whereas single spin asymmetries are related to the imaginary part.

3.3.1 Comparison of Positron-Proton and Electron-Proton Scattering

A direct experimental test of the two-photon exchange formalism can be obtained by the comparison of the elastic positron-proton (e^+p) and the elastic electron-proton (e^-p) scattering cross sections. The ratio of these cross sections is defined as:

$$R_{e^+e^-} = \frac{\sigma_R(e^+p \to e^+p)}{\sigma_R(e^-p \to e^-p)}. \tag{3.18}$$

The cross sections in the Born approximation are the same for e^+p and e^-p scattering, but the interference term of the 1γ and 2γ-amplitudes in the cross section changes its sign under

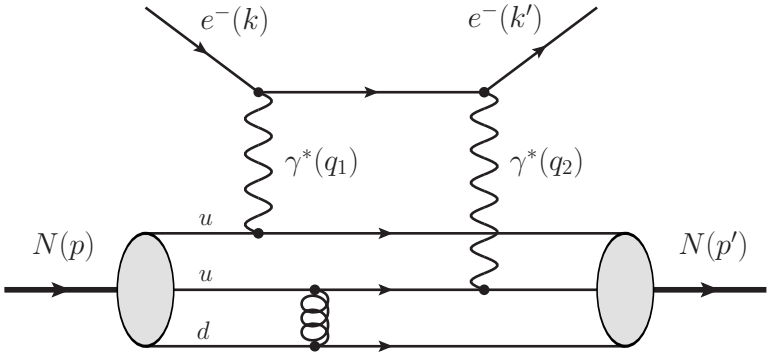

Figure 3.5: One possible diagram for elastic ep-scattering with hard two-photon exchange. The gray blobs correspond to the DAs of the incoming and outgoing nucleon, respectively.

the interchange of e^- and e^+. Therefore the 2γ-exchange contribution appears as a deviation of $R_{e^+e^-}$ from unity. The cross section ratio can be written as

$$\begin{aligned} R_{e^+e^-} &= \frac{|\mathcal{M}_{1\gamma}|^2 - 2\mathrm{Re}[\mathcal{M}_{1\gamma}^* \mathcal{M}_{2\gamma}]}{|\mathcal{M}_{1\gamma}|^2 + 2\mathrm{Re}[\mathcal{M}_{1\gamma}^* \mathcal{M}_{2\gamma}]} \\ &\approx 1 - 2\,\delta_{2\gamma}, \end{aligned} \tag{3.19}$$

where $\delta_{2\gamma}$ is the two-photon exchange contribution to the cross section and $\mathcal{M}_{1\gamma}$ and $\mathcal{M}_{2\gamma}$ are the amplitudes of the 1γ and 2γ processes as discussed in Eq. (3.13). Hence a measurement of $R_{e^+e^-}$ gives direct access to the real part of the 2γ-exchange amplitudes and consequently allows for tests of the two-photon exchange formalism.

Early comparisons of e^+p and e^-p scattering could not yield to a clear constraint on the two-photon exchange effects. The existing data, which have quite large uncertainties, had mostly been taken at low Q^2 and larger values of ε, where the 2γ-corrections are expected to be small. However, new experiments, which attempt to measure $R_{e^+e^-}$ with higher accuracy, are underway. The Olympus experiment at DESY [61], the E07-005 experiment performed at JLab [62], as well as the results taken at the VEPP-III storage ring in Novosibirsk [63], will provide cross section comparisons over a wide kinematic range. The Novosibirsk experiment already reported data for two values of ε and Q^2 [64]:

$$\begin{aligned} R_{e^+e^-} &= 1.0160 \pm 0.011 \quad \pm 0.003, \quad \text{for} \quad \varepsilon = 0.5, \quad Q^2 = 1.43\,\mathrm{GeV}^2 \\ R_{e^+e^-} &= 0.9976 \pm 0.0009 \pm 0.003, \quad \text{for} \quad \varepsilon = 0.95, \; Q^2 = 0.23\,\mathrm{GeV}^2. \end{aligned} \tag{3.20}$$

Further results of these experiments will give insight into the 2γ-formalism and disentangle different models applied for calculating two-photon exchange corrections.

3.3.2 Beam-Normal and Target-Normal Spin Asymmetries

The imaginary part of the two-photon amplitudes can be accessed through a single-spin asymmetry (SSA), when either the target or the beam is polarized normally to the scattering

plane of the reaction. Due to time-reversal invariance, the SSA vanishes in the 1γ-exchange approximation and is suppressed by α_{em}.

The target-normal SSA A_n is defined as

$$A_n = \frac{\sigma_{N\uparrow} - \sigma_{N\downarrow}}{\sigma_{N\uparrow} + \sigma_{N\downarrow}}, \tag{3.21}$$

where $\sigma_{N\uparrow}\,(\sigma_{N\downarrow})$ denotes the cross section for a nucleon spin parallel (anti-parallel) to the direction normal to the scattering plane. A_n is expected to be of order of $\alpha_{\mathrm{em}} \sim 10^{-2}$. It can be expressed through the generalized form factors, which have been introduced in Eq. (3.9),

$$A_n = \sqrt{\frac{2\varepsilon(1+\varepsilon)}{\tau}}\frac{1}{\sigma_R}\left\{-G_M\,\mathrm{Im}\left[\delta\tilde{G}_E + \frac{\nu}{m_N^2}\tilde{F}_3\right] + G_E\,\mathrm{Im}\left[\delta\tilde{G}_M + \frac{2\varepsilon}{1+\varepsilon}\frac{\nu}{m_N^2}\tilde{F}_3\right]\right\}, \tag{3.22}$$

and depends on the imaginary part of the two-photon amplitudes $\delta\tilde{G}_M$, $\delta\tilde{G}_E$ and $\tilde{F}_3$.

Polarizing an ultra-relativistic particle normally to its momentum leads to a suppression of m/E, where m is the mass and E is the energy of the particle. Hence, the beam-normal SSA, which requires a polarized electron beam, is suppressed by an additional factor of $m_e/E_e \sim 10^{-3} - 10^{-4}$ and is expected to be of the order of $\sim 10^{-5} - 10^{-6}$. It vanishes explicitly for $m_e = 0$, as it includes an electron-helicity flip. The general form of the matrix element including the electron-helicity flip, which has been derived in Ref. [65], contains six independent amplitudes, hence three additional structures besides the amplitudes introduced in Eq. (3.9).

3.4 Determination of Two-Photon Exchange Amplitudes from Elastic ep-Scattering Data

3.4.1 Measurement of Effects beyond the Born Approximation in Polarization Transfer Observables

In 2010 the results of the GEp2γ experiment [50], which was performed at JLab/Hall C, have been published. The aim of the experiment was the search for effects beyond the Born approximation in polarized elastic electron-proton scattering. The polarization ratio R, defined by

$$R = -\mu_p\sqrt{\frac{\tau(1+\varepsilon)}{2\varepsilon}}\frac{P_t}{P_l}, \tag{3.23}$$

and the longitudinal polarization component P_l have been measured separately at fixed momentum transfer of $\mathrm{Q}^2 = 2.5$ GeV^2 as a function of ε with high precision.

The results of the experiment can be seen from Fig 3.6. The new data of the ratio R are presented by the filled blue circles in the left plot, together with the results of the polarization ratio from the earlier GEp-I experiment [67] (open triangle). It can be clearly seen that the data of the GEp2γ experiment improve the precision of the previous measurement. No evidence of an ε dependence of the polarization ratio R has been found within the uncertainties of $\sim 1\%$. In contrast, the results of the polarization component P_l/P_l^{Born}, presented in the right panel of Fig 3.6, show an ε dependent behavior, with an enhancement of P_l/P_l^{Born} of 2.3 % $\pm$ 0.6% at $\varepsilon = 0.785$.

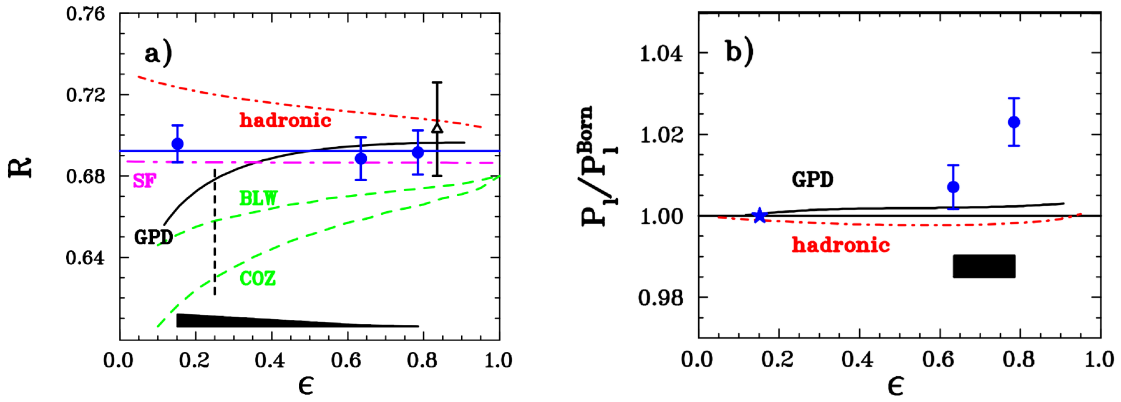

Figure 3.6: Results of the GEp2γ experiment (blue circles) of R (left panel) and P_l/P_l^{Born} (right panel) as a function of ε at $Q^2 = 2.5$ GeV^2. The blue solid line shows a constant fit to the data, the other curves correspond to predictions of different models [51,56,57,66]. The open triangle represents the result of the earlier GEp-I experiment. The star in the right plot indicates the ε value at which the results have been normalized. The systematic uncertainties are presented by the black bands at the bottom of the panels. The figure is adapted from Ref. [50].

In addition, predictions of three theoretical models, which have been discussed in Section 3.2, are presented in Fig. 3.6. One notices, that no model is able to explain both findings of the experiment, the ε independent behavior of R as well as the effect of $\sim 2\%$ on P_l/P_l^{Born} at larger ε values, even though the predicted ε dependence for R of the different models varies significantly. The hadronic model [51] as well as the GPD-based approach [56] and the pQCD calculation [57] find a larger effect on R for smaller values of ε, while the results of the calculations differ in the sign of the two-photon contribution. Furthermore, using the GPD model and the hadronic model, one obtains an insignificant effect on the ε dependence of P_l/P_l^{Born}, which is below 1%.

Only the calculation of radiative corrections of Ref. [66] does not predict any measurable ε dependent effect on R. Within this approach the so-called structure function method has been used to calculate radiative corrections to elastic ep-scattering in quasi-elastic kinematics. The authors of Ref. [66] found, that the 2γ-exchange corrections are negligible, but receive larger contributions through initial state emission. However, several approximations have been applied in the analysis and the results strongly depend on the experimental conditions. To calculate the box-diagrams of two-photon exchange, it has been assumed that both photons carry approximately half of the transferred momentum.

The discussed precise measurement of the polarization observables, which cannot be explained by existing 2γ-exchange model calculations, motivates to extract the two-photon amplitudes from the existing data within a phenomenological approach.

3.4.2 Phenomenological Extraction of Two-Photon Exchange Amplitudes from ep-Scattering Data

For the extraction of the three 2γ-amplitudes $\delta\tilde{G}_M$, $\delta\tilde{G}_E$, and $\tilde{F}_3$, which have been introduced in Eq. (3.9), it is convenient to define the real part of the two-photon amplitudes relative to the magnetic form factor,

$$\begin{aligned} Y_M(\nu,Q^2) &= \mathrm{Re}\left(\frac{\delta\tilde{G}_M}{G_M}\right), \qquad Y_E(\nu,Q^2) = \mathrm{Re}\left(\frac{\delta\tilde{G}_E}{G_M}\right), \\ Y_3(\nu,Q^2) &= \frac{\nu}{m_N^2}\,\mathrm{Re}\left(\frac{\tilde{F}_3}{G_M}\right), \end{aligned} \tag{3.24}$$

since these combinations appear in the expression of the observables.

The reduced cross section of the reaction including the 2γ-corrections divided by G_M^2 then reads

$$\frac{\sigma_R}{G_M^2} = 1 + \frac{\varepsilon}{\tau}\frac{G_E^2}{G_M^2} + 2\,Y_M + 2\varepsilon\frac{G_E}{\tau G_M}\,Y_E + 2\varepsilon\left(1+\frac{G_E}{\tau G_M}\right)Y_3. \tag{3.25}$$

The polarization transfer ratio R in the presence of 2γ-exchange can be written as:

$$\frac{R}{\mu_P} = -\sqrt{\frac{\tau(1+\varepsilon)}{2\varepsilon}}\frac{P_t}{P_l} = \frac{G_E}{G_M} + Y_E - \frac{G_E}{G_M}\,Y_M + \left(1-\frac{2\varepsilon}{1+\varepsilon}\frac{G_E}{G_M}\right)Y_3. \tag{3.26}$$

For P_l separately, its expression relative to the 1γ-result P_l^{Born} of Eq. (2.31) is given by :

$$\begin{aligned} \frac{P_l}{P_l^{\mathrm{Born}}} = 1 - 2\varepsilon\left(1+\frac{\varepsilon}{\tau}\frac{G_E^2}{G_M^2}\right)^{-1} \times \Bigg\{ &\left[\frac{\varepsilon}{1+\varepsilon}\left(1-\frac{G_E^2}{\tau G_M^2}\right)+\frac{G_E}{\tau G_M}\right]Y_3 \\ &+ \frac{G_E}{\tau G_M}\left[Y_E - \frac{G_E}{G_M}Y_M\right]\Bigg\}. \end{aligned} \tag{3.27}$$

For the analysis of the two-photon exchange contribution to elastic electron-proton scattering the data for the ε dependence of P_t/P_l and P_l/P_l^{Born} at Q^2= 2.5 GeV^2 [50] are used, which have been discussed before, and are combined with a high-precision Rosenbluth measurement of σ_R performed at JLab/Hall A [20], where data of the cross section have been taken at a similar value, $Q^2 = 2.64$ GeV^2. Neglecting the small difference between the two values of momentum transfer (2.5 and 2.64 GeV^2), the combination of both experiments allows for having three observables at the same value of Q^2 to extract the three two-photon amplitudes Y_M , Y_E, and Y_3.

Firstly, the data for the polarization ratio R is fitted, which is displayed in Fig. 3.7. The JLab/Hall C experiment does not see any systematic 2γ-effect on P_t/P_l within their error bars of the order of 1%. We performed a fit of $-\mu_p\sqrt{\frac{\tau(1-\varepsilon)}{2\varepsilon}}\frac{P_t}{P_l}$ assuming an ε independent part A, which in the Born approximation equals $\mu_p\frac{G_E}{G_M}$, supplemented an ε dependent part:

$$-\mu_p\sqrt{\frac{\tau(1-\varepsilon)}{2\varepsilon}}\frac{P_t}{P_l} = A + B\varepsilon^c(1-\varepsilon)^d. \tag{3.28}$$

Using a range of values for c and d, it has been found, that the value B is zero within the present error and that the extracted values of A are all equal within their error bars.

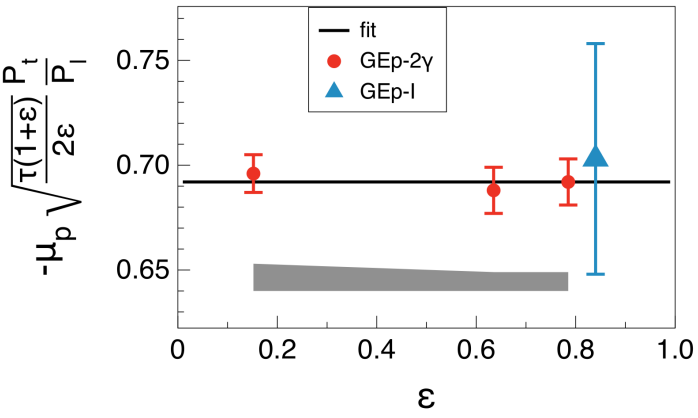

Figure 3.7: The ratio $-\mu_p\sqrt{\frac{\tau(1+\varepsilon)}{2\varepsilon}}\frac{P_t}{P_l}$ as a function of ε for $Q^2 = 2.5$ GeV^2. The data points are from the GEp-I experiment [9,67] (blue triangle) and from the GEp-2γ experiment [50] (red circles): the error bars show the statistical errors, the systematic errors are given by the gray band. The solid curve is an ε independent fit, given by Eq. (3.29).

Therefore we conclude, that the precision of the present data [50] at $Q^2 = 2.5$ GeV^2 does not allow to extract any ε dependent part, in addition to the constant value A.

For this reason, an ε independent fit is used in the analysis, which yields:

$$R = -\mu_p\sqrt{\frac{\tau(1+\varepsilon)}{2\varepsilon}}\frac{P_t}{P_l} = 0.693 \pm 0.006_{\text{stat.}} \pm 0.010_{\text{sys.}}, \tag{3.29}$$

indicated by the solid line in Fig. 3.7.

The fitted value of R can be used in order to extract the ratio G_E/G_M of the 1γ-form factors at $Q^2 = 2.5$ GeV^2, which is a constant at fixed Q^2. These procedure is motivated by the Regge limit assumption, which predicts, that the 2γ-corrections to P_t/P_l vanish for $\varepsilon \to 1$. Hence, in this limit R is directly related to $\mu_p G_E/G_M$. Since we assume that the ratio R is independent of ε for Q^2=2.5 GeV^2, R can be identified with the form factor ratio:

$$R = R(\varepsilon \to 1) = \mu_p \frac{G_E}{G_M}\bigg|_{Q^2=2.5\text{GeV}^2} = 0.693. \tag{3.30}$$

In the next step the longitudinal polarization component is analyzed. P_l is conventionally divided by its 1γ-value P_l^{Born}, which is calculated according to Eq. (2.31), using the value of Eq. (3.30) as input for G_E/G_M. To fit the ε-dependence of P_l/P_l^{Born}, we first specify its behavior for the limits $\varepsilon \to 0$ and $\varepsilon \to 1$, where the 2γ-contributions to P_l are expected to be zero. As can be seen from Eq. (3.27), for the limit $\varepsilon \to 0$ these statement can be derived from the model independent expression of the observable P_l/P_l^{Born} in terms of Y_M, Y_E, and Y_3, giving rise to

$$\frac{P_l}{P_l^{\text{Born}}} \xrightarrow{\varepsilon \to 0} 1. \tag{3.31}$$

The second assumed limiting behavior can again be motivated from the Regge limit assumption for $\varepsilon \to 1$, as discussed above.

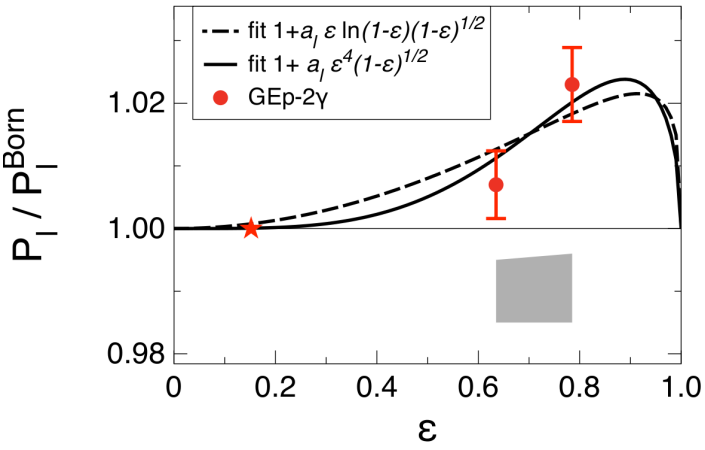

Figure 3.8: The ratio P_l/P_l^{Born} as a function of ε for $Q^2 = 2.5$ GeV^2. The data points are from the $GEp-2\gamma$ experiment [50]: the error bars show the statistical errors, the systematic errors are given by the gray band in the bottom. The star indicates the ε value at which the data have been normalized to the value 1. The two curves correspond to the fits described in Eq. (3.32): Fit 1 (solid curve), Fit 2 (dashed curve).

Furthermore, perturbative QCD calculations of 2γ-exchange corrections [57,58] find, that $P_l/P_l^{\rm Born}$ behaves as

$$\frac{P_l}{P_l^{\rm Born}} - 1 \to \begin{cases} (1-\varepsilon)^{1/2} & \text{for } \varepsilon \to 1. \\ \varepsilon^2 & \text{for } \varepsilon \to 0. \end{cases} \tag{3.32}$$

Nevertheless, the pQCD prediction is not expected to hold accurately at the relatively low value of $Q^2 = 2.5$ GeV^2, so we refer to the pQCD behavior only as an example. Although the data for $P_l/P_l^{\rm Born}$ show a decrease for $\varepsilon \to 0$, the fall-off at $Q^2 = 2.5$ GeV^2 is faster than predicted from pQCD. At this values of Q^2 one expects to receive sizeable corrections to the predicted behavior. Hence, we will not use the exact form of the perturbative QCD prediction, but modify the simple functional form in order to find the best fit to the available data, taking the predicted endpoint behavior into account .

Therefore, as fit of the data for P_l/P_l^{Born} two different, purely phenomenological, functional forms are used, which depend on one parameter a_l:

$$\frac{P_l}{P_l^{\rm Born}} = 1 + \begin{cases} a_l\,\varepsilon^4(1-\varepsilon)^{1/2} & \text{(Fit 1).} \\ a_l\,\varepsilon\ln(1-\varepsilon)(1-\varepsilon)^{1/2} & \text{(Fit 2).} \end{cases} \tag{3.33}$$

The fits to the data, shown in Fig. 3.8, lead to the values

$$\begin{aligned} a_l &= 0.11 \pm 0.03_{\rm stat.} \pm 0.06_{\rm sys.} && \text{(Fit 1).} \\ a_l &= -0.032 \pm 0.008_{\rm stat.} \pm 0.020_{\rm sys.} && \text{(Fit 2).} \end{aligned} \tag{3.34}$$

Now we take a closer look on the Rosenbluth measurements of the reduced cross section. As presented in Fig. 3.9, the precise data of the JLab/Hall A Rosenbluth measurement [20]

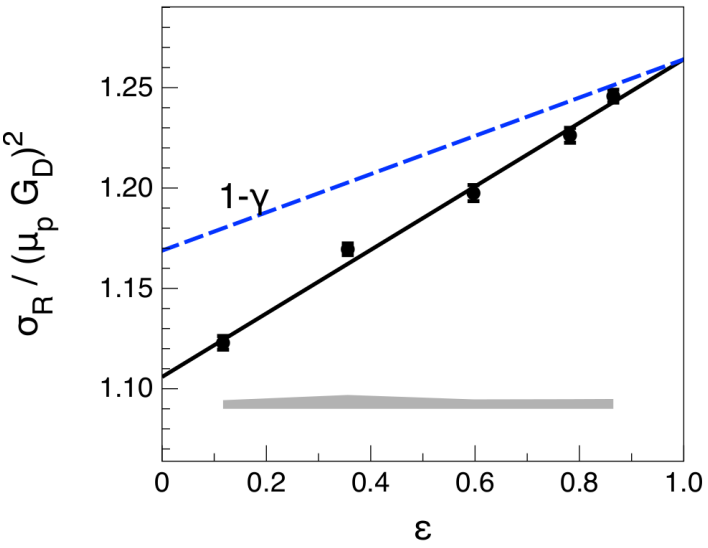

Figure 3.9: Rosenbluth plots for elastic ep-scattering: reduced cross section σ_R divided by $\mu_p^2/(1+Q^2/0.71^2)$ as a function of ε at $Q^2 = 2.64$ GeV^2. Solid curve: linear fit to the JLab/Hall A cross section data (circles) [20]. Dashed curve: Result in the one-photon approximation, using the slope from the polarization data of G_E/G_M. The gray band shows the systematic errors.

of σ_R at Q^2=2.64 GeV^2 show a linear increase of the cross section with respect to ε, therefore

$$\frac{\sigma_R}{(\mu_p G_D)^2} = a + b\varepsilon \tag{3.35}$$

is suggested, where the standard dipole form factor G_D has been factored out, which has defined in Eq. (2.28).

The fit to the data yields

$$a = 1.106 \pm 0.006, \qquad b = 0.160 \pm 0.009. \tag{3.36}$$

For the analysis, the 1γ-form factors G_E/G_M as well as G_M^2 are needed. To extract the 2γ-amplitudes as well as the form factor combinations G_E/G_M and G_M^2 from the three observables, we have to make two assumptions. The first one was made in Eq. (3.28), where the ε independent part gives G_E/G_M, see Eq. (3.30). To fix the value of G_M^2, it has been assumed, that the 2γ-corrections to σ_R vanish in the limit $\varepsilon \to 1$, which is again motivated by the Regge limit and in addition can be found as a result of model calculations of 2γ-exchange, e.g. in Ref. [57]. By means of the aforementioned assumptions, the reduced cross section at $\varepsilon \to 1$ is found as

$$\sigma_R(\varepsilon = 1, Q^2) = G_M^2 + \frac{G_E^2}{\tau}. \tag{3.37}$$

The G_E/G_M value extracted from the fit to P_t/P_l and the fitted values of the parameters a and b entering in Eq. (3.35) allow to fix the value of G_M^2 as

$$\left(\frac{G_M}{\mu_p G_D}\right)^2 = \frac{a+b}{1+\frac{1}{\tau}(G_E/G_M)^2}. \tag{3.38}$$

For $Q^2 = 2.64$ GeV^2 one obtains:

$$\left(\frac{G_M}{\mu_p G_D}\right)^2 = 1.168 \pm 0.010. \tag{3.39}$$

Having specified the fits of the observables P_t/P_l, P_l/P_l^{Born}, and σ_R defined in Eqs. (3.29), (3.32), (3.35), we next proceed to extract the two-photon amplitudes Y_M, Y_E, and Y_3.

The fitting procedure involves three steps. Firstly, a standard χ^2-fit of the data for P_t/P_l (1 parameter), P_l/P_l^{Born} (1 parameters) and σ_R (2 parameters) is performed, using the assumptions of the limit behavior for $\varepsilon \to 1$ and $\varepsilon \to 0$ as described above. Secondly, by solving Eqs. (3.25)-(3.27) with respect to the amplitudes Y_i, the 2γ-amplitude as a function of the fitting parameters and G_M^2 and G_E/G_M are obtained. Thirdly, the 1σ error bands of Y_i are computed from the statistical errors in the fitted observables, again using Eqs. (3.25)-(3.27). In the same way the systematic uncertainties of the data are estimated.

The results are presented in Fig. 3.10, where the 2γ amplitudes as a function of ε are shown including the 1σ statistical error bands. The systematic errors are indicated by the horizontal bands at the bottom of Fig. 3.10. The two differently colored bands correspond to the two different fits, which have been used for P_l/P_l^{Born}, given by Eq. (3.34). One notices, that all three amplitudes are of the order of 2-3 %, which is in agreement with the predicted effects allowing to reconcile the discrepancy as found in Ref. [19].

The amplitude, which is best constrained by the available data, is Y_M. This is because the amplitude Y_M is mainly driven by the 2γ-effects on the cross section, for which several precise data points over a large ε range exist. Neglecting the smaller terms in the cross section, which are multiplied with G_E/G_M, leads to a 2γ-contribution $\sigma_R^{2\gamma}$ of the form

$$\sigma_R^{2\gamma} \;\simeq\; Y_M + \varepsilon\, Y_3, \tag{3.40}$$

dominated by Y_M for smaller values of ε. The error bands on Y_M originating from the two different fits for P_l largely overlap. Except for the region where ε is large, the dominance of Y_M by the Rosenbluth data results in its approximate linear rise with ε. For $\varepsilon \to 1$, Y_M has to become non-linear in order to provide, that $Y_M + \varepsilon Y_3$ remains linear in this limit, which we assumed in our analysis. How far the linearity of the Rosenbluth plot extends when approaching $\varepsilon \to 1$ is an open question, which will be addressed by the results of a dedicated experiment [68].

In contrast to Y_M, the amplitudes Y_E and Y_3 are mainly driven by the polarization data. One notices from Fig. 3.10 that the error bands overlap in the range where data for all three observables exist ($\varepsilon > 0.6$). In the range of smaller ε, where there are less constraints from the polarization data, one sees clear deviations between the two different functional forms for the ε-dependence. We checked, that the same conclusion is reached for other forms of P_l/P_l^{Born}. Hence one can conclude that the available data allow to extract these amplitudes only in the range $\varepsilon > 0.6$.

The amplitudes Y_E and Y_3 are at the 2-3 % level, showing a similar ε dependence, but having opposite sign. This can be explained by having a closer look at the ratio P_t/P_l. One can see from Eq. (3.26), that the leading contribution of 2γ-exchange to P_t/P_l is given by

$$\left(\frac{P_t}{P_l}\right)^{2\gamma} \;\simeq\; Y_E + Y_3. \tag{3.41}$$

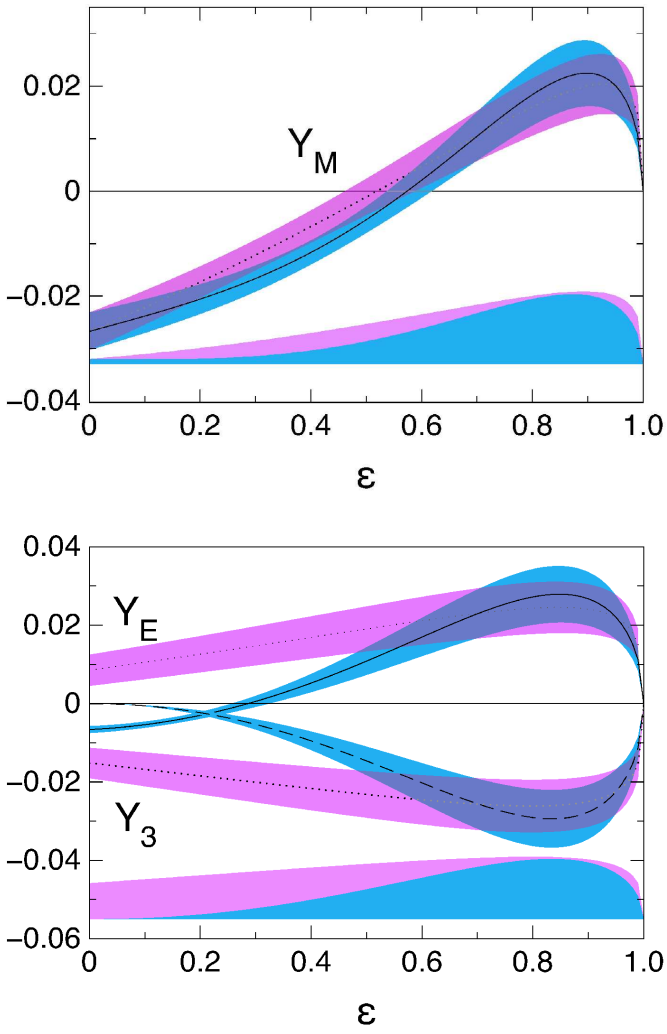

Figure 3.10: Extracted 2γ-amplitudes as a function of ε at $Q^2 = 2.64$ GeV^2 together with their 1σ-error bands. The two different colored bands indicate the fits of P_l/P_l^{Born} as described in Eq.(3.32): Fit 1 (purple bands); Fit 2 (blue bands). The horizontal bands at the bottom of the plots show the systematic errors.

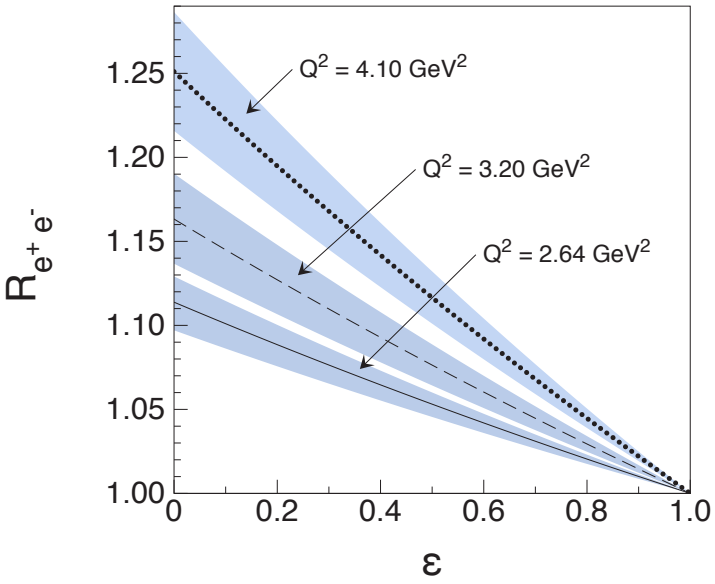

Figure 3.11: Predictions for the e^+p/e^-p elastic cross section ratio $R_{e^+e^-}$ as a function of ε, together with their 1σ error bands.

The absence of 2γ-effects in P_t/P_l implies, that Y_E and Y_3 are of equal magnitude and of opposite sign. Furthermore, the value of Y_3 is nearly entirely driven by the data for P_l, as can be seen from Eq. (3.27). When neglecting the small terms proportional to G_E/G_M, one finds that the observable is given by

$$P_l^{2\gamma} \simeq -2\varepsilon^2/(1+\varepsilon)\, Y_3. \tag{3.42}$$

To improve on the extraction of Y_E and Y_3 will require a further improvement in precision of the polarization experiments and an accurate data set covering a larger range of ε for both polarization observables.

3.4.3 Positron-Proton versus Electron-Proton Scattering

The comparison of positron-proton to electron-proton scattering, discussed in section 3.3.1, provides a defined test of the 2γ-exchange formalism. The e^+p elastic scattering observables are obtained from the ones for e^-p (Eqs. (3.25)-(3.27)) by merely changing the sign in front of the 2γ-amplitudes. Therefore the ratio of the positron-proton to electron-proton elastic scattering cross section $R_{e^+e^-}$, Eq. (3.18), gives rise to the 2γ-contributions to the cross section.

The extracted 2γ-amplitudes at $Q^2 = 2.64$ GeV^2 allowing for predictions of the ratio $R_{e^+e^-}$. The results of $R_{e^+e^-}$ are shown in Fig. 3.11 together with their 1σ error bands, where Fit 1 in Eq. (3.32) has been used. The ratio is dominated over most of the ε range by the amplitude Y_M, which is mainly determined from the cross section, and therefore $R_{e^+e^-}$ depends very weakly on the functional form of P_l. In the previous section, it has been found, that the amplitude Y_M can be reliably extracted from the existing data. Consequently, the present data allow to provide a prediction for $R_{e^+e^-}$ at $\mathrm{Q}^2 = 2.64$ GeV^2 over the full range of ε, under the assumption that the Rosenbluth plot extends linearly all the way up to $\varepsilon \to 1$.

One notices that for $Q^2 = 2.64$ GeV^2, $R_{e^+e^-}$ rises linearly to small ε, reaching $R_{e^+e^-} = 1.053 \pm 0.004$ for $\varepsilon = 0.5$.

Measurements of $R_{e^+e^-}$ are underway at several experiments. The Olympus experiment will cover an ε region of $\varepsilon \sim 0.4$ -0.9 and a momentum transfer up to $\sim Q^2 = 2.25$ GeV^2, measuring $R_{e^+e^-}$ with an aimed accuracy of order of 1%. For the measured range of this experiment, the 2γ-corrections to the e^+p/e^-p elastic cross section ratio are found to vary in the 1 - 6 % range.

In Fig. 3.11, also predictions for two other values of momentum transfer are provided, $Q^2 = 3.20$ GeV^2 and $Q^2 = 4.20$ GeV^2, where the high-precision Rosenbluth experiment at JLab [20] has taken data of σ_R. At these higher values of Q^2, a systematic measurement of the ε-dependence of the polarization observables has not yet been performed. For our analysis of the $Q^2 = 3.2$ GeV^2 and $Q^2 = 4.1$ GeV^2 data, we therefore have assumed that P_t/P_l can be fitted by its 1γ-value proportional to G_E/G_M. One sees from Fig. 3.11, that for a fixed value of ε, the ratio increases with Q^2. Nevertheless, for a detailed analysis of the Q^2 dependence of the 2γ-amplitude and the ratio $R_{e^+e^-}$ precise data for the polarization observables at higher momentum transfer values are needed.

3.5 Conclusions

In this chapter the combined analysis of high-precision Rosenbluth data and considerably measurements of the polarization observables has been performed. This analysis allows for an extraction of the three 2γ-amplitudes using empirical results for the three observables and assuming, that for $\varepsilon \to 1$ the 2γ-amplitudes vanishes. The amplitudes are found to be at the 2-3 % level, where one amplitude (Y_M) can be reliably extracted from the corrections to the unpolarized cross section. Predictions of the e^+p/e^-p cross section ratio can be provided, for which dedicated experiments are underway.

To improve on the extraction, further accurate data, in particular of the polarization observables are required, covering a larger range of ε. If a measurement of the polarization observables at further common values of Q^2 will be performed, conclusions concerning the Q^2 dependence of the 2γ-amplitudes and the e^+p/e^-p cross section ratio can be drawn.

Chapter 4

Two-Photon Exchange in the Timelike Region

A complete understanding of the electromagnetic nucleon structure can only be achieved by complementing the study of the spacelike nucleon form factors by its timelike counterparts.

The elastic scattering process is related to the corresponding annihilation processes via the crossing symmetry. Since two-photon exchange plays a crucial role in the extraction of the spacelike electromagnetic form factors from elastic electron-proton scattering, investigating its influence in the timelike region seems to be an obvious task. Nevertheless, in the timelike region no comparable calculation has been done to determine the two-photon exchange effects for the annihilation processes. However, forthcoming form factor measurements at PANDA@FAIR or BES-III are aiming precisions that can be comparable in size to the two-photon exchange corrections. With the prospect of such high-accuracy measurements, a detailed knowledge of corrections, as two-photon exchange, is necessary.

In this chapter the influence of two-photon exchange on the timelike annihilation reactions $p\bar{p} \to e^+e^-$ and $e^+e^- \to p\bar{p}$ is studied. Firstly, the general properties of timelike 2γ-exchange processes are presented in terms of generalized two-photon amplitudes, similarly to the amplitudes introduced in chapter 3. Since a quantitative determination of the 2γ-amplitudes cannot be achieved from first principles, one has to resort to model descriptions. In this chapter, two different approaches will be discussed, both based on the principle of factorization. This basic concept describes the possibility to separate (factorize) soft and hard momenta in the amplitude, which schematically can be expressed as

$$\mathcal{M} = \mathcal{M}_{\text{soft}} \otimes \mathcal{M}_{\text{hard}} \ + \mathcal{O}\left(1/Q\right), \tag{4.1}$$

where $\otimes$ stands for a convolution. The hard part of the amplitude can be calculated perturbatively, whereas the soft part, which contains information on the internal structure of the nucleon, has to be handled phenomenologically. The variable Q denotes a large scale and the expression $\mathcal{O}\left(1/Q\right)$ indicates, that the factorized amplitude receives corrections from terms which are suppressed in the $1/Q$ expansion. In the factorization model the fast-moving proton and antiproton behave as a set of free partons. This allows to compute the process as a convolution of the annihilation reaction performed at the parton-level and the distribution functions for finding the corresponding partonic configuration in the nucleon.

For the purpose of studying two-photon exchange effects for the process $p\bar{p} \to e^-e^+$, we consider two different models. First, the 2γ-exchange corrections at large momentum transfer are analyzed within the framework of pQCD, where the concept of nucleon Distribution Amplitudes (DAs) is introduced in order to deal with the soft part of the amplitude. Moreover, as an alternative approach, an estimate of the 2γ-effects within a partonic calculation is

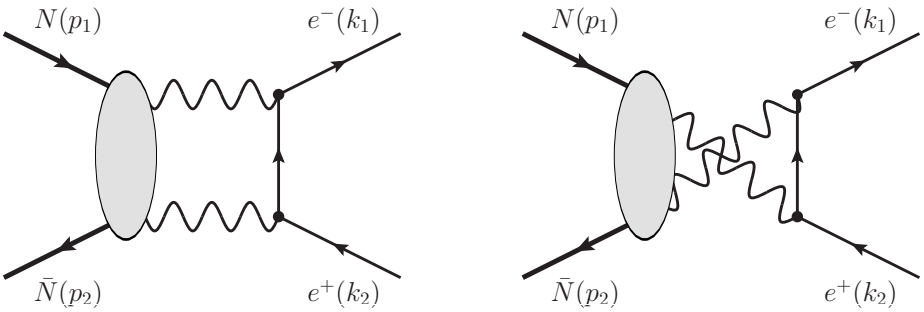

Figure 4.1: Direct and crossed box diagrams of the timelike 2γ-exchange in the annihilation process $p\bar{p} \to e^- e^+$

given, where the 2γ-exchange process is related to the Generalized Distribution Amplitudes (GDAs), the timelike analogon of the Generalized Parton Distributions.

4.1 Timelike Two-Photon Exchange: General Formalism

For the analysis of the 2γ-exchange in the timelike region, we consider the annihilation process of a proton and a antiproton into a lepton pair,

$$p(p_1, \lambda_{N_1}) + \bar{p}(p_2, \lambda_{N_2}) \to l^-(k_1, h_1) + l^+(k_2, h_2), \tag{4.2}$$

where the momenta of the proton (antiproton) and lepton (antilepton) are given by p_1 (p_2) and k_1 (k_2), and λ_{N_1}, λ_{N_2}, h_1 and h_2 denote the helicities of the nucleons and leptons, respectively. The two-photon exchange corrections are given by the direct and crossed box diagrams in Fig. 4.1. We will concentrate on the $p\bar{p}$-annihilation process, but the results for the reversed reaction, $e^+ e^- \to p\bar{p}$, can easily be inferred from these calculations.

In order to describe the process, we introduce the variables

$$q^2 = (p_1 + p_2)^2, \qquad P^\mu = \frac{p_1^\mu - p_2^\mu}{2}, \qquad K^\mu = \frac{k_1^\mu - k_2^\mu}{2}, \tag{4.3}$$

and the Mandelstam variables

$$s = q^2 = (p_1 + p_2)^2, \quad t = (p_1 - k_2)^2, \quad u = (p_1 - k_1)^2. \tag{4.4}$$

The annihilation process can be described through two independent kinematical invariants, which are chosen as variables q^2 and t.

In the 1γ-exchange approximation the cross section, given by Eq. (2.42), depends on the electric and magnetic form factor as

$$\left(\frac{d\sigma}{d\cos\theta}\right)_{1\gamma} \propto \left[\left|G_M(q^2)\right|^2(1+\cos^2\theta) + \frac{1}{\tau}\left|G_E(q^2)\right|^2\sin^2\theta\right]. \tag{4.5}$$

As for the spacelike scattering process, the part of the cross section containing $|G_E(q^2)|^2$ is suppressed for larger momentum transfer by $1/q^2$. Hence, an extraction of both form factors from the measured cross section at larger q^2 values is very sensitive to even small corrections

as 2γ-exchange, in particular when one of the form factors contributes only a few percent to the cross section.

Similarly to the spacelike analysis, for vanishing lepton masses the matrix element including multi-photon exchange can be parametrized by three independent generalized form factors. Using crossing relations, the amplitude including multi-photon exchange can be found as

$$\begin{aligned}\mathcal{M} = & -\frac{e^2}{q^2}\,\bar{u}(k_2,h_1)\,\gamma_\mu\,v(k_1,-h_1)\\ & \times\ \bar{N}(p_2,\lambda_{N_2})\left[\tilde{G}_M(q^2,t)\,\gamma^\mu - \tilde{F}_2(q^2,t)\,\frac{1}{m_N}P^\mu + \tilde{F}_3(q^2,t)\,\frac{1}{m_N^2}P^\mu \not{K}\right] N(p_1,\lambda_{N_1}),\end{aligned} \tag{4.6}$$

where neglecting the masses of the leptons implies, that the electron and the positron have opposite helicities. The generalized form factors $\tilde{G}_M$, $\tilde{F}_2$ and $\tilde{F}_3$ are complex functions of q^2 and t. One can equivalently introduce

$$\tilde{G}_E(q^2,t) \ \equiv\ \tilde{G}_M(q^2,t) - \big(1-\tau\big)\tilde{F}_2(q^2,t). \tag{4.7}$$

In order to identify the 1γ- and 2γ-exchange contributions, it is convenient to use the decompositions

$$\begin{aligned}\tilde{G}_M(q^2,t) \ &\equiv\ G_M(q^2) + \delta\tilde{G}_M(q^2,t),\\ \tilde{G}_E(q^2,t) \ &\equiv\ G_E(q^2) + \delta\tilde{G}_E(q^2,t),\\ \tilde{F}_3(q^2,t) \ &\equiv\ \delta\tilde{F}_3(q^2,t),\end{aligned} \tag{4.8}$$

where, like in the spacelike region, the form factors $\delta\tilde{G}_M(q^2,t)$, $\delta\tilde{G}_E(q^2,t)$, and $\delta\tilde{F}_3(q^2,t)$ are complex functions, corresponding to processes where at least two photons are exchanged and G_E and G_M are the timelike electromagnetic form factors, introduced in Eq. (2.39). The 2γ-amplitudes are suppressed by $\alpha_{\rm em}$ compared to the 1γ-form factors.

The process is considered in the c.m. frame of the nucleon pair, with the momenta given by Eqs. (2.40) and (2.41). The variable t can be related to the c.m. scattering angle θ between the incident proton and the outgoing electron through

$$t = m_N^2 - \frac{s}{2}(1+\cos\theta). \tag{4.9}$$

The cross section including the leading order 2γ-exchange corrections can be expressed as

$$\begin{aligned}\left(\frac{d\sigma}{d\cos\theta}\right) \ = \ & \frac{\alpha_{\rm em}^2\pi}{8m^2\sqrt{\tau(\tau-1)}}\Bigg\{|G_M|^2(1+\cos^2\theta) + \frac{1}{\tau}\,|G_E|^2\sin^2\theta\\ & +\ 2{\rm Re}\big[G_M\,\delta\tilde{G}_M^*\big](1+\cos^2\theta) + 2\,\frac{1}{\tau}\,{\rm Re}\big[G_E\,\delta\tilde{G}_E^*\big]\sin^2\theta\\ & +\ 2\Big({\rm Re}\big[G_M\,\tilde{F}_3^{\,*}\big] - \frac{1}{\tau}{\rm Re}\big[G_E\,\tilde{F}_3^{\,*}\big]\Big)\sqrt{\tau(\tau-1)}\cos\theta\sin^2\theta\Bigg\}.\end{aligned} \tag{4.10}$$

In the 1γ-exchange approximation, only the first line of Eq. (4.10) contributes to the cross section and the expression reduces to the well known formula of the unpolarized cross section, given by Eq. (2.42). The second part of Eq. (4.10) represents the interference of 1γ- and 2γ-exchange processes. Due to the complex nature of the timelike form factors, the cross section depends on the real as well as on the imaginary parts of the two-photon amplitudes.

As discussed in Ref. [69], the 2γ-amplitudes have a defined behavior with respect to the c.m. scattering angle θ:

$$\begin{aligned} \delta\tilde{G}_{E,M}(Q^2,-\cos\theta) &= -\delta\tilde{G}_{E,M}(Q^2,\cos\theta), \\ \tilde{F}_3(Q^2,-\cos\theta) &= \tilde{F}_3(Q^2,\cos\theta), \end{aligned} \tag{4.11}$$

which can be derived from the $\mathcal{C}$-invariance of the electromagnetic hadronic current. Consequently, the two-photon contribution to the cross section, as presented in Eq. (4.10), is an odd function with respect to the transformation $\cos\theta \leftrightarrow -\cos\theta$, in contrast to the Born cross section, which in an even function of $\cos\theta$. Hence, the forward-backward asymmetry, defined by

$$A_{\cos\theta} = \left(\frac{d\sigma}{d\cos\theta}\right)(\cos\theta) - \left(\frac{d\sigma}{d\cos\theta}\right)(-\cos\theta) = 2\left(\frac{d\sigma}{d\cos\theta}\right)_{2\gamma}(\cos\theta), \tag{4.12}$$

allows a direct extraction of the two-photon exchange corrections from the measured cross sections, where $(d\sigma/d\cos\theta)_{2\gamma}$ refers to the 2γ-contributions of $(d\sigma/d\cos\theta)$.

The forward-backward asymmetry have been analyzed in Ref. [70] using the available data of the process $p\bar{p} \to e^+e^-\gamma$ of Ref. [30], which have been taken in the energy range of $q^2 \sim 4 - 7.3$ GeV^2. No systematic θ dependence has been observed within the uncertainties of the experiment and an averaged value of the asymmetry over the measured range has been found as $A_{\cos\theta} = 0.01 \pm 0.02$. However, since the present data have large uncertainties, more data with higher accuracy are needed for a detailed analysis of the forward-backward symmetry.

The unpolarized cross section allows to access the absolute value of the timelike form factors. Their phases can be investigated by means of polarization observables. These observables can be affected by two-photon exchange corrections as well, even though the effect is expected to be small. One observable enabling access to the imaginary part of the electric and magnetic form factor, is the single spin asymmetry, Eq. (2.45), when either the proton or antiproton is polarized normally to the scattering plane, which does not require a polarization of the leptons in the final state. In the case of a polarized proton the single spin asymmetry including 2γ-exchange corrections up to next order in $\alpha_{\rm em}$ is given by

$$\begin{aligned} A_y = -\frac{1}{\sqrt{\tau}\,\mathcal{D}}\, 2\sin\theta \Bigg\{ & \Big(\mathrm{Im}[G_E G_M^*] + \mathrm{Im}[G_E \delta\tilde{G}_M^*] + \mathrm{Im}[\delta\tilde{G}_E G_M^*]\Big)\cos\theta \\ & + \sqrt{\tau(\tau-1)}\Big(\mathrm{Im}[G_M \tilde{F}_3^*]\cos^2\theta + \mathrm{Im}[G_E \tilde{F}_3^*]\sin^2\theta\Big)\Bigg\}, \end{aligned} \tag{4.13}$$

with

$$\mathcal{D} = |G_M|^2(1+\cos^2\theta) + \frac{1}{\tau}|G_E|.$$

In contrast to spacelike processes, the SSA A_y in the timelike region does not vanish in the Born approximation. Hence, the two-photon exchange appears in the asymmetry only as a correction term.

Additional possibilities for extracting the phases of G_E and G_M can be offered by double polarization measurements, when both the proton and the antiproton are polarized. Two-photon exchange corrections to double polarization observables in terms of the 2γ-amplitudes $\delta\tilde{G}_E$, $\delta\tilde{G}_M$, and $\tilde{F}_3$ can be found in Ref. [71].

4.2 Timelike Two-Photon Exchange Corrections at Large q^2: Perturbative QCD Result

The description of the timelike 2γ-exchange corrections presented in the previous section is model independent, as it is derived from the general effective current-current expression (Eq. (4.6)). However, for a quantitative determination of the 2γ-amplitudes a model approach is needed. Only one model calculation of timelike 2γ-exchange corrections has been performed so far, namely a hadronic approach [72] using a nucleon as intermediate state in the box graphs, which is expected to be applicable only in the region of small values of momentum transfer.

Due to the fact, that the planned high precision measurements of the timelike form factors attempt to achieve values of momentum transfer of $q^2 \sim 30$ GeV^2 and based on the experience, that 2γ-exchange affects the spacelike form factor extraction particularly at larger momentum transfer, we take a model description into account, which is suitable to study 2γ-exchange corrections at higher values of q^2. This approach is based on the principle of QCD factorization giving rise to the nucleon distribution amplitudes, which will be firstly introduced. Subsequently, the computation of the timelike 2γ-exchange within this approach will be presented.

4.2.1 Nucleon Distribution Amplitudes and Perturbative QCD Factorization Approach

For the study of exclusive high-energy processes the concept of factorization has successfully been used, which allows to separate the short-distance and long-distance physics. The idea behind this is, that for processes with higher momentum transfer the hadrons can be considered as defined partonic states for the short period of interaction.

Based on the factorization scheme of Ref. [73], the hadronic amplitude of a process can be expressed as a convolution of a hard scattering part H and a soft contribution. The hard process can be calculated directly within the framework of perturbative QCD and the soft non-perturbative contribution is parametrized by the so-called hadron distribution amplitudes, describing the hadronic structure effects. We will refer to this concept as pQCD factorization approach. Such an approach is valid for sufficient large values of the momentum transfer Q.

For this purpose, it is convenient to use light-cone coordinates (see Appendix A), defined

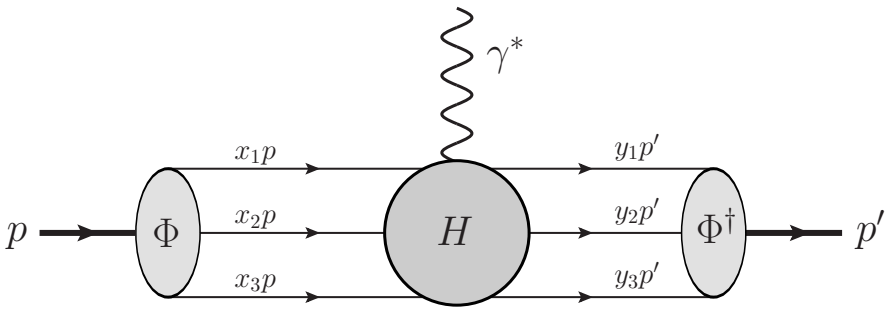

Figure 4.2: Proton form factor in the framework of pQCD factorization. The hard scattering amplitude H corresponds to the process $\gamma qqq \to qqq$. Φ ($\Phi^\dagger$) indicates the DA of the initial (final) proton state.

by the light-cone basis

$$\begin{aligned} &n^\mu = (1,0,0,-1), \quad \bar{n}^\mu = (1,0,0,1), \\ &\quad \text{with} \quad n^2 = \bar{n}^2 = 0 \quad \text{and } n\cdot\bar{n} = 2, \\ &a_\perp^\mu = (0, a_1, a_2, 0), \end{aligned} \tag{4.14}$$

where n and $\bar{n}$ are two light-like vectors and $a_\perp^\mu$ is denoted as the transverse component of the four-momentum a^μ. Any four-vectors can be decomposed in that basis as

$$p^\mu = \frac{\bar{n}^\mu}{2}\underbrace{(n\cdot p)}_{p^+} + \frac{n^\mu}{2}\underbrace{(\bar{n}\cdot p)}_{p^-} + p_\perp^\mu, \tag{4.15}$$

where commonly the short-hand notation

$$p^\mu \to (p^+, p^-, p_\perp) \equiv (n\cdot p,\, \bar{n}\cdot p,\, p_\perp) \tag{4.16}$$

is used. Particles moving in the p^+ direction are denoted as collinear particles, while particles along the p^- direction are denoted as anti-collinear particles. Additionally, we introduce the projectors

$$\Lambda^+ = \frac{\bar{\not{n}}\not{n}}{4}, \qquad \Lambda^- = \frac{\not{n}\bar{\not{n}}}{4}, \tag{4.17}$$

which project a spinor onto its "plus" and "minus" components. The spinor of a nucleon $N(p,\lambda_p)$ can be decomposed as

$$\begin{aligned} N(p,\lambda_p) &= \Lambda^+ N(p,\lambda_p) + \Lambda^- N(p,\lambda_p) \\ &\equiv N^+(p,\lambda_p) + N^-(p,\lambda_p), \end{aligned} \tag{4.18}$$

where in the case of a collinear particle N^+ and N^- scale as

$$N^+(p,\lambda_p) \sim \sqrt{p^+}, \qquad N^- \sim 1/\sqrt{p^+}. \tag{4.19}$$

Using the pQCD factorization approach, one can for instance evaluate the spacelike electromagnetic form factors at large momentum transfer $Q^2 = -q^2$ in the elastic ep-scattering

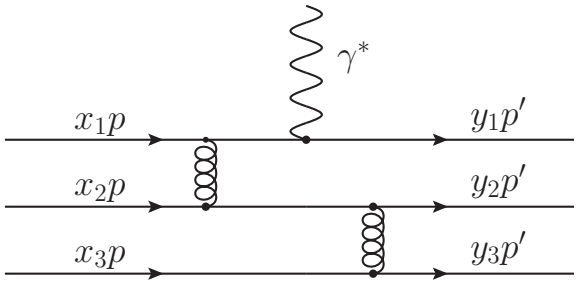

Figure 4.3: Hard subprocess $\gamma qqq \to qqq$ within the framework of pQCD factorization.

reaction. For this purpose the process, as shown in Fig. 4.2, is examined using the infinite momentum frame. The incoming proton is fast moving along the z-axis, i.e. with momentum $p \sim p^+$, and is struck by a highly virtual photon with large transverse momentum $q_\perp^2 \sim Q^2$.

The matrix element can be expressed by a distribution amplitude of $\Phi(x_i)$ for finding a given partonic state in the hadron and a function H, which describes the hard scattering at the partonic level. The subprocess consists of three valence quarks moving approximately collinear, each carrying a momentum fraction x_i of the proton momentum, with $\sum_{i=1}^{3} x_i = 1$. Conventionally, x_3 is chosen to be the momentum fraction of the valence d-quark.

Within this approach, for instance the magnetic form factor G_M can be factorized as

$$G_M(Q^2) = \int_0^1 dx_i \int_0^1 dy_i \Phi^\dagger(y_i) H(Q^2, x_i, y_i) \Phi(x_i). \tag{4.20}$$

The amplitude H characterizes the subprocess of the 3-valence quark state scattering with the virtual photon and producing three (nearly collinear) quarks in the final state, which is illustrated in Fig. 4.3. It can be calculated from the Born diagram contributions of

$$\gamma^*(q) + q(x_1p) + q(x_2p) + q(x_3p) \to q(y_1p) + q(y_2p) + q(y_3p) \tag{4.21}$$

using pQCD. The hard four-momentum of the virtual photon is transferred from quark line to quark line via gluon exchange. According to this, the exchange of at least two hard gluons is required for the scattering of one photon with large virtuality. Contributions of higher order Fock states are suppressed and vanish for $Q^2 \to \infty$.

The DA Φ is the probability amplitude for finding the three valence quark state in the incoming nucleon. It converts the proton into the three valence quark state, describing how the momentum p is shared between the constituents. The probability amplitude $\Phi^\dagger$ describes the overlap of the final quark state with the hadron. The distribution amplitudes are process independent quantities, i.e. they do not depend on the explicit form of the hard scattering amplitude H. Therefore, the same proton DAs can be used for the calculation of two-photon exchange processes, for both spacelike as well as timelike 2γ-exchange reactions.

The nucleon DAs are fundamental non-perturbative functions, which at present cannot be calculated from first principles. They refer to proton-to-vacuum matrix elements built up of quark and gluon fields. In the infinite momentum frame, the three quark matrix element is given by

$$\left\langle 0 \left| \varepsilon^{ijk} u_\alpha^i(z_1 n) u_\beta^j(z_2 n) d_\sigma^k(z_3 n) \right| p(p, \lambda_p) \right\rangle \tag{4.22}$$

in coordinate space, where $\left|p(p, \lambda_p)\right\rangle$ defines the proton state with momentum p and helicity λ_p and u, d are the quark-field operators of the up and down quarks, respectively. The Latin

letters i, j, k refer to color and the Greek letters α, β, γ stand for Dirac indices. The vector n is an arbitrary light-like vector and z_i are real numbers satisfying $\sum_i z_i = 1$.

The matrix element of Eq. (4.22) has been transformed into an expression given by a complete set of independent matrices. For this purpose the three spinor product of Eq. (4.22) has been decomposed into a product of two spinors and one remaining spinor, for which a matrix representation can be used. These two matrices have been expanded in terms of the Dirac bilinears.

The most general decomposition of the proton-to-vacuum matrix element, taking Lorentz invariance, parity and spin conservation into account, can be expressed by 24 independent functions giving rise to the DAs [74]. The decomposition can be examined with respect to the dependence on $p^+ \sim Q$ of the different contributions.

To the leading-order expansion in $1/p^+$, denoted as leading-twist or twist 3, only three DAs contribute, the vector- (V), axial-vector (A), and tensor (T) DAs. The proton-to-vacuum matrix element given as parametrization of the three leading-order DAs reads [74]:

$$\begin{aligned} 4\left\langle 0\left|\varepsilon^{ijk}u^i_\alpha(z_1 n)u^j_\beta(z_2 n)d^k_\sigma(z_3 n)\right|p\right\rangle = \quad & V(z_i\, n\cdot p)\; p\!\!\!/^+\left[\left(\frac{1}{2}\bar{n}\cdot\gamma\right)\;\mathcal{C}\right]_{\alpha\beta}\left[\gamma_5 N^+\right]_\sigma \\ + \quad & A(z_i\, n\cdot p)\; p\!\!\!/^+\left[\left(\frac{1}{2}\bar{n}\cdot\gamma\right)\gamma_5\,\mathcal{C}\right]_{\alpha\beta}\left[N^+\right]_\sigma \\ + \quad & T(z_i\, n\cdot p)\; p^+\left[\frac{1}{2}i\sigma_{\perp\bar{n}}\;\mathcal{C}\right]_{\alpha\beta}\left[\gamma^\perp\gamma_5 N^+\right]_\sigma, \end{aligned} \tag{4.23}$$

where $\mathcal{C}$ is the charge conjugation matrix and $\gamma^\perp$ corresponds to the transverse component of γ^μ. The expression $\sigma_{\perp\bar{n}}$ is the shorthand notation for

$$\sigma_{\perp\bar{n}} \;=\; \bar{n}^\mu\,\sigma_{\perp\mu}, \qquad \text{with} \quad \sigma_{\perp\mu} = \frac{i}{2}[\gamma_\perp, \gamma_\mu]. \tag{4.24}$$

In momentum space, the DAs are given by the following expression:

$$X(z_i\, n\cdot p) = \int d[x_i]\; X(x_1,x_2,x_3)\,\exp\left\{-\mathrm{i}\,(p\cdot n)\sum_i z_i x_i\right\}, \quad X = \{V, A, T\} \tag{4.25}$$

with

$$d[x_i] = dx_1 dx_2 dx_3\,\delta(1-x_1-x_2-x_3), \tag{4.26}$$

where x_i is the collinear momentum fraction of the proton carried by quark i.

Due to the symmetry between the two up-quarks, the vector and tensor DAs are symmetric under the interchange of the first two arguments, whereas the axial DA is antisymmetric:

$$\begin{aligned} V(x_1,x_2,x_3) &= \;\; V(x_2,x_1,x_3), \\ T(x_1,x_2,x_3) &= \;\; T(x_2,x_1,x_3), \\ A(x_1,x_2,x_3) &= -A(x_2,x_1,x_3). \end{aligned} \tag{4.27}$$

In addition, the following property holds

$$T(x_1,x_2,x_3) = \frac{1}{2}[V-A](x_1,x_3,x_2) + \frac{1}{2}[V-A](x_2,x_3,x_1), \tag{4.28}$$

which allows to define a single independent leading twist-3 proton DA given by a scalar function Φ_3 with mixed symmetry,

$$\Phi_3(x_1, x_2, x_3) = [V - A](x_1, x_2, x_3). \tag{4.29}$$

Therefore, the DAs can be rewritten as

$$\begin{aligned} V(x_1, x_2, x_3) &= \frac{1}{2}\big[\Phi_3(x_1, x_2, x_3) + \Phi_3(x_2, x_1, x_3)\big], \\ A(x_1, x_2, x_3) &= \frac{1}{2}\big[\Phi_3(x_2, x_1, x_3) - \Phi_3(x_1, x_2, x_3)\big], \\ T(x_1, x_2, x_3) &= \frac{1}{2}\big[\Phi_3(x_1, x_3, x_2) + \Phi_3(x_2, x_3, x_1)\big]. \end{aligned} \tag{4.30}$$

The dependence of the DAs on the momentum transfer scale Q^2 is weak. This dependence is specified by a renormalization group equation, which requires, that Φ is only logarithmically dependent on Q^2 [73].

4.2.2 Timelike Two-Photon Exchange within a pQCD Factorization Approach

To calculate the two-photon exchange contribution of

$$p(p_1, \lambda_{N_1}) + \bar{p}(p_2, \lambda_{N_2}) \to e^-(k_1, h_1) + e^+(k_2, -h_1) \tag{4.31}$$

at large momentum transfer q^2, the factorization approach, which has been discussed in the previous subsection, is considered. We follow the experience gained by the spacelike process $ep \to ep$, for which the 2γ-amplitudes $\delta\tilde{G}_M$ and $\tilde{F}_3$ were computed at large momentum transfer Q within a perturbative QCD factorization approach [57, 58], which can be generalized to the annihilation channel $p\bar{p} \to e^+e^-$.

A typical diagram of the leading order contribution to the 2γ-exchange corrections is illustrated in Fig. 4.4, where the gray blobs correspond to the DAs of the proton and antiproton, and the hard part H is given by a three quark state and a three antiquark state, which annihilate into two virtual photons. The 2γ-amplitudes can be expressed as convolution of H and the non-perturbative part, e.g. $\delta\tilde{G}_M$ can be written as

$$\delta\tilde{G}_M(q^2, t) = \int d[x_i] \int d[y_i] \Phi(x_i) H(q^2, t, x_i, y_i) \Phi^\dagger(y_i), \tag{4.32}$$

where the momentum fractions of the participating quarks and antiquarks are denoted by x_i and y_i, respectively, which satisfy $\sum_i x_i = 1$ and $\sum_i y_i = 1$.

The subprocess H is specified by the exchange of two photons, which couple to two different quarks. The third quark interacts via the exchange of a hard gluon. Contributions where the two photons couple to the same quark are suppressed due to the fact, that this implies at least one additional gluon exchange, which includes the factor α_s/q^2.

An important feature of the approach is, that both photon virtualities, q_1 and q_2, must be large:

$$q_1^2 \sim q_2^2 \sim q^2. \tag{4.33}$$

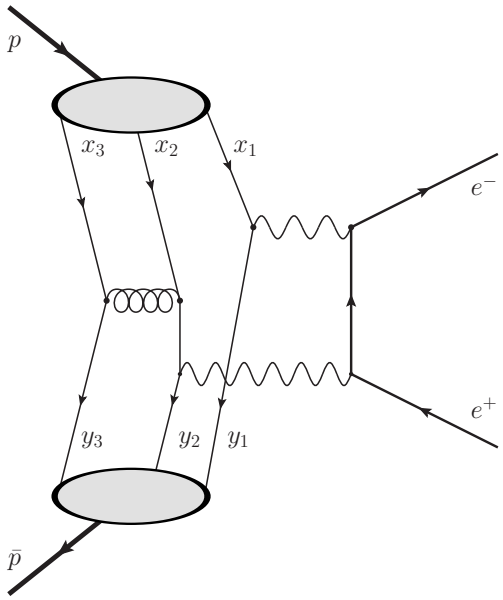

Figure 4.4: Diagram for $p\bar{p} \to e^+e^-$ describing the exchange of two hard photons using the framework of pQCD factorization. The gray blobs refer to the proton and antiproton DAs. The perturbative subprocess is given by the annihilation of a three quark state and a three antiquark state into two highly virtual photons.

As all spectator quarks are involved in the hard scattering process described by Eq. (4.32), we refer to it as the hard rescattering contribution.

Such an approach is valid at (asymptotic) large values of q^2. However, it is still an open question at which energy the asymptotic behavior sets in. One may expect, that at intermediate energies of ~ 10 GeV^2 the scale defining the applicability of the perturbative expansion is already large enough to apply the present formalism. A test of the validity of this approach can possibly be provided by future experiments.

In the case of $s, t \gg m_N^2$, the mass of the nucleons can be neglected and the momenta of the proton and antiproton in the c.m.-frame can be expressed in the light-cone basis by the light-like vectors n and $\bar{n}$,

$$\begin{aligned} p_1^\mu &\simeq \sqrt{s}\,\frac{\bar{n}^\mu}{2} = (\sqrt{s},\,0,\,0), \\ p_2^\mu &\simeq \sqrt{s}\,\frac{n^\mu}{2} = (0,\,\sqrt{s},\,0), \end{aligned} \tag{4.34}$$

where the initial proton is moving collinearly and the antiproton anticollinearly in the z-direction. Consequently, the momentum transfer q is given by

$$q^\mu = -p_2^\mu - p_1^\mu = (-\sqrt{s}, -\sqrt{s}, 0). \tag{4.35}$$

The lepton momenta in the light-cone basis are defined as

$$\begin{aligned} k_1^\mu &= \bar{\eta}\frac{\sqrt{s}}{2}\,n^\mu + \eta\frac{\sqrt{s}}{2}\,\bar{n}^\mu + k_\perp^\mu = (\,\eta\sqrt{s},\ \bar{\eta}\sqrt{s},\ k_\perp), \\ k_2^\mu &= \eta\frac{\sqrt{s}}{2}\,n^\mu + \bar{\eta}\frac{\sqrt{s}}{2}\,\bar{n}^\mu - k_\perp^\mu = (\,\eta\sqrt{s},\ \bar{\eta}\sqrt{s},\ -k_\perp), \end{aligned} \tag{4.36}$$

where, at large momentum transfer, η, $\bar{\eta}$ and $k_\perp$ can be determined from

$$\eta \simeq -\frac{t}{s}, \qquad \bar{\eta} \equiv 1-\eta \simeq -\frac{u}{s}, \qquad k_\perp^2 \simeq \eta\bar{\eta}s, \tag{4.37}$$

with the restriction $0 < \eta < 1$. The kinematic variable η can be expressed by the electron c.m. scattering angle θ:

$$\eta \simeq \frac{1}{2}(1+\cos\theta). \tag{4.38}$$

The proton-to-vacuum matrix element parametrized by the proton DAs V, A and T, which has been introduced in Eq. (4.23), can for the given process be expressed as:

$$\begin{aligned} & 4\langle 0|\varepsilon^{ijk}u_\alpha^i(z_1\,n)u_\beta^j(z_2\,n)d_\gamma^k(z_3\,n)|p(p_1,\lambda_{N_1})\rangle \\ = \quad & V(z_i\,n\cdot p_1)\ \left[\frac{\sqrt{s}}{2}(\bar{n}\cdot\gamma)\,\mathcal{C}\right]_{\alpha\beta}\left[\gamma_5 N^+\right]_\gamma + A(z_i\,n\cdot p_1)\ \left[\frac{\sqrt{s}}{2}(\bar{n}\cdot\gamma)\gamma_5\,\mathcal{C}\right]_{\alpha\beta}\left[N^+\right]_\gamma \\ & +\ T(z_i\,n\cdot p_1)\ \left[\frac{\sqrt{s}}{2}i(\sigma_{\perp\bar{n}}\,\mathcal{C})\right]_{\alpha\beta}\left[\gamma^\perp\gamma_5 N^+\right]_\gamma \\ \equiv \quad & V\ \left[\Gamma_V^u\right]_{\alpha\beta}\left[\Gamma_V^d\,N^+\right]_\gamma + A\ \left[\Gamma_A^u\right]_{\alpha\beta}\left[\Gamma_A^d\,N^+\right]_\gamma + T\ \left[\Gamma_T^u\right]_{\alpha\beta}\left[\Gamma_T^d\,N^+\right]_\gamma. \end{aligned} \tag{4.39}$$

Similarly, the matrix element of the antiproton state in terms of DAs yields

$$\begin{aligned} & 4\langle 0|\varepsilon^{i'j'k'}\bar{u}_{\beta'}^{j'}(z_1'\,\bar{n})\,\bar{u}_{\alpha'}^{i'}(z_2'\,\bar{n})\,\bar{d}_{\gamma'}^{k'}(z_3'\,\bar{n})|\bar{p}(p_2,\lambda_{N_2})\rangle \\ = \quad & -\ V^\dagger(z_1'\,\bar{n}\cdot p_2)\left[\frac{\sqrt{s}}{2}\,\mathcal{C}\,(n\cdot\gamma)\right]_{\beta'\alpha'}\left[\bar{N}^+\gamma_5\right]_{\gamma'} - A^\dagger(z_2'\,\bar{n}\cdot p_2)\left[\frac{\sqrt{s}}{2}\,\mathcal{C}\,\gamma_5(n\cdot\gamma)\right]_{\beta'\alpha'}\left[\bar{N}^+\right]_{\gamma'} \\ & +\ T^\dagger(z_3'\,\bar{n}\cdot p_2)\ \left[\frac{\sqrt{s}}{2}\mathcal{C}i\sigma_{\perp n}\right]_{\beta'\alpha'}\left[\bar{N}^+\gamma^\perp\gamma_5\right]_{\gamma'} \\ \equiv \quad & V'\ \left[\Gamma_{V'}^u\right]_{\beta'\alpha'}\left[\bar{N}^+\,\Gamma_{V'}^d\right]_{\gamma'} + A'\ \left[\Gamma_{A'}^u\right]_{\beta'\alpha'}\left[\bar{N}^+\,\Gamma_{A'}^d\right]_{\gamma'} + T'\ \left[\Gamma_{T'}^u\right]_{\beta'\alpha'}\left[\bar{N}^+\,\Gamma_{T'}^d\right]_{\gamma'}, \end{aligned} \tag{4.40}$$

where the complex conjugated DAs read

$$X'(z_i'\,\bar n\cdot p_2)\;\equiv X^\dagger(z_i'\,\bar n\cdot p_2)=\int d[y_i]\;X(y_1,y_2,y_3)\exp\left\{\mathrm{i}\,(\bar n\cdot p_2)\sum_i y_i z_i\right\},\qquad \text{with}\quad X'=\{V',A',T'\}. \tag{4.41}$$

The structures Γ^u_X, Γ^d_X, $\Gamma^u_{X'}$, and $\Gamma^d_{X'}$ presented in Eqs. (4.39, 4.40) are defined by

$$\Big[\Gamma^u_V\Big]_{\alpha\beta}=\frac{\sqrt{s}}{2}\Big[\bar{\not n}\;\mathcal{C}\Big]_{\alpha\beta},\quad \Big[\Gamma^u_A\Big]_{\alpha\beta}=\frac{\sqrt{s}}{2}\Big[\bar{\not n}\;\gamma_5\,\mathcal{C}\Big]_{\alpha\beta},\quad \Big[\Gamma^u_T\Big]_{\alpha\beta}=\frac{\sqrt{s}}{2}\Big[i\sigma_{\perp\bar n}\mathcal{C}\Big]_{\alpha\beta},$$
$$\Big[\Gamma^d_V\Big]_{\gamma}=[\gamma_5]_\gamma,\qquad \Big[\Gamma^d_A\Big]_{\gamma}=[1]_\gamma,\qquad \Big[\Gamma^d_T\Big]_{\gamma}=[\gamma^\perp\gamma_5]_\gamma \tag{4.42}$$

$$\Big[\Gamma^u_{V'}\Big]_{\beta'\alpha'}=-\frac{\sqrt{s}}{2}\Big[\mathcal{C}\,\not n\Big]_{\beta'\alpha'},\quad \Big[\Gamma^u_{A'}\Big]_{\beta'\alpha'}=-\frac{\sqrt{s}}{2}\Big[\mathcal{C}\,\gamma_5\,\not n\Big]_{\beta'\alpha'},\quad \Big[\Gamma^u_{T'}\Big]_{\beta'\alpha'}=\frac{\sqrt{s}}{2}\Big[\mathcal{C}\,i\sigma_{\perp n}\Big]_{\beta'\alpha'},$$
$$\Big[\Gamma^d_{V'}\Big]_{\gamma'}=[\gamma_5]_{\gamma'},\qquad \Big[\Gamma^d_{A'}\Big]_{\gamma'}=[1]_{\gamma'},\qquad \Big[\Gamma^d_{T'}\Big]_{\gamma'}=[\gamma_5\,\gamma^\perp]_{\gamma'}. \tag{4.43}$$

The leading contribution to the 2γ-exchange corrections is shown in the left panel of Fig. 4.5. It can be factorized in the following way

$$\begin{aligned}A_{2\gamma}=&\int d[z_j']\big\langle 0\big|\bar u^j_{\beta'}(z_1n)\bar u^i_{\alpha'}(z_2n)\bar d^k_{\gamma'}(z_3n)\big|p_2\big\rangle\cdot\int d[z_i]\big\langle 0\big|u^i_\alpha(z_1n)u^j_\beta(z_2n)d^k_\gamma(z_3n)\big|p_1\big\rangle\\&\cdot\bar u_l(k_1)\,\Gamma_l\,v_l(k_2)\cdot\mathcal{L}^{i'i}_{\alpha'\alpha}\otimes\mathcal{L}^{j'j}_{\beta'\beta}\otimes\mathcal{L}^{k'k}_{\gamma'\gamma}\\=&\sum_{X'=V',A',T'}\;\sum_{X=V,A,T}\int d[y_i]\,X'(y_i)\int d[x_i]\,X(x_i)\cdot\bar u_l(k_1)\,\Gamma_l\,v(k_2)\\&\times\Big[\bar N^+(p_2)\;\Gamma^d_{X'}\Big]_{\gamma'}\Big[\Gamma^d\Big]^{\gamma'\gamma}\Big[\Gamma^d_X\;N^+(p_1)\Big]_\gamma\Big[\Gamma^u_{X'}\Big]_{\beta'\alpha'}\Big[\Gamma^{u_1}\Big]^{\alpha'\alpha}\Big[\Gamma^{u_2}\Big]^{\beta'\beta}\Big[\Gamma^u_X\Big]_{\alpha\beta}\end{aligned} \tag{4.44}$$

The second line characterizes the hard rescattering process H, where

$$\bar u_l\,\Gamma_l\,v_l=\bar u_l(k_1,h_1)\,\Gamma_l\,v_l(k_2,-h_1) \tag{4.45}$$

denotes the leptonic part of the subprocess and

$$\mathcal{L}^{i'i}_{\alpha'\alpha}\otimes\mathcal{L}^{j'j}_{\beta'\beta}\otimes\mathcal{L}^{k'k}_{\gamma'\gamma} \tag{4.46}$$

represents the quark annihilation process. Γ^q, with $q=\{u_1,u_2,d\}$, is associated with the expression for the quark spinor line in the momentum space. The indices α (β) and α' (β') correspond to the u-quark line and $\bar u$-quark line carrying the momentum x_1p_1 (x_2p_1) and y_1p_2 (y_2p_2), respectively. The indices γ, and γ' refer to the d-quark and $\bar d$-quark lines. The

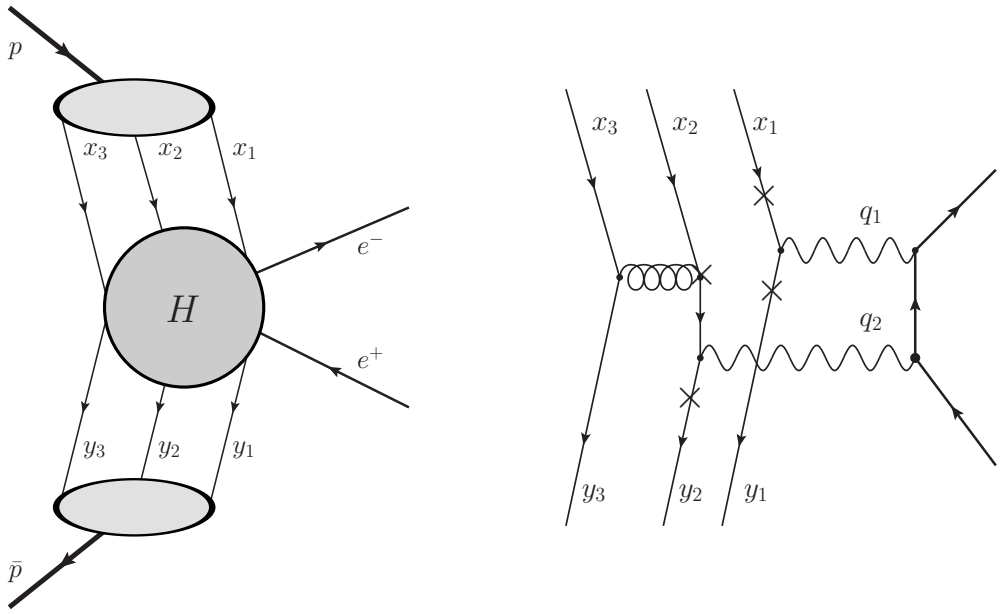

Figure 4.5: Leading pQCD contribution to the 2γ exchange corrections for $p\bar{p} \to e^+e^-$. Left diagram: Factorized amplitude of the process. Right diagram: One possible contribution to the hard rescattering contribution H, where both photons couple to the u-quarks. The $\times$'s indicate the other possibility to attach the gluon. The other diagrams, where the photons interact with the u and d-quarks, are not shown for simplicity.

explicit expressions for Γ^q can be obtained from the Feynman rules of the elastic rescattering process

$$\begin{aligned} q_{u_1}(x_1\,p_1)\,q_{u_2}(x_2\,p_1)\,q_d(x_3\,p_1) + \bar{q}_{u_1}(y_1\,p_2)\,\bar{q}_{u_2}(y_2\,p_2)\,\bar{q}_d(y_3\,p_2) &\to \gamma^*(q_1) + \gamma^*(q_2) \\ &\to e^-(k_1) + e^+(k_2). \end{aligned} \tag{4.47}$$

In the right panel of Fig. 4.5, one possible contribution to the hard rescattering kernel is presented. The leading order contribution of the hard rescattering amplitude A_H can be introduced in the following way:

$$A_H = Q_u^2 A^{uu} + Q_u Q_d (A^{u_1 d} + A^{u_2 d}). \tag{4.48}$$

A^{uu} denotes the amplitudes, where the photons couple to the two up-quarks, $A^{u_1 d}$ ($A^{u_2 d}$) stands for one photon coupling to the u-quark with the momentum fraction x_1 (x_2), the other photon to the d-quark, with the charge fraction of the quarks $Q_u = +2/3$, and $Q_d = -1/3$. For each of these photon couplings four possibilities of gluon exchange between the quarks lines have to be considered, illustrated by the $\times$'s in Fig. 4.5:

$$A^{ij} = D_1^{ij} + D_2^{ij} + D_3^{ij} + D_4^{ij}. \tag{4.49}$$

Each diagram D^{ij} includes the sum of the direct and crossed box diagram. Consequently, all together one finds 24 diagrams for the leading 2γ-exchange corrections, which can be

computed using pQCD. For instance, the hard subprocess contribution, which is illustrated in the right panel of Fig. 4.5, can be obtained from the corresponding Feynman rules as

$$\begin{aligned} D_1^{uu} &= \mathcal{G}\, ie^4 g_s^2 \frac{1}{p_u^2\; p_g^2\, q_1^2\, q_2^2}\, \frac{1}{(q_2-k_2)^2} u_l(k_1)\gamma^\mu(-\not{q}_2-\not{k}_2)\gamma^\nu v_l(k_2) \\ &\times\; \bar{v}(y_1p_2)\,\gamma_\mu\, u(x_1p_1)\,\bar{v}(y_2p_2)\,\gamma_\nu \not{p}_u\,\gamma^i\, u(x_2p_1)\,\bar{v}(y_3p_2)\gamma_i u(x_3p_1), \end{aligned} \tag{4.50}$$

where $\mathcal{G}$ is a global factor and $g_s^2(-q^2) = 4\pi\,\alpha_s(-q^2)$ is the coupling strength of the strong force. The momenta of the exchanged gluon and the fermion propagator are given by

$$p_g = -x_1p_1 - y_1p_2, \qquad p_u = y_3p_2 + (1-x_1)p_1. \tag{4.51}$$

The contributions of the different diagrams as well as the corresponding Feynman graphs are given in Appendix B.

The results of the perturbative calculation are embedded into Eq. (4.44) in order to obtain the 2γ-amplitudes as a function of the DAs V,A, and T. Finally, the timelike 2γ-exchange amplitudes $\delta\tilde{G}_M$ and $s/m^2\tilde{F}_3$ can be found as :

$$\begin{aligned} \delta\tilde{G}_M(q^2,\eta) &= -\frac{\alpha_{em}\alpha_s}{q^4}\left(\frac{2\pi}{3}\right)^2 \int \frac{d[y_i]}{y_1y_2\bar{y}_2}\frac{d[x_i]}{x_1x_2\bar{x}_2}\frac{4(2\eta-1)\,x_2\,y_2}{[x_2\bar{\eta}+y_2\eta-x_2y_2]\,[x_2\eta+y_2\bar{\eta}-x_2y_2]} \\ &\times \Big\{ {Q_u}^2\,\left[(V'+A')(V+A)+4T'T\right](3,2,1) \\ &+ Q_uQ_d\left[(V'+A')(V+A)+4T'T\right](1,2,3) + 2Q_uQ_d\left[V'V+A'A\right](1,3,2)\Big\}, \end{aligned} \tag{4.52}$$

$$\begin{aligned} \frac{s}{m^2}\tilde{F}_3(q^2,\eta) &= \frac{\alpha_{em}\alpha_s}{q^4}\left(\frac{2\pi}{3}\right)^2 \int \frac{d[y_i]}{y_1y_2\bar{y}_2}\frac{d[x_i]}{x_1x_2\bar{x}_2}\frac{2(x_2\,\bar{y}_2+\bar{x}_2\,y_2)}{[x_2\bar{\eta}+y_2\eta-x_2y_2]\,[x_2\eta+y_2\bar{\eta}-x_2y_2]} \\ &\times \Big\{ {Q_u}^2\,\left[(V'+A')(V+A)+4T'T\right](3,2,1) \\ &+ Q_uQ_d\left[(V'+A')(V+A)+4T'T\right](1,2,3) + 2Q_uQ_d\left[V'V+A'A\right](1,3,2)\Big\}, \end{aligned} \tag{4.53}$$

where the numbers in the brackets define the order of the momentum fraction arguments of the DAs, e.g.

$$V'V(3,2,1) = V'(y_1,y_2,y_3)V(x_1,x_2,x_3), \tag{4.54}$$

and the abbreviations

$$\bar{x}_i = 1-x_i, \qquad \bar{y}_i = 1-y_i \tag{4.55}$$

have been used. As one can seen from Eqs. (4.52) and (4.53), the leading behavior of the

	f_N (10^{-3} GeV^2)	r_-	r_+
COZ [76]	5.0 ± 0.5	4.0 ± 1.5	1.1 ± 0.3
BLW [77]	5.0 ± 0.5	1.37	0.35
QCDSF [78]	3.23	1.06	0.33

Table 4.1: Parameters entering the proton DA (at $\mu = 1$ GeV) for three parametrizations (COZ [76], BLW [77], and the lattice evaluation from QCDSF [78]) used in this work.

helicity conserving 2γ-amplitudes is

$$\delta\tilde{G}_M \sim \frac{1}{q^4}, \qquad \frac{s}{m^2}\tilde{F}_3 \sim \frac{1}{q^4}. \tag{4.56}$$

The helicity-flip amplitude $\delta\tilde{F}_2$ is suppressed in the large momentum transfer limit, since its behavior is be found as

$$\delta\tilde{F}_2 \sim \frac{1}{q^6}. \tag{4.57}$$

Therefore, the amplitude is obtained to be zero in the leading order expansion of the analysis.

In general, the timelike amplitudes are complex functions, but at tree level the expressions of Eqs. (4.52) and (4.53) do not contain an imaginary part explicitly. In the calculation we receive nontrivial imaginary contributions by computing leading logarithms with the renormalization of the strong coupling α_s. The imaginary part is generated by timelike logarithms, like

$$\ln(-q^2 - i\varepsilon) = \ln(q^2) - i\pi. \tag{4.58}$$

For the coupling α_s in the timelike region we adopt the analytic continuation [75]:

$$\alpha_s(-q^2) = \frac{\alpha_s(q^2)}{1 - i\beta_0\alpha_s(q^2)/4} + \cdots, \tag{4.59}$$

where

$$\beta_0 = 11 - \frac{2}{3}n_f \tag{4.60}$$

is the leading term of the QCD β-function.

In an analogous manner, one receives an imaginary contribution which originates from the evolution of the DAs. Nevertheless, the resulting imaginary contributions provide small numerical effects in the regions of q^2 which will be discussed below. We assume, that the scale of the running coupling $a_s(\mu_R^2)$ is smaller than q^2 and use $\mu_R = 0.6\,q^2$ for our numerical calculations. However, this procedure has only a small effect on the results, changing μ_R^2 in the interval $[0.5q^2,\ q^2]$, we find for the 2γ-exchange contribution to the cross section a maximum variation in the hard scattering amplitude of about 10%.

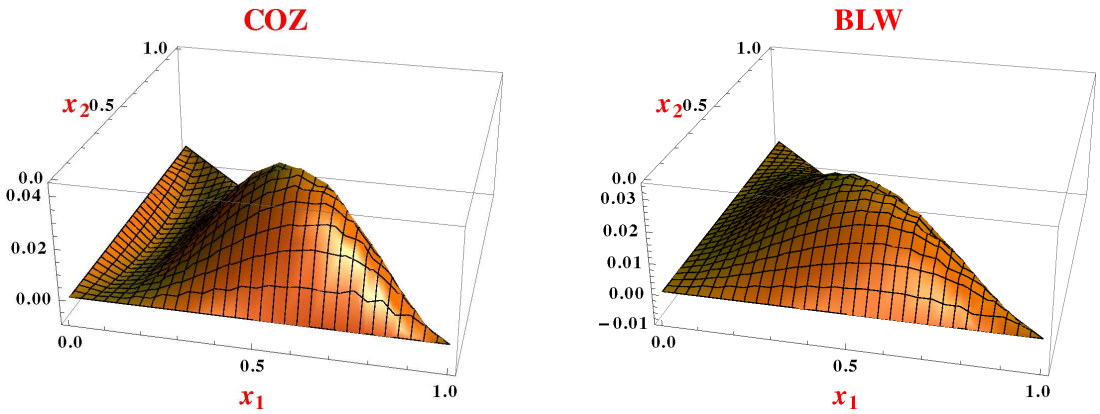

Figure 4.6: 3-dimensional plot of the DA Φ_3 according to the parametrizations in Eq. (4.61) as a function of x_1 and x_2. The left (right) panel corresponds to the results found for the COZ (BLW) model. The dependence on x_3 has been removed due to $\sum_i x_i = 1$.

To evaluate the convolution integrals given in Eqs. (4.52, 4.53), a model for the DAs is needed. In Ref. [74], a parametrization of the DAs is given by:

$$\begin{aligned} V(x_i) &\simeq 120\, x_1 x_2 x_3\, f_N \left[1 + r_+(1-3x_3)\right], \\ A(x_i) &\simeq 120\, x_1 x_2 x_3\, f_N\, r_-(x_2 - x_1), \\ T(x_i) &\simeq 120\, x_1 x_2 x_3\, f_N \left[1 + \frac{1}{2}\,(r_- - r_+)\,(1-3x_3)\right], \end{aligned} \tag{4.61}$$

where the DAs depend on the three parameters, namely f_N, r_+ and r_-. For the calculation two phenomenological models for the DAs, which have been discussed in the literature, are considered, which will be referred to as COZ [76] and BLW model [77], as well as one description based on lattice QCD calculations (QCDSF) [78]. The corresponding parameters at $\mu = 1$ GeV^2 are presented in Table 4.1. One notices, that the parameters r_+ and r_- in the BLW model and from lattice calculations are nearly comparable, whereas the overall normalization f_N is about a factor 2/3 smaller for the lattice DA than in the description of the BLW model. In contrast to the BLW model and the lattice calculations, the parameters r_+ and r_- are about three times larger in the COZ description of the nucleon DAs.

The DA Φ_3 as a function of x_1 and x_2 is shown in Fig. 4.6, where in the left (right) panel the DA obtained in the COZ (BLW) model is presented. One notices, that the dependence on x_1 and x_2 is similar for both models of the DAs, even though the COZ model gives a larger DA as when the BLW model is used.

Below, we will provide calculations using the first two models, COZ and BLW. The results following from the lattice calculations can easily be approximated by scaling the BLW results. All parameters from Table 4.1 have been evolved according to the procedure given in Ref. [74].

Using the parametrization of Eq. (4.61), the convolutions integrals can be computed and

the following expressions of the 2γ-amplitudes are obtained:

$$\begin{aligned}
\delta\tilde{G}_M &= -\left(\frac{2\pi}{3}\right)^2 (120 f_N)^2 \frac{8}{9}\frac{\alpha_{em}\alpha_s}{q^4} \\
&\quad \times \Bigg\{ (\phi_1+\phi_0)\Big[(\bar\eta-\eta)\eta\bar\eta \ln^2\left(\frac{\bar\eta}{\eta}\right) - 4\eta\bar\eta \ln\left(\frac{\bar\eta}{\eta}\right) + (\eta-\bar\eta)(1-\eta\bar\eta\pi^2)\Big] \\
&\quad + \phi_2\Big[-3(\eta\bar\eta)^2(\eta-\bar\eta)\ln^2\left(\frac{\bar\eta}{\eta}\right) + \eta\bar\eta(1-12\eta\bar\eta)\ln\left(\frac{\bar\eta}{\eta}\right) \\
&\quad + 3(\eta-\bar\eta)\eta\bar\eta(1-\eta\bar\eta\pi^2) + \frac{1}{4}(\eta-\bar\eta)\Big] \Bigg\}, \qquad (4.62)
\end{aligned}$$

$$\begin{aligned}
\frac{s}{m^2}\tilde{F}_3 &= \left(\frac{2\pi}{3}\right)^2 (120 f_N)^2 \frac{8}{9}\frac{\alpha_{em}\alpha_s}{q^4} \\
&\quad \times \Bigg\{ -2(\phi_1+2\phi_0)\Big[(\eta-\bar\eta)\ln\left(\frac{\bar\eta}{\eta}\right) - \eta\bar\eta\ln^2\left(\frac{\bar\eta}{\eta}\right) + 1 - \eta\bar\eta\pi^2\Big] \\
&\quad + \phi_2\Big[-2\eta\bar\eta(1-6\eta\bar\eta)\ln^2\left(\frac{\bar\eta}{\eta}\right) - 12\zeta\bar\eta(2\eta-1)\ln\left(\frac{\bar\eta}{\eta}\right) \\
&\quad + 1 - 12\eta\bar\eta - 2\eta\bar\eta(1-6\eta\bar\eta)\pi^2\Big] \Bigg\}, \qquad (4.63)
\end{aligned}$$

where the notation ϕ_i denotes the following combinations of parameters r_+, r_-:

$$\begin{aligned}
\phi_0 &= \frac{3}{4} + \frac{1}{2}r_- - \frac{1}{9}r_-^2 - \frac{3}{2}r_+ - r_+^2 + \frac{1}{3}r_+r_-. \\
\phi_1 &= \frac{1}{2}r_- + \frac{1}{9}r_-^2 + \frac{3}{2}r_+ + \frac{5}{2}r_+^2 - \frac{5}{6}r_+r_-, \qquad (4.64) \\
\phi_2 &= \frac{7}{18}r_-^2 - \frac{11}{2}r_+^2 + \frac{4}{3}r_+r_-.
\end{aligned}$$

4.2.3 Results

We calculate the relative 2γ-contribution to the differential cross section $\delta_{2\gamma}$, which is defined by

$$\left(\frac{d\sigma}{d\cos\theta}\right) = \left(\frac{d\sigma}{d\cos\theta}\right)_{1\gamma}(1+\delta_{2\gamma}), \qquad (4.65)$$

where the cross section $d\sigma/d\cos\theta$ is given by Eq. (4.10) and the cross section in the Born approximation $(d\sigma/d\cos\theta)_{1\gamma}$ has been introduced in Eq. (2.42). The two-photon exchange contribution $\delta_{2\gamma}$ depends on the c.m. scattering angle θ and the c.m. energy $s = q^2$ as well as on the model for the nucleon DAs. Furthermore, a description of the timelike electromagnetic form factors G_E and G_M, which enter the 1γ- as well as the 2γ-parts of the cross section, is needed.

We first start with a simple description of the magnetic factor G_M, which is inspired by the predictions of pQCD for the electromagnetic form factors (Model 1):

$$|G_M| = \frac{\mathcal{B}}{q^4 \left(\ln^2 \frac{q^2}{\Lambda^2} + \pi^2 \right)}. \tag{4.66}$$

The parameter Λ is given by $\Lambda = 0.3$ GeV and $\mathcal{B}$ a free parameter, which can be extracted from fitting data. In addition, for the first form factor parameterization, the assumption $|G_M| = |G_E|$ is used and the imaginary parts of the form factors have been neglected.

As an alternative possibility (Model 2), following [79], an improved fit of the form factor ratio $F_2(Q^2)/F_1(Q^2)$ is considered, which includes logarithmic corrections to the power law fall-off expected from pQCD.

In the previous section it was mentioned, that the value of two-photon amplitude $\delta\tilde{F}_2$ is unknown due to the suppression of $\delta\tilde{F}_2$ within the factorization approach. Therefore, $\delta\tilde{G}_E$ is estimated using a simple model:

$$\delta\tilde{G}_E \simeq \lambda\, \delta\tilde{G}_M, \tag{4.67}$$

where λ is a numerical parameter, for which $-1 < \lambda < 1$ is used, which can account for the expectation, that δG_E scales as δG_M in the large q^2 limit.

The results for $\delta_{2\gamma}$ can be found in Fig. 4.7, where the relative 2γ-contribution to the cross section for two different values of momentum transfer, $s = 6$ GeV^2 and $s = 20$ GeV^2 is shown as a function of $\cos\theta$. The two aforementioned parametrizations of G_E and G_M are associated with the blue (Model 1) and green (Model 2) colored bands. The bands describe the variation of the parameter λ in Eq. (4.67). Furthermore, two different models for the nucleon DAs have been used, the COZ and BLW description, which correspond to the left and right plots in Fig. 4.7, respectively. One notices, that for both parametrizations of the electromagnetic form factors the results differ only slightly. The corresponding bands overlap for a large range of $\cos\theta$.

The relative effect of the two-photon exchange corrections is found to be smaller than 1%. For s = 20 GeV^2, a slightly larger 2γ-exchange contribution is obtained as for the lower value of q^2. Both models of DAs produce a similar angular dependence, while the COZ model leads to a contribution which is twice as large as when using the BLW model. For the assumed parametrization of $\delta\tilde{G}_E$, the impact of the parameter λ on the results is small. The 2γ-corrections show the required odd behavior with respect to $\cos\theta$ and are increasing for $|\cos\theta| \to 1$.

Moreover, we consider one further model to parametrize the 1γ-form factors G_E and G_M and compare the results with the 2γ-exchange corrections we have obtained above. We take a VMD based model into account, according to Ref. [48], which assumes, that the electromagnetic interaction is described through the exchange of the lowest lying vector mesons ρ, ω, and ϕ, as discussed in Sec. 2.4.

The results are presented in Fig. 4.8, where $\delta_{2\gamma}$ has been calculated for $q^2 = 6$ GeV^2 using the COZ model (left) and the BLW model (right) for the nucleon DAs and the bands again refer to the influence of the parameter λ in Eq. (4.67). The red bands correspond to the findings of the VMD model and the blue bands indicate the results when using the pQCD inspired model (Model 1) as parametrization of G_E and G_M. One notices, that both models lead to a similar angular behavior and to comparable quantitative results.

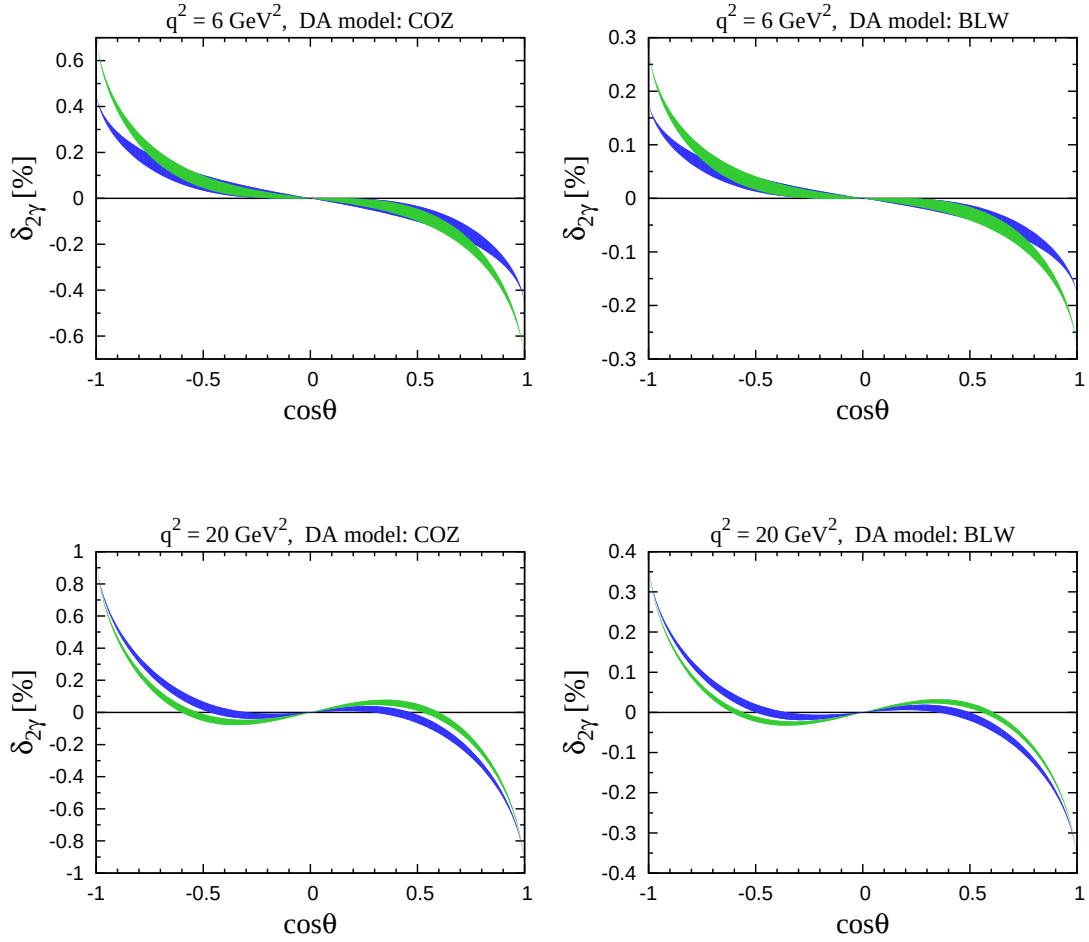

Figure 4.7: Relative two-photon contribution to the cross section at s = 6 GeV^2 and s = 20 GeV^2 as a function of $\cos\theta_{\rm cm}$ for two models of G_E and G_M as indicated in the text. Model 1: blue bands. Model 2: green bands. The bands describe the contribution for different values of $\delta\tilde{G}_E$ given by $-\delta\tilde{G}_E < \delta\tilde{G}_M < \delta\tilde{G}_E$. The left (right) panel correspond to the calculation using the COZ (BLW) model for the nucleon DAs.

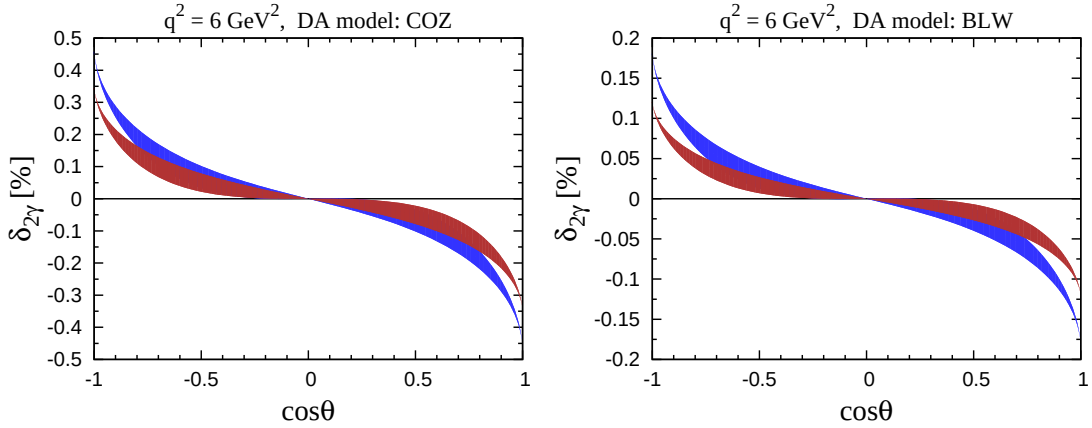

Figure 4.8: Relative 2γ-contribution to the cross section for q^2= 6 GeV^2 calculated with the COZ model (left plot) and BLW (right plot) using two different parametrizations of the form factors. Blue bands: Model 1 (purely real form factors). Red bands: Form factors of Ref. [48] (VMD model). The bands describe the contribution for different values of $\delta\tilde{G}E$ given by $-\delta\tilde{G}_M < \delta\tilde{G}_E < \delta\tilde{G}_M$.

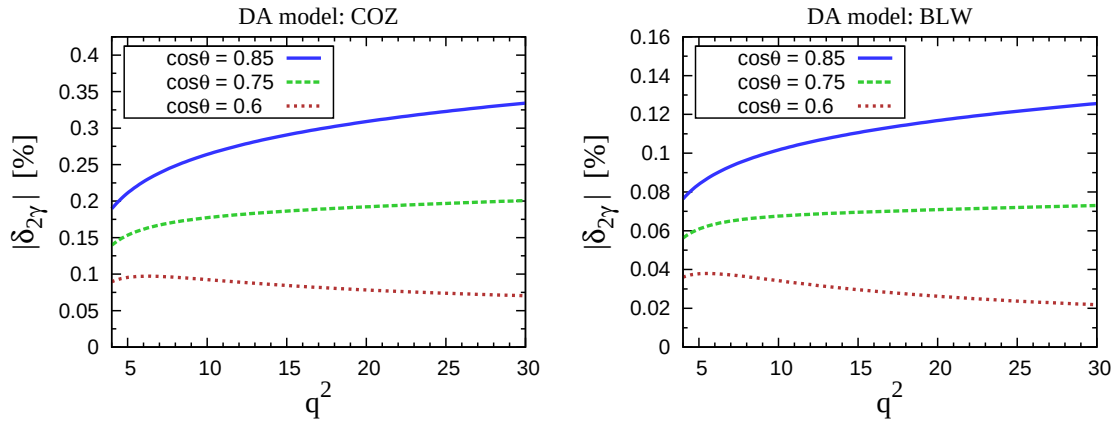

Figure 4.9: Magnitude of the relative two-photon contribution as a function of q^2 for $\cos\theta$ = 0.6 (red dotted curve), $\cos\theta = 0.75$ (green dashed curve), $\cos\theta = 0.85$ (blue solid curve) using Model 1 as 1γ form factor parametrization (purely real form factor) and $\delta G_E = 0$. The left (right) panel indicates the corrections calculated with the COZ (BLW) model for the nucleon DAs.

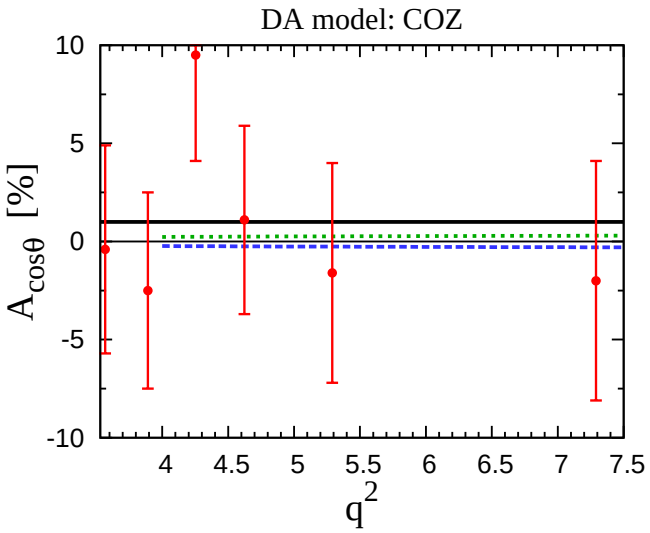

Figure 4.10: Forward-backward asymmetry according to Eq. (4.12) as a function on q^2. Blue dashed curve (green dotted curve): Results within pQCD factorization approach for $\cos\theta = 0.9$ ($\cos\theta = -0.9$) calculated with the COZ model using Model 1 as 1γ-form factor parametrization (purely real form factor) and $\delta G_E = 0$. Black solid curve: $A_{\cos\theta} = 1\%$ as it has been found in the analysis of Ref. [70]. The data points correspond to the results of the analysis at each q^2 value, for which the data of Ref. [30] has been used.

The dependence of $\delta_{2\gamma}$ on the momentum transfer q^2 is shown in Fig. 4.9. The 2γ-corrections have been calculated as a function of q^2 for $\delta G_E = 0$ using three different values of the c.m. scattering angle: $\cos\theta = 0.6,\ 0.75$ and 0.85 in the range of $q^2 = 4{-}30\ \mathrm{GeV}^2$, where the parametrization of Eq. (4.66) (Model 1) has been used as model for the 1γ-form factors. One finds, that the absolute value of the corrections is increasing with q^2 for larger values of $\cos\theta$. Since this growth is only logarithmic, it cannot change the effect quantitatively.

The obtained results allow us to predict the forward-backward asymmetry $A_{\cos\theta}$, defined in Eq. (4.12), which gives rise to the two-photon corrections to the cross section. The findings for the asymmetry calculated within the pQCD description are shown in Fig. (4.10) for $\cos\theta = 0.9$ (blue dashed curve) and $\cos\theta = -0.9$ (green dotted curve) using Model 1 for the electromagnetic form factors and the COZ description of the DAs. Since the 2γ-exchange affects the cross section only slightly, the predicted asymmetry is small, especially in the smaller q^2 range, where $A_{\cos\theta}$ has been analyzed. The solid black line indicates $A_{\cos\theta} = 1\%$, which has been found as average value of the forward-backward asymmetry in the analysis of the data of the BaBar experiment [30]. The experimental results of the asymmetry including the error bars, which have been found at the individual values of q^2, are given by the data points in Fig. (4.10). The current data are affected with quite large uncertainties of $\sim 5\%$, which do not enable to constrain the two-photon exchange corrections so far.

In order to find constraints on two-photon exchange effects in the timelike region, data of $A_{\cos\theta}$ with higher precision are needed. In particular due to the fact that the form factor extraction is more sensitive to small corrections at larger momentum transfer, an extension of the measured q^2 range to higher values seems to be reasonable.

Furthermore, the single spin asymmetry A_y (introduced in Eq. (4.13)) has been analyzed. As discussed in the previous section, only small imaginary parts of the 2γ-amplitudes $\delta\tilde{G}_M$ and $\tilde{F}_3$ are obtained within the factorization approach. Therefore the 2γ-contribution to the SSA mostly results from the interference of the real part of the 2γ-amplitudes and the imaginary part of the form factors G_E and G_M. The relative contribution to A_y is found to be small for all parametrizations of G_E and G_M discussed above. Logically, the resulting 2γ-contribution to A_y using the 1γ-form factor Model 1 of Eq. (4.66) is negligible due to the purely real structure of G_E and G_M in this model. A 2γ-effect of the order of about 1% can be found when considering the two form factors parametrizations (Model 2 and VMD model), which include imaginary contributions of G_E and G_M.

To summarize the results, using a pQCD factorization approach we obtain small 2γ-exchange corrections to the cross section in the process $p\bar{p} \to e^+e^-$ of about $\delta_{2\gamma} \lesssim 1\%$ in the studied momentum transfer range of $4 - 30$ GeV^2. The small 2γ-effect makes it challenging to observe such effects in unpolarized cross section measurements. e.g. by PANDA@FAIR. Feasibility studies of the annihilation process at PANDA have been performed in [28]. Since the value of the 2γ-contribution is sensitive to the choice of the DAs, a precise measurement of the process would in addition allow to probe and constrain the DAs of the proton and antiproton.

4.3 Partonic Calculation of Timelike Two-Photon Exchange: Generalized Distribution Amplitude Approach

As an alternative approach for investigating the two-photon exchange in the timelike region we present a partonic description, which has been applied to obtain 2γ-exchange corrections in elastic electron proton scattering using the concept of generalized parton distributions [55, 56]. The results of the calculations have been presented in Sec. 3.2. In order to deal with annihilation processes the timelike counterparts of the GPDs have to be introduced, the generalized distribution amplitudes (GDAs), which parametrize the matrix element between a system of hadrons and the vacuum.

4.3.1 Generalized Distribution Amplitudes

In order to describe the timelike two-photon exchange within another model, we assume the factorization approach, as shown in Fig 4.11, where the amplitude of the process $p\bar{p} \to e^+e^-$ appears as convolution of a soft transition matrix element, parametrized by the GDAs, and a hard subprocess H, where just a single quark-antiquark pair annihilates into a lepton pair, $H(q\bar{q} \to e^+e^-)$.

This so-called handbag factorization is expected to be valid in the kinematical region where s, $-t$ and $-u$ are large compared to the hadronic scale ($s, |t|, |u| \gg m_N^2$). For this kinematical region the handbag contribution is assumed to be dominant, as long as the momentum transfer values are not asymptotically large. At high momentum transfer the leading contribution with three valence quarks participating in the subprocess dominates, which has been discussed in Sec. 4.2. The value of momentum transfer, which is sufficiently large for the perturbative QCD approach to dominate, is still an unsolved problem.

The validity of the factorization scheme has been proven for several spacelike processes, as deep inelastic scattering or the Drell-Yan processes, but no proof of the discussed timelike

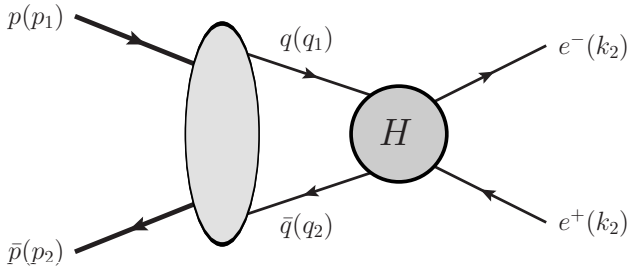

Figure 4.11: Sketch of a handbag approximation for the process $p\bar{p} \to e^+e^-$. The left blob represents the GDAs, H denotes the hard subprocess.

factorization approach exists. Arguments for the applicability of such a factorization have been discussed in Ref. [80].

The generalized distribution amplitudes, indicated by the left gray blob in Fig (4.11), are complex quantities, which encode the physics of the soft transition,

$$p(p_1) + \bar{p}(p_2) \to q(q_1) + \bar{q}(q_2), \tag{4.68}$$

and cannot be calculated from first principles. They are functions of three variables, the c.m. energy $s = (p_1 + p_2)^2$, the momentum fraction carried by the quark

$$z = \frac{q_1^+}{(p_1 + p_2)^+}, \tag{4.69}$$

and the so-called skewness ζ,

$$\zeta = \frac{p_1^+}{(p_1 + p_2)^+}, \tag{4.70}$$

which describes how the total momentum of the $p\bar{p}$-pairs is shared between the nucleons.

GDAs have been introduced in Ref. [80] in order to study two-photon annihilation into baryon-antibaryon pairs and have been used to analyze of the process $\bar{p}p \to \pi^0\gamma$ within the handbag factorization approach in Ref. [81]. The GDAs parametrize the matrix element between a baryon state and the vacuum (or vice versa), as follows [80]

$$\begin{aligned}
&\frac{(p_1+p_2)^+}{2}\int\frac{dx^-}{2\pi}e^{izP^+x^-}\left\langle 0\middle|\bar{q}(0)\gamma^+q(\bar{x})\middle|N(p_1,\lambda_{N_1})\bar{N}(p_2,\lambda_{N_2})\right\rangle \\
&= \phi_V^q(z,\zeta,s)\bar{v}(p_2,\lambda_{N_2})\gamma^+u(p_1,\lambda_{N_1}) + \phi_S^q(z,\zeta,s)\frac{(p_1+p_2)^+}{2m}\bar{v}(p_2,\lambda_{N_2})u(p_1,\lambda_{N_1}), \\
&\frac{(p_1+p_2)^+}{2}\int\frac{dx^-}{2\pi}e^{izP^+x^-}\left\langle 0\middle|\bar{q}(0)\gamma^+\gamma_5q(\bar{x})\middle|N(p_1,\lambda_{N_1})\bar{N}(p_2,\lambda_{N_2})\right\rangle \\
&= \phi_A^q(z,\zeta,s)\bar{v}(p_2,\lambda_{N_2})\gamma^+\gamma_5u(p_1,\lambda_{N_1}) - \phi_P^q(z,\zeta,s)\frac{(p_1+p_2)^+}{2m}\bar{v}(p_2,\lambda_{N_2})\gamma_5u(p_1,\lambda_{N_1}),
\end{aligned} \tag{4.71}$$

where ϕ_i^q with $i = V, S, A, P$ is the vector, scalar, axial and pseudoscalar GDA, and q refers to the quark flavor. GDAs are process independent quantities and accordingly can be applied to the 2γ-exchange process for $\bar{p}p \to e^+e^-$.

Integrating Eq. (4.71) over z leads to the following sum rules:

$$\begin{aligned} F_i^q(s) &= \int_0^1 dz\, \phi_i^q(z,\zeta,s), \quad \text{for } i = V, A, P \\ (1-2\zeta)F_S^q(s) &= \int_0^1 dz\, \phi_S^q(z,\zeta,s), \end{aligned} \tag{4.72}$$

where F_i^q are the quark form factors. Appropriate combinations of the quark form factors give rise to the nucleon form factors of the electromagnetic and weak current, as

$$G_M(s) = \sum_q Q_q F_V^q(s), \qquad F_2(s) = \sum_q Q_q F_S^q(s). \tag{4.73}$$

4.3.2 Timelike Two-Photon Exchange within a GDA based Approach

For the analysis of

$$p(p_1, \lambda_{N_1}) + \bar{p}(p_2, \lambda_{N_2}) \to e^+(k_1, h) + e^-(k_2, -h). \tag{4.74}$$

within a handbag factorization approach we use a symmetric frame and choose the axes of the c.m. frame such that the 3-momenta of the incoming nucleons are in the positive or negative x-direction and the process takes place in the x-z plane. Using light-cone variables, with the shorthand notation $p = (p^+, p^-, p_\perp)$, the momenta of the nucleons can be chosen as

$$\begin{aligned} p_1 &= \frac{\sqrt{s}}{2}\,(\,1, 1,\ \ \beta\vec{e}_1\,)\,, \\ p_2 &= \frac{\sqrt{s}}{2}\,(\,1, 1, -\beta\vec{e}_1)\,, \end{aligned} \tag{4.75}$$

with

$$\beta = \sqrt{1 - \frac{4m_N^2}{s}} = \sqrt{\frac{\tau - 1}{\tau}}, \tag{4.76}$$

and $\vec{e}_1 = (1, 0)$. The positron momentum (k_1) and electron momentum (k_2) are given by

$$\begin{aligned} k_1 &= \frac{\sqrt{s}}{2}\,(1 + \sin\theta, 1 - \sin\theta,\ \cos\theta\vec{e}_1\,)\,, \\ k_2 &= \frac{\sqrt{s}}{2}\,(1 - \sin\theta, 1 + \sin\theta, -\cos\theta\vec{e}_1)\,, \end{aligned} \tag{4.77}$$

with the c.m. scattering angle θ. Using the Mandelstam variables

$$s = q^2 = (p_1 + p_2)^2, \qquad t = (p_1 - k_1)^2, \qquad u = (p_1 - k_2)^2, \tag{4.78}$$

the c.m. scattering angle θ can be expressed with respect to s, t and u:

$$\cos\theta = \frac{u - t}{\sqrt{s(s - 4m_N^2)}}, \qquad \sin\theta = \frac{2\sqrt{ut - m_N^4}}{\sqrt{s(s - 4m_N^2)}}. \tag{4.79}$$

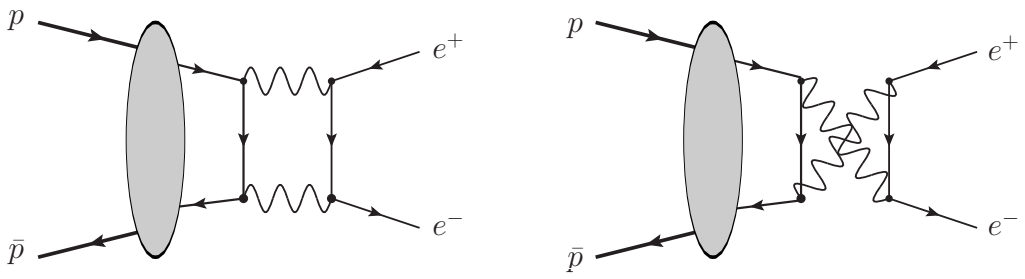

Figure 4.12: Two-photon exchange processes of $p\bar{p} \to e^+e^-$ in the handbag approximation.

The process in the handbag approximation in terms of a soft $p\bar{p} \to q\bar{q}$ transition and the hard subprocess $q\bar{q} \to e^+e^-$, which occurs through the exchange of two photons, is shown in Fig. 4.12. The amplitude has a similar structure as the one of the $\gamma\gamma \to p\,\bar{p}$ process, appearing as a convolution of the GDAs ϕ_i and the hard process H. Following Ref. [80], it can be found as:

$$\begin{aligned} T_{h,\lambda_{N_1},\lambda_{N_2}} = \frac{1}{(p_1+p_2)^+}\Bigg\{ & \frac{1}{2}\left[H_{h,\frac{1}{2}} + H_{h,-\frac{1}{2}}\right]\Big(R_V(s)\,\bar{N}(p_2,\lambda_{N_2})\,\gamma^+\,N(p_1,\lambda_{N_1}) \\ & + (1-2\zeta)\,R_S(s)\,\frac{(p_1+p_2)^+}{2m_N}\bar{N}(p_2,\lambda_{N_2})N(p_1,\lambda_{N_1})\Big) \\ & + \frac{1}{2}\left[H_{h,\frac{1}{2}} - H_{h,-\frac{1}{2}}\right]\Big(R_A(s)\,\bar{N}(p_2,\lambda_{N_2})\,\gamma^+\gamma_5\,N(p_1,\lambda_{N_1}) \\ & - R_P(s)\,\frac{(p_1+p_2)^+}{2m_N}\,\bar{N}(p_2,\lambda_{N_2})\,\gamma_5\,N(p_1,\lambda_{N_1})\Big)\Bigg\}, \end{aligned} \tag{4.80}$$

with the annihilation form factors R_i, which are obtained by integrating ϕ_i over z

$$\begin{aligned} R_i(s) &= \sum_q Q_q^2 \int_0^1 dz\,\phi_i^q(z,\zeta,s), \qquad i = A,V,P \\ (1-2\zeta)R_S(s) &= \sum_q Q_q^2 \int_0^1 dz\,\phi_S^q(z,\zeta,s). \end{aligned} \tag{4.81}$$

Due to the choice of the reference frame with a skewness of $\zeta = 1/2$, the scalar form factor, entering with a factor $1-2\zeta$, decouples and does not contribute to the amplitude.

The hard partonic subprocess, the annihilation of a quark-antiquark pair into a lepton pair,

$$q(q_1,\lambda_q) + \bar{q}(q_2,-\lambda_q) \to e^+(k_1,-h) + e^-(k_2,h), \tag{4.82}$$

contains the direct and crossed box diagram of the 2γ-exchange process, presented in Fig 4.13.

It has been shown [80], that the $p\bar{p} \to q\bar{q}$ transition can only be soft if the quarks have small virtualities and approximately carry the momenta of the proton and antiproton, respectively. Therefore, the subprocess has been calculated using the assumption, that the quarks are on-shell.

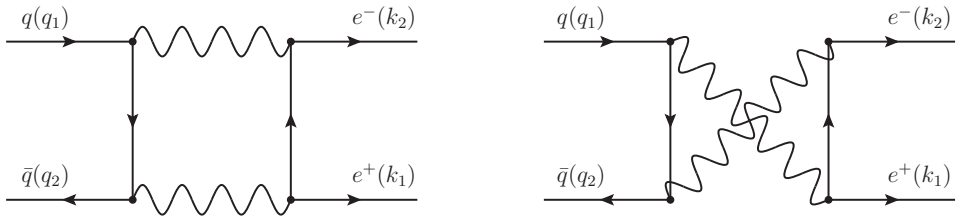

Figure 4.13: Direct and crossed box diagrams of the hard subprocess $q\bar{q} \to e^+e^-$ including the exchange of two photons

By means of the approximation, that the masses of the quarks and of the leptons can be neglected, the general amplitude of the two-photon part is given by the expression

$$\begin{aligned} H_{h,\lambda_q} = {} & \frac{e^2}{q^2}\,\bar{u}\,(k_2,h)\,\gamma_\mu v\,(k_1,-h) \\ & \times\ \bar{v}\,(q_2,-\lambda_q)\left(\tilde{f}_1^q\gamma^\mu + \tilde{f}_3^q\,\frac{q_1^\mu - q_2^\mu}{2}\,\frac{\not{k}_2 - \not{k}_1}{2}\right) u\,(q_1,\lambda_q)\,, \end{aligned} \tag{4.83}$$

with the quark helicity $\lambda_q = \pm\frac{1}{2}$. For massless quarks, the helicity of the antiquark is opposite to the quark helicity and no analogon of the form factor $\tilde{F}_2$ in Eq. (4.6) emerges in the amplitude of the subprocess. We only consider contributions were both photons have non-zero virtualities. The form factors $\tilde{f}_1^q$, and $\tilde{f}_3^q$ can be obtained from the results of two-photon exchange corrections for the reaction $e^+e^- \to \mu^+\mu^-$, for the case that none of the photons are soft. These calculations have been performed in Refs. [82,83], and the results have been confirmed in the course of the GPD calculation of 2γ-exchange in the crossed scattering channel [56]. The real part of the form factors has been found as

$$\begin{aligned} \mathrm{Re}\,\tilde{f}_1^q &= \frac{e^2}{4\pi^2}\left\{\frac{1}{2}\ln\left|\frac{\hat{t}}{\hat{u}}\right| + \frac{\hat{t}-\hat{u}}{4\,\hat{t}\,\hat{u}}\left(\hat{t}\ln^2\left|\frac{\hat{t}}{\hat{s}}\right| + \hat{u}\ln\left|\frac{\hat{u}}{\hat{s}}\right|\right)\right\} \\ \mathrm{Re}\,\tilde{f}_3^q &= \frac{e^2}{4\pi^2}\,\frac{1}{\hat{t}\,\hat{u}}\,\left\{\hat{t}\ln\left|\frac{\hat{t}}{\hat{s}}\right| + \hat{u}\ln\left|\frac{\hat{u}}{\hat{s}}\right| + \frac{\hat{t}-\hat{u}}{2}\left(\frac{\hat{t}}{\hat{u}}\ln^2\left|\frac{\hat{t}}{\hat{s}}\right| - \frac{\hat{u}}{\hat{t}}\ln^2\left|\frac{\hat{u}}{\hat{s}}\right|\right)\right\}. \end{aligned} \tag{4.84}$$

The variables $\hat{s}$, $\hat{t}$, and $\hat{u}$ are the Mandelstam variables of the subprocess:

$$\begin{gathered} \hat{s} = (q_1+q_2)^2, \qquad \hat{t} = (q_1-k_1)^2, \qquad \hat{u} = (q_2-k_1)^2, \\ \text{with} \quad q^2 = \hat{s} = -\hat{t} - \hat{u}. \end{gathered} \tag{4.85}$$

The hard annihilation amplitude results in

$$\begin{aligned} H_{h,\lambda_q} &= \frac{e^2}{\widehat{s}}\left(-\tilde{f}_1^q\left(2h\,2\lambda_q\cdot\widehat{s} + \widehat{u} - \widehat{t}\,\right) + \tilde{f}_3^q\left(-\widehat{u}\,\widehat{t}\,\right)\right) \\ \Rightarrow\quad \frac{1}{2}\left[H_{h,\frac{1}{2}} + H_{h,-\frac{1}{2}}\right] &= \frac{e^2}{\widehat{s}}\left(\tilde{f}_1^q(\,\widehat{t} - \widehat{u}\,) - \tilde{f}_3^q\,\widehat{t}\,\widehat{u}\,\right) \\ \frac{1}{2}\left[H_{h,\frac{1}{2}} - H_{h,-\frac{1}{2}}\right] &= -\frac{e^2}{\widehat{s}}\,\tilde{f}_1^q\cdot\widehat{s}\cdot 2h. \end{aligned} \tag{4.86}$$

Since the momenta of the quark and antiquark have to be close to the nucleon momenta, the hard annihilation process H will be evaluated using

$$\hat{t} \simeq t, \qquad \hat{u} \simeq u, \tag{4.87}$$

for the Mandelstam variables of the subprocess.

The amplitude in the factorized process can be rewritten using the vector

$$\tilde{n}^\mu = \frac{1}{(p_1+p_2)^+}(1,0,0,-1), \tag{4.88}$$

which yields

$$\begin{aligned} T_{h,\lambda_{N_1},\lambda_{N_2}} \;=\; & \frac{1}{2}\left[H_{h,\frac{1}{2}} + H_{h,-\frac{1}{2}}\right] R_V(s)\; \bar{N}(p_2,\lambda_{N_2})\; \tilde{\not{n}}\, N(p_1,\lambda_{N_1}) \\ & + \frac{1}{2}\left[H_{h,\frac{1}{2}} - H_{h,-\frac{1}{2}}\right] \Big(R_A(s)\, \bar{N}(p_2,\lambda_{N_2})\, \tilde{\not{n}}\gamma_5\, N(p_1,\lambda_{N_1}) \\ & - R_P(s)\, \frac{1}{2m_N}\, \bar{N}(p_2,\lambda_{N_2})\, \gamma_5\, N(p_1,\lambda_{N_1}) \Big). \end{aligned} \tag{4.89}$$

The Dirac structures are then evaluated with respect to the nucleon helicities λ_{N_1} and λ_{N_2}, using

$$\begin{aligned} \bar{N}(p_2,\lambda_{N_2})\; \tilde{\not{n}}\, N(p_1,\lambda_{N_1}) &= -\frac{1}{2}\big(1 - 4\lambda_{N_1}\lambda_{N_2}\big), \\ \bar{N}(p_2,\lambda_{N_2})\, \tilde{\not{n}}\, \gamma_5\, N(p_1,\lambda_{N_1}) &= \frac{m_N}{\sqrt{s}}\big(1 + 4\lambda_{N_1}\lambda_{N_2}\big) - \sqrt{\frac{s-4m_N^2}{4s}}\,\big(2\lambda_{N_1} - 2\lambda_{N_2}\big), \\ \bar{N}(p_2,\lambda_{N_2})\, \gamma_5\, N(p_1,\lambda_{N_1}) &= -\frac{\sqrt{s}}{2}\big(1 + 4\lambda_{N_1}\lambda_{N_2}\big), \end{aligned} \tag{4.90}$$

which leads to

$$\begin{aligned} T_{h,\lambda_{N_1},\lambda_{N_2}} \;=\; & -\frac{1}{2}\left[H_{h,\frac{1}{2}} + H_{h,-\frac{1}{2}}\right] R_V(s)\, \frac{1}{2}\big(1 - 4\lambda_{N_1}\lambda_{N_2}\big) \\ & + \frac{1}{2}\left[H_{h,\frac{1}{2}} - H_{h,-\frac{1}{2}}\right] \Bigg\{ - R_P(s)\, \frac{\sqrt{s}}{4m_N}\big(1 + 4\lambda_{N_1}\lambda_{N_2}\big) \\ & - R_A(s) \left(\frac{m_N}{\sqrt{s}}\big(1 + 4\lambda_{N_1}\lambda_{N_2}\big) - \sqrt{\frac{s-4m_N^2}{4s}}\,\big(2\lambda_{N_1} - 2\lambda_{N_2}\big) \right) \Bigg\}. \end{aligned} \tag{4.91}$$

The most general parametrization of the $p\bar{p} \to e^+e^-$ amplitude (Eq. (4.6)), depending on the generalized form factors $\tilde{G}_M$, $\tilde{F}_2$, and $\tilde{F}_3$, can be evaluated as a function of the helicity

of the proton and antiproton as well:

$$
\begin{aligned}
T_{h,\lambda_{N_1},\lambda_{N_2}} &= \frac{e^2}{s}\,\bar{u}(k_2,h)\,\gamma_\mu\,v(k_1,-h) \\
&\quad\times \bar{N}\,(p_2,\lambda_{N_2})\left[\tilde{G}_M\gamma^\mu - \tilde{F}_2\frac{P^\mu}{m_N} + \tilde{F}_3\frac{P^\mu}{m_N^2}(\not{k}_2-\not{k}_1)\right] N\,(p_1,\lambda_{N_1}) \\
&= \frac{e^2}{s}\left\{\tilde{G}_M\left[-2m_N\sqrt{\frac{ut-m^4}{s-4m_N^2}}\Big(2\lambda_{N_1}+2\lambda_{N_2}\Big) - \frac{s}{2}\Big(2\lambda_{N_1}-2\lambda_{N_2}\Big)\right.\right. \\
&\quad\left. - \frac{u-t}{2}\sqrt{\frac{s}{s-4m_N^2}}\Big(1-4\lambda_{N_1}\lambda_{N_2}\Big)\right] \\
&\quad + \frac{\tilde{F}_2}{m_N}\left[-\sqrt{\left(ut-m_N^4\right)\left(s-4m_N^2\right)}\;\frac{1}{2}\Big(2\lambda_{N_1}+2\lambda_{N_2}\Big)\right] \\
&\quad + \frac{\tilde{F}_3}{m_N^2}\left[\frac{m_N(u-t)\sqrt{ut-m_N^4}}{\sqrt{s-4m_N^2}}\;\frac{1}{2}\Big(2\lambda_{N_1}+2\lambda_{N_2}\Big)\right. \\
&\quad\left.\left. - \sqrt{\frac{s}{s-4m_N^2}}\;\left(ut-m_N^4\right)\;\frac{1}{2}\Big(1-4\lambda_{N_1}\lambda_{N_2}\Big)\right]\right\}.
\end{aligned}
\tag{4.92}
$$

A comparison of Eqs. (4.91) and (4.92) allows to extract the 2γ-amplitudes and express them in terms of the GDAs, which leads to

$$
\begin{aligned}
\delta\tilde{G}_M &= -\sqrt{\frac{s-4m_N^2}{s}}\;\frac{1}{s}\cdot A, \\
\delta\tilde{G}_E &= \sqrt{\frac{s-4m_N^2}{s}}\;\left(\frac{u-t}{4(ut-m_N^4)}\cdot C + \frac{1}{2\sqrt{ut-m_N^4}}\cdot B\right), \\
\tilde{F}_3 &= \sqrt{\frac{s-4m_N^2}{s}}\;\frac{m_N^2}{ut-m_N^4}\cdot C,
\end{aligned}
\tag{4.93}
$$

where the variables A, B, C have been introduce, defined as

$$
A = \int_0^1 dz\tilde{f}_1^q\cdot\hat{s}\sum_q Q_q^2\;\phi_A^q = \hat{s}\,\tilde{f}_1^q\,R_A, \tag{4.94}
$$

$$
B = \int_0^1 dz\tilde{f}_1^q\cdot\hat{s}\left(\sum_q Q_q^2\;\phi_A^q + \frac{s}{4m_N^2}\sum_q Q_q^2\;\phi_P^q\right) = \tilde{f}_1^q\,\hat{s}\left(R_A + \frac{s}{4m_N^2}R_P\right). \tag{4.95}
$$

$$\begin{aligned} C &= \frac{u-t}{s}\int_0^1 dz\, \tilde{f}_1^q \cdot \hat{s} \sum_q Q_q^2\, \phi_A^q + \int_0^1 dz\, \left(\tilde{f}_1^q(\hat{t}-\hat{u}) - \tilde{f}_3^q \hat{t}\,\hat{u}\right) \sum_q Q_q^2\, \phi_V^q \\ &= \frac{u-t}{s}\,\hat{s}\,\tilde{f}_1^q\, R_A + \left(\tilde{f}_1^q(\hat{t}-\hat{u}) - \tilde{f}_3^q\,\hat{t}\,\hat{u}\right) R_V, \end{aligned} \tag{4.96}$$

4.3.3 Results

For an analysis of the two-photon exchange contributions within the handbag approximation, information on the annihilation form factors is required. However, no model calculation of these form factors or GDAs exists so far. On account of this, in previous studies the form factors have been extracted phenomenologically (see e.g. Refs. [80,81]).

Combining Eqs. (4.73) and (4.81), one can relate the vector annihilation form factor R_V to the magnetic form factor G_M. We assume, that the u- and the d-quark form factors of the proton fulfill

$$F_i^u = \frac{1}{2} F_i^d, \tag{4.97}$$

and neglect the form factor contributions of strange quarks and heavier quarks, which yields $R_V(s) = G_M(s)$.

The magnetic form factor has been extracted by fitting the timelike form factor data. The widest data set at higher momentum transfer values is provided by the BaBar experiment [31], where the effective timelike form factor G_{eff} (defined in Eq. (2.44)) has been measured in the reaction $e^+e^- \to p\,\bar{p}\,\gamma$ up to energies of $s \sim 20$ GeV^2. A fit of G_{eff} to the data above $s = 5$ GeV^2 leads to

$$s^2\, G_{\text{eff}} \;\simeq\; 3.35 \text{ GeV}^4. \tag{4.98}$$

The results are presented in Fig. 4.14.

The frequently used assumption $|G_M| = |G_E|$ yields $G_{\text{eff}} = |G_M|$, therefore we will use as parametrization for R_V:

$$s^2\, |R_V(s)| \;=\; s^2\, |G_M(s)| \;\simeq\; 3.35 \text{ GeV}^4. \tag{4.99}$$

In an analogous manner the axial annihilation form factor R_A can be expressed in terms of the axial form factor of the nucleon, G_A. In the case of isospin symmetry, the nucleon matrix element of the axial current operator $A^{a,\mu}(0)$ is parametrized by two form factors,

$$\begin{aligned} \left\langle N(p')\right| A^{a,\mu}(0) \left|N(p)\right\rangle &= \left\langle N(p')\right| \bar{q}\,(0)\,\gamma^\mu\gamma_5\,\frac{\tau^a}{2}\,q(0)\left|N(p)\right\rangle \\ &= \bar{N}(p')\left[\gamma^\mu\gamma_5 G_A(q^2) + \frac{p'^\mu - p^\mu}{2m_N} G_P(q^2)\right]\frac{\tau^a}{2}\,N(p), \end{aligned} \tag{4.100}$$

where G_A is the axial form factor, G_P the pseudoscalar form factor and τ^a are the Pauli matrices. Using Eqs. (4.81) and (4.97), one finds $R_A = G_A$.

In the spacelike region the measurements of $G_A(Q^2)$ indicates, that the form factor can be described very well by a dipole fit. We will adopt the dipole fit as parametrization of $G_A(s)$ in the timelike region, because no data of the axial form factor in the timelike regime exist so far. Hence R_A can be found as

$$R_A(s) \;=\; G_A(s) \;=\; \frac{g_A}{\left(1 - \frac{s}{m_A^2}\right)^2}, \tag{4.101}$$

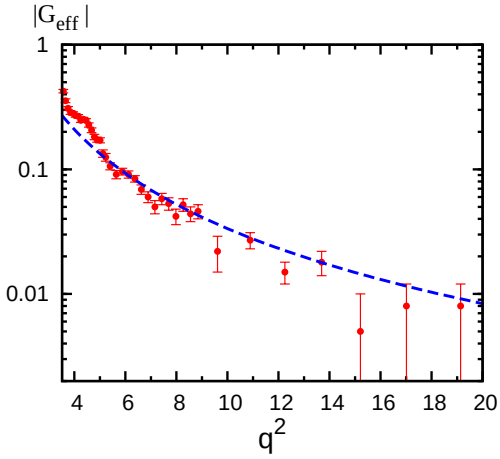

Figure 4.14: The timelike effective form factor $|G_{\text{eff}}|$ as a function of q^2. The blue dashed curve represents the fit according to Eq. (4.99) for $q^2 > 5$ GeV^2. The data are taken from Ref. [31].

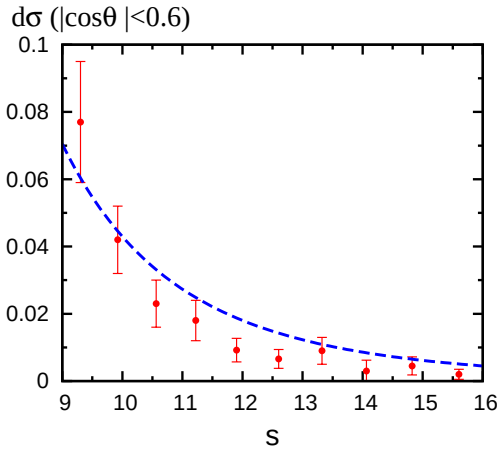

Figure 4.15: Integrated cross section $d\sigma(|\cos\theta < 0.6|)$ for $\gamma\gamma \to p\bar{p}$ as a function of s. The blue dashed curve represents the fit given by Eq. (4.103). The data are taken from Ref. [85].

with the axial coupling constant $g_A = 1.27$ and the axial mass m_A, for which we use $m_A = 1.026$ GeV [84].

In Ref. [80] the process $\gamma\gamma \to p\bar{p}$ has been evaluated within a handbag factorization approach and the differential cross section has been found as

$$\begin{aligned} \frac{d\sigma}{dt} =& \frac{4\pi\alpha_{\text{em}}^2}{s^2}\,\frac{1}{\sin^2\theta}\left\{\left|R_{\text{eff}}\right|^2 + \left|R_V\right|^2\cos^2\theta\right\} \\ \text{with} \quad R_{\text{eff}} =& \left(\left|R_A + R_P\right|^2 + \tau\left|R_P\right|^2\right)^{1/2}. \end{aligned} \tag{4.102}$$

Since the GDAs and consequently the annihilation form factors R_i are process independent quantities, Eq. (4.102) can be fitted to the data of the $\gamma\gamma \to p\bar{p}$ cross section in order to obtain R_{eff}, which can be used to extract R_P. In our analysis, we use the data of the two-photon annihilation process $\gamma\gamma \to p\bar{p}$ collected at the BELLE experiment at the KEK-B factory [85], where we take the results of the integrated cross section $d\sigma(|\cos\theta| < 0.6)$ at the highest measured s values, with 9 GeV$^2 < s <$ 16 GeV^2, into account. The result of the fit, which gives

$$s^2\,R_{\text{eff}} \;\simeq\; 5.02\ \text{GeV}^4, \tag{4.103}$$

which is presented in Fig. 4.15. In the analysis the description of Eq. (4.99) has been used as vector form factor R_V in Eq. (4.102).

The ratio $|R_P|/|R_A|$ can be written as

$$\frac{|R_P|}{|R_A|} = -\frac{1}{1+\tau}\cos\delta + \frac{1}{1+\tau}\sqrt{(1+\tau)\,\frac{R_{\text{eff}}^2}{|R_A|^2} - (1+\tau) + \cos^2\delta} \tag{4.104}$$

where δ is the relative phase of R_A and R_P.

After specifying the parametrizations of the annihilation form factors, Eqs. (4.99), (4.101) and (4.104), we can estimate the two-photon exchange contribution to the cross section. In addition, an explicit expression of the electromagnetic form factors $G_{E,M}$ is needed, for which a VMD based model is used, as given in Ref. [48].

The results are shown in Fig. 4.16, where the relative contribution of the 2γ-exchange corrections to the cross section, $\delta_{2\gamma}$, has been calculated as a function of $\cos\theta$ for three different values of c.m. energies, $s = 6$ GeV^2, 9 GeV^2, and 12 GeV^2. We only present results for the intermediate angular range, because the GDA factorization description is applicable only for $s \sim t \sim u \gg m_N^2$. One finds a 2γ-contribution of $\sim 1\%$ in maximum, which is increasing with the momentum transfer. The angular dependence is found to be similar to the behavior obtained in Sec. 4.2, when using the pQCD factorization approach, even though the results are inversed at $\cos\theta = 0$. Their relative contribution is slightly larger within the GDA model approach. The colored bands in Fig. 4.16 correspond to the unknown relative phase of R_A and R_P, with $-1 < \cos\delta < 1$.

The relative 2γ-exchange contribution to the cross section as a function of the c.m. energy s is presented in Fig. 4.17 for three values of the c.m. scattering angle, $\cos\theta = 0.3$, 0.4 and 0.5, where the colored bands again stand for the variation of the phase $\cos\delta$. One notices, that the 2γ-exchange corrections are increasing with s at smaller values of momentum transfer and reaching a maximum at $s \sim 17$ GeV^2. For $\cos\theta = 0.5$, the contribution is found to be $|\delta_{2\gamma}| \sim 1.6$ % in the maximum.

The results for the forward-backward symmetry $A_{\cos\theta}$, defined in Eq. (4.12), are shown in Fig. 4.18, where $A_{\cos\theta}$ has been analyzed for $\cos\theta = 0.5$ (blue dashed curve) and $\cos\theta = -0.5$ (green dotted curve) using $\cos\delta = -1$. The magnitude of $A_{\cos\theta}$ is increasing with the momentum transfer, approaching $\sim 0.5\,\%$ for the largest considered values of s. The average value of the asymmetry, $A_{\cos\theta} = 1\,\% \pm 2\,\%$, obtained in Ref. [70] is given by the black solid curve. Even though the results for the GDA model calculation are larger as when using the pQCD factorization approach, the existing data do not allow for significant tests of the model calculations for two-photon exchange corrections so far.

A more precise understanding of the annihilation form factors or the GDAs will certainly improve the analysis of the 2γ-exchange within a GDA based approach.

4.4 Conclusions

In this chapter the two-photon exchange contributions to the timelike annihilation process $p\bar{p} \to e^+e^-$ have been analyzed within two different factorization approaches and predictions for the 2γ-exchange corrections to the cross section as well as the forward-backward asymmetry have been provided. With the view to forthcoming accurate form factors measurements in the timelike region, it is important to be aware of these corrections.

The pQCD factorization approach gives a 2γ-exchange contribution which is less than 1% over the studied kinematical range. However, at smaller momentum transfer one is probably outside of the validity of such an approach. Using a GDA based model, the 2γ-corrections are found to be somewhat larger, reaching values of $\sim 2\,\%$ in the intermediate angular region, where this approach is expected to be applicable. The results are smaller than the 2γ-corrections found for the spacelike *ep*-scattering process, which indicates that the 2γ-exchange effects are less significant for timelike form factor extraction than for the spacelike case.

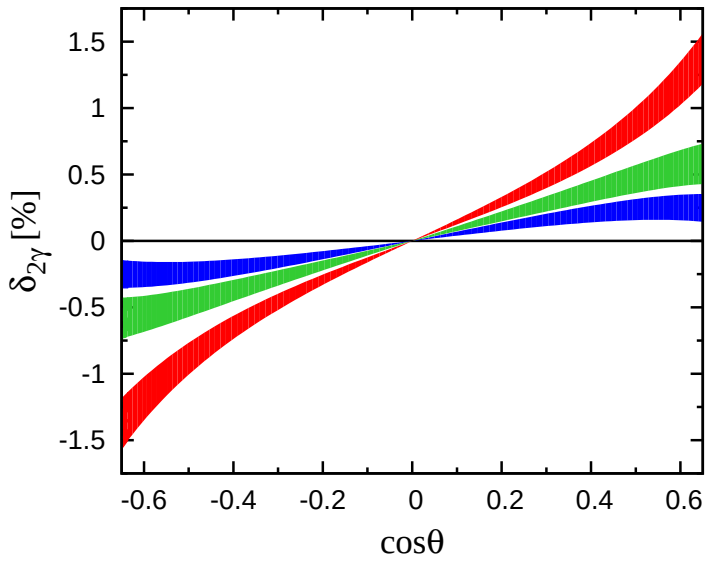

Figure 4.16: Relative two-photon contribution to the cross section of $p\bar{p} \to e^+e^-$ as a function of $\cos\theta$ within a GDA based approach for selected values of c.m. energies. Blue curve: $s = 6$ GeV^2; green curve: $s = 9$ GeV^2; red curve: $s = 12$ GeV^2. The colored bands indicate the variation of the phase $\cos\delta$ in Eq. (4.104).

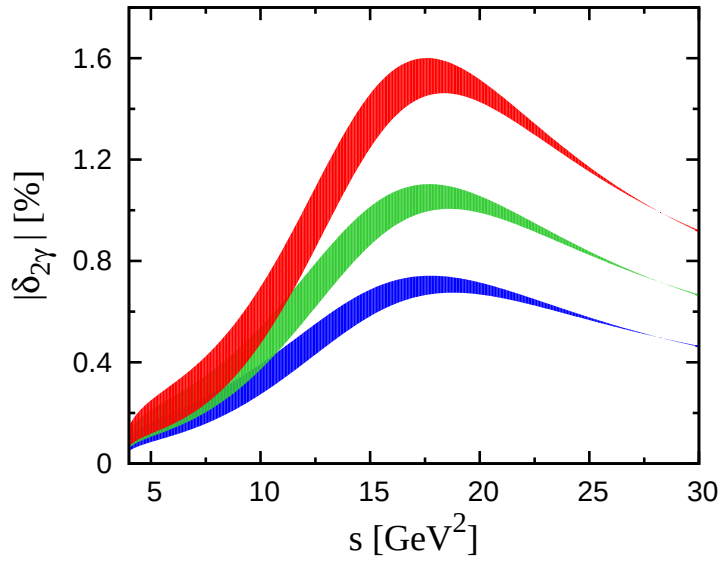

Figure 4.17: Relative two-photon contribution to the cross section of $p\bar{p} \to e^+e^-$ as a function of s within a GDA based approach for selected values of c.m. scattering angles. Blue curve: $\cos\theta = 0.3$; green curve $\cos\theta = 0.4$; red curve: $\cos\theta = 0.5$. The colored bands indicate the variation of the phase $\cos\delta$ in Eq. (4.104).

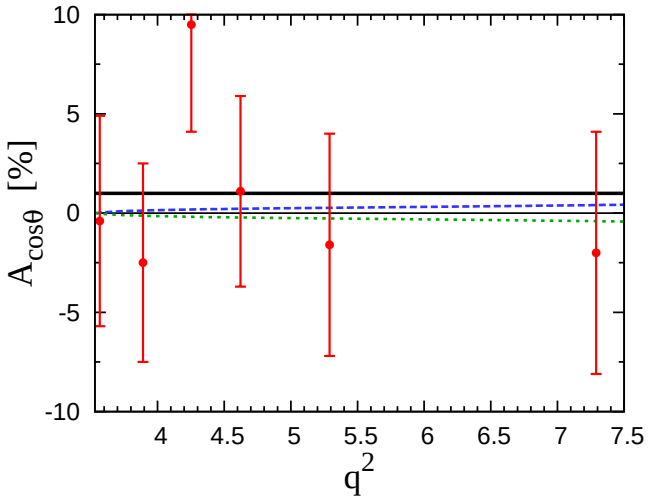

Figure 4.18: Forward-backward asymmetry according to Eq. (4.12) as a function of q^2. Blue dashed curve (green dotted curve): Results within the GDA approach for $\cos\theta = 0.5$ ($\cos\theta = -0.5$) calculated for $\cos\delta = -1$. Black solid curve: $A_{\cos\theta} = 1\%$ as it has been found in the analysis of Ref. [70]. The data points correspond to the results of the analysis at each q^2 value, for which the data of Ref. [30] have been used.

The existing data in the timelike region have not yet reached the required precision which allows to find constraints on (timelike) 2γ-exchange, as it could be realized through an accurate measurement of the forward-backward asymmetry. The predicted size of the asymmetry is found to be still below the uncertainties of the available data. A precise measurement provides a test of the timelike two-photon exchange and offers the possibility to probe the theoretical models used in this work.

Chapter 5

Two-Boson Exchange in Parity-Violating Electron-Proton Scattering

In this chapter the influence of two-boson exchange in parity-violating *ep*-scattering is discussed. Aside from a transmitted photon, the Standard Model provides the possibility that electron-proton scattering occurs through the exchange of a Z boson. This Z boson exchange, even though it is suppressed at lower energies, manifests itself in a parity-violating (PV) contribution to the scattering cross section. The resulting parity-violating asymmetry offers a method to study the matrix elements of the neutral weak current operator of the proton and provides access to the strange quark content of the nucleon as well as dedicated tests of the Standard Model. This asymmetry can be affected by two-boson exchange, in particular the exchange of a photon and Z boson (γZ).

General aspects of parity-violating electron-proton scattering will be presented in the first section of this chapter. In the second part, two-boson exchange effects are calculated within the pQCD factorization approach, which has been introduced in the previous chapter and which has been used to study 2γ-corrections to the process $\bar{p}\,p \to e^+e^-$.

5.1 Parity-Violating Electron-Proton Scattering

The leading contribution to elastic *ep*-scattering is given by the one-photon exchange amplitude. Besides the electromagnetic mechanism, the scattering can proceed through the neutral weak interaction via the exchange of the neutral Z boson. Due to the large mass of the Z boson, with $m_Z = 91.19$ GeV, the neutral weak process is suppressed compared to the electromagnetic one in the considered kinematical range of relatively low momentum transfer. Since the neutral weak current does not conserve parity, PV contributions arise from the interference terms between the electromagnetic and the weak amplitudes. These PV effects can be accessed through asymmetries which are sensitive to the interference term.

The neutral weak current operator j_Z^μ is a linear combination of a vector and an axial-vector coupling to the Z boson. For two pointlike fermions the matrix element of the operator is given by

$$\big\langle f(k')\big|j_Z^\mu(0)\big|f(k)\big\rangle = \left(\frac{-g}{4\cos\theta_W}\right)\bar{u}_f(k')\,\gamma^\mu\left(g_V^f - g_A^f\gamma_5\right)\,u_f(k), \tag{5.1}$$

where $u_f(k)$ and $\bar{u}_f(k')$ are the Dirac spinors of the incident and outgoing fermions with momentum k and k', respectively. The expressions g_V^f and g_A^f are associated with the vector and axial-vector couplings of the particles:

$$g_V^f = 2\,T_3^f - 4Q_f\sin^2\theta_W, \qquad g_A^f = 2\,T_3^f, \tag{5.2}$$

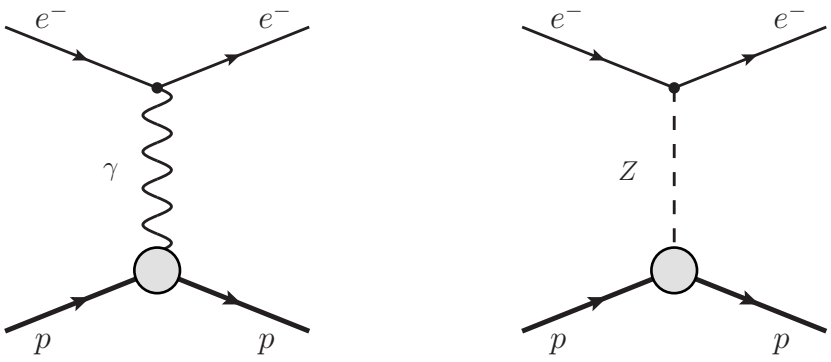

a) 1γ-exchange b) Z-exchange

Figure 5.1: Born diagrams of ep-scattering for one-photon and single Z exchange.

where T_3^f is the third component of the weak isospin and Q_f the charge fraction of the particle f. The angle θ_W is the so-called Weinberg angle or weak mixing angle, which can be expressed by the masses of the Z boson, m_Z, and the $\mathrm{W}^{\pm}$ bosons, m_W,

$$\cos\theta_W = \frac{m_W}{m_Z}, \quad \text{with } \sin^2\theta_W(m_Z) = 0.231 \text{ [86]}. \tag{5.3}$$

The vector and axial-vector couplings of the electron and light quarks are given in table 5.1.

The lowest-order amplitude of ep-scattering including neutral weak currents is illustrated in Fig. 5.1, where the leading order contribution of the weak interaction corresponds to the exchange of a single Z boson between the electron and the proton. It can be expressed through the neutral weak leptonic current operator j_Z^μ and the neutral weak hadronic current operator J_Z^μ connected with the propagator of the Z boson as

$$\mathrm{i}\mathcal{M}_Z = -\big\langle l(k',h')\big|j_Z^\nu(0)\big|l(k,h)\big\rangle \frac{\mathrm{i}g_{\mu\nu}}{m_Z^2 - q^2} \big\langle N(p',\lambda_{p'})\big|J_Z^\mu(0)\big|N(p,\lambda_p)\big\rangle, \tag{5.4}$$

where k (k') and p (p') are the momenta of the initial (final) electron and proton, respectively, h and h' are the helicities of the incoming and outgoing electrons, λ_p and $\lambda_{p'}$ of the initial and final protons.

particle	Q_f	T_3^f	g_V^f	g_A^f
e^-	-1	$-1/2$	$-(1-4\sin^2\theta_W)$	-1
u	$2/3$	$1/2$	$(1-\frac{8}{3}\sin^2\theta_W)$	1
d	$-1/3$	$-1/2$	$-(1-\frac{4}{3}\sin^2\theta_W)$	-1
s	$-1/3$	$-1/2$	$-(1-\frac{4}{3}\sin^2\theta_W)$	-1

Table 5.1: Vector and axial-vector couplings of the electron and the light quarks u, d, s.

The matrix element of the weak leptonic current operator is found as

$$\left\langle l(k',h')\middle|j_Z^\mu(0)\middle|l(k,h)\right\rangle = \left(\frac{-g}{4\cos\theta_W}\right)\bar{u}_l(k',h')\,\gamma^\mu(g_V^e - g_A^e\gamma_5)u_l(k,h), \tag{5.5}$$

where the vector-coupling g_V^e and the axial vector coupling g_A^e of the electron to the weak current have been introduced, which are given by

$$g_V^e = -(1-4\sin^2\theta_W), \quad g_A^e = -1. \tag{5.6}$$

The weak coupling g is connected with the electromagnetic coupling via $g = e\sin\theta_W$.

The most general expression of the matrix element of the neutral weak hadronic current operator is parametrized by 4 form factors,

$$\begin{aligned}&\left\langle N(p',\lambda_{p'})\middle|J_Z^\mu(0)\middle|N(p,\lambda_p)\right\rangle \\ &= \left(\frac{-g}{4\cos\theta_W}\right)\bar{N}(p',\lambda_{p'})\left\{F_1^Z\,\gamma^\mu + \ F_2^Z\,\frac{\mathrm{i}}{2m_N}\sigma^{\mu\nu}q_\nu + G_A^Z\,\gamma^\mu\gamma_5 + G_p^Z\,\frac{q^\mu}{m_N}\gamma_5\right\}N(p,\lambda_p).\end{aligned} \tag{5.7}$$

The weak form factors F_1^Z, F_2^Z, G_A^Z, and G_p^Z are real functions of the momentum transfer Q^2 in the spacelike region. The last structure of Eq. (5.7), which is related to the weak pseudoscalar form factor G_p, does not contribute to the amplitude, due to electromagnetic gauge invariance, which implies $q^\mu j_{Z,\mu} = 0$. Therefore, the pseudoscalar structure vanishes when contracting with the neutral weak leptonic current.

In the momentum transfer region of interest the relation $Q^2 = -q^2 \ll m_Z^2$ is valid. Therefore q^2 can be neglected in the denominator of the Z boson propagator in Eq. (5.4), $1/(m_Z^2 - q^2) \simeq 1/m_Z^2$, and one obtains

$$\begin{aligned}\mathrm{i}\mathcal{M}_Z \ &\simeq \ \frac{-\mathrm{i}\,g^2}{16m_Z^2\cos^2\theta_W}\,\bar{u}_l(k',h')\,\gamma_\mu(-1+4\sin^2\theta_W+\gamma_5)\,u_l(k,h) \\ &\quad\times\ \bar{N}(p',\lambda_{p'})\left\{F_1^Z(Q^2)\,\gamma^\mu + F_2^Z(Q^2)\,\frac{\mathrm{i}}{2m_N}\sigma^{\mu\nu}q_\nu + G_A^Z(Q^2)\,\gamma^\mu\gamma_5\right\}N(p,\lambda_p) \\ &= \ -\frac{\mathrm{i}G_F}{2\sqrt{2}}\,\bar{u}_l(k',h')\,\gamma_\mu(-1+4\sin^2\theta_W+\gamma_5)\,u_l(k,h) \\ &\quad\times\ \bar{N}(p',\lambda_p')\left\{F_1^Z(Q^2)\,\gamma^\mu + F_2^Z(Q^2)\,\frac{\mathrm{i}}{2m_N}\sigma^{\mu\nu}q_\nu + G_A^Z(Q^2)\,\gamma^\mu\gamma_5\right\}N(p,\lambda_p),\end{aligned} \tag{5.8}$$

where the commonly used Fermi constant G_F has been introduced:

$$\frac{G_F}{\sqrt{2}} = \frac{g^2}{8m_Z^2\cos^2\theta_W} = \frac{e^2}{8m_W^2}. \tag{5.9}$$

As for electromagnetic form factors, it is more convenient to use the Sachs form factors G_E^Z and G_M^Z of the neutral weak current, defined by the linear combinations

$$\begin{aligned}G_E^Z(Q^2) \ &= F_1^Z(Q^2) - \tau F_2^Z(Q^2), \\ G_M^Z(Q^2) \ &= F_1^Z(Q^2) + F_2^Z(Q^2).\end{aligned} \tag{5.10}$$

The matrix elements of the proton weak current operator can be expressed in terms of the individual quark flavor current operators. Neglecting contributions of heavy quarks, the c, b and t quarks, one finds

$$\begin{aligned}
&\left\langle N(p')\,\middle|\,J_Z^\mu(0)\,\middle|\,N(p)\right\rangle \left(\frac{-g}{4\cos\theta}\right)^{-1} \\
&= \left\langle N(p')\middle|\left(1-\frac{8}{3}\sin^2\theta_W\right)\bar{u}\gamma^\mu u - \left(1-\frac{4}{3}\sin^2\theta_W\right)\bar{d}\gamma^\mu d - \left(1-\frac{4}{3}\sin^2\theta_W\right)\bar{s}\gamma^\mu s\right. \\
&\quad \left. - \left(\bar{u}\gamma^\mu\gamma_5 u - \bar{d}\gamma^\mu\gamma_5 d - \bar{s}\gamma^\mu\gamma_5 s\right)\middle|N(p)\right\rangle \\
&= \bar{N}(p')\left\{\sum_{q=u,d,s}(2T_3^q - 4Q_q\sin^2\theta_W)\left(F_1^q\gamma^\mu + F_2^q\frac{\mathrm{i}}{2m_N}\sigma^{\mu\nu}q_\nu\right) + 2\,T_3^q\,G_A^{q,Z}\,\gamma^\mu\gamma_5\right\}N(p),
\end{aligned} \tag{5.11}$$

where the flavor form factors $F_{1,2}^q$, which parametrize the vector current, have been defined in Eq. (2.15). The quark flavor form factors give rise to the form factors of the neutral weak hadronic current:

$$G_{E,M}^Z = \left(1-\frac{8}{3}\sin^2\theta_W\right)G_{E,M}^u - \left(1-\frac{4}{3}\sin^2\theta_W\right)G_{E,M}^d - \left(1-\frac{4}{3}\sin^2\theta_W\right)G_{E,M}^s. \tag{5.12}$$

Assuming isospin symmetry, one can use Eqs. (2.17) and (5.12) to express the weak form factors $G_{E,M}^Z$ in terms of the electromagnetic form factors of the proton and the neutron as well as the strange form factor:

$$G_{E,M}^Z = \left(1-4\sin^2\theta_W\right)G_{E,M}^p - G_{E,M}^n - G_{E,M}^s. \tag{5.13}$$

The weak axial form factor G_A^Z can be related to the axial form factor of the nucleon:

$$G_A^Z(Q^2) = G_A(Q^2). \tag{5.14}$$

The axial form factor G_A appears when parametrizing the nucleon matrix element of the axial current operator, which has been introduced before in Eq. (4.100).

The leading-order amplitude of elastic ep-scattering including Z-exchange is given by the sum of the the electromagnetic amplitude defined in Eq. (2.21), which is denoted as $\mathcal{M}_\gamma$ in this section, and the neutral weak amplitude $\mathcal{M}_Z$, given by Eq. (5.4):

$$\begin{aligned}
d\sigma \propto |\mathcal{M}|^2 &= |\mathcal{M}_\gamma + \mathcal{M}_Z|^2 \\
&\simeq |\mathcal{M}_\gamma|^2 + 2\mathrm{Re}\left[\mathcal{M}_\gamma\mathcal{M}_Z^*\right].
\end{aligned} \tag{5.15}$$

Due to the Z propagator, the amplitude $\mathcal{M}_Z$ is suppressed by a factor q^2/m_Z^2 compared to the electromagnetic amplitude at lower Q^2 values.

Instead of measuring the Z-exchange contribution to the cross section, one can access the neutral weak amplitude through the parity-violating asymmetry A^{PV}, which arises in polarized ep-scattering from the interference of the electromagnetic and weak amplitudes.

The electromagnetic interaction, as a vector-current interaction, conserves parity, whereas the mixed vector and axial-vector structure of the neutral weak current, violates parity conservation. The PV asymmetry is defined as

$$A^{PV} = \frac{d\sigma_R - d\sigma_L}{d\sigma_R + d\sigma_L}, \tag{5.16}$$

where $d\sigma_R$ ($d\sigma_L$) refers to the cross section for a right-handed (left-handed) electron, i.e. an electron with helicity $+1/2$ ($-1/2$). The neutral weak current for a right and left handed electron can be written as:

$$\left\langle l(k')\right| j^{R,L}_{Z,\mu}(0) \left|l(k)\right\rangle \;=\; \left(\frac{-\,g}{\cos\theta_W}\right) \bar{u}(k',h')\,\gamma_\mu\big[g_V^e - g_A^e\gamma_5\big]P_{R,L}\,u(k,h), \tag{5.17}$$

with $P_{R,L} = \frac{1}{2}(1 \pm \gamma_5)$, and where $d\sigma_R$ and $d\sigma_L$ are associated with $\mathcal{M}$ as

$$d\sigma_R \propto |\mathcal{M}\big(h=+1/2\big)|^2, \quad d\sigma_L \propto |\mathcal{M}\big(h=-1/2\big)|^2. \tag{5.18}$$

In the leading-order approximation, the asymmetry is given by the interference term of $\mathcal{M}_\gamma$ and $\mathcal{M}_Z$:

$$A^{PV}_{\text{Born}} \;\simeq\; \frac{2\text{Re}\big[\mathcal{M}_\gamma(h=+1/2)\,\mathcal{M}_Z^*(h=+1/2) - \mathcal{M}_\gamma(h=-1/2)\,\mathcal{M}_Z^*(h=-1/2)\big]}{|\mathcal{M}_\gamma(h=+1/2)|^2 + |\mathcal{M}_\gamma(h=-1/2)|^2}. \tag{5.19}$$

A^{PV}_{Born} can be written as:

$$\begin{aligned} A^{PV}_{\text{Born}} &= -\,\frac{G_F Q^2}{e^2\sqrt{2}} \;\cdot\; \frac{A_E + A_M + A_A}{\tau\, G_M^2 + \varepsilon\, G_E^2}, \\ \text{with} \quad A_E &= \varepsilon \;\cdot\; G_E\, G_E^Z, \\ A_M &= \tau \;\cdot\; G_M\, G_M^Z, \\ A_A &= -\,(1 - 4\sin^2\theta_W)\,\sqrt{\tau(1+\tau)}\sqrt{1-\varepsilon^2} \;\cdot\; G_M\, G_A^Z. \end{aligned} \tag{5.20}$$

The asymmetry provides access to the weak charge of the proton Q_W^p:

$$Q_W^p \;=\; 1 - 4\sin^2\theta_W. \tag{5.21}$$

Due to an accurate prediction of Q_W^p within the Standard Model, based on the Q^2 dependence of $\sin^2\theta_W$, a precise measurement of Q_W^p provides a significant test of the validity of the Standard Model. Such measurements are for instance performed at the JLab (Q-weak experiment [87]) and are proposed for the new MESA facility at Mainz.

The asymmetry can alternatively be expressed through the proton and neutron electromagnetic form factors, the strangeness form factors $G^s_{E,M}$ and the axial form factors G^p_A, separating A^{PV} into vector (A_V), strange (A_S) and axial contributions (A_A). Using Eq. (5.13)

yields

$$A^{PV}_{\text{Born}} = \frac{G_F Q^2}{\sqrt{2}e^2} \frac{A_V + A_S + A_A}{\varepsilon \left(G_E^p\right)^2 + \tau \left(G_M^p\right)^2},$$

$$\begin{aligned} \text{with} \quad A_V &= -\left[\varepsilon (G_E^p)^2 + \tau (G_M^p)^2\right] \left(1 - 4\sin^2\theta_W\right) + \varepsilon G_M^p G_E^n + \tau G_M^p G_M^n, \\ A_S &= \varepsilon G_E^p G_E^s + \tau G_M^p G_M^s, \\ A_A &= \left(1 - 4\sin^2\theta_W\right) \sqrt{(1-\varepsilon^2)\tau(1+\tau)} G_M^p G_A^Z. \end{aligned} \tag{5.22}$$

The strangeness form factors G_E^s and G_M^s can be extracted from A_S. Measurements of A^{PV} with the aim to access the strangeness contributions of the nucleon have been performed at several facilities, e.g. the SAMPLE experiment run at MIT-Bates [88, 89], HAPPEX undertaken at JLab/HALL A [90–93], the PVA4 experiment performed at MAMI [94–96] and the G0 experiment at JLab/HALL C [97, 98]. Since the strangeness contributions are small, the extraction from the measured asymmetry can be very sensitive to even small corrections, as two-boson exchange effects.

5.2 Two-Boson-Exchange Effects in Parity-Violating ep-Scattering

5.2.1 General Formalism

Due to the possibility to access the small strangeness contribution or the weak mixing angle from high precision PV asymmetries, it is necessary to be aware of radiative corrections as two-boson exchange (TBE) to the PV asymmetry A^{PV}.

For this purpose, we consider TBE in the process

$$p(p, \lambda_p) + e^-(k, h) \to p(p', \lambda_{p'}) + e^-(k', h'), \tag{5.23}$$

using the four-vectors and variables introduced in Eqs. (3.2) and (3.3).

The leading-order TBE corrections to PV *ep*-scattering arise from different contributions. The γZ-exchange process, given by the γZ-direct and crossed box graphs, contributes through the interference with the 1γ-exchange process, and the 2γ-exchange as interference term with Z-exchange Born diagram. Furthermore, the effects of the interference between 1γ-exchange and 2γ-exchange processes appear in the denominator of A^{PV}. The corresponding Feynman graphs are presented in Fig. 5.2.

The invariant amplitude characterizing the γZ-exchange can be written in terms of 5 generalized form factors:

$$\begin{aligned} \mathrm{i}\mathcal{M}_{\gamma Z} = &\frac{-\mathrm{i}G_F}{2\sqrt{2}} \bar{u}_l(k', h') \gamma_\mu (g_V^e - g_A^e \gamma_5) u_l(k, h) \\ &\times \bar{N}(p', \lambda_{p'}) \left\{ \gamma^\mu \delta\tilde{G}_M^Z - \frac{P^\mu}{m_N} \delta\tilde{F}_2^Z + \frac{P^\mu \not{K}}{m_N^2} \tilde{F}_3^Z + \gamma^\mu \gamma_5 \delta\tilde{G}_A^Z + \frac{P^\mu \not{K}}{m_N^2} \gamma_5 \tilde{G}_{3A} \right\} N(p, \lambda_p). \end{aligned} \tag{5.24}$$

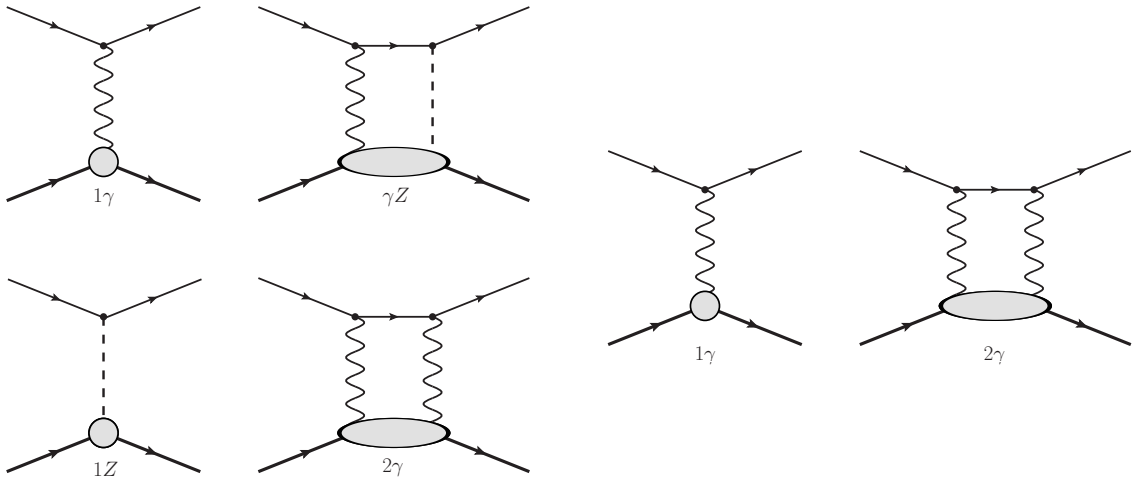

Figure 5.2: TBE corrections to A^{PV}: Contributions appearing in the numerator are illustrated on the left panel ($1\gamma \times \gamma Z$ and $1Z \times 2\gamma$ interference terms), corrections to the leading term in the denominator on the right panel ($1\gamma \times 2\gamma$ interference). For clarity, the crossed box diagrams are not shown.

These generalized weak form factors, $\delta\tilde{G}_M^Z$, $\delta\tilde{F}_2^Z$, $\tilde{F}_3^Z$, $\delta\tilde{G}_A^Z$ and $\tilde{G}_{3A}$ are, as the 2γ-amplitudes, complex functions of two variables, e.g. Q^2 and $\nu = K \cdot P$. They are suppressed by $\alpha_{\rm em}$ compared to the neutral weak form factors. Equivalently, one can introduce

$$\delta\tilde{G}_E^Z(Q^2) = \delta\tilde{G}_M^Z(Q^2) - (1+\tau)\delta\tilde{F}_2(Q^2). \tag{5.25}$$

By means of the relations

$$\begin{aligned}
\bar{u}_l \not{P} u_l \, \bar{N} \not{K} N &= \nu\, \bar{u}_l \gamma_\mu u_l \, \bar{N}\gamma^\mu N - \frac{Q^2}{4}\, \bar{u}_l \gamma_\mu\gamma_5 u_l \, \bar{N}\gamma^\mu\gamma_5 N, \\
\bar{u}_l \not{P}\gamma_5 u_l \, \bar{N} \not{K} N &= \nu\, \bar{u}_l \gamma_\mu\gamma_5 u_l \, \bar{N}\gamma^\mu N - \frac{Q^2}{4}\, \bar{u}_l \gamma_\mu u_l \, \bar{N}\gamma^\mu\gamma_5 N, \\
\bar{u}_l \not{P} u_l \, \bar{N} \not{K}\gamma_5 N &= \nu\, \bar{u}_l \gamma_\mu u_l \, \bar{N}\gamma^\mu\gamma_5 N - P^2\, \bar{u}_l \gamma_\mu\gamma_5 u_l \, \bar{N}\gamma^\mu N + m_N\, \bar{u}_l \gamma_\mu\gamma_5 u_l \, \bar{N} P^\mu N, \\
\bar{u}_l \not{P}\gamma_5 u_l \, \bar{N} \not{K}\gamma_5 N &= \nu\, \bar{u}_l \gamma_\mu\gamma_5 u_l \, \bar{N}\gamma^\mu\gamma_5 N - P^2\, \bar{u}_l \gamma_\mu u_l \, \bar{N}\gamma^\mu N + m_N\, \bar{u}_l \gamma_\mu u_l \, \bar{N} P^\mu N,
\end{aligned} \tag{5.26}$$

the structures of the matrix element of γZ-exchange, Eq. (5.24), can be reduced to 6 independent structures of the form

$$\begin{aligned}
&\bar{u}_l \gamma_\mu u_l \, \bar{N}\gamma^\mu N \, \tilde{\mathcal{G}}_1, \qquad \bar{u}_l \gamma_\mu u_l \, \bar{N} \frac{P^\mu}{m_N} N \, \tilde{\mathcal{G}}_2, \qquad \bar{u}_l \gamma_\mu\gamma_5 u_l \, \bar{N}\gamma^\mu\gamma_5 N \, \tilde{\mathcal{G}}_3, \\
&\bar{u}_l \gamma_\mu\gamma_5 u_l \, \bar{N}\gamma^\mu N \, \tilde{\mathcal{G}}_4, \qquad \bar{u}_l \gamma_\mu\gamma_5 u_l \, \bar{N} \frac{P^\mu}{m_N} N \, \tilde{\mathcal{G}}_5, \qquad \bar{u}_l \gamma_\mu u_l \, \bar{N}\gamma^\mu\gamma_5 N \, \tilde{\mathcal{G}}_6.
\end{aligned} \tag{5.27}$$

It is convenient to study the process in the laboratory frame and express the cross sections and asymmetries as functions of Q^2 (or τ), the photon polarization ε and ν. In order

to compare corrections from the interference of different pairs of diagrams, the different contributions are calculated separately. The interference between one-photon exchange and the γZ-exchange reads

$$\begin{aligned} A_{1\gamma\times\gamma Z} &= A^{PV}_{\text{Born}}\left(1+\delta_{1\gamma\times\gamma Z}\right) \\ &= -\frac{G_F Q^2}{\sqrt{2}e^2}\frac{1}{\varepsilon G_E^2+\tau G_M^2}\,\text{Re}\Big[\tau\, G_M\,\delta\tilde{G}_M^Z+\varepsilon\, G_E\,\delta\tilde{G}_E^Z+\frac{\varepsilon\nu}{m_N^2}\left(\tau\, G_M\,\tilde{F}_3^Z+G_E\,\tilde{F}_3^Z\right) \\ &\quad -\left(1-4\sin^2\theta_W\right)\left(\varepsilon'\, G_M\,\delta\tilde{G}_A^Z+\varepsilon\,\tau\,(1+\tau)\,G_M\,\tilde{G}_{3A}\right)\Big], \end{aligned} \tag{5.28}$$

where the expression

$$\varepsilon' = \sqrt{\left(1-\varepsilon^2\right)\tau\left(1+\tau\right)} \tag{5.29}$$

has been introduced.

The invariant amplitude giving rise to the 2γ-exchange corrections reads

$$\mathcal{M}_{2\gamma} = \frac{e^2}{Q^2}\bar{u}_l(k')\,\gamma_\mu\,u_l(k)\,\bar{N}(p')\left[\delta\tilde{G}_M\,\gamma^\mu-\delta\tilde{F}_2\,\frac{P^\mu}{m_N}+\tilde{F}_3\,\frac{P^\mu \not{K}}{m_N^2}\right]N(p) \tag{5.30}$$

where the form factors $\delta\tilde{G}_M$, $\delta\tilde{F}_2$, and $\tilde{F}_3$ are the two-photon amplitudes introduced in Eq. 3.9.

Corrections to the asymmetry arising from the interference of the 2γ-amplitude and the Born amplitude of Z-exchange can be found as

$$\begin{aligned} A_{Z\times 2\gamma} &= A^{PV}_{\text{Born}}\left(1+\delta_{Z\times 2\gamma}\right) \\ &= -\frac{G_F Q^2}{\sqrt{2}e^2}\frac{1}{\varepsilon G_E^2+\tau G_M^2}\,\text{Re}\Big[\tau\, G_M^Z\,\delta\tilde{G}_M+\varepsilon\, G_E^Z\,\delta\tilde{G}_E+\frac{\varepsilon\nu}{m_N^2}\left(\tau G_M^Z\tilde{F}_3+G_E^Z\tilde{F}_3\right) \\ &\quad -\left(1-4\sin^2\theta_W\right)\left(\varepsilon'\, G_A^Z\delta\,\tilde{G}_M+\varepsilon\,\tau\,(1+\tau)\,G_A^Z\,\tilde{F}_3\right)\Big]. \end{aligned} \tag{5.31}$$

The effects of the 2γ-exchange amplitude interfering with the 1γ-exchange amplitude appearing in the denominator yields:

$$\begin{aligned} A_{1\gamma\times 2\gamma} &= A^{PV}_{\text{Born}}\left(1+\delta_{1\gamma\times 2\gamma}\right) \\ &= -\frac{G_F Q^2}{\sqrt{2}e^2}\left\{\tau\, G_M\, G_M^Z+\varepsilon\, G_E\, G_E^Z-\left(1-4\sin^2\theta_W\right)\varepsilon'\, G_M\, G_A^Z\right\} \\ &\quad\times\left\{\varepsilon\Big(G_E^2+2\text{Re}[G_E\delta\tilde{G}_E]\Big)+\tau\Big(G_M^2+2\text{Re}[G_M\delta\tilde{G}_M]\Big)+\frac{2\varepsilon\nu}{m_N^2}\left(G_E+\tau G_M\right)\text{Re}\tilde{F}_3\right\}^{-1}. \end{aligned} \tag{5.32}$$

Consequently, the PV asymmetry including the leading order corrections in $\alpha_{\rm em}$ caused by TBE is

$$
\begin{aligned}
A^{PV} &= A^{PV}_{\rm Born}\,(1+\delta) \\
&= -\frac{G_F\,Q^2}{\sqrt{2}e^2}\Bigg[\tau\,G_M\,G_M^Z + \varepsilon\,G_E\,G_E^Z - (1-4\sin^2\theta_W)\varepsilon'\,G_M\,G_A^Z \\
&\quad + \mathrm{Re}\left[\tau\left(G_M^Z\,\delta\tilde{G}_M + G_M\,\delta\tilde{G}_M^Z\right) + \varepsilon\,\left(G_E^Z\,\delta\tilde{G}_E + G_E\,\delta\tilde{G}_E^Z\right)\right] \\
&\quad + \frac{\varepsilon\nu}{m_N^2}\,\mathrm{Re}\left[\tau\left(G_M^Z\,\tilde{F}_3 + G_M\,\tilde{F}_3^Z\right) + \left(G_E^Z\,\tilde{F}_3 + G_E\,\tilde{F}_3^Z\right)\right] \\
&\quad - (1-4\sin^2\theta_W)\mathrm{Re}\left[\varepsilon'\,\left(G_A^Z\,\delta\tilde{G}_M + G_M\,\delta\tilde{G}_A^Z\right) + (1+\tau)\,\varepsilon\,\tau\,\left(G_A^Z\,\tilde{F}_3 + G_M\,\tilde{G}_{3A}\right)\right]\Bigg] \\
&\quad \times\left\{\varepsilon\Big(G_E^2 + 2\mathrm{Re}[G_E\delta\tilde{G}_E]\Big) + \tau\Big(G_M^2 + 2\mathrm{Re}[G_M\delta\tilde{G}_M]\Big) + \frac{2\varepsilon\nu}{m_N^2}\,(G_E+\tau G_M)\,\mathrm{Re}\tilde{F}_3\right\}^{-1}.
\end{aligned}
\tag{5.33}
$$

Two-photon exchange and γZ-exchange effects in PV ep-scattering have been calculated in Refs. [99, 100] within a parton factorization approach using GPDs, and within a hadronic approach in Refs. [101, 102]. Several theoretical studies have been performed in order to receive the γZ-corrections to the asymmetry at zero (or very small) momentum transfer [103–106], which corresponds to forward scattering, e.g. within dispersion relation frameworks.

5.2.2 Two-Boson Exchange within a perturbative QCD Factorization Approach

Analogously to the 2γ-exchange processes studied in Chapter 4, the pQCD factorization approach can be applied in order to examine two-boson exchange effects in PV elastic ep-scattering. Since the distribution amplitudes are process independent quantities, the same DAs as discussed for the 2γ-exchange corrections in Sec. 4.2 appear in the TBE formalism.

The effects of 2γ-exchange on the PV asymmetry within a pQCD factorization approach can be directly obtained from the results of the generalized 2γ-amplitudes, $\delta\tilde{G}_M$, $\delta\tilde{G}_E$, and $\tilde{F}_3$, found within this model, which have been derived in Ref. [57], and adopting these expressions for Eqs. (5.31) and (5.32).

To compute the corrections caused by the γZ-box contributions, at first the formulas of the γZ-exchange amplitudes, namely $\delta\tilde{G}_M^Z$, $\delta\tilde{G}_E^Z$, $\tilde{F}_3^Z$, $\delta\tilde{G}_A^Z$ and $\tilde{G}_{3A}$, in terms of the DAs have to be defined.

For this purpose, the process is analyzed in the Breit frame, assuming that $s=(p+k)^2$ and the momentum transfer Q^2 are large, $s,\,Q^2 \gg m_N^2$. Therefore the masses of the proton and the electron can be neglected in the calculation. The momenta of the initial and final state proton can be expressed in the light-cone basis n^μ and $\bar{n}^\mu$ as:

$$
p^\mu \;=\; \frac{Q}{2}\,\bar{n}^\mu, \qquad p'^\mu \;=\; \frac{Q}{2}\,n^\mu, \qquad q^\mu \;=\; \frac{Q}{2}\,n^\mu - \frac{Q}{2}\,\bar{n}^\mu, \tag{5.34}
$$

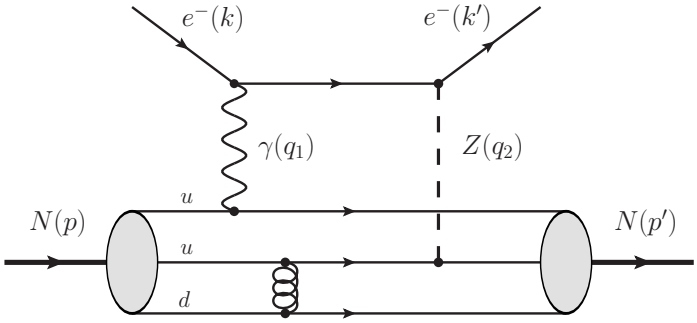

Figure 5.3: Diagram of γZ-exchange using pQCD factorization: The hard kernel describes the electron scattering off a three-quark state via photon and Z boson exchange. The gray blobs indicate the DAs of the initial and final nucleon.

and the momenta of the incident and scattered leptons are

$$k^\mu = \zeta\,\frac{Q}{2}\,n^\mu - (1-\zeta)\,\frac{Q}{2}\bar{n}^\mu + k_\perp, \qquad k'^\mu = -(1-\zeta)\,\frac{Q}{2}\,n^\mu + \zeta\,\frac{Q}{2}\bar{n}^\mu + k_\perp,$$
$$\text{with} \qquad |k_\perp|^2 = -\zeta(1-\zeta)Q^2, \qquad \zeta = \frac{(1+\xi)^2}{4\xi}, \qquad \xi = \frac{k^+}{P^+}. \tag{5.35}$$

Using pQCD factorization, the amplitude of the γZ-exchange is given as a convolution of the DAs of the incoming and outgoing nucleon and a hard scattering kernel, where the electron scatters at a three valence quark state via the exchange of a photon and a Z boson. A typical diagram of the factorized process is presented in Fig. 5.3. In the subprocess, the initial quarks carry the momentum fraction x_i of the proton, while after the scattering the quarks have the momentum $y_i\,p'$, with $\sum_i x_i = \sum_i y_i = 1$.

The proton-to-vacuum matrix element as parametrized by the leading-order DAs of the proton has been introduced in Eq. (4.23). The DAs which convert the three valence quark state into a hadron with momentum p' can be deduced from the hermitian conjugate expression of the proton-to-vacuum matrix element in terms of the proton DAs.

In the leading-order expansion, the amplitude characterizing the γZ-exchange is found as

$$\begin{aligned} A_{\gamma Z} = &\sum_{\tilde{X}=\tilde{V},\tilde{A},\tilde{T}} \;\sum_{X=V,A,T} \int d[y_i]\,\tilde{X}(y_i) \int d[x_i]\,X(x_i) \\ &\times \left(\frac{\mathrm{i}\,g}{4\cos\theta_W}\right) \bar{u}_l(k')\;(g_V^e\gamma_\mu - g_A^e\gamma_\mu\gamma_5)\;u_l(k) \\ &\times \Big[\bar{N}^+(p')\;\Gamma^d_{\tilde{X}}\Big]_{\gamma'}\Big[\Gamma^d\Big]^{\gamma'\gamma}\Big[\Gamma^d_X\;N^+(p)\Big]_\gamma\Big[\Gamma^u_{\tilde{X}}\Big]_{\beta'\alpha'}\Big[\Gamma^{u_1}\Big]^{\alpha'\alpha}\Big[\Gamma^{u_2}\Big]^{\beta'\beta}\Big[\Gamma^u_X\Big]_{\alpha\beta}, \end{aligned} \tag{5.36}$$

where V, A and T denote the vector, axial and tensor DA of the proton. The expression $\tilde{X}$ refers to the DAs of the outgoing nucleon defined by

$$\tilde{X}(z_i'\,\bar{n}\cdot p') \;\equiv X^\dagger(z_i'\,\bar{n}\cdot p') = \int d[y_i]\;X(y_1,y_2,y_3)\exp\left\{\mathrm{i}\,(\bar{n}\cdot p')\sum_i y_i z_i\right\}, \tag{5.37}$$

$$\begin{aligned} &\text{with} \quad \tilde{X} \;=\; \{\tilde{V}, \tilde{A}, \tilde{T}\}, \\ &\text{and} \quad d[y_i] \;=\; dy_1\, dy_2\, dy_3\, \delta(1-y_1-y_2-y_3). \end{aligned} \tag{5.38}$$

The structures $\Gamma_X^{u,d}$ and $\Gamma_{\tilde{X}}^{u,d}$ are given by

$$\begin{aligned} &\Big[\Gamma_V^u\Big]_{\alpha\beta} = \frac{Q}{2}\Big[\not{\bar{n}}\,\mathcal{C}\Big]_{\alpha\beta}, \qquad \Big[\Gamma_A^u\Big]_{\alpha\beta} = \frac{Q}{2}\Big[\not{\bar{n}}\,\gamma_5\,\mathcal{C}\Big]_{\alpha\beta}, \qquad \Big[\Gamma_T^u\Big]_{\alpha\beta} = \frac{Q}{2}\Big[\not{\bar{n}}\gamma^\perp\mathcal{C}\Big]_{\alpha\beta}, \\ &\Big[\Gamma_V^d\Big]_{\gamma} = [\gamma_5]_\gamma, \qquad \Big[\Gamma_A^d\Big]_{\gamma} = [1]_\gamma, \qquad \Big[\Gamma_T^d\Big]_{\gamma} = [\gamma^\perp\gamma_5]_\gamma, \\ &\Big[\Gamma_{\tilde{V}}^u\Big]_{\beta'\alpha'} = \frac{Q}{2}\Big[\mathcal{C}\not{n}\Big]_{\beta'\alpha'}, \quad \Big[\Gamma_{\tilde{A}}^u\Big]_{\beta'\alpha'} = \frac{Q}{2}\Big[\mathcal{C}\,\gamma_5\not{n}\Big]_{\beta'\alpha'}, \quad \Big[\Gamma_{\tilde{T}}^u\Big]_{\beta'\alpha'} = -\frac{Q}{2}\Big[\mathcal{C}\not{n}\gamma^\perp\Big]_{\beta'\alpha'}, \\ &\Big[\Gamma_{\tilde{V}}^d\Big]_{\gamma'} = [\gamma_5]_{\gamma'}, \qquad \Big[\Gamma_{\tilde{A}}^d\Big]_{\gamma'} = [1]_{\gamma'}, \qquad \Big[\Gamma_{\tilde{T}}^d\Big]_{\gamma'} = [\gamma_5\,\gamma^\perp]_{\gamma'}. \end{aligned} \tag{5.39}$$

In Eq. (5.36), Γ^q, with $q = \{u_1, u_2, d\}$, corresponds to the expression of the quark spinor lines in momentum space. The indices α (β) and α' (β') are associated with the initial and final u-quark lines, respectively, while the indices γ and γ' refer to the incoming and outgoing d-quarks.

The hard scattering process is given by the electron-scattering off a three quark state,

$$e^-(k) + q(x_1p)\, q(x_2p)\, q(x_3p) \to e^-(k') + q(y_1p')\, q(y_2p')\, q(y_3p'), \tag{5.40}$$

where a photon and a Z boson are exchanged. Similarly to the two-photon exchange reaction, the contributions where the two bosons couple to different quarks have to be considered in the subprocess, since other diagrams are suppressed. The third quark is involved in the scattering process through the exchange of a hard gluon. Taking all possibilities to attach the photon and the Z boson to the quarks and all possible gluon exchanges into account, the leading-order hard scattering process includes 48 diagrams (given in Appendix B).

Inserting the results of the hard scattering process into Eq. (5.36) gives rise to the weak γZ-form factors as functions of the DAs, which yields

$$\begin{aligned} \delta G_M^Z = &-\left(\frac{4\pi}{3}\right)^2 \frac{\alpha_{em}\alpha_S}{Q^4} \int d[x_i] \frac{1}{x_1\bar{x}_1x_2} \int d[y_i] \frac{1}{y_1\bar{y}_1y_2}\, \frac{1}{\mathcal{D}_1}(2\zeta-1)x_1y_1 \\ &\times \Big\{ \bar{x}_1\bar{y}_1 \Big[Q_u\, g_V^u \{(V'-A')(V-A) + 4T'T\}(1,3,2) \\ &+\; Q_u\, g_V^d \{(V'-A')(V-A) + 4T'T\}(1,2,3) +\; 2Q_d\, g_V^u \{V'V + A'A\}(3,2,1) \Big] \\ &+\; x_1y_1 \Big[Q_u\, g_V^u \{(V'-A')(V-A) + 4T'T\}(1,3,2) \\ &+\; Q_d\, g_V^u \{(V'-A')(V-A) + 4T'T\}(1,2,3) + 2Q_u\, g_V^d \{V'V + A'A\}(3,2,1) \Big] \Big\}, \end{aligned} \tag{5.41}$$

$$\frac{Q^2}{m_N^2}\,F_3^Z = -\left(\frac{4\pi}{3}\right)^2\frac{\alpha_{em}\alpha_S}{Q^4}\int d[x_i]\frac{1}{x_1\bar{x}_1x_2}\int d[y_i]\frac{1}{y_1\bar{y}_1y_2}\,\frac{1}{\mathcal{D}_1}\,2(x_1+y_1-2x_1y_1)$$
$$\times\Big\{\bar{x}_1\bar{y}_1\Big[Q_u\,g_V^u\{(V'-A')(V-A)+4T'T\}(1,3,2)$$
$$+\;Q_u\,g_V^d\{(V'-A')(V-A)+4T'T\}(1,2,3)+\;2Q_d\,g_V^u\{V'V+A'A\}(3,2,1)\Big]$$
$$+\;x_1y_1\Big[Q_u\,g_V^u\{(V'-A')(V-A)+4T'T\}(1,3,2)$$
$$+\;Q_d\,g_V^u\{(V'-A')(V-A)+4T'T\}(1,2,3)+2Q_u\,g_V^d\{V'V+A'A\}(3,2,1)\Big]\Big\}, \tag{5.42}$$

$$\delta G_A^Z = -\left(\frac{4\pi}{3}\right)^2\frac{\alpha_{em}\alpha_S}{Q^4}\int d[x_i]\frac{1}{x_1\bar{x}_1x_2}\int d[y_i]\frac{1}{y_1\bar{y}_1y_2}\,\frac{1}{\mathcal{D}_1}(2\zeta-1)x_1y_1$$
$$\times\Big\{\bar{x}_1\bar{y}_1\Big[Q_u\{(V'-A')(V-A)-4T'T\}(1,3,2)$$
$$+\;Q_u\{(V'-A')(V-A)-4T'T\}(1,2,3)+2Q_d\{V'A+A'V\}(3,2,1)\Big] \tag{5.43}$$
$$+\;x_1y_1\Big[-Q_u\{(V'-A')(V-A)+4T'T\}(1,3,2)$$
$$-\;Q_d\{(V'-A')(V-A)+4T'T\}(1,2,3)+2Q_u\{V'V+A'A\}(3,2,1)\Big]\Big\},$$

$$\frac{Q^2}{m_N^2}\,G_{3A} = -\left(\frac{4\pi}{3}\right)^2\frac{\alpha_{em}\alpha_S}{Q^4}\int d[x_i]\frac{1}{x_1\bar{x}_1x_2}\int d[y_i]\frac{1}{y_1\bar{y}_1y_2}\,\frac{1}{\mathcal{D}_1}\,2(x_1+y_1-2x_1y_1)$$
$$\times\Big\{\bar{x}_1\bar{y}_1\Big[Q_u\{(V'-A')(V-A)-4T'T\}(1,3,2)$$
$$+\;Q_u\{(V'-A')(V-A)-4T'T\}(1,2,3)+2Q_d\{V'A+A'V\}(3,2,1)\Big]$$
$$+\;x_1y_1\Big[-Q_u\{(V'-A')(V-A)+4T'T\}(1,3,2)$$
$$-\;Q_d\{(V'-A')(V-A)+4T'T\}(1,2,3)+2Q_u\{V'V+A'A\}(3,2,1)\Big]\Big\}, \tag{5.44}$$

with

$$\mathcal{D}_1 = \big[\bar{x}_1\zeta+\bar{y}_1\bar{\zeta}-\bar{x}_1\bar{y}_1+i\epsilon\big]\big[\bar{x}_1\bar{\zeta}+\bar{y}_1\zeta-\bar{x}_1\bar{y}_1+i\epsilon\big].$$

In an analogous manner to the analysis of the 2γ-exchange in the timelike region, the helicity-flip amplitude F_2^Z, which behaves as $F_2^Z \sim 1/Q^6$, is suppressed within the pQCD calculation.

Using the form factor expressions in terms of the DAs, the influence of the γZ-exchange to the PV asymmetry can be derived from Eq. (5.28).

The 2γ-amplitudes for ep-scattering have been calculated within a pQCD factorization approach in Ref. [57] and have been found as

$$\begin{aligned}\delta G_M = &-\left(\frac{4\pi}{6}\right)^2 \frac{\alpha_{\rm em}\alpha_s}{Q^4}(2\zeta-1)\int \frac{d[x_i]d[y_i]}{\mathcal{D}_2}\,\frac{x_1 y_1}{[x_1\bar{x}_1 x_2][y_1\bar{y}_1 y_2]}\\ &\times\Big[Q_u^2\left[(V'-A')(V-A)+4T'T)\right](1,3,2)+\;2Q_uQ_d(V'V+A'A)(2,3,1)\\ &+\;Q_uQ_d\big[(V'-A')(V-A)+4T'T)\big](1,2,3)\Big],\end{aligned} \tag{5.45}$$

$$\begin{aligned}\frac{\nu}{m_N^2}F_3 = &-\left(\frac{4\pi}{6}\right)^2 \frac{\alpha_{em}\alpha_s}{Q^4}\int \frac{d[x_i]d[y_i]}{\mathcal{D}_2}\,\frac{2(x_1+y_1-2x_1y_1)}{[x_1\bar{x}_1 x_2][y_1\bar{y}_1 y_2]}\\ &\times\Big[Q_u^2\left[(V'-A')(V-A)+4T'T)\right](1,3,2)+\;2Q_uQ_d(V'V+A'A)(2,3,1)\\ &+\;Q_uQ_d\big[(V'-A')(V-A)+4T'T)\big](1,2,3)\Big],\end{aligned} \tag{5.46}$$

with

$$\mathcal{D}_2 = \left[x_1\bar{\zeta}+y_1\zeta-x_1y_1+\mathrm{i}\epsilon\right]\left[x_1\zeta+y_1\bar{\zeta}-x_1y_1+\mathrm{i}\epsilon\right].$$

The third 2γ-amplitude $\delta\tilde{F}_2$ is suppressed in this approach (as in the timelike case). The results have been inserted into Eqs. (5.31) and (5.32) in order to receive the 2γ-exchange corrections to the PV asymmetry.

As parametrization of the DAs the formulas given in Eq. (4.61) have been used, with the parameters of the COZ and BLW model (table 4.1). To compute the TBE corrections, an explicit expression of the form factors is needed. For the magnetic form factor of the proton a variation of a polynomial model is used [107], where the free parameters of the model have been obtained from a fit to the Rosenbluth data of G_M, while the form factors ratio $\mu_p G_E/G_M$ is parametrized by a fit of P_t/P_l to the results of polarization transfer measurements [11], giving rise to:

$$\begin{aligned}G_M(Q^2) &= \frac{\mu_p}{1+3.19Q^2+1.355Q^4+0.151Q^6},\\ \frac{\mu_p G_E(Q^2)}{G_M(Q^2)} &= 1+0.13\left(Q^2-0.04\right).\end{aligned} \tag{5.47}$$

The neutral weak form factors are expressed through the electromagnetic form factors of the proton and neutron:

$$G_{E,M}^Z = \left(1-4\sin^2\theta_W\right)G_{E,M}^p - G_{E,M}^n, \tag{5.48}$$

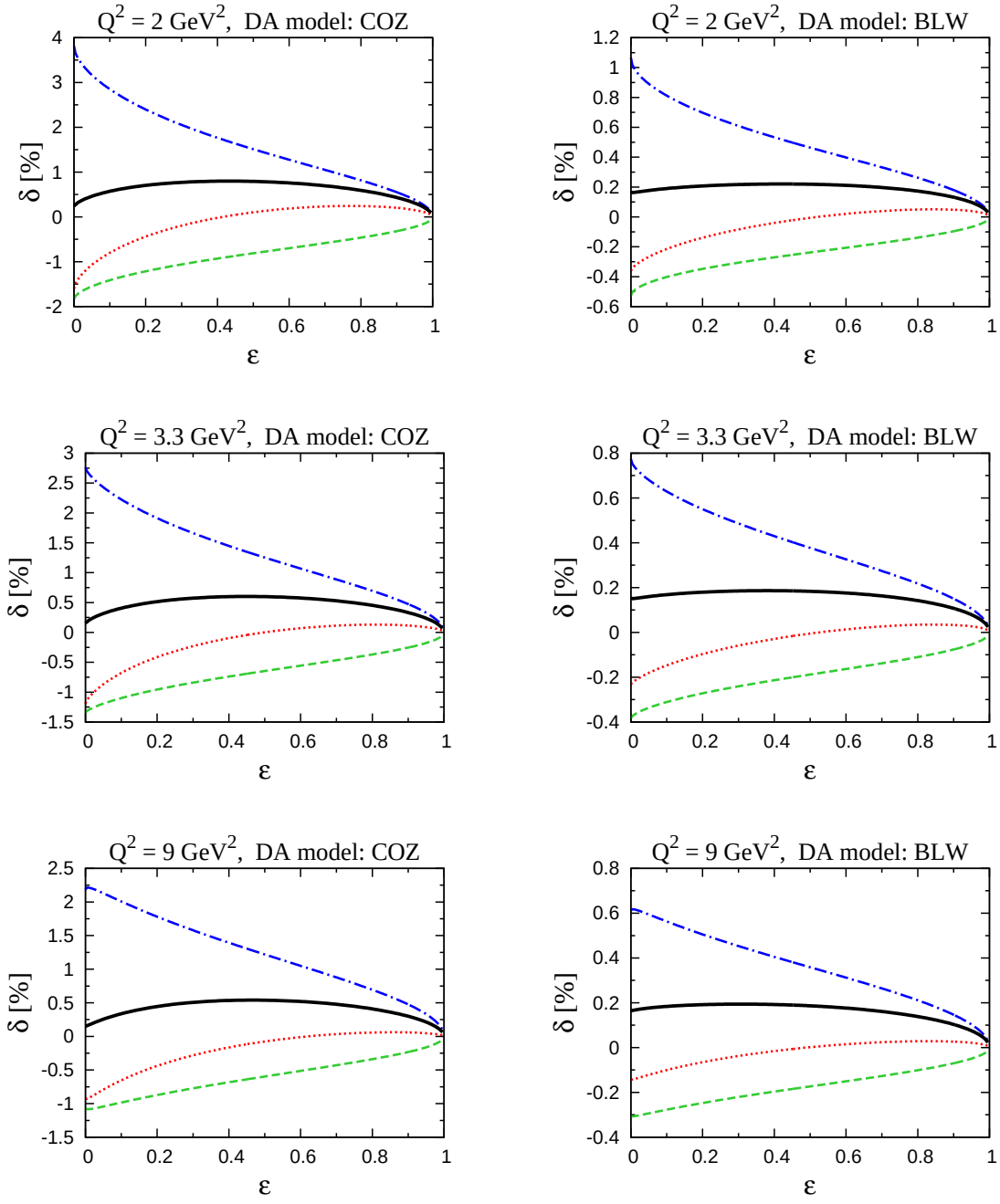

Figure 5.4: Two-Boson exchange contributions to the PV asymmetry A^{PV} as a function of ε for different values of momentum transfer using the COZ (left panel) and BLW model (right panel) as parametrization of the DAs. Black solid curve: total corrections; red dotted curve: $1\gamma \times \gamma Z$-contribution; green dashed curve: $Z \times 2\gamma$-contribution; blue dashed-dotted curve: $1\gamma \times 2\gamma$-contribution.

where the electromagnetic strangeness form factors have been neglected. The form factors $G^n_{E,M}$ of the neutron have been parametrized using the ansatz of Ref. [108]. The axial form factor is expressed by a dipole fit [84]:

$$G_A(Q^2) = \frac{g_A}{\left(1 + \frac{Q^2}{m_A^2}\right)^2}, \tag{5.49}$$

with $g_A = 1.27$ and the axial mass $m_A = 1.026$ GeV.

In Fig. 5.4 the results of the total TBE corrections to the asymmetry arising from γZ-exchange as well as 2γ-exchange, defined by

$$A^{PV} \;=\; A^{PV}_{\text{Born}}\,(1+\delta), \tag{5.50}$$

are shown as a function of ε for three selected values of momentum transfer, $\mathrm{Q}^2 = 2$, 3.3, and 9 GeV^2. The plots in the left and right columns correspond to the COZ and BLW models, respectively, which have been used for parametrizing the DAs. The total corrections, illustrated by the black curves, are of order of 1% in maximum, where the TBE effects within the COZ model are about twice as large as when using the BLW description. The TBE effects are decreasing for increasing Q^2. For higher momentum transfer, the dependence of the TBE corrections on Q^2 is found to be small.

In addition to the total corrections, the contribution to A^{PV} from different pairs of diagrams are shown in Fig. 5.4. The largest corrections result from the interference between 1γ- and 2γ-exchange ($1\gamma \times 2\gamma$), entering in the denominator of the asymmetry, which is shown by the blue curve. The effects of the 1γ- and γZ-interference ($1\gamma \times \gamma Z$) and Z- and 2γ-interference ($Z \times 2\gamma$) are somewhat smaller compared to the $1\gamma \times 2\gamma$ contribution and have the opposite sign over a wide ε range. Therefore the corrections partially cancel each other, giving rise to small TBE effects in total.

These results are similar to the findings of the hadronic calculation and the GPD based calculations, presented in Refs. [99–101]. Even though the $Z \times 2\gamma$ contribution calculated within the hadronic model differs in sign, the results show similar ε dependencies as well as comparable total corrections [101]. However, the total TBE corrections obtained within the GPD calculation in Ref. [100] are slightly larger, leading to effects of $\sim 0.5 - 2.5$ % for the considered kinematical range.

5.3 Conclusions

In this chapter the two-boson exchange corrections to parity-violating elastic ep-scattering have been studied within a perturbative QCD factorization approach, which are of particular interest with regard to high-precision measurements of PV asymmetries. Using two different parametrizations of the proton DAs, the TBE corrections are found to be of the order of 1% or less. The contributions arising from the different types of diagrams are at the few percent level, but have opposite sign. Therefore, the corrections partially cancel each other, giving rise to small total effects.

Chapter 6

Nucleon Form Factors in the Unphysical Region

The electromagnetic form factors of the nucleon have been studied extensively in the spacelike region by means of elastic electron-proton scattering, and forthcoming experiments claim to measure the timelike form factors with high accuracy in the annihilation reactions $p\bar{p} \to e^+ e^-$ and $e^+ e^- \to p\bar{p}$. But the region of momentum transfer, which is reachable, is exactly bound by the invariant mass of the nucleon pair, which requires a momentum transfer of at least $q^2_{\text{thr}} = 4m^2_N$. The timelike region below the two nucleon threshold, $0 < q^2 < 4m^2_N$, which is denoted as the unphysical region, is not accessible by the aforementioned annihilation processes.

However, due to the correlation of the spacelike and timelike regions, the knowledge of the form factors in the unphysical region would be an important help towards finding a complementary picture of the nucleon electromagnetic structure. The spacelike and timelike regions are connected through dispersion relations, which offer a model-independent framework to study the electromagnetic form factors of the nucleons simultaneously in both regions. Since several models predict a form factor behavior, which is dominated by large contributions of vector mesons in the below threshold region, an investigation of the form factors in the unphysical region provides the opportunity to test and constrain such models. The data would be of particular interest in order to improve form factor approaches, which allow to connect the spacelike and timelike form factors.

Therefore, in Refs. [45, 109] the annihilation process, where in addition a neutral pion is produced,

$$p + \bar{p} \;\to\; \pi^0 + e^+ + e^-, \tag{6.1}$$

has been studied. Since the outgoing pion takes a part of the energy of the reaction, the production of a lepton pair with an invariant mass below the $(p + \bar{p})$-annihilation threshold is possible and thus this reaction can be used to study the electromagnetic form factors in the unphysical region. Moreover, this reaction offers the possibility to access the relative phases of G_E and G_M. An investigation of the discussed process is proposed for the PANDA experiment at FAIR. Feasibility studies for a measurement at PANDA have been performed in Ref. [110]. However, a study of the timelike form factors from the $p\bar{p} \to \pi^0 e^+ e^-$ process requires a model in order to deal with the unknown hadronic interaction.

In this chapter, the process $p\bar{p} \to \pi^0 e^+ e^-$ is analyzed as a means to provide constraints on timelike nucleon form factors. In order to calculate the unknown hadronic reaction $p\bar{p} \to \pi^0 \gamma^*$, an approach inspired by Regge theory is used. To check the consistency of this Regge pole model, we first test the approach on the process of real photon production, $p\bar{p} \to \pi^0 \gamma$, where data of the angular distribution of the cross section exist. Subsequently, the Regge pole model is applied to the process $p\bar{p} \to \pi^0 e^+ e^-$.

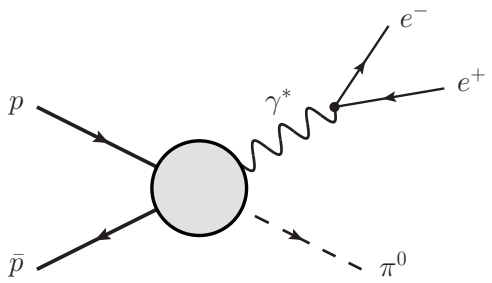

Figure 6.1: Sketch of the process $p\bar{p} \to \pi^0 e^+ e^-$

6.1 Probing Nucleon Form Factors in the Unphysical Region

6.1.1 Timelike Pion Electroproduction

As discussed in Ref. [45], the reaction

$$\begin{aligned} \bar{p}(p_1, \lambda_{N_1}) + p(p_2, \lambda_{N_2}) &\to \pi^0(q_\pi) + \gamma^*(q, \lambda_\gamma) \\ &\to \pi^0(q_\pi) + e^-(k_1, h_1) + e^+(k_2, h_2), \end{aligned} \tag{6.2}$$

where the lepton pair is produced from a photon with momentum q, as shown in Fig. 6.1, allows for studying the unphysical region $q^2 < q^2_{\text{thr}} = 4m_N^2$. We will refer to this process as timelike pion electroproduction.

The momenta of the $p\bar{p} \to \pi^0\gamma^*$ reaction can be combined to the Mandelstam variables,

$$\begin{aligned} s &= (p_1 + p_2)^2 = (q_\pi + q)^2, \\ u &= (p_2 - q_\pi)^2 = (p_1 - q)^2, \\ t &= (p_1 - q_\pi)^2 = (p_2 - q)^2, \end{aligned} \tag{6.3}$$

which satisfy the relation

$$s + t + u = 2m_N^2 + m_\pi^2 + q^2, \tag{6.4}$$

where m_π is the pion mass and q^2 is the virtuality of the photon.

The amplitude of the process consists of the leptonic and the hadronic part, connected by the photon propagator

$$\mathcal{A}_{\gamma^*} = \mathcal{L}^\nu \left(\frac{-g_{\mu\nu}}{q^2} \right) \mathcal{M}^\mu_{\gamma^*}. \tag{6.5}$$

The hadronic amplitude $\mathcal{M}^\mu_{\gamma^*}$ characterizes the process $p\bar{p} \to \pi^0\gamma^*$ and the leptonic contribution $\mathcal{L}^\nu$ describes the lepton pair production $\gamma^* \to e^+e^-$,

$$\mathcal{L}^\nu = -e\, \bar{u}_l(k_1)\, \gamma^\nu\, v_l(k_2), \tag{6.6}$$

which is calculable using QED. On the contrary, for the investigation of the hadronic subprocess a model description is needed in order to deal with the unknown interplay of the participating hadrons.

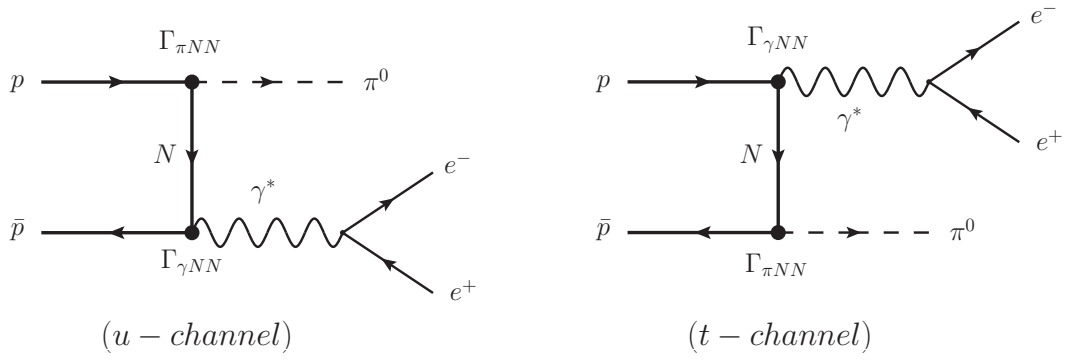

Figure 6.2: Born diagram model for $p\bar{p} \to \pi^0 e^+ e^-$ described by a single nucleon exchange in the u-channel and t-channel Feynman diagrams.

In Ref. [109], the process $p\bar{p} \to \pi^0 e^+ e$ has been studied within a Born diagram model, in which the interaction of the hadronic part results from the exchange of a single nucleon. The two corresponding Feynman diagrams, which are shown in Fig. 6.2, are given by a u-channel and t-channel nucleon exchange. Another analysis of the reaction has been performed within a factorization approach, using the concept of the transition distribution amplitudes [111, 112]. This approach is applicable in the kinematic range of larger momentum transfer s at forward and backward kinematics, where a lepton pair with high invariant mass is produced. Thus this model does not cover the region of interest, where the invariant mass of the produced lepton pair is below the production threshold q^2_{thr}. Consequently, in the following we will examine the Born diagram model in more detail.

The amplitudes of the diagrams describing the nucleon exchange can be written as

$$\begin{aligned}
\mathcal{A}_{\gamma*,u} &= -\frac{1}{q^2}\,\mathcal{L}_\mu\,\mathcal{M}^\mu_{\pi^0\gamma^*,\,u} \\
&= -\frac{1}{q^2}\,\mathcal{L}_\mu\,\bar{N}(p_1)\,\Gamma^\mu_{\gamma NN}(q)\left(\frac{\gamma\cdot(p_2-q_\pi)+m_N}{u-m_N^2}\right)\Gamma_{\pi NN}(q_\pi)\,N(p_2), \\
\mathcal{A}_{\gamma*,t} &= -\frac{1}{q^2}\,\mathcal{L}_\mu\,\mathcal{M}^\mu_{\pi^0\gamma^*,\,t} \\
&= -\frac{1}{q^2}\,\mathcal{L}_\mu\cdot\bar{N}(p_1)\,\Gamma_{\pi NN}(q_\pi)\left(\frac{\gamma\cdot(q_\pi-p_1)+m_N}{t-m_N^2}\right)\Gamma^\mu_{\gamma NN}(q)\,N(p_2), \\
&\text{with}\quad \mathcal{M}^\mu_{\gamma^*} = \mathcal{M}^\mu_{\pi^0\gamma^*,\,u} + \mathcal{M}^\mu_{\pi^0\gamma^*,\,t}\,,
\end{aligned} \tag{6.7}$$

where the subscripts u and t of $\mathcal{A}_{\gamma^*}$ refer to the amplitude with u-channel and t-channel nucleon exchange, respectively, and $\bar{N}(p_1)$ ($N(p_2)$) corresponds to the Dirac spinor of the antiproton (proton). The structures $\Gamma^\mu_{\gamma NN}$ and $\Gamma_{\pi NN}$ are the parametrization of the $\gamma^* NN$ and πNN vertices, as indicated in Fig. 6.2.

Within this approach, off-shell effects of the exchanged nucleons have been neglected, hence the $\gamma^* NN$ vertices are parametrized by the on-shell proton electromagnetic form factors, in

terms of the Dirac and Pauli form factors F_1 and F_2 given by

$$\Gamma^{\mu}_{\gamma NN}(q) \;=\; e\left[F_1(q^2)\gamma^{\mu} - \frac{i}{2m_N}F_2(q^2)\sigma^{\mu\nu}q_{\nu}\right]. \tag{6.8}$$

To describe the πNN vertex both cases of pseudoscalar as well as pseudovector πNN coupling are taken into account:

$$\Gamma_{\pi NN}(q_\pi) \;=\; g_{\pi NN}(m_\pi^2)\left(\lambda\gamma_5 + (1-\lambda)\frac{q_\pi\cdot\gamma}{2m}\gamma_5\right), \tag{6.9}$$

where $\lambda = 1$ ($\lambda = 0$) leads to a vertex with a purely pseudoscalar (pseudovector) coupling, with the pion-nucleon constant $g_{\pi NN}(m_\pi^2)$.

It is important to take both t-channel and u-channel nucleon exchange into account in order to construct a model, which satisfies the electromagnetic gauge invariance. The amplitudes $\mathcal{M}^{\mu}_{\pi^0\gamma^*,u}$ and $\mathcal{M}^{\mu}_{\pi^0\gamma^*,t}$ themselves are not gauge invariant, but since

$$\begin{aligned}
q_\mu\,\mathcal{M}^{\mu}_{\pi^0\gamma^*,u} \;&=\; e\,g_{\pi NN}(m_\pi^2)\,\bar N(p_1)\,F_1(q^2)\left(-m_N + \not p_2 - \not q_\pi\right)\left(\frac{\not p_2 - \not q_\pi + m_N}{u-m_N^2}\right)\\
&\quad\times\left(\lambda\gamma_5 + (1-\lambda)\frac{\gamma\cdot q_\pi}{2m_N}\gamma_5\right)N(p_2)\\
&=\; e\,g_{\pi NN}(m_\pi^2)\,F_1(q^2)\,\bar N(p_1)\left(\lambda\gamma_5 + (1-\lambda)\frac{\gamma\cdot q_\pi}{2m_N}\gamma_5\right)N(p_2),\\
q_\mu\,\mathcal{M}^{\mu}_{\pi^0\gamma^*,t} \;&=\; e\,g_{\pi NN}(m_\pi^2)\,\bar N(p_1)\left(\lambda\gamma_5 + (1-\lambda)\frac{\gamma\cdot q_\pi}{2m_N}\gamma_5\right)\left(\frac{\not q_\pi - \not p_1 + m_N}{t-m_N^2}\right)\\
&\quad\times F_1(q^2)\left(\not p_1 - \not q_\pi + m_N\right)N(p_2)\\
&=\; -\,e\,g_{\pi NN}(m_\pi^2)\,F_1(q^2)\,\bar N(p_1)\left(\lambda\gamma_5 + (1-\lambda)\frac{\gamma\cdot q_\pi}{2m_N}\gamma_5\right)N(p_2),
\end{aligned} \tag{6.10}$$

it follows

$$q_\mu\,\mathcal{M}^{\mu}_{\gamma^*} \;=\; q_\mu\left(\mathcal{M}^{\mu}_{\pi^0\gamma^*,u} + \mathcal{M}^{\mu}_{\pi^0\gamma^*,t}\right) \;=\; 0. \tag{6.11}$$

Nevertheless, it should be kept in mind, that the discussed approach implies that the process can be approximately described by the exchange of a single nucleon in the u- and t-channel, which is treated to be on-shell. When making such assumptions, the question of the validity of such a model arises, calling for the possibility to test the considered approach.

6.1.2 Real Photoproduction

Since at present no data of the process of timelike pion electroproduction (Eq. (6.2)) exist, we study the reaction of real photoproduction,

$$\bar p(p_1) + p(p_2) \to \pi^0(q_\pi) + \gamma(q), \tag{6.12}$$

which has been measured at Fermi National Accelerator Laboratory (Fermilab) [113], and we test the predictions of the Born diagram model with the results of this experiment. Data

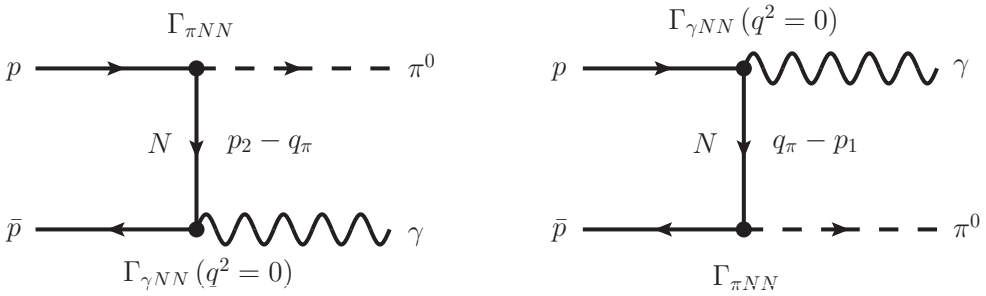

Figure 6.3: Born diagram model for $p\,\bar{p} \to \pi^0\,\gamma$

of the angular dependence of the differential cross section $d\sigma/d\cos\theta_\pi$, where θ_π is the c.m. scattering angle of the pion, is available in the c.m. energy range of

$$2.911\,\text{GeV} \leq \sqrt{s} \leq 3.686\,\text{GeV}, \tag{6.13}$$

covering an angular region of approximately $-0.6 \leq \cos\theta_\pi \leq 0.6$.

The unpolarized cross section has the following form

$$\begin{aligned} d\sigma = & \frac{1}{4\sqrt{(p_1 \cdot p_2)^2 - m_N^4}} \left(\frac{d^3\vec{q}_\pi}{(2\pi)^3 2E_\pi}\right) \left(\frac{d^3\vec{q}}{(2\pi)^3 2q^0}\right) \\ & \times\ (2\pi)^4 \delta^{(4)}\big(p_1 + p_2 - q_\pi - q\big)\, \frac{1}{4} \sum_{\lambda_{N_i},\lambda_\gamma} |\mathcal{A}_\gamma|^2, \end{aligned} \tag{6.14}$$

where the subscript γ of the amplitude $\mathcal{A}_\gamma$ refers of the process of real photoproduction.

The u- and t-channel amplitudes within the Born diagram model, as seen in Fig. 6.3, are obtained as

$$\begin{aligned} \mathcal{A}_{\gamma,u} &= \varepsilon_\mu^* \cdot \mathcal{M}^\mu_{\pi^0\gamma,\,u} \\ &= \varepsilon_\mu^*(q,\lambda_\gamma) \cdot \bar{N}(p_1)\, \Gamma^\mu_{\gamma NN}(q^2 = 0) \left(\frac{\gamma \cdot (p_2 - q_\pi) + m_N}{u - m_N^2}\right) \Gamma_{\pi NN}(q_\pi)\, N(p_2), \\ \mathcal{A}_{\gamma,t} &= \varepsilon_\mu^* \cdot \mathcal{M}^\mu_{\pi^0\gamma,\,t} \\ &= \varepsilon_\mu^*(q,\lambda_\gamma) \cdot \bar{N}(p_1)\, \Gamma_{\pi NN}(q_\pi) \left(\frac{\gamma \cdot (q_\pi - p_1) + m_N}{t - m_N^2}\right) \Gamma^\mu_{\gamma NN}(q^2 = 0)\, N(p_2), \end{aligned} \tag{6.15}$$

where $\varepsilon^\mu(q,\lambda_\gamma)$ is the photon polarization vector. For real photons, one has two polarization states, $\lambda_\gamma = \pm 1$, with $q_\mu\,\varepsilon^\mu(q,\lambda_\gamma) = 0$. In the description of $\Gamma^\mu_{\gamma NN}$ in Eq. (6.15) the form factors

$$F_1(q^2 = 0) = 1, \qquad F_2(q^2 = 0) = \kappa_p = 1.79 \tag{6.16}$$

have been used.

For the spin-averaged squared matrix element one finds

$$\frac{1}{4} \sum_{\lambda_{N_i},\lambda_\gamma} \big|\mathcal{A}_\gamma\big|^2 = \frac{1}{4} \sum_{\lambda_{N_i},\lambda_\gamma} \left|\varepsilon_\mu^* \left(\mathcal{M}^\mu_{\pi^0\gamma,\,u} + \mathcal{M}^\mu_{\pi^0\gamma,\,t}\right)\right|^2. \tag{6.17}$$

The process has been evaluated in the c.m. frame of the $(\bar{p}p)$-pair, in which the momentum of the antiproton has been chosen as the z-direction and the process takes place in the x-z plane. The nucleon momenta are given by

$$p_1 = \frac{\sqrt{s}}{2}\left(1,0,0,\sqrt{\frac{s-4m_N^2}{s}}\right), \qquad p_2 = \frac{\sqrt{s}}{2}\left(1,0,0,-\sqrt{\frac{s-4m_N^2}{s}}\right), \tag{6.18}$$

and the momenta of the mesons are

$$\begin{aligned} q &= (q^0,\vec{q}) = (q^0, |\vec{q}|\sin\theta_\gamma,\, 0,\, |\vec{q}|\cos\theta_\gamma), \\ q_\pi &= (E_\pi, -\vec{q}), \end{aligned} \tag{6.19}$$

with the photon and pion energies

$$q^0 = \frac{s-m_\pi^2}{2\sqrt{s}}, \qquad E_\pi = \frac{s+m_\pi^2}{2\sqrt{s}}. \tag{6.20}$$

The unpolarized differential cross section is given by

$$\frac{d\sigma}{d\cos\theta_\gamma} = \frac{1}{16\pi\, s\,\sqrt{s-4m_N^2}}\,|\vec{q}|\,\frac{1}{4}\sum_{\lambda_{N_i}}(-g_{\mu\nu})\left|\mathcal{M}^{\mu}_{\pi^0\gamma,\ u} + \mathcal{M}^{\mu}_{\pi^0\gamma,\ t}\right|^2. \tag{6.21}$$

Using the Born diagram model for $p\,\bar{p} \to \pi^0\gamma$, we are not able to reproduce the results obtained in the E760 experiment at Fermilab. The cross section $d\sigma/d\cos\theta_\pi$ found within the Born diagram model is about 4 to 5 orders of magnitude larger then the data, depending on the value of the c.m. energy $\sqrt{s}$. Simple fixes by introducing strong suppressions through off-shell form factors do not lead to a correct energy dependence of the cross sections.

For this reason, one can assume, that the Born diagram model is not suitable to describe this process and thus the process $p\,\bar{p} \to \pi^0 e^+ e^-$ as well. Therefore, we consider an alternative model, which is inspired by Regge theory. Within this model, the exchange of a class of particles with same internal quantum numbers is taken into account, instead of a single particle exchange as in the Born diagram model.

6.2 Regge Theory

Before the advent of QCD as theory of the strong interaction, Regge theory was been established as an approach to describe hadronic reactions at high c.m. energies at forward and backward scattering angles. It is based on the idea of an analytical continuation of the scattering amplitude in the complex angular momentum plane [114].

Scattering processes have been analyzed by taking specific properties of the S-matrix into account. The S-matrix, which describes the transition of an initial particle state $|a\rangle$ to a final state $|b\rangle$, is given by

$$S_{ab} = \langle a|S|b\rangle = \delta_{ab} + \mathrm{i}(2\pi)^4\,\delta\left(\sum_a p_a - \sum_b p_b\right)\mathcal{A}_{ab}, \tag{6.22}$$

where $\mathcal{A}_{ab}$ is the scattering amplitude. In the case of a $2 \to 2$ particle scattering process, $\mathcal{A}$ can be expressed as function of the invariant Mandelstam variables s and t: $\mathcal{A}(s,t)$. Crossing symmetry correlates the amplitudes of s-, t-, and u-channel exchange, which are described by the same function $\mathcal{A}$ for a different parameter space of the Mandelstam variables. Besides using unitarity of the S-matrix, $S\,S^\dagger = 1$, Regge theory postulates, that the S-matrix can be analytically continuated in the complex angular momentum plane, having only isolated singularities.

A detailed discussion of Regge theory can be found in Ref. [115]. Only the basic principles are outlined here.

A $2 \to 2$ particle scattering process is studied in the so-called Regge limit, where the momentum transfer s is large and $s \gg |t|$ (or equivalently $s \gg |u|$). For simplicity, we first consider a reaction where the four external particles have equal masses and do not carry internal spin. The partial wave series of the amplitude in the t-channel is given by

$$\begin{aligned} \mathcal{A}(s,t) &= \sum_l (2l+1)\, A_l(t)\, P_l(\cos\theta_t), \\ &\text{with} \quad A_l(t) = \frac{1}{2}\int_{-1}^{1} d\cos\theta\, P_l(\cos\theta_t)\mathcal{A}(s,t) \\ &\text{and} \quad \cos\theta_t = 1 + \frac{2s}{t-4m^2}, \end{aligned} \tag{6.23}$$

where l is the angular momentum and P_l are Legendre polynomials.

The partial wave series can be rewritten as a contour integral in the complex angular-momentum plane, where the contour C_1 surrounds the positive real-axis,

$$\mathcal{A}(s,t) = -\frac{1}{2\mathrm{i}} \oint_{C_1} dl\,(2l+1)\,\frac{A(l,t)}{\sin\pi l}\, P_l(-\cos\theta_t), \tag{6.24}$$

which is known as Sommerfeld-Watson transformation. $A(l,t)$ is the analytic continuation for complex values of l, which matches $A_l(t)$, if l reaches an integer value:

$$A(l,t) = A_l(t) \quad \text{for } l = 0,1,2,\ldots\ . \tag{6.25}$$

Using Cauchy's integral theorem, the residues of the integrand at the integer values $l = n$ with $\sin(n\pi) \to (-1)^n(l-n)\pi$ give rise to Eq. (6.23).

The contour C_1 can be deformed to another contour, as presented by the dashed curves in Fig. (6.4), given by C along $\mathrm{Re}(l) = -1/2$ and the semi-circle, which is extended to infinity, where the singularities α_i in the complex l-plane have to be included. To ensure that the integration over the semi-circle vanishes at infinity, $A(l,t)$ has to converge for $l \to \infty$. To guarantee the convergence, one has to separate the even and odd partial waves, such that

$$\begin{aligned} A^+(l,t) &= A_l(t) \quad \text{for } l = 0,2,4,\ldots\ , \\ A^-(l,t) &= A_l(t) \quad \text{for } l = 1,3,5\ldots\ , \end{aligned} \tag{6.26}$$

where $A^\pm$ are the analytic continuations of the even and odd partial wave amplitudes, respectively. On this account, the signature $\mathcal{S} = \pm 1$ has to be introduced, where $\mathcal{S} = +1$ ($\mathcal{S} = -1$) corresponds to even (odd) partial waves.

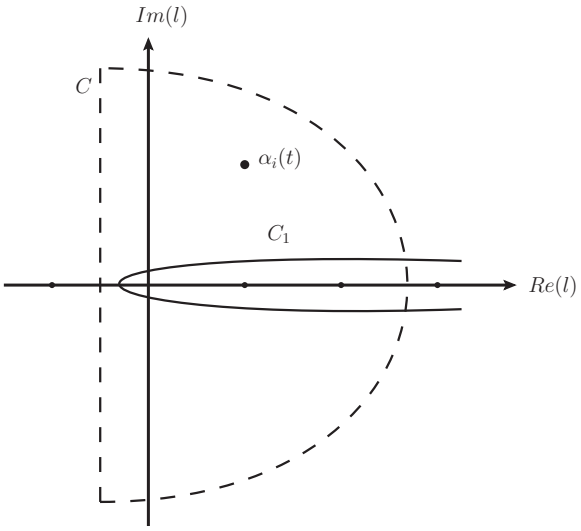

Figure 6.4: Integration contours C_1 and C in the complex angular momentum plane as well as the Regge pole indicated by $l = \alpha_i(t)$.

The integration can be performed by taking the singularities of $A^{\mathcal{S}}(l,t)$ in the angular momentum plane, $l = \alpha_i^{\mathcal{S}}(t)$, into account by adding up their residues $\beta_i^{\mathcal{S}}(t)$, which leads to

$$\begin{aligned}\mathcal{A}^{\mathcal{S}}(s,t) \;&= \frac{1}{2\mathrm{i}}\int_C dl\,(2l+1)\,\frac{\mathcal{S}+\mathrm{e}^{-i\pi\,\alpha_i^{\mathcal{S}}(t)}}{2}A^{\mathcal{S}}(l,t)P_l(-\cos\theta_t)\\ &\quad -\pi\sum_i(2\alpha_i^{\mathcal{S}}(t)+1)\,\frac{\mathcal{S}+\mathrm{e}^{-i\pi\,\alpha_i^{\mathcal{S}}(t)}}{2}\,\frac{\beta_i^{\mathcal{S}}(t)}{\sin\left(\pi\alpha_i^{\mathcal{S}}(t)\right)}P_{\alpha_i^{\mathcal{S}}(t)}(-\cos\theta),\end{aligned} \tag{6.27}$$

where the latter term on the r.h.s. of Eq. (6.27) is denoted as a Regge pole. The expressions $(\mathcal{S}+\mathrm{e}^{-i\pi\,\alpha_i^{\mathcal{S}}(t)})/2$ are the signature factors giving rise to the separated partial wave amplitudes $A^{\pm}$. In the high energy Regge limit, the dominant contribution to the amplitude results from the pole term. The contour integral over C along the imaginary axis has a $s^{-\frac{1}{2}}$ dependence and can be neglected for $s \to \infty$. Hence the amplitude reduces to the second part given in Eq. (6.27). Applying the Regge limit to Eq. (6.27), one finds that the leading contribution to $\mathcal{A}$ can be written as

$$\mathcal{A}^{\mathcal{S}}(s,t) \propto \sum_i \frac{\mathcal{S}+\mathrm{e}^{-i\pi\alpha_i^{\mathcal{S}}(t)}}{2}\,\frac{\beta_i^{\mathcal{S}}(t)}{\Gamma[\alpha_i^{\mathcal{S}}(t)+1]\sin\left(\pi\alpha_i^{\mathcal{S}}(t)\right)}\left(\frac{s}{s_0}\right)^{\alpha_i^{\mathcal{S}}(t)}, \tag{6.28}$$

where the scaling factor s_0 is conventionally chosen to be $s_0 = 1\ \mathrm{GeV}^2$. The Gamma function suppresses poles in the unphysical (negative) angular momentum region.

For processes involving particles with spin $1/2$, such as annihilation of two baryons into a meson pair, which are relevant for the processes studied in this chapter, the Regge amplitude is given by [116]:

$$\mathcal{A}^{\mathcal{S}} \propto \sum_i \frac{1}{\Gamma\left[\alpha_i^{\mathcal{S}}(t)+\frac{1}{2}\right]}\,\frac{\mathcal{S}+\mathrm{e}^{-i\pi\left(\alpha_i^{\mathcal{S}}(t)+\frac{1}{2}\right)}}{2}\,\frac{1}{\sin\pi\left(\alpha_i^{\mathcal{S}}(t)+\frac{1}{2}\right)}\left(\frac{s}{s_0}\right)^{\alpha_i^{\mathcal{S}}(t)-\frac{1}{2}}. \tag{6.29}$$

The appropriate expression for the Regge amplitude corresponding to u-channel exchange can be found in an analogous manner in the Regge limit with $s \gg |u|$.

In the limit $l \to \alpha_i(t)$, the Regge pole reduces to the Feynman pole, describing a single particle exchange:

$$\mathcal{A}(s,t) \xrightarrow{l \to \alpha_i(t)} \frac{\beta_i(t)}{t - m_i^2}, \tag{6.30}$$

where $1/(t - m_i^2)$ represents the Feynman pole. The residue β_i can be determined from the vertex structure of the single particle exchange amplitude. When such a Regge pole occurs through an integer value of the angular momentum l, it corresponds to a particle (or a resonance). For a t-channel process, one expects to have poles which are associated with the exchange of a particle with mass m_i and spin j_i as

$$\alpha_i(t = m_i^2) = j_i. \tag{6.31}$$

It is possible to group the particles and resonances with same internal quantum numbers, but different spin, into families, which lie on a given Regge trajectory α. Phenomenologically, it has been found that the Regge trajectories can be parametrized through a straight line:

$$\alpha_i(t) = \alpha_i(0) + \alpha_i'(t - m_i^2), \tag{6.32}$$

where $\alpha(0)$ is the spin and m_i is the mass of the first materialization of the trajectory. Such Regge trajectories are named after the lowest-lying particle of $\alpha_i(t)$.

This procedure allows for converting amplitudes describing the exchange of a single particle, which is the first materialization of a Regge trajectory, to Regge amplitudes of a given trajectory. These so-called reggeization is carried out by replacing a usual Feynman propagator through a Regge propagator, e.g. for baryon exchange as

$$\frac{1}{t - m_i^2} \;\longrightarrow\; D_i^{\text{Regge}}(t,s) = \frac{s^{\alpha_i(t) - \frac{1}{2}}}{\Gamma\left[\alpha_i(t) + \frac{1}{2}\right]} \frac{\mathcal{S} + \mathrm{e}^{-i\pi\left(\alpha_i(t) + \frac{1}{2}\right)}}{2} \frac{\pi\alpha_i'}{\sin\pi\left(\alpha_i(t) + \frac{1}{2}\right)}, \tag{6.33}$$

which corresponds to an effective summing up of higher-spin particles lying on the corresponding Regge trajectory.

Phenomenologically, it has been found that trajectories often satisfy the so-called weak degeneracy, which means, that both even- and odd-partial wave trajectories are equal: $\alpha^+(t) = \alpha^-(t)$. In addition, the condition of the strong degeneracy implies, that both vertex functions of the process are the same. As a consequence, the corresponding amplitude of a trajectory fulfilling the strong degeneracy is characterized by the trajectory α^+ with the residue β^+. Such a degenerate trajectory can be obtained by adding or subtracting the trajectories of different signatures,

$$\beta(t)\left(\frac{\mathcal{S} + \mathrm{e}^{-i\pi\left(\alpha_i(t) + \frac{1}{2}\right)}}{2} + \frac{\pm\mathcal{S} + \mathrm{e}^{-i\pi\left(\alpha_i(t) + \frac{1}{2}\right)}}{2}\right) = \beta(t)\begin{cases} \mathrm{e}^{-i\pi\left(\alpha_i(t) + \frac{1}{2}\right)}. \\ 1. \end{cases} \tag{6.34}$$

This leads to a degenerate trajectory, which has either a rotating or a constant phase. In this work we assume strong degeneracy of the baryon trajectories.

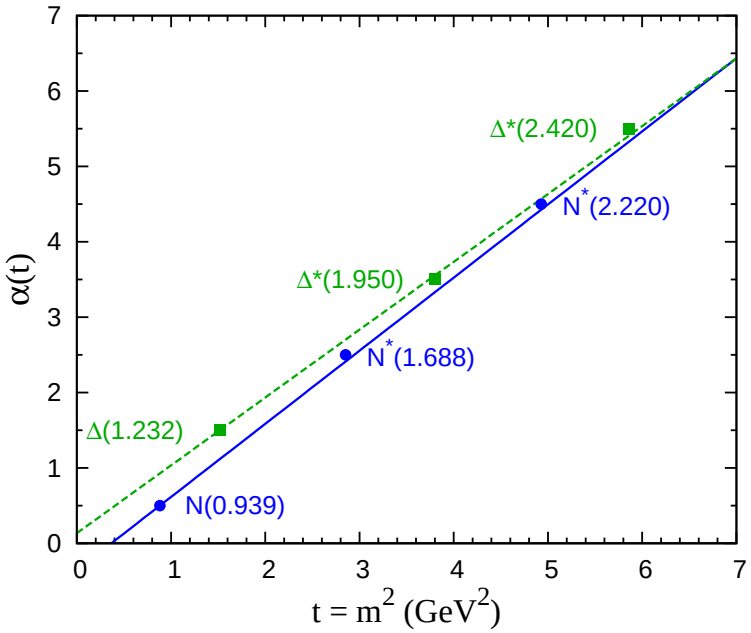

Figure 6.5: Trajectories $\alpha(t)$ of the nucleon (blue solid curve) and the $\Delta(1232)$ resonance (green dashed curve). The data points correspond to the particle positions in the m^2-spin-plane.

In Fig. 6.5 the trajectories of the nucleon and Δ resonance are shown, which can approximately be expressed through

$$\begin{aligned} \alpha_N(t) &= \frac{1}{2} + 0.97\,\mathrm{GeV}^{-2}\left(t - m_N^2\right), \\ \alpha_\Delta(t) &= \frac{3}{2} + 0.9\ \mathrm{GeV}^{-2}\ \left(t - m_\Delta^2\right), \end{aligned} \tag{6.35}$$

which correspond to the blue solid (α_N) and green dashed line (α_Δ) in Fig. 6.5. The points indicate the position of the particles in the mass-spin plane.

Using the expression of the Regge propagator in Eq. (6.33), the cross section of a process, which is dominated by a given Regge trajectory, behaves as

$$\frac{d\sigma}{dt} \propto \frac{1}{s^2}\left|\mathcal{A}(s,t)\right|^2 \propto F(t)\, s^{2\alpha(t)-2}. \tag{6.36}$$

If more than one trajectory is involved, at sufficient large values of s relative to a typical hadronic scale of 1 GeV^2 (for given t), only the trajectory with the largest value of $\alpha(t)$ will provide a significant contribution. Such trajectories are denoted as leading trajectories.

6.3 Real Photoproduction within a Regge Framework

To investigate the $p\bar{p} \to \pi^0\gamma$ annihilation process a Regge pole description is considered, which is based on the exchange of leading baryon Regge trajectories in the u-channel and t-channel. This approach allows to take the exchange of particles with higher spins and higher

masses into account, which are expected to contribute significantly at large momentum transfer. Such a phenomenological Regge pole approach has been successfully applied to electroproduction and photoproduction of pions and kaons, see e.g. Refs. [117, 118]. In particular, it has been widely applied in order to extract π^+ and K^+ electromagnetic form factors from the π^+ and K^+ electroproduction process [119, 120].

The kinematic region of this approach, which has been introduced before as Regge limit, are the ranges of forward and backward angles, $s \gg |t|$ and $s \gg |u|$. In the kinematical region $s \sim -t \sim -u$ the reaction has been investigated within the framework of generalized distribution amplitudes in Ref. [81].

The dominant trajectories for the process $p\bar{p} \to \pi^0\gamma$ are the nucleon (N) trajectory and Δ trajectory associated with the $\Delta(1232)$ resonance [115]. The amplitude for Regge trajectory exchange can be obtained from the Born diagram by replacing the usual Feynman propagator of the single exchanged particle by the Regge propagator, while leaving the Feynman structure, giving rise to the residue of the Regge pole, unchanged. We assume, that the trajectories are degenerate, which leads to a smooth behavior of the cross section [115]. Non-degenerate trajectories would manifest themselves in dips appearing in the cross section. Since the data do not show any dips in the measured range, such an assumption seems to be reasonable.

In case of an exchanged nucleon, the pole-like Feynman propagators of the u-channel and t-channel, given by $1/(u - m_N^2)$ and $1/(t - m_N^2)$, are replaced in the following way

$$\begin{aligned}
\frac{1}{u - m_N^2} \;&\Rightarrow D_N^{\text{Regge}}(u,s) = \frac{s^{\alpha_N(u)-\frac{1}{2}}}{\Gamma\left[\alpha_N(u)+\frac{1}{2}\right]}\,\pi\alpha'_N\,\frac{\mathrm{e}^{-i\pi\left(\alpha_N(u)+\frac{1}{2}\right)}}{\sin\pi\left(\alpha_N(u)+\frac{1}{2}\right)}, \\
\frac{1}{t - m_N^2} \;&\Rightarrow D_N^{\text{Regge}}(t\,,s) = \frac{s^{\alpha_N(t)-\frac{1}{2}}}{\Gamma\left[\alpha_N(t)\,+\frac{1}{2}\right]}\,\pi\alpha'_N\,\frac{\mathrm{e}^{-i\pi\left(\alpha_N(t)+\frac{1}{2}\right)}}{\sin\pi\left(\alpha_N(t)\,+\frac{1}{2}\right)},
\end{aligned} \tag{6.37}$$

where the nucleon trajectory α_N is of the form

$$\alpha_N(u) = \frac{1}{2} + \alpha'_N\left(u - m_N^2\right), \qquad \alpha_N(t) = \frac{1}{2} + \alpha'_N\left(t - m_N^2\right), \tag{6.38}$$

with $\alpha'_N = 0.97\ \text{GeV}^{-2}$.

Analogously to the findings of photoproduction and electroproduction of pions at high energies within a Regge pole model [117, 118], we consider a πNN coupling of the pseudoscalar type, as

$$\Gamma_{\pi NN}(q_\pi) = g_{\pi NN}(m_\pi^2)\gamma_5, \tag{6.39}$$

where $g_{\pi NN}(m_\pi^2)$ is the pion-nucleon coupling constant.

Besides including the nucleon Regge propagators, the exchange of the Δ trajectory is taken into account. Starting from the Feynman diagrams in a Born model with a single $\Delta(1232)$ resonance exchange, as illustrated in Fig. 6.6, the amplitudes of the u- and t-channel process can be expressed by

$$\mathcal{A}_\gamma^\Delta = \varepsilon_\mu^* \cdot \left(\mathcal{M}_{\pi^0\gamma,u}^{\Delta,\mu} + \mathcal{M}_{\pi^0\gamma,t}^{\Delta,\mu}\right) \tag{6.40}$$

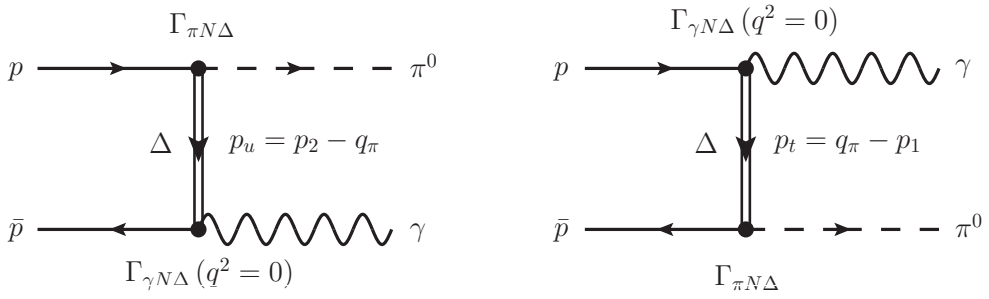

Figure 6.6: Born model for $p + \bar{p} \to \pi^0 + \gamma$ described by the exchange of $\Delta(1232)$.

with

$$\begin{aligned}
\mathcal{M}^{\Delta,\,\mu}_{\pi^0\gamma,u} =& \bar{v}(p_1)\,\Gamma^{\alpha}_{\gamma N\Delta}\frac{-\mathrm{i}}{u - m_\Delta^2}(\gamma\cdot p_u + m_\Delta) \\
&\times\left\{g_{\alpha\beta} - \frac{1}{3}\gamma_\alpha\gamma_\beta - \frac{\gamma_\alpha p_{u,\beta} - \gamma_\beta p_{u,\alpha}}{3m_\Delta} - \frac{2p_{u,\alpha}\,p_{u,\beta}}{3m_\Delta^2}\right\}\Gamma^{\beta}_{N\gamma\Delta}u(p_2), \\
\mathcal{M}^{\Delta,\,\mu}_{\pi^0\gamma,t} =& \bar{v}(p_1)\,\Gamma^{\alpha}_{\pi N\Delta}\frac{-\mathrm{i}}{t - m_\Delta^2}(\gamma\cdot p_t + m_\Delta) \\
&\times\left\{g_{\alpha\beta} - \frac{1}{3}\gamma_\alpha\gamma_\beta - \frac{\gamma_\alpha p_{t,\beta} - \gamma_\beta p_{t,\alpha}}{3m_\Delta} - \frac{2p_{t,\alpha}\,p_{t,\beta}}{3m_\Delta^2}\right\}\Gamma^{\beta}_{N\gamma\Delta}u(p_2),
\end{aligned} \tag{6.41}$$

with $p_u = p_2 - q_\pi$, and $p_t = q_\pi - p_1$ and the mass of the Δ resonance $m_\Delta = 1.232$ GeV. The structures $\Gamma_{\gamma N\Delta}$ and $\Gamma_{\pi N\Delta}$ are describing the $\gamma N\Delta$ vertices and $\pi N\Delta$ vertices, respectively. The $\Gamma_{\pi N\Delta}$ vertex can be parametrized as follows [121]:

$$\begin{aligned}
\Gamma^{\alpha}_{\gamma N\Delta}(q) =& \mathrm{i}\sqrt{\frac{2}{3}}\,\frac{3e(m_\Delta + m_N)}{2m_N((m_\Delta + m_N)^2 - q^2)}\Big\{g_M(q^2)\,\varepsilon^{\alpha\mu\rho\sigma}\,p_{\Delta,\rho}\,q_\sigma \\
&+ g_E(q^2)\,\left(q^\alpha p_\Delta^\mu - q\cdot p_\Delta g^{\alpha\mu}\right)\mathrm{i}\gamma_5 + g_C(q^2)\,\left(q^\alpha q^\mu - q^2 g^{\alpha\mu}\right)\mathrm{i}\gamma_5\Big\},
\end{aligned} \tag{6.42}$$

where p_Δ is the 4-momentum of the intermediate Δ state. In Eq. (6.42) the vertex depends on three electromagnetic form factors, $g_M(q^2)$, $g_E(q^2)$ and $g_C(q^2)$, representing the strength of the magnetic dipole, electric quadrupole and Coulomb quadrupole $N \to \Delta$ transitions. In the calculation, the electric and Coulomb quadrupole terms have been neglected since their contributions have been found to be of the order of a few % [122]. Therefore the $\gamma N\Delta$ vertex depends only on $g_M(q^2)$, for which $g_M(0) = 3.02$ is used as $\gamma N\Delta$ coupling strength. Both amplitudes of Eq. (6.41) satisfy electromagnetic gauge invariance due to

$$q_\mu\,\varepsilon^{\alpha\mu\rho\sigma}\,p_{\Delta,\rho}\,q_\sigma = 0. \tag{6.43}$$

The parametrization of the $\pi N\Delta$-vertex can be written as

$$\Gamma^{\alpha}_{\pi N\Delta}(q_\pi) = -\frac{h_A}{2f_\pi m_\Delta}\gamma^{\alpha\mu\nu}q_{\pi,\mu}\,p_{\Delta,\nu}\,T_a^\dagger. \tag{6.44}$$

The operator $T_a^\dagger$ is the isospin $1/2 \to 3/2$ transition operator, f_π denotes the pion decay constant and $h_A \simeq 2.85$ is the $\pi N\Delta$ coupling constant.

The Feynman propagators in Eq. (6.41) are then replaced by the Regge propagators:

$$\begin{aligned}
\frac{1}{u-m_\Delta^2} \;\Rightarrow\; D_\Delta^{\text{Regge}}(u,s) &= \frac{s^{\alpha_\Delta(u)-\frac{3}{2}}}{\Gamma\left[\alpha_\Delta(u)+\frac{1}{2}\right]}\,\pi\alpha'_\Delta\,\frac{\mathrm{e}^{-i\pi\left(\alpha_\Delta(u)-\frac{1}{2}\right)}}{\sin\pi\left(\alpha_\Delta(u)-\frac{1}{2}\right)}, \\
\frac{1}{t-m_\Delta^2} \;\Rightarrow\; D_\Delta^{\text{Regge}}(t,s) &= \frac{s^{\alpha_\Delta(t)-\frac{3}{2}}}{\Gamma\left[\alpha_\Delta(t)+\frac{1}{2}\right]}\,\pi\alpha'_\Delta\,\frac{\mathrm{e}^{-i\pi\left(\alpha_\Delta(t)-\frac{1}{2}\right)}}{\sin\pi\left(\alpha_\Delta(t)-\frac{1}{2}\right)},
\end{aligned} \tag{6.45}$$

where the Δ Regge trajectory is of the form

$$\alpha_\Delta(u) = \frac{3}{2} + \alpha'_\Delta\left(u-m_\Delta^2\right), \qquad \alpha_\Delta(t) = \frac{3}{2} + \alpha'_\Delta\left(t-m_\Delta^2\right), \tag{6.46}$$

with $\alpha'_\Delta = 0.9\ \text{GeV}^{-2}$.

The amplitude of the process reggeized in the following way, which ensures gauge invariance of the Regge model amplitudes:

$$\mathcal{M}^N_{\pi^0\gamma,t} = D_N^{\text{Regge}}(t\,,s)\,(t-m_N^2)\,\left[\mathcal{M}_u+\mathcal{M}_t\right], \tag{6.47}$$

$$\mathcal{M}^N_{\pi^0\gamma,u} = D_N^{\text{Regge}}(u,s)\,(u-m_N^2)\,\left[\mathcal{M}_u+\mathcal{M}_t\right], \tag{6.48}$$

and analogous expressions for the Δ-exchange diagrams. Contracting with the photon momentum yields

$$\begin{aligned}
q_\mu\left(\mathcal{M}^N_{\pi^0\gamma,t}\right)^\mu &= D_N^{\text{Regge}}(t\,,s)\,(t-m_N^2)\,\left[q_\mu\,\mathcal{M}_u^\mu + q_\mu\,\mathcal{M}_t^\mu\right] = 0, \\
q_\mu\left(\mathcal{M}^N_{\pi^0\gamma,u}\right)^\mu &= D_N^{\text{Regge}}(u,s)\,(u-m_N^2)\,\left[q_\mu\,\mathcal{M}_u^\mu + q_\mu\,\mathcal{M}_t^\mu\right] = 0.
\end{aligned} \tag{6.49}$$

Note that the Regge approach implies $s \gg |t|$, $s \gg |u|$, so that both forward and backward regions are kinematically separated. In the kinematic region $s \gg |t|$ the Regge amplitude of Eq. (6.47) is dominating, whereas in region of $s \gg |u|$ the u-channel Regge amplitude (Eq. (6.48)) is the dominant one. Only in these limits there is no double counting in this procedure. In the intermediate angular region one is outside the range of the validity of a Regge approach.

We next discuss the inclusion of the Δ-exchange Regge trajectories. As for the Δ we are further away from the pole position than in the nucleon case, the description of the residues of the Regge poles through their on-shell couplings can be expected to be modified. We allow for such a reduction of the coupling strengths of the Δ Regge pole residue, leading to the amplitude

$$\mathcal{A}_\gamma^{\mathcal{F}} = \varepsilon_\mu^* \cdot \left(\mathcal{M}^N_{\pi^0\gamma} + \mathcal{F}\cdot\mathcal{M}^\Delta_{\pi^0\gamma}\right), \tag{6.50}$$

where the parameter $\mathcal{F}$ will be obtained by a fit to the data.

In Fig. 6.7, results for $d\sigma/d\cos\theta_\pi$ for several c.m. energies $\sqrt{s}$ including N trajectory exchange and $(N+\Delta)$ trajectories exchange are presented as well as results using the approach of Eq. (6.50) in comparison with the data taken at the Fermilab [113]. Fitting the available data leads to $\mathcal{F} \approx 0.5$. One notices, that the angular dependence of the data in the forward and backward regions is well reproduced.

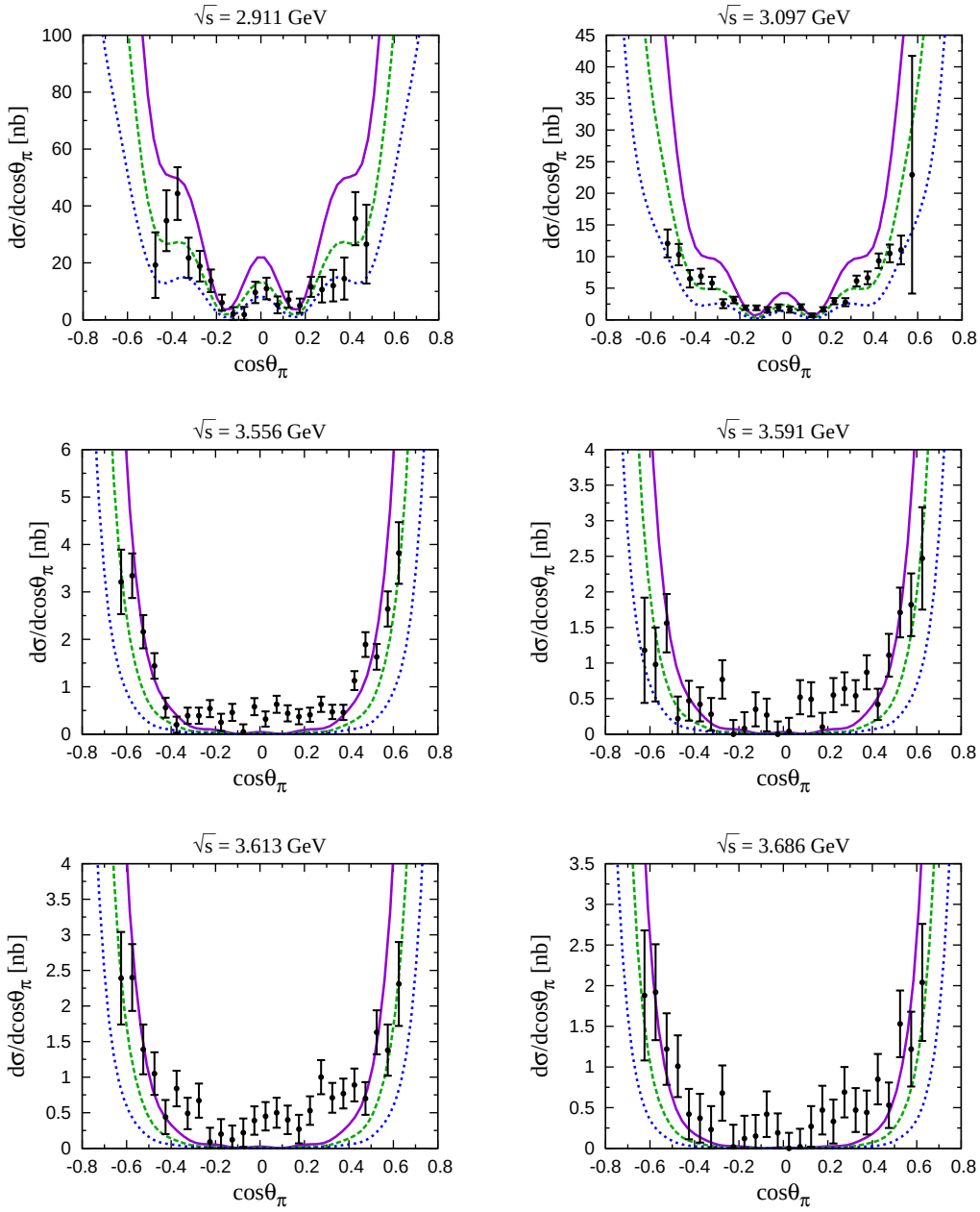

Figure 6.7: Differential cross section $d\sigma/d\cos\theta_\pi$ of $p\bar{p} \to \pi^0\gamma$ for different c.m. energies $\sqrt{s}$; blue (dotted) curve: N trajectory contribution; purple (solid) curve: cross section including $(N + \Delta)$ Regge trajectory exchange; green (dashed) curve: $(N + \Delta)$ contribution including a reduction of the Δ pole residue ($\mathcal{F} \approx 0.5$) according to Eq. (6.50). The data are taken from Ref. [113].

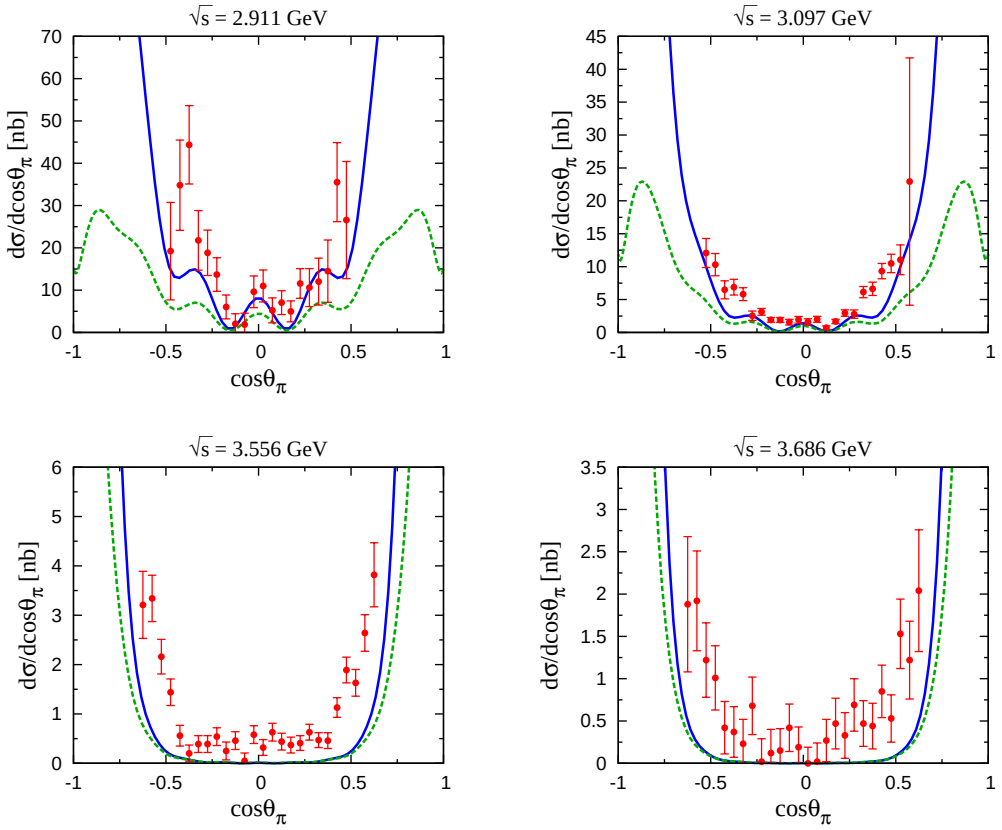

Figure 6.8: Differential cross section $d\sigma/d\cos\theta_\pi$ of $p\bar{p} \to \pi^0\gamma$ for different c.m. energies $\sqrt{s}$ including nucleon Regge trajectory exchange in the t-channel and u-channel: the blue (solid) curve corresponds to a pseudoscalar coupling of the πNN vertex (given by Eq. (6.39)), the green (dashed) curve describes a pseudovector coupling (given by Eq. (6.51)). The data are taken from Ref. [113].

The Regge model including N and Δ trajectory exchange describes the available data very well. When only a N trajectory exchange is included in the amplitude, presented by the blue dotted curve in Fig. 6.7, the obtained cross sections lie somewhat below the data points, in particular for larger values of momentum transfer s. The Regge pole model gives a better description of the data when taking both N and Δ trajectory exchange into account, even though the calculation gives to some extent a larger cross section than the results of the experiment. The cross section including the reduction factor $\mathcal{F}$ of the Δ-pole residue is in very good agreement with the experiment, as one can see from the green dashed curve in Fig. 6.7, especially in the regions $s \gg |t|$ and $s \gg |u|$.

In addition to the parametrization of the πNN vertex in Eq. (6.39), we considered a πNN coupling of the pseudovector type,

$$\Gamma_{\pi NN}(q_\pi) = g_{\pi NN}(m_\pi^2)\,\frac{\not{q}_\pi}{2m_N}\,\gamma_5. \tag{6.51}$$

The results of the differential cross section $d\sigma/d\cos\theta_\pi$ including N trajectory exchange are shown in Fig. 6.8 for several c.m. energies $\sqrt{s}$ using two different pion-nucleon couplings,

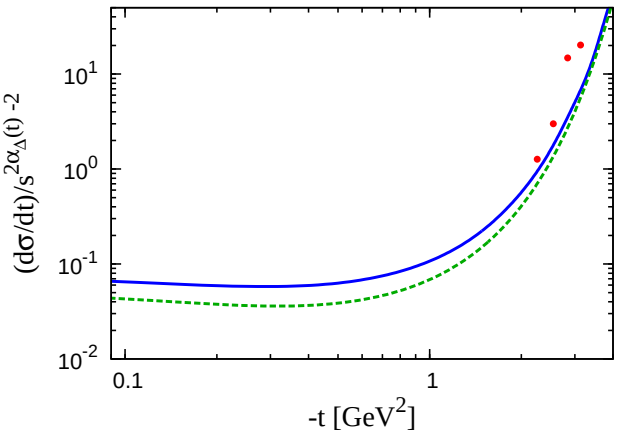

Figure 6.9: Cross section $d\sigma/dt$ divided by $s^{2\alpha_\Delta(t)-2}$ for the process $p\bar{p} \to \pi^0\gamma$ as a function of $-t$ for different values of $\sqrt{s}$ using the description according to Eq. (6.50); blue solid curve: $\sqrt{s} = 3.686$ GeV; green dashed curve: $\sqrt{s} = 10$ GeV; the data correspond to the cross section measured at $\sqrt{s} = 3.686$ GeV [113].

pseudoscalar, indicated by the blue solid curve, and pseudovector coupling, shown by the green dashed curve. As one can see in Fig. 6.8, one did not find a satisfactory description of the data in the forward and backward regions when a pseusovector type of the coupling is used.

Since Regge theory gives as asymptotic behavior of the cross section

$$\begin{aligned} \frac{d\sigma}{dt} &\propto F(t)\, s^{2\alpha(t)-2}, \quad \text{for } |t| \ll s, \\ \text{and} \quad \frac{d\sigma}{du} &\propto F(u)\, s^{2\alpha(u)-2}, \quad \text{for } |u| \ll s, \end{aligned} \tag{6.52}$$

the cross section $d\sigma/dt$, divided by the expected s dependence of the leading Regge trajectory is analyzed, in order to test the applicability of the model. At high energies the dominant t dependence of the cross section is expected to arise rather from the $s^{\alpha(t)}$ term than from $F(t)$.

For small values of t or u the Δ trajectory is the dominant one, therefore we compute the cross section divided by $s^{2\alpha_\Delta(t)-2}$:

$$\frac{d\sigma/dt}{s^{2\alpha_\Delta(t)-2}} \propto F(t) \quad \text{for } t \to 0. \tag{6.53}$$

The results are presented in Fig. 6.9, where the cross section $d\sigma/dt$ divided by $s^{2\alpha_\Delta(t)-2}$ is given as a function of $-t$ for two different c.m. energies. One notices, that for $-t \to 0$ the cross section $(d\sigma/dt)/s^{2\alpha_\Delta(t)-2}$ shows a behavior, which is approximately independent of s, as expected from Regge theory, and approaches a constant value. The existing cross section data, as indicated by the data taken at $\sqrt{s} = 3.686$ GeV in Fig. 6.9, have not yet reached the region of such small values of $-t$, where an extrapolation of $(d\sigma/dt)/s^{2\alpha_\Delta(t)-2}$ could be performed by a constant.

6.4 Timelike Pion Photoproduction within a Regge Framework

6.4.1 General Analysis of the Annihilation Cross Section

After specifying the Regge pole model, we study the process

$$\begin{aligned}\bar{p}(p_1,\lambda_{N_1}) + p(p_2,\lambda_{N_2}) &\rightarrow \pi^0(q_\pi) + \gamma^*(q,\lambda_\gamma) \\ &\rightarrow \pi^0(q_\pi) + e^-(k_1,h_1) + e^+(k_2,h_2),\end{aligned} \tag{6.54}$$

in the framework of one-photon exchange, starting with a model independent analysis of the annihilation cross section, which will be performed by taking properties of the electromagnetic interaction into account. The 5-fold differential cross section for the process is defined as

$$\begin{aligned}d\sigma =& \frac{1}{4\sqrt{(p_1\cdot p_2)^2 - m_N^4}} \left(\frac{d^3\vec{q}_\pi}{(2\pi)^3\, 2E_\pi}\right)\left(\frac{d^3\vec{k}_1}{(2\pi)^3\, 2k_1^0}\right)\left(\frac{d^3\vec{k}_2}{(2\pi)^3\, 2k_2^0}\right) \\ &\times (2\pi)^4\,\delta\big(p_1+p_2-q_\pi-k_1-k_2\big)\,\frac{1}{4}\sum_{\lambda_{N_i},h_i}|\mathcal{A}_{\gamma^*}|^2,\end{aligned} \tag{6.55}$$

with the spin-averaged squared matrix element $|\overline{\mathcal{A}_{\gamma^*}}|^2$,

$$|\overline{\mathcal{A}_{\gamma^*}}|^2 = \frac{1}{4}\sum_{\lambda_{N_i},h_i}|\mathcal{A}_{\gamma^*}|^2, \tag{6.56}$$

where the amplitude $\mathcal{A}_{\gamma^*}$ has been introduced in Eq. (6.5). In the analysis, the dependence on the pion variables as well as on the kinematic variables of the lepton pair are taken into account, which is associated with an experimental setup, where all three particles of the final state are detected.

The squared amplitude $|\overline{\mathcal{A}_{\gamma^*}}|^2$ can be decomposed into a hadronic and a leptonic contribution:

$$\begin{aligned}|\overline{\mathcal{A}_{\gamma^*}}|^2 &= \sum_{\lambda_\gamma=0,\pm1}\ \frac{1}{4}\sum_{\lambda_{N_i},h_i}\left|\left(\mathcal{M}^\mu_{\gamma^*}\cdot\varepsilon^*_\mu(q,\lambda_\gamma)\right)\frac{1}{q^2}\left(\varepsilon_\nu(q,\lambda_\gamma)\bar{u}(k_1)\,e\gamma^\nu\,v(k_2)\right)\right|^2, \\ &= \frac{1}{q^4}\sum_{\lambda_\gamma=0,\pm1}\ \frac{1}{4}\sum_{\lambda_{N_i},h_i}\left|\mathcal{M}^\mu_{\gamma^*}\cdot\varepsilon^*_\mu(q,\lambda_\gamma)\right|^2\left|\varepsilon_\nu(q,\lambda_\gamma)\mathcal{L}^\nu\right|^2,\end{aligned} \tag{6.57}$$

where $\varepsilon(q,\lambda_\gamma)$ is the polarization vector of the virtual photon. $\mathcal{M}^\mu_{\gamma^*}$ is the amplitude of the hadronic process $p\bar{p}\rightarrow\pi^0\gamma^*$ and $\mathcal{L}^\mu$ is the amplitude of the leptonic reaction. In the unpolarized case it is given by:

$$\sum_{h_1,h_2}\mathcal{L}^\mu\mathcal{L}^{\nu^*} \;=\; 4e^2\left(k_1^\mu\,k_2^\nu + k_1^\nu\,k_2^\mu - \frac{1}{2}k^2 g^{\mu\nu}\right), \tag{6.58}$$

which is symmetric with respect to the interchange $\mu\leftrightarrow\nu$. An explicit form of the hadronic contribution is not given at this point of the analysis. The separation of the amplitude is independent of any specific form of the hadronic interaction.

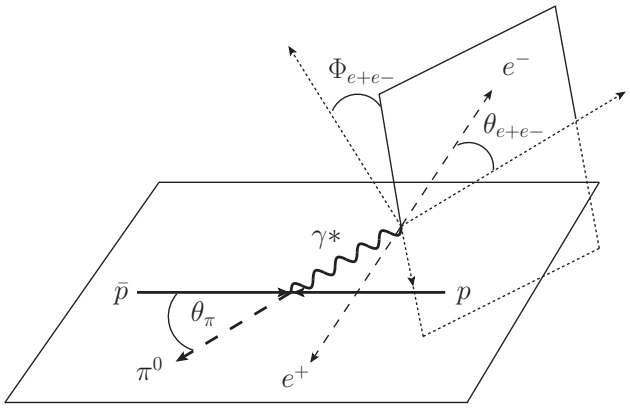

Figure 6.10: Kinematics of the $\bar{p}p \to \pi^0 e^+ e^-$ process.

Both contributions of Eq. (6.57),

$$\left|\mathcal{M}^{\mu}_{\gamma^*}\,\varepsilon^*_\mu(q,\lambda_\gamma)\right|^2 \quad \text{and} \quad \left|\varepsilon_\nu(q,\lambda_\gamma)\bar{u}(k_1)\,e\gamma^\nu\,v(k_2)\right|^2, \tag{6.59}$$

are Lorentz invariants, thus one can choose any reference frame for the calculation. The advantage of such a separation is, that one can easily calculate the hadronic and leptonic processes in two different reference frames.

The hadronic process, taking place in the hadronic plane, which is chosen to be the x-z-plane, is considered in the c.m.-frame of the nucleon pair, with the three-momentum of the antiproton pointing in the direction of the z-axis. The hadron and meson momenta have been introduced in Eq. (6.19). In the case of a virtual photon, the photon and pion energies are

$$q^0 = \frac{s - m_\pi^2 + q^2}{2\sqrt{s}}, \qquad E_\pi = \frac{s + m_\pi^2 - q^2}{2\sqrt{s}}. \tag{6.60}$$

The leptonic subprocess $\gamma^* \to e^+e^-$ is computed in the γ^*-rest frame, with the 4-momentum of the virtual photon given by

$$q = \left(\sqrt{q^2}, 0, 0, 0\right) \tag{6.61}$$

and where the lepton momenta can be written as

$$\begin{aligned} k_1 =& \frac{\sqrt{q^2}}{2}\left(1,\ \sin\theta_{e^+e^-}\cos\Phi_{e^+e^-},\ \sin\theta_{e^+e^-}\sin\Phi_{e^+e^-}, \cos\theta_{e^+e^-}\right), \\ k_2 =& \frac{\sqrt{q^2}}{2}\left(1, -\sin\theta_{e^+e^-}\cos\Phi_{e^+e^-}, -\sin\theta_{e^+e^-}\sin\Phi_{e^+e^-}, -\cos\theta_{e^+e^-}\right). \end{aligned} \tag{6.62}$$

Therefore, the angles $\theta_{e^+e^-}$ and $\Phi_{e^+e^-}$ are chosen as two independent kinematic variables describing the leptonic subprocess. The hadronic part of the amplitude depends on the c.m. energy $\sqrt{s}$, the virtuality of the photon q^2, and the Mandelstam variable t, which give rise to the pion scattering angle θ_π. The kinematics is illustrated in Fig. 6.10. Such a choice of the reference frames enables a simple identification of the allowed kinematical range in terms of the 5 variables.

The integration over the phase space can be performed using

$$\begin{aligned}
&\frac{1}{(2\pi)^5}\left(\frac{d^3\vec{q}_\pi}{2E_\pi}\right)\left(\frac{d^3\vec{k}_1}{2k_1^0}\right)\left(\frac{d^3\vec{k}_2}{2k_2^0}\right)\delta^{(4)}\big(p_1+p_2-q_\pi-k_1-k_2\big) \\
&= \frac{1}{(2\pi)^5}\left(\frac{d^3\vec{q}_\pi}{2E_\pi}\right)\left(\frac{d^3\vec{q}}{2q^0}\right)\delta^{(4)}\big(p_1+p_2-q_\pi-q\big)dq^2\left(\frac{d^3\vec{k}_1}{2k_1^0}\right)\left(\frac{d^3\vec{k}_2}{2k_2^0}\right)\delta^{(4)}\big(q-k_1-k_2\big).
\end{aligned} \tag{6.63}$$

The leptonic part in the γ^* rest frame is

$$\left(\frac{d^3\vec{k}_1}{2k_1^0}\right)\left(\frac{d^3\vec{k}_2}{2k_2^0}\right)\delta^{(4)}\big(q-k_1-k_2\big) \;=\; \frac{1}{8}\,d\Omega_{e^+e^-}, \tag{6.64}$$

with the leptonic solid angle $d\Omega_{e^+e^-}$. Evaluating the phase space of the hadronic subprocess in the c.m. frame leads to

$$\left(\frac{d^3\vec{q}_\pi}{2E_\pi}\right)\left(\frac{d^3\vec{q}}{2q^0}\right)\delta^{(4)}\big(p_1+p_2-q_\pi-q\big)dq^2 = \frac{1}{4\sqrt{s}}\,|\vec{q}|\,dq^2 d\Omega_\gamma, \tag{6.65}$$

where $|\vec{q}|$ refers to the momentum of the virtual photon in the c.m. frame. Finally, the expression of the differential cross section is received as

$$\frac{d\sigma}{dt\,dq^2\,d\Omega_{e^+e^-}} = \frac{1}{(2\pi)^4 64 s(s-4m_N^2)}\,|\overline{\mathcal{A}_{\gamma^*}}|^2. \tag{6.66}$$

Using the decomposition of the amplitude as presented in Eq. (6.57), the differential cross section of the reaction can be expressed by

$$\frac{d\sigma}{dt\,dq^2\,d\Omega_{e^+e^-}} = \frac{1}{16\pi^2 s(s-4m_N^2)}\,\frac{e^2}{(4\pi)^2\,8\,q^2}\,\frac{4\pi}{3}\cdot\mathcal{W}(\theta_{e^+e^-},\Phi_{e^+e^-}), \tag{6.67}$$

where $\mathcal{W}(\theta_{e^+e^-},\Phi_{e^+,e^-})$ is the decay angular distribution of the e^+e^- pair, giving rise to the angular dependence of the lepton pair:

$$\begin{aligned}
\mathcal{W}(\theta_{e^+e^-},\Phi_{e^+e^-}) =& \frac{3}{4\pi}\Big[\sin^2\theta_{e^+e^-}\rho_{00} + (1+\cos^2\theta_{e^+e^-})\rho_{11} \\
&+ \sqrt{2}\sin 2\theta_{e^+e^-}\cos\Phi_{e^+e^-}\mathrm{Re}[\rho_{10}] \;+\; \sin^2\theta_{e^+e^-}\cos 2\Phi_{e^+e^-}\mathrm{Re}[\rho_{1-1}]\Big].
\end{aligned} \tag{6.68}$$

The density matrix $\rho_{\lambda\lambda'}$ is defined as

$$\rho_{\lambda\lambda'} = \Big(\mathcal{M}^\mu_{\gamma^*}\,\varepsilon^*_\mu(\lambda_\gamma)\Big)\Big(\mathcal{M}^\mu_{\gamma^*}\,\varepsilon^*_\mu(\lambda'_\gamma)\Big)^*, \quad \text{for } \lambda_\gamma,\lambda'_\gamma = 0,\pm 1. \tag{6.69}$$

The expression of $\mathcal{W}(\theta_{e^+e^-},\Phi_{e^+e^-})$ in Eq. (6.68) is model independent, which means that it is not related to any particular choice of the hadronic interaction in the process. All dependences on the lepton variables $\theta_{e^+e^-}$ and $\Phi_{e^+e^-}$ are fully contained in the expression of Eq. (6.68), which is a function of four different independent angular structures, namely

$$1, \qquad \cos^2\theta_{e^+e^-}, \qquad \sin 2\theta_{e^+e^-}\,\cos\Phi_{e^+e^-}, \qquad \sin^2\theta_{e^+e^-}\,\cos 2\Phi_{e^+e^-}. \tag{6.70}$$

Hence, the density matrix elements can be determined using different angular configurations. The dependence on the hadronic variables s, $\cos\theta$ and q^2 is completely absorbed in the density matrix elements ρ.

Not all of the density matrix elements $\rho_{\lambda\,\lambda'}$ are independent. From Eq. (6.69) one can easily see, that the density matrix satisfies

$$\rho_{\lambda\,\lambda'} \;=\; \rho^{*}_{\lambda'\,\lambda}. \tag{6.71}$$

Furthermore, from parity conservation one finds the constraints

$$\rho_{-\lambda\,-\lambda'} \;=\; \big(-1\big)^{\lambda_\gamma-\lambda'_\gamma}\,\rho_{\lambda\,\lambda'}. \tag{6.72}$$

6.4.2 Results within a Regge Framework

In the previous subsection the process has been analyzed in the most general way, without defining the explicit form of the hadronic amplitude $\mathcal{M}_{\gamma^*}$. The expressions found in Eqs. (6.68) and (6.67) are model independent. However, in order to obtain numerical results one has to use a model to characterize the hadronic subprocess. We choose the Regge pole model, which has been used in Sec. 6.1.1 for investigating the $p\bar{p}\to\pi^0\gamma$ process.

Since a virtual photon is produced, one has to specify the electromagnetic form factors parametrizing the γ^*NN and $\gamma^*N\Delta$ vertices. For the electromagnetic form factors of the nucleon a VMD model is used, given in [48], for the purpose of the computation of the cross section. Eventually, the aim of the present work is to provide a further constraint on future extractions of timelike nucleon form factors.

For the magnetic dipole form factor of the $N\to\Delta$ transition, we use the results in the large N_c limit, which can be written as [123]:

$$g_M(q^2) = \frac{g_M(0)}{\kappa_V}\left[F_2^p(q^2) - F_2^n(q^2)\right], \tag{6.73}$$

where F_2^p (F_2^n) is the Pauli form factor of the proton (neutron), for which the description of the VMD model will be used, and $\kappa_V = \kappa_p - \kappa_n = 3.70$.

The results of the differential cross section $d\sigma/dt\,dq^2\,d\Omega_{e^+e^-}$ as a function of $\cos\theta_{e^+e^-}$ are presented in Fig. 6.11 for several kinematical conditions. We display the N trajectory contributions, corresponding to the red curves, and $(N+\Delta)$ trajectory contributions as introduced in Eq. (6.50), indicated by the blue curves, for the angles $\Phi_{e^+e^-} = 0$ and $\Phi_{e^+e^-} = \pi$. The dependence on the angle $\Phi_{e^+e^-}$ appears as an asymmetric behavior of the cross section with respect to $\cos\theta_{e^+e^-}$. As virtuality of the photon $q^2 = 0.5$ GeV^2 and $q^2 = 1$ GeV^2 has been chosen for the calculation.

For $\Phi_{e^+e^-} = \pi/2$, the resulting cross section is symmetric, which can be derived from the general form of the decay angular distribution $\mathcal{W}$, given by Eq. (6.68). The only structure of $\mathcal{W}$ being an odd function of $\cos\theta$, the factor in front of ρ_{10}, vanishes for $\Phi_{e^+e^-} = \pi/2$.

Using the Born diagram model suggested in Ref. [109], one obtains a cross section, which is 1 to 4 orders of magnitude larger than the results of the Regge pole model, depending on the variation of the kinematic parameters s, q^2 and θ_π.

The integrated cross sections can be used to investigate the density matrix elements $\rho_{\lambda,\,\lambda'}$.

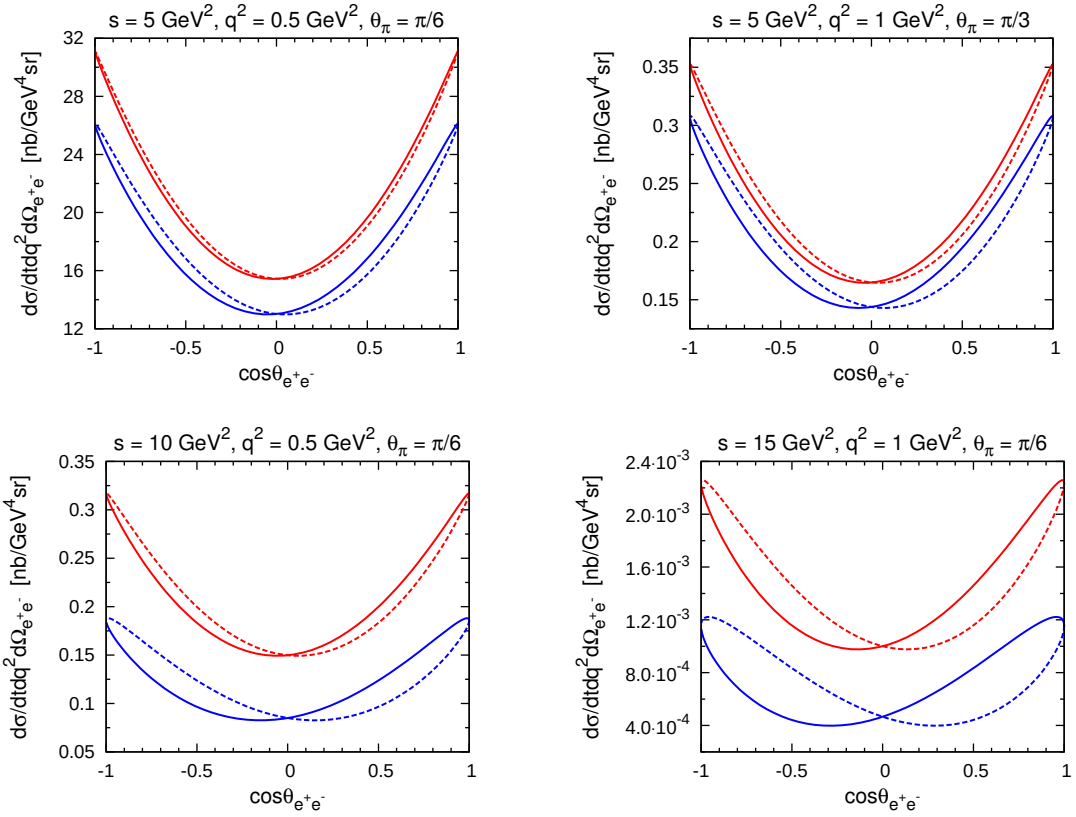

Figure 6.11: Differential cross section $d\sigma/dt\,dq^2\,d\Omega_{e^+e^-}$ of $p\bar{p} \to \pi^0 e^+ e^-$ as a function of $\cos\theta_{e^+e^-}$. Red curves correspond to the N trajectory contribution; red solid curve: $\Phi_{e^+e^-} = 0$; red dashed curve: $\Phi_{e^+e^-} = \pi$. Blue curves correspond to the $(N + \Delta)$ trajectory contribution including a reduction of the Δ pole residue ($\mathcal{F} \approx 0.5$) according to Eq. (6.50); blue solid curve: $\Phi_{e^+e^-} = 0$; blue dashed curve: $\Phi_{e^+e^-} = \pi$.

The cross section integrated over the azimuthal angle $\Phi_{e^+e^-}$

$$\begin{aligned}\frac{d\sigma}{d\cos\theta_\pi\, dq^2\, d\cos\theta_{e^+e^-}} &= \int_0^{2\pi} d\Phi_{e^+e^-} \frac{d\sigma}{d\cos\theta_\pi\, dq^2\, d\Omega_{e^+e^-}} \\ &= \frac{|\vec{q}|\, e^2}{(16)^2\, 4\,\pi^3\, q^2\, s\sqrt{s - 4m_N^2}} \left[\sin^2\theta_{e^+e^-}\rho_{00} + \left(1 + \cos^2\theta_{e^+e^-}\right)\rho_{11}\right]\end{aligned} \tag{6.74}$$

is sensitive to ρ_{00} and ρ_{11} and the cross section integrated over the polar angle $\theta_{e^+e^-}$

$$\begin{aligned}\frac{d\sigma}{d\cos\theta_\pi\, dq^2\, d\Phi_{e^+e^-}} &= \int_{-1}^{1} d\cos\theta_{e^+e^-} \frac{d\sigma}{d\cos\theta_\pi\, dq^2\, d\Omega_{e^+e^-}} \\ &= \frac{|\vec{q}|e^2}{(16)^2\,\pi^4\, q^2\, s\sqrt{s - 4m_N^2}} \frac{1}{6}\Big[\rho_{00} + 2\rho_{11} + \cos 2\Phi_{e^+e^-}\mathrm{Re}\left[\rho_{1-1}\right]\Big]\end{aligned} \tag{6.75}$$

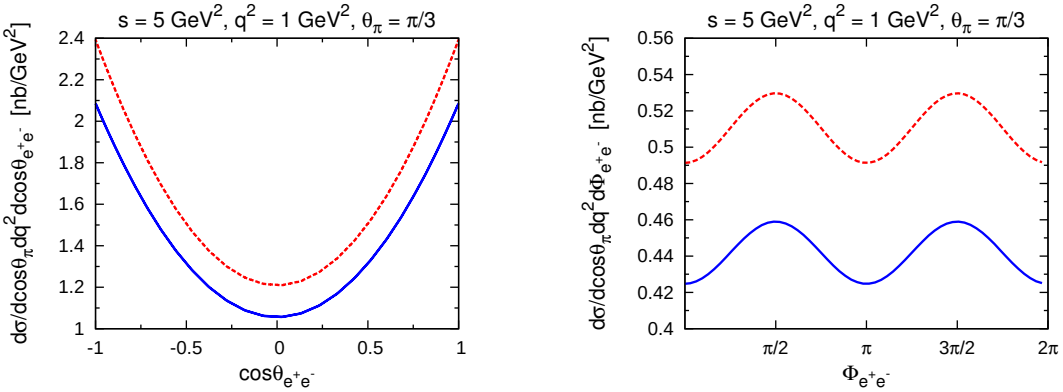

Figure 6.12: Cross sections defined by Eq. (6.74) (left) and Eq. (6.75) (right) of $p\bar{p} \to \pi^0 e^+ e^-$ as a function of $\cos\theta_{e^+e^-}$ and $\Phi_{e^+e^-}$, respectively: Red (dashed) curve: N trajectory contribution; blue (solid) $(N + \Delta)$ trajectory contribution according to Eq. (6.50).

can be analyzed in order to obtain in addition information on ρ_{1-1} from the Φ dependence of the cross section.

The cross section integrated over the full lepton phase space is given by

$$\begin{aligned} \frac{d\sigma}{d\cos\theta_\pi\, dq^2} &= \int d\Omega_{e^+e^-} \frac{d\sigma}{d\cos\theta_\pi\, dq^2\, d\Omega_{e^+e^-}} \\ &= \frac{|\vec{q}|e^2}{(16)^2\,\pi^3\, q^2\, s\,\sqrt{s-4m_N^2}}\,\frac{1}{3}\left[\rho_{00} + 2\rho_{11}\right], \end{aligned} \tag{6.76}$$

depending on the density matrix elements ρ_{00} and ρ_{11}.

Accordingly, an investigation of the differential cross sections $d\sigma/dt\, dq^2\, d\Omega_{e^+e^-}$, as well as the cross sections integrated over the azimuthal angle $\Phi_{e^+e^-}$ and the polar angle $\theta_{e^+e^-}$, and $d\sigma/d\cos\theta_\pi dq^2$ allows to access all four density matrix elements $\rho_{\lambda\lambda'}$ through a separation of the matrix elements from the angular dependencies of the cross sections.

As selective predictions, the results of the cross sections (6.74), and (6.75) for $s = 5$ GeV^2, $q^2 = 1$ GeV^2 and $\theta_\pi = \pi/3$ are shown in Fig. 6.12, using both N trajectory and $(N + \Delta)$ trajectory exchange given by Eq. (6.50). The cross section integrated over the polar angle, shown in the left panel of Fig. 6.12, is symmetric with respect to $\cos\theta$, as one can infer from the general expression given in Eq. (6.74). The integrated cross section of Eq. (6.75), presented in the right panel of Fig. 6.12, has a periodicity of π due to the $\cos 2\Phi_{e^+e^-}$ structure.

The t dependence of the density matrix elements $\rho_{\lambda\lambda'}$ is presented in Fig. 6.13 using a $(N + \Delta)$ trajectory exchange as introduced in Eq. (6.50) for the region $s \gg |t|$, which is dominated by the t-channel Regge amplitude. The density matrix element ρ_{11}, shown in the left panel of Fig. 6.13, yields the dominant contribution to the cross section, since it is about one order of magnitude larger compared to the three other structures, presented in the right panel of Fig. 6.13.

An alternative calculation is the evaluation of the whole process in the γ^* rest frame. In

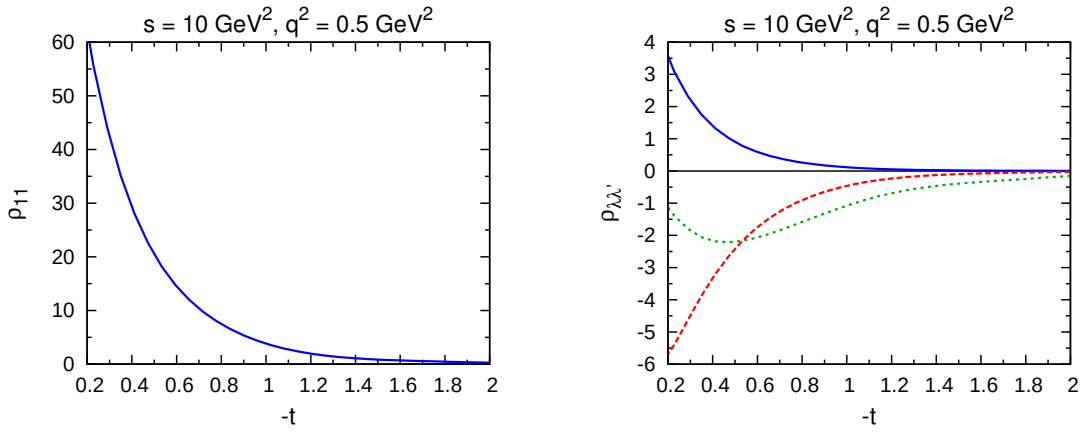

Figure 6.13: Density matrix elements as functions of $-t$ (in GeV^2) for $s = 10$ GeV^2 and q^2=0.5 GeV^2 using a Regge model with N and Δ trajectory exchange according to Eq. (6.50). Left panel: density matrix ρ_{11}; Right panel: ρ_{00} (blue solid curve), ρ_{10} (red dashed curve), ρ_{1-1} (green dotted curve).

this reference rest frame the polarization vectors of the virtual photon are given by

$$\begin{aligned} \varepsilon(\lambda_\gamma = \pm 1) &= \frac{1}{\sqrt{2}}(0, \mp 1, -\mathrm{i}, 0), \\ \varepsilon(\lambda_\gamma = 0) &= (0, 0, 0, 1). \end{aligned} \tag{6.77}$$

Using the short-hand notation of the hadronic matrix element

$$\mathcal{M}^{\mu\nu} \equiv \mathcal{M}^{\mu}_{\gamma^*} \left(\mathcal{M}^{\nu}_{\gamma^*}\right)^* \tag{6.78}$$

the squared matrix element in terms of the hadronic tensor can be found as

$$\begin{aligned} \left|\mathcal{A}_{\gamma^*}\right|^2 &= \left|\mathcal{L}_\mu \frac{1}{q^2} \mathcal{M}^\mu\right|^2 = \frac{2e^2}{q^2} \frac{4\pi}{3} \mathcal{W}(\theta_{e^+e^-}, \Phi_{e^+e^-}) \\ &= \frac{2e^2}{q^2}\Big[\mathcal{M}^{33}(1 - \cos\theta_{e^+e^-}) + \left(\mathcal{M}^{11} + \mathcal{M}^{22}\right)\left(1 - \frac{1}{2}\sin^2\theta\right) \\ &\quad - \sin\theta_{e^+e^-}\cos\theta_{e^+e^-}\cos\Phi_{e^+e^-}\left(\mathcal{M}^{31} + \mathcal{M}^{13}\right) \\ &\quad + \frac{1}{2}\cos^2\theta_{e^+e^-}\cos 2\Phi_{e^+e^-}(\mathcal{M}^{11} + \mathcal{M}^{22})\Big]. \end{aligned} \tag{6.79}$$

Integrating the angular decay distribution over the azimuthal angle and polar angle gives

$$\begin{aligned} \int_0^{2\pi} \left|\mathcal{A}_{\gamma^*}\right|^2 d\Phi_{e^+e^-} &= \frac{2e^2}{q^2}\frac{4\pi}{3}\int_0^{2\pi} \mathcal{W}(\theta_{e^+e^-}, \Phi_{e^+e^-})\, d\Phi_{e^+e^-} \\ &= 2\pi\frac{e^2}{q^2}\Big[\left(2\mathcal{M}^{33} + \mathcal{M}^{11} + \mathcal{M}^{22}\right) + \cos^2\theta_{e^+e^-}\left(\mathcal{M}^{11} + \mathcal{M}^{33} - 2\mathcal{M}^{33}\right)\Big], \end{aligned}$$

$$\begin{aligned}
\int_{-1}^{1} \left|\mathcal{A}_{\gamma^*}\right|^2 d\cos\theta_{e^+e^-} &= \frac{2e^2}{q^2}\,\frac{4\pi}{3}\int_0^{2\pi} \mathcal{W}\left(\theta_{e^+e^-},\Phi_{e^+e^-}\right) d\cos\theta_{e^+e^-} \\
&= \frac{8}{3}\,\frac{e^2}{q^2}\left[\mathcal{M}^{33}+\mathcal{M}^{11}+\mathcal{M}^{22}-\frac{1}{2}\cos 2\Phi_{e^+e^-}\left(\mathcal{M}^{11}-\mathcal{M}^{22}\right)\right], \\
\int \left|\mathcal{A}_{\gamma^*}\right|^2 d\Omega_{e^+e^-} &= \frac{2e^2}{q^2}\,\frac{4\pi}{3}\int \mathcal{W}\left(\theta_{e^+e^-},\Phi_{e^+e^-}\right) d\Omega_{e^+e^-} \\
&= \frac{16\pi}{3}\,\frac{e^2}{q^2}\left[\mathcal{M}^{33}+\mathcal{M}^{11}+\mathcal{M}^{22}\right],
\end{aligned} \tag{6.80}$$

which is in agreement with the results presented in Ref. [110], where the analysis of the reaction has been performed in the γ^* rest frame. Such observables allow to access different combinations of the hadronic matrix elements.

6.5 Conclusions

In this chapter the process $p\bar{p} \to \pi^0 e^+ e^-$ has been studied, giving a model independent expression of the cross section in terms of the lepton pair angular distribution and presenting results within a Regge pole approach. Such a model description is applicable for high-energy processes in the forward and backward angular regions.

It has been found that a model based on nucleon and Δ Regge trajectory exchanges provides a good description of the data of the real photoproduction process $p\bar{p} \to \pi^0\gamma$ in the energy range of $s \simeq 8.5 - 14$ GeV^2. Applying this model to $p\bar{p} \to \pi^0 e^+ e^-$ allows for predictions of the angular dependence of the differential cross section, which can be used to extract the timelike form factors in the unphysical region as well as their phases, in kinematics which will be accessible by the PANDA@FAIR experiment.

The Regge approach can be extended to study polarization observables for $p\bar{p} \to \pi^0 e^+ e^-$ and furthermore, to the analysis of other processes, such as two-pion production, $p\,\bar{p} \to \pi^0\pi^0$ and $p\,\bar{p} \to \pi^-\pi^+$, or the spacelike reaction $\gamma^* p \to \pi^0 p$ in the forward and backward angular regime.

Chapter 7

Conclusions and Outlook

In this thesis different aspects of probing the structure of the nucleon by means of the electromagnetic interaction have been studied. The electromagnetic interaction offers a clear probe, which provides access to the electromagnetic form factors, which are one of the most basic observables regarding the composite structure of the nucleon.

The main focus of the thesis was on two-photon exchange corrections in form factor measurements, which are expected to explain the discrepancy between the results of the form factor ratio G_E/G_M found in unpolarized Rosenbluth measurements and polarization experiments of elastic electron-proton scattering. Understanding this discrepancy is of particular importance towards finding a consistent description of the electromagnetic form factors. The appearance of the contradicting form factor results has triggered a new field studying the influence of two-photon exchange corrections in order to reconcile both experimental methods.

In this thesis a combined analysis of high-precision Rosenbluth data and polarization observables for elastic electron-proton scattering has been presented. The available cross section data and the results of polarization measurements, both performed at similar values of momentum transfer, allows for an empirical determination of the two-photon amplitudes. Using the assumption that two-photon exchange is the source of the discrepancy, the two-photon amplitudes have been found to be in the 2-3 % range. One amplitude (Y_M) can be reliably extracted from the corrections to the unpolarized cross section. Improving on the extraction of the other two amplitudes requires a further improvement in the precision of the polarization experiments. The determination of the two-photon amplitudes allows for a prediction of the e^+p/e^-p cross section ratio, for which dedicated experiments are underway, giving rise to effects of several percent for the measured kinematical range of the experiments.

Furthermore, 2γ-exchange in the corresponding crossed timelike annihilation processes has been studied. With regard to forthcoming high precision measurements of the timelike form factors, it is important to estimate such corrections. Two different approaches have been used in order to perform the calculation of the two-photon exchange contribution to the timelike annihilation process $p\bar{p} \to e^+e^-$, both based on the concept of factorization. These studies are the first calculations of timelike two-photon exchange corrections covering the region of intermediate and larger momentum transfers, for which the form factor measurements will be performed.

The first method is based upon perturbative QCD factorization, allowing to factorize the amplitude of the process into a non-perturbative part and a hard subprocess, in which all three valence quarks of the nucleon participate. The non-perturbative contribution is represented by the Distribution Amplitudes of the proton and antiproton. Using different parametrizations of the DAs, the 2γ-corrections to the cross section were found to be small, leading to effects of $\sim 1\%$ at most. In the second approach the concept of Generalized

Distribution Amplitudes has been applied, which are the timelike analogon of the Generalized Parton Distributions. Within this model, the annihilation process takes places only at a single quark-antiquark pair in the hard part of the amplitude. The two-photon corrections obtained within this approach are slightly larger, reaching values of $\sim 2\%$ in maximum. However, the timelike 2γ-corrections are smaller than those found for the spacelike process, which suggests that the impact of two-photon exchange is less important for the extraction of the form factors in the timelike region. The small 2γ-exchange contributions make it challenging to observe such effects in unpolarized cross section measurements.

Two-photon exchange in the reaction $p\bar{p} \to e^+e^-$ manifests itself in an odd contribution with respect to forward and backward c.m. scattering angles, giving rise to a forward-backward asymmetry. Since the obtained two-photon contributions depend on the parametrizations of the DAs and GDAs, respectively, an extraction of the corrections through an accurate measurement of the asymmetry offers the opportunity to probe and constrain these non-perturbative objects.

Moreover, the perturbative QCD factorization approach has been applied to investigate the two-boson exchange contributions appearing in parity-violating elastic electron-proton scattering. Parity violating asymmetries are sensitive to the interference term of one-photon and Z boson exchange amplitudes of elastic ep-scattering, providing access to the strange quark contribution and the weak charge of the nucleon. Applying the pQCD factorization approach, it was found that the two-boson exchange corrections to the asymmetry are in the range of $\lesssim 1\%$, where the contributions of different exchange diagrams have opposite signs and partially cancel each other, leading to small corrections in total.

In addition, the process $p\,\bar{p} \to \pi^0 e^+e^-$ has been analyzed, which attracted attention due to the possibility to probe the nucleon electromagnetic form factors in the unphysical region below the two-nucleon production threshold within this reaction. No data of this process exist so far, but measurements are planned by forthcoming experiments. Data of the form factors in the unphysical region would certainly improve our understanding of nucleon structure.

The annihilation process has been investigated within a phenomenological model based on Regge theory. Prior to this, the validity of the Regge approach has been tested in the process of real photoproduction $p\,\bar{p} \to \pi^0\gamma$, for which data in the energy range of $s \simeq 8.5 - 14$ GeV^2 exist. It has been found that an approach including nucleon and Δ Regge trajectory exchange provides a good description of the data of real photoproduction over the measured range. Subsequently, the reaction $p\,\bar{p} \to \pi^0 e^+e^-$ has been analyzed, where model independent expressions of the cross section in terms of the angular distribution of the lepton pair as well as predictions of the angular dependence of the cross section within the Regge approach has been presented.

The discussed Regge based model can be extended to the analysis of further processes, such as the spacelike reaction $\gamma^* p \to \pi^0 p$, or two-pion production, $p\,\bar{p} \to \pi^0\pi^0$ and $p\,\bar{p} \to \pi^-\pi^+$, in the forward and backward angular regime. The latter process represents an important background reaction with respect to timelike form factor measurements, which are planned in the near future by the PANDA experiment at FAIR.

Appendix

Appendix A

Notations and Conventions

A.1 Lorentz Vectors

The contravariant representation x^μ and covariant representation x_μ of Lorentz vectors, which are given by

$$x^\mu \equiv (x^0, x^1, x^2, x^3) = (x^0, \vec{x}), \quad \text{and} \quad x_\mu \equiv (x_0, x_1, x_2, x_3) = (x^0, -\vec{x}), \tag{A.1}$$

respectively, are connected through

$$x^\mu = g^{\mu\nu} x_\nu. \tag{A.2}$$

The metric tensor $g^{\mu\nu}$ is defined by

$$g^{\mu\nu} := \begin{pmatrix} +1 & 0 & 0 & 0 \\ 0 & -1 & 0 & 0 \\ 0 & 0 & -1 & 0 \\ 0 & 0 & 0 & -1 \end{pmatrix}. \tag{A.3}$$

A.2 Light-Cone Coordinates

Light-cone coordinates have been introduced with respect to the light-cone basis n and $\bar{n}$ and the transverse contribution $a_\perp$:

$$\begin{aligned} \bar{n}^\mu &= \big(1,0,0,1\big), \quad n^\mu = \big(1,0,0,-1\big), \\ &\text{with} \quad \bar{n}^2 = n^2 = 0. \quad \bar{n}\cdot n = 2 \\ a_\perp^\mu &= \big(0, a^1, a^2, 0\big). \end{aligned} \tag{A.4}$$

Any 4-vector can be decomposed with respect to the light-cone basis as

$$p^\mu = \frac{\bar{n}^\mu}{2} \underbrace{(n\cdot p)}_{p^+} + \frac{n^\mu}{2} \underbrace{(\bar{n}\cdot p)}_{p^-} + p_\perp^\mu, \tag{A.5}$$

and can been expressed through the shorthand notation using $p^+, p^-, p_\perp$:

$$p^\mu = \big(p^+, p^-, p_\perp\big) \equiv \big(n\cdot p, \bar{n}\cdot p, p_\perp\big). \tag{A.6}$$

The scalar-product of two vectors is given by:

$$\begin{aligned} p_1 \cdot p_2 &= p_1^+ \cdot p_2^- + p_1^- \cdot p_2^+ + p_{1\perp} \cdot p_{2\perp}, \\ &\text{in particular:} \quad p^2 = 2p^+ \cdot p^- + p_\perp^2. \end{aligned} \tag{A.7}$$

A.3 Pauli and Dirac Matrices

The Pauli matrices are 2×2 matrices defined as

$$\sigma^1 = \begin{pmatrix} 0 & 1 \\ 1 & 0 \end{pmatrix}, \qquad \sigma^2 = \begin{pmatrix} 0 & -i \\ i & 0 \end{pmatrix}, \qquad \sigma^3 = \begin{pmatrix} 1 & 0 \\ 0 & -1 \end{pmatrix}, \tag{A.8}$$

which satisfy

$$\sigma_i \sigma_j = \mathbb{1} + \mathrm{i} \sum_{k=1}^{3} \epsilon_{ijk} \sigma_k. \tag{A.9}$$

The Pauli spinors are defined by

$$\chi_{s=\frac{1}{2}} = \begin{pmatrix} 1 \\ 0 \end{pmatrix}, \quad \chi_{s=-\frac{1}{2}} = \begin{pmatrix} 0 \\ 1 \end{pmatrix}. \tag{A.10}$$

The Dirac matrices are $d \times d$ matrices ($d \geq 4$), fulfilling the anticommutator relation

$$\{\gamma^\mu, \gamma^\nu\} \equiv \gamma^\mu \gamma^\nu + \gamma^\nu \gamma^\mu = 2g^{\mu\nu}. \tag{A.11}$$

In this thesis, only the case $d = 4$ has been considered. Additionally, the following combinations of Dirac matrices have been used:

$$\gamma_5 \equiv i\gamma^0\gamma^1\gamma^2\gamma^3, \quad \sigma^{\mu\nu} \equiv \frac{\mathrm{i}}{2}[\gamma^\mu, \gamma^\nu] = \frac{\mathrm{i}}{2}\left(\gamma^\mu\gamma^\nu - \gamma^\nu\gamma^\mu\right), \tag{A.12}$$

where γ_5 fulfills

$$\{\gamma_5, \gamma^\mu\} = 0, \qquad \gamma_5^2 = 1. \tag{A.13}$$

Using light-cone coordinates, the combinations

$$\gamma^\pm \equiv \left(\gamma^0 \pm \gamma^3\right), \qquad \gamma_\perp^\mu \equiv \left(0, \gamma^1, \gamma^2, 0\right) \tag{A.14}$$

can be introduced. Furthermore, one obtains the following relations:

$$\begin{aligned} \gamma^{\mu,\dagger} &= \gamma^0\gamma^\mu\gamma^0, \qquad \gamma_5^\dagger = \gamma_5, \qquad \gamma_5^T = \gamma_5, \\ \{\gamma^\pm, \gamma^\pm\} &= 0, \qquad \{\gamma^\pm, \gamma^\mp\} = 4, \qquad \{\gamma^\pm, \gamma_\perp^\mu\} = 0. \end{aligned} \tag{A.15}$$

For the traces over Dirac matrices one finds:

$$\begin{aligned} \mathrm{Tr}[\gamma^\mu\gamma^\nu] &= 4g^{\mu\nu} \\ \mathrm{Tr}[\gamma^\mu\gamma^\nu\gamma^\rho\gamma^\sigma] &= 4(g^{\mu\nu}g^{\rho\sigma} - g^{\mu\rho}g^{\nu\sigma} + g^{\mu\sigma}g^{\nu\rho}) \\ \mathrm{Tr}[\gamma^{\mu_1}\cdots\gamma^{\mu_n}] &= 0 \qquad \text{for } n \text{ odd} \\ \mathrm{Tr}[\gamma_5] &= 0 \\ \mathrm{Tr}[\gamma_5\gamma^\mu\gamma^\nu] &= 0 \\ \mathrm{Tr}[\gamma_5\gamma^\mu\gamma^\nu\gamma^\rho\gamma^\sigma] &= -4\mathrm{i}\epsilon^{\mu\nu\rho\sigma} \\ \mathrm{Tr}[\gamma_5\gamma^{\mu_1}\cdots\gamma^{\mu_n}] &= 0 \qquad \text{for } n \text{ odd}. \end{aligned} \tag{A.16}$$

As an explicit representation of the Dirac matrices the Dirac representation has been used:

$$\gamma^0 = \begin{pmatrix} \mathbb{1}_{2\times2} & 0 \\ 0 & -\mathbb{1}_{2\times2} \end{pmatrix}, \qquad \gamma^i = \begin{pmatrix} 0 & \sigma^i \\ -\sigma^i & 0 \end{pmatrix} \qquad \gamma_5 = \begin{pmatrix} 0 & \mathbb{1}_{2\times2} \\ \mathbb{1}_{2\times2} & 0 \end{pmatrix}, \tag{A.17}$$

where σ^i are the Pauli matrices.

A.4 Dirac Spinors

The expansion of a fermion field is

$$\begin{aligned}\psi(x) &= \int \frac{d^3\vec{p}}{(2\pi)^3}\frac{1}{\sqrt{2p^0}}\sum_s \left\{a(p,s)u(p,s)\exp(-\mathrm{i}px) + b^\dagger(p,s)v(p,s)\exp(\mathrm{i}px)\right\},\\ \bar{\psi}(x) &= \int \frac{d^3\vec{p}}{(2\pi)^3}\frac{1}{\sqrt{2p^0}}\sum_s \left\{b(p,s)\bar{v}(p,s)\exp(-\mathrm{i}px) + a^\dagger(p,s)\bar{u}(p,s)\exp(\mathrm{i}px)\right\},\end{aligned} \tag{A.18}$$

where $a^\dagger$ and $b^\dagger$ create a particle of kind a and b and $u(p,s)$ and $v(p,s)$ are the Dirac spinors, which satisfy

$$\begin{aligned}(\gamma^\mu p_\mu - m)\, u(p,s) &= 0,\\ (\gamma^\mu p_\mu + m)\; v(p.s) &= 0.\end{aligned} \tag{A.19}$$

The spinors fulfill the completeness relations

$$\begin{aligned}\sum_s u(p,s)\bar{u}(p,s) &= \not{p} + m,\\ \sum_s v(p,s)\bar{v}(p,s) &= \not{p} - m.\end{aligned} \tag{A.20}$$

In order to study transformation properties of $\bar{\psi}\Gamma\psi$, where $\psi(x)$ is a Dirac spinor and Γ is an arbitrary 4×4 matrix, it is convenient to decompose the expression with respect to its transformation properties.

A basis contains 16 4×4 matrices, which are given by anti-symmetric combinations of the Dirac matrices:

1	scalar	1
γ^μ	vector	4
$\sigma^{\mu\nu}$	tensor	6
$\gamma^\mu\gamma_5$	pseudovector	4
γ_5	pseudoscalar	1

(A.21)

where in the middle the transformation property of the matrix and on the r.h.s the number of matrices are given.

The spinor of a spin-1/2-particle, with momentum $\vec{p}$ given by

$$\vec{p} = |\,\vec{p}\,| \begin{pmatrix} \sin\theta\cos\phi \\ \sin\theta\sin\phi \\ \cos\theta \end{pmatrix} \tag{A.22}$$

and

$$E^2 = m^2 + |\vec{p}|^2 \tag{A.23}$$

can be parametrized as

$$
\begin{aligned}
u(p,+) &= \sqrt{E+m}\begin{pmatrix} \cos\frac{\theta}{2} \\ \sin\frac{\theta}{2}\,(\cos\phi+\mathrm{i}\sin\phi) \\ \frac{|\vec{p}|}{E+m}\,\cos\frac{\theta}{2} \\ \frac{|\vec{p}|}{E+m}\,\sin\frac{\theta}{2}\,(\cos\phi+\mathrm{i}\sin\phi) \end{pmatrix}, \\
u(p,-) &= \sqrt{E+m}\begin{pmatrix} \sin\frac{\theta}{2}\,(-\cos\phi+\mathrm{i}\sin\phi) \\ \cos\frac{\theta}{2} \\ \frac{|\vec{p}|}{E+m}\,\sin\frac{\theta}{2}\,(\cos\phi-\mathrm{i}\sin\phi) \\ -\frac{|\vec{p}|}{E+m}\,\cos\frac{\theta}{2} \end{pmatrix},
\end{aligned}
\tag{A.24}
$$

and for antiparticles

$$
\begin{aligned}
v(p,+) &= \sqrt{E+m}\begin{pmatrix} \frac{|\vec{p}|}{E+m}\,\sin\frac{\theta}{2}\,(\cos\phi-\mathrm{i}\sin\phi) \\ -\frac{|\vec{p}|}{E+m}\,\cos\frac{\theta}{2} \\ \sin\frac{\theta}{2}\,(-\cos\phi+\mathrm{i}\sin\phi) \\ \cos\frac{\theta}{2} \end{pmatrix}, \\
v(p,-) &= \sqrt{E+m}\begin{pmatrix} -\frac{|\vec{p}|}{E+m}\,\cos\frac{\theta}{2} \\ -\frac{|\vec{p}|}{E+m}\,\sin\frac{\theta}{2}\,(\cos\phi+\mathrm{i}\sin\phi) \\ -\cos\frac{\theta}{2} \\ -\sin\frac{\theta}{2}\,(\cos\phi+\mathrm{i}\sin\phi) \end{pmatrix}.
\end{aligned}
\tag{A.25}
$$

In some cases it is convenient to use light front helicity spinors. The expression of these spinors is obtained by a transformation of a spinor in the rest frame via a longitudinal and a transverse boost. The light front helicity spinors are given by

$$
\begin{aligned}
u(p,+) &= \mathcal{N}\begin{pmatrix} p^+ + m \\ p^1 + \mathrm{i}p^2 \\ p^+ - m \\ p^1 + \mathrm{i}p^2 \end{pmatrix}, \qquad u(p,-) = \mathcal{N}\begin{pmatrix} -p^1 + \mathrm{i}p^2 \\ p^+ + m \\ p^1 - \mathrm{i}p^2 \\ -p^+ + m \end{pmatrix}, \\
v(p,+) &= -\mathcal{N}\begin{pmatrix} -p^1 + \mathrm{i}p^2 \\ p^+ - m \\ p^1 - \mathrm{i}p^2 \\ -p^+ - m \end{pmatrix}, \qquad v(p,-) = -\mathcal{N}\begin{pmatrix} p^+ - m \\ p^1 + \mathrm{i}p^2 \\ p^+ + m \\ p^1 + \mathrm{i}p^2 \end{pmatrix},
\end{aligned}
\tag{A.26}
$$

$$
\text{with} \quad \mathcal{N}^{-1} = \sqrt{2p^+},
$$

where the "+" and "−" correspond to a light-cone helicity state of the particle with $h = {}^{+1}/_{2}$ and $h = {}^{-1}/_{2}$, respectively. For $m \to 0$ the light front helicity spinors are equivalent to the ordinary helicity spinors.

For a particle with four-momentum p^μ, which is moving fast in the +-direction, one finds

$$u(p,+) = \mathcal{N} \begin{pmatrix} (p^+ + m)\,\chi_+ \\ (p^+ - m)\,\chi_+ \end{pmatrix}, \qquad u(p,-) = \mathcal{N} \begin{pmatrix} (p^+ + m)\,\chi_- \\ -(p^+ - m)\,\chi_- \end{pmatrix},$$

$$v(p,+) = \mathcal{N} \begin{pmatrix} -(p^+ - m)\,\chi_- \\ (p^+ + m)\,\chi_- \end{pmatrix}, \qquad v(p,-) = \mathcal{N} \begin{pmatrix} -(p^+ - m)\,\chi_+ \\ -(p^+ + m)\,\chi_+ \end{pmatrix}, \tag{A.27}$$

$$\text{with} \quad \chi_+ = \begin{pmatrix} 1 \\ 0 \end{pmatrix}, \quad \chi_- = \begin{pmatrix} 0 \\ 1 \end{pmatrix}.$$

Using the projectors

$$\Lambda^+ = \frac{\not{\vec{n}}\not{n}}{4} = \frac{\gamma^-\gamma^+}{4}, \qquad \Lambda^- = \frac{\not{n}\not{\vec{n}}}{4} = \frac{\gamma^+\gamma^-}{4}, \tag{A.28}$$

gives

$$\Lambda^+ u(p,\pm) \sim \mathcal{N}\, p^+ \begin{pmatrix} \chi_\pm \\ \pm\chi_\pm \end{pmatrix} \sim \sqrt{p^+}, \qquad \Lambda^- u(p,\pm) \sim \mathcal{N}\, m \begin{pmatrix} \chi_\pm \\ \mp\chi_\pm \end{pmatrix} \sim \frac{1}{\sqrt{p^+}},$$

$$\Lambda^+ v(p,\pm) \sim \mathcal{N}\, p^+ \begin{pmatrix} -\chi_\mp \\ \pm\chi_\mp \end{pmatrix} \sim \sqrt{p^+}, \qquad \Lambda^- v(p,\pm) \sim \mathcal{N}\, m \begin{pmatrix} \chi_\mp \\ \pm\chi_\mp \end{pmatrix} \sim \frac{1}{\sqrt{p^+}}. \tag{A.29}$$

Appendix B

Amplitudes within a pQCD Factorization Approach

In this appendix the results of the different diagrams of the hard subprocesses contributing to the 2γ-amplitude and γZ-amplitude calculated within the pQCD factorization approach are given.

B.1 Results of Two-Photon Exchange Contributions

The amplitude for timelike two-photon exchange can be separated as

$$\begin{aligned} A_{2\gamma} &= Q_u^2 A^{uu} + Q_u Q_d (A^{u_1 d} + A^{u_2 d}) \\ &= Q_u^2 \left(A_{12}^{uu} + A_{34}^{uu}\right) + Q_u Q_d \left(A_{12}^{u_1 d} + A_{34}^{u_1 d} + A_{12}^{u_2 d} + A_{34}^{u_2 d}\right), \end{aligned} \tag{B.1}$$

with

$$A_{ij}^{q_1 q_2} = D_i^{q_1 q_2} + D_j^{q_1 q_2} + \text{crossed}. \tag{B.2}$$

The superscript of $A^{q_1 q_2}$ indicates to which quarks the two photons couple in the hard subprocess. The diagrams contributing to the subprocess are presented in table B.1. The indices k of D_k in Eq. (B.2) refer to the gluon exchange as indicated in the diagrams of table B.1. The amplitudes of the different contributions are found as

$$\begin{aligned} A_{12}^{uu} =& \frac{8\mathcal{G}_1}{s^3}\ \bar{u}_l \gamma_\mu v_{l'} \\ & \cdot \int \frac{d[x_i] d[y_i]}{(x_2 \bar{x}_2 x_3)(y_2 \bar{y}_2 y_3)} \frac{((V'+A')(V+A)+4T'T)(1,2,3)}{[\bar{x}_2(\eta-\bar{y}_2)+\bar{y}_2\bar{\eta}][\bar{x}_2(y_2-\eta)+\bar{y}_2\eta]} \\ & \cdot\ \bar{N}\left((2\eta-1)x_2 y_2 \gamma_\perp^\mu - \frac{P^\mu \not{K}_\perp}{s} 2(x_2+y_2-2x_2y_2)\right) N, \end{aligned} \tag{B.3}$$

$$\begin{aligned} A_{34}^{uu} =& \frac{8\mathcal{G}_1}{s^3}\ \bar{u}_l \gamma_\mu v_{l'} \\ & \cdot \int \frac{d[x_i] d[y_i]}{(x_2 \bar{x}_2 x_3)(y_2 \bar{y}_2 y_3)} \frac{((V'+A')(V+A)+4T'T)(1,2,3)}{[\bar{x}_2(\eta-\bar{y}_2)+\bar{y}_2\bar{\eta}][\bar{x}_2(y_2-\eta)+\bar{y}_2\eta]} \\ & \cdot\ \bar{N}\left((2\eta-1)x_2 y_2 \gamma_\perp^\mu - \frac{P^\mu \not{K}_\perp}{s} 2(x_2+y_2-2x_2y_2)\right) N, \end{aligned} \tag{B.4}$$

$$
\begin{aligned}
A_{12}^{u_1 d} =& \frac{8\mathcal{G}_1}{s^3}\ \bar{u}_l \gamma_\mu v_{l'} \\
& \cdot \int \frac{d[x_i] d[y_i]}{(x_1 x_2 \bar{x}_2)(y_1 y_2 \bar{y}_2)} \frac{((V'+A')(V+A)+4T'T)(1,2,3)}{[\bar{x}_2(\eta-\bar{y}_2)+\bar{y}_2\bar{\eta}][\bar{x}_2(y_2-\eta)+\bar{y}_2\eta]} \\
& \cdot\ \bar{N}\left((2\eta-1)x_2 y_2 \gamma_\perp^\mu - \frac{P^\mu \not{K}_\perp}{s} 2(x_2+y_2-2x_2 y_2)\right) N,
\end{aligned}
\tag{B.5}
$$

$$
\begin{aligned}
A_{34}^{u_1 d} =& \frac{16\mathcal{G}_1}{s^3}\ \bar{u}_l \gamma_\mu v_{l'} \\
& \cdot \int \frac{d[x_i] d[y_i]}{(x_1 x_2 \bar{x}_2)(y_1 y_2 \bar{y}_2)} \frac{(V'V+A'A)(1,3,2)}{[\bar{x}_2(\eta-\bar{y}_2)+\bar{y}_2\bar{\eta}][\bar{x}_2(y_2-\eta)+\bar{y}_2\eta]} \\
& \cdot\ \bar{N}\left((2\eta-1)x_2 y_2 \gamma_\perp^\mu - \frac{P^\mu \not{K}_\perp}{s} 2(x_2+y_2-2x_2 y_2)\right) N,
\end{aligned}
\tag{B.6}
$$

$$
\begin{aligned}
A_{12}^{u_2 d} =& \frac{8\mathcal{G}_1}{s^3}\ \bar{u}_l \gamma_\mu v_{l'} \\
& \cdot \int \frac{d[x_i] d[y_i]}{(x_1 x_2 \bar{x}_2)(y_1 y_2 \bar{y}_2)} \frac{((V'+A')(V+A)+4T'T)(1,2,3)}{[\bar{x}_2(\eta-\bar{y}_2)+\bar{y}_2\bar{\eta}][\bar{x}_2(y_2-\eta)+\bar{y}_2\eta]} \\
& \cdot\ \bar{v}_{N'}\left((2\eta-1)x_2 y_2 \gamma_\perp^\mu - \frac{P^\mu \not{K}_\perp}{s} 2(x_2+y_2-2x_2 y_2)\right) u_N,
\end{aligned}
\tag{B.7}
$$

$$
\begin{aligned}
A_{34}^{u_2 d} =& \frac{16\mathcal{G}_1}{s^3}\ \bar{u}_l \gamma_\mu v_{l'} \\
& \cdot \int \frac{d[x_i] d[y_i]}{(x_1 x_2 \bar{x}_2)(y_1 y_2 \bar{y}_2)} \frac{(V'V+A'A)(1,3,2)}{[\bar{x}_2(\eta-\bar{y}_2)+\bar{y}_2\bar{\eta}][\bar{x}_2(y_2-\eta)+\bar{y}_2\eta]} \\
& \cdot\ \bar{N}\left((2\eta-1)x_2 y_2 \gamma_\perp^\mu - \frac{P^\mu \not{K}_\perp}{s} 2(x_2+y_2-2x_2 y_2)\right) N,
\end{aligned}
\tag{B.8}
$$

with $\mathcal{G}_1 = \frac{e^2}{4}\left(\frac{4\pi}{3!}\right)^2 \alpha_{em}\alpha_s$.

B.2 Results of γZ-Exchange Contributions

The amplitude for γZ-exchange in ep-scattering can be expressed as

$$
\begin{aligned}
A_{\gamma Z} &= Q_u(A^{uu} + A^{ud_Z}) + Q_d A^{u_Z d}, \\
\text{with} \quad A^{uu} &= A_{12}^{u1u2_Z} + A_{34}^{u1u2_Z} + A_{12}^{u1_Z u2} + A_{34}^{u1_Z u2}, \\
A^{ud_Z} &= A_{12}^{u_1 d_Z} + A_{34}^{u_1 d_Z} + A_{12}^{u_2 d_Z} + A_{34}^{u_2 d_Z}, \\
A^{u_Z d} &= A_{12}^{u_{1_Z} d} + A_{34}^{u_{1_Z} d} + A_{12}^{u_{2_Z} d} + A_{34}^{u_{2_Z} d},
\end{aligned}
\tag{B.9}
$$

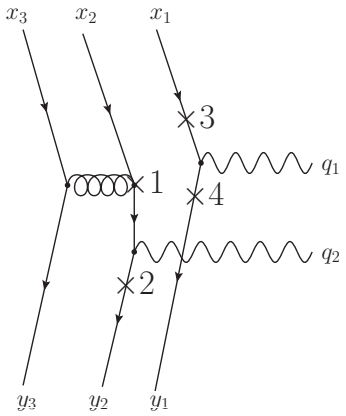

$$A^{uu} = A_{12}^{uu} + A_{34}^{uu}$$
$$= D_1^{uu} + D_2^{uu} + D_3^{uu} + D_4^{uu} + \text{crossed}$$

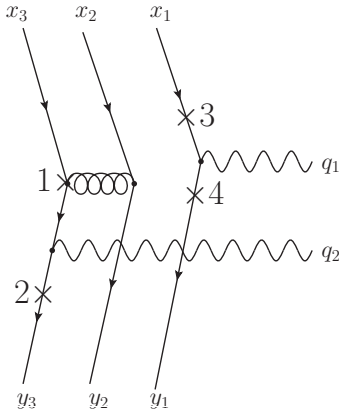

$$A^{u1d} = A_{12}^{u_1 d} + A_{34}^{u_1 d}$$
$$= D_1^{u_1 d} + D_2^{u_1 d} + D_3^{u_1 d} + D_4^{u_1 d} + \text{crossed}$$

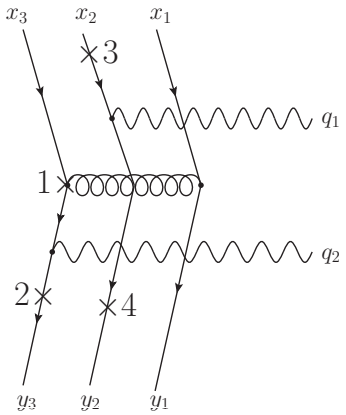

$$A^{u2d} = A_{12}^{u_2 d} + A_{34}^{u_2 d}$$
$$= D_1^{u_2 d} + D_2^{u_2 d} + D_3^{u_2 d} + D_4^{u_2 d} + \text{crossed}$$

Table B.1: Diagrams contributing to the subprocess of 2γ-exchange within the pQCD factorization approach. The $\times$'s indicate the possibilities to attach the gluon. The subscripts 1-4 of D_i refer to the gluon exchange as given in the Feynman diagrams.

Again, the superscript of A indicates to which quarks the photon and the Z boson couple, while the subscript Z refers to the Z boson coupling. The Feynman diagrams of the subprocess are presented in table B.2.

The amplitudes have been decomposed with respect to the vector (V) and axial-vector (A) contribution, corresponding to a vector and axial-vector coupling of the hadronic current, respectively:

$$\begin{aligned} A^{uu,\,V} = {} & \frac{8\mathcal{G}_2}{Q^4}\, g_V^u\ u_{l'}\,\gamma_\mu(g_V^e - g_A^e\gamma_5)u_l \\ & \times \int \frac{d\,[x_i]\,d[y_i]}{x_1\bar{x}_1x_2\,y_1\bar{y}_1y_2}\,\frac{1}{[\bar{x}_1(y_1-\zeta)+\bar{y}_1\zeta+i\varepsilon]\,\big[[\bar{x}_1(\zeta-\bar{y}_1)+\bar{y}_1\bar{\zeta}+i\varepsilon]} \\ & \times \Big\{2\left[(V'-A')(V-A)+4TT'\right](1,3,2)\,(\bar{x}_1\bar{y}_1+x_1y_1) \\ & \times\ \bar{N}\,\gamma_\perp^\mu\left\{(2\zeta-1)x_1y_1+\frac{\not{K}_\perp P^\mu}{Q^2}2(x_1+y_1-2x_1y_1)\right\}N, \end{aligned} \tag{B.10}$$

$$\begin{aligned} A^{uu,\,A} = {} & \frac{8\mathcal{G}_2}{Q^4}\, g_A^u\ u_{l'}\,\gamma_\mu(g_V^e - g_A^e\gamma_5)u_l \\ & \times \int \frac{d\,[x_i]\,d[y_i]}{x_1\bar{x}_1x_2\,y_1\bar{y}_1y_2}\,\frac{1}{[\bar{x}_1(y_1-\zeta)+\bar{y}_1\zeta+i\varepsilon]\,\big[[\bar{x}_1(\zeta-\bar{y}_1)+\bar{y}_1\bar{\zeta}+i\varepsilon]} \\ & \times \Big\{-2\left[(V'-A')(V-A)-4TT'\right](1,3,2)\,\bar{x}_1\bar{y}_1 \\ & \qquad +2\left[(V'-A')(V-A)+4TT'\right](1,3,2)\,x_1y_1\Big\} \\ & \times\ \bar{N}\,\gamma_5\,\gamma_\perp^\mu\left\{(2\zeta-1)x_1y_1+\frac{\not{K}_\perp P^\mu}{Q^2}2(x_1+y_1-2x_1y_1)\right\}N, \end{aligned} \tag{B.11}$$

$$\begin{aligned} A^{u_1Z^d,\,V} = {} & \frac{8\mathcal{G}_2}{Q^4}\, g_V^d\ u_{l'}\,\gamma_\mu(g_V^e - g_A^e\gamma_5)u_l \\ & \times \int \frac{d\,[x_i]\,d[y_i]}{x_1\bar{x}_1x_2\,y_1\bar{y}_1y_2}\,\frac{1}{[\bar{x}_1(y_1-\zeta)+\bar{y}_1\zeta+i\varepsilon]\,\big[[\bar{x}_1(\zeta-\bar{y}_1)+\bar{y}_1\bar{\zeta}+i\varepsilon]} \\ & \times \Big\{2\left[(V'-A')(V-A)+4TT'\right](1,2,3)\,\bar{x}_1\bar{y}_1+4\left[V'V+A'A\right](3,2,1)\,x_1y_1\Big\} \\ & \times\ \bar{N}\,\gamma_\perp^\mu\left\{(2\zeta-1)x_1y_1+\frac{\not{K}_\perp P^\mu}{Q^2}2(x_1+y_1-2x_1y_1)\right\}N, \end{aligned} \tag{B.12}$$

$$
\begin{aligned}
A^{u_2 Z\, d,\, V} = & + \frac{8\mathcal{G}_2}{Q^4}\, g_V^u\ u_{l'}\, \gamma_\mu (g_V^e - g_A^e \gamma_5) u_l \\
& \times \int \frac{d\,[x_i]\, d[y_i]}{x_1 \bar{x}_1 x_2\, y_1 \bar{y}_1 y_2} \frac{1}{\left[\bar{x}_1 (y_1 - \zeta) + \bar{y}_1 \zeta + i\varepsilon\right] \left[\left[\bar{x}_1 (\zeta - \bar{y}_1) + \bar{y}_1 \bar{\zeta} + i\varepsilon\right]\right.} \\
& \times \Big\{ 2\left[(V' - A')(V - A) + 4TT'\right](1,2,3)\, x_1 y_1 + 4\left[V'V + A'A\right](3,2,1)\, \bar{x}_1 \bar{y}_1 \Big\} \\
& \times\ \bar{N}\, \gamma_\perp^\mu \left\{ (2\zeta - 1) x_1 y_1 + \frac{\not{K}_\perp P^\mu}{Q^2} 2(x_1 + y_1 - 2x_1 y_1) \right\} N,
\end{aligned}
\tag{B.13}
$$

$$
\begin{aligned}
A^{u_1 Z\, d,\, A} = & \frac{8\mathcal{G}_2}{Q^4}\, g_A^d\ u_{l'}\, \gamma_\mu (g_V^e - g_A^e \gamma_5) u_l \\
& \times \int \frac{d\,[x_i]\, d[y_i]}{x_1 \bar{x}_1 x_2\, y_1 \bar{y}_1 y_2} \frac{1}{\left[\bar{x}_1 (y_1 - \zeta) + \bar{y}_1 \zeta + i\varepsilon\right] \left[\left[\bar{x}_1 (\zeta - \bar{y}_1) + \bar{y}_1 \bar{\zeta} + i\varepsilon\right]\right.} \\
& \times \Big\{ 2\left[(V' - A')(V - A) - 4TT'\right](1,2,3)\, \bar{x}_1 \bar{y}_1 + 4\left[V'V + A'A\right](3,2,1)\, x_1 y_1 \Big\} \\
& \times\ \bar{N}\, \gamma_5\, \gamma_\perp^\mu \left\{ (2\zeta - 1) x_1 y_1 + \frac{\not{K}_\perp P^\mu}{Q^2} 2(x_1 + y_1 - 2x_1 y_1) \right\} N,
\end{aligned}
\tag{B.14}
$$

$$
\begin{aligned}
A^{u_2 Z\, d,\, A} = & \frac{8\mathcal{G}_2}{Q^4}\, g_V^u\ u_{l'}\, \gamma_\mu (g_V^e - g_A^e \gamma_5) u_l \\
& \times \int \frac{d\,[x_i]\, d[y_i]}{x_1 \bar{x}_1 x_2\, y_1 \bar{y}_1 y_2} \frac{1}{\left[\bar{x}_1 (y_1 - \zeta) + \bar{y}_1 \zeta + i\varepsilon\right] \left[\left[\bar{x}_1 (\zeta - \bar{y}_1) + \bar{y}_1 \bar{\zeta} + i\varepsilon\right]\right.} \\
& \times \Big\{ 2\left[(V' - A')(V - A) + 4TT'\right](1,2,3)\, x_1 y_1 + 4\left[V'A + A'V\right](3,2,1)\, \bar{x}_1 \bar{y}_1 \Big\} \\
& \times\ \bar{N}\, \gamma_5\, \gamma_\perp^\mu \left\{ (2\zeta - 1) x_1 y_1 + \frac{\not{K}_\perp P^\mu}{Q^2} 2(x_1 + y_1 - 2x_1 y_1) \right\} N,
\end{aligned}
\tag{B.15}
$$

$$
\text{with} \quad \mathcal{G}_2 = \frac{1}{16} \left(\frac{4\pi}{3} \right)^2 \alpha_{\rm em}\, \alpha_S\, \frac{G_F}{2\sqrt{2}}.
$$

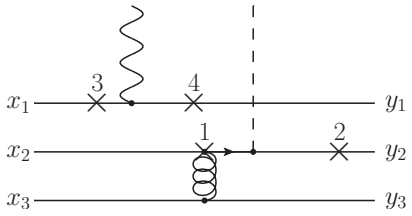

$$A^{u_1u_{2Z}} = A^{u_1u_{2Z},V} + A^{u_1u_{2Z},A}$$
$$= D_1^{u_1u_{2Z}} + D_2^{u_1u_{2Z}} + D_3^{u_1u_{2Z}} + D_4^{u_1u_{2Z}} + \text{crossed}$$

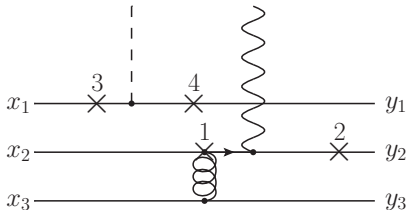

$$A^{u_1Zu_2} = A^{u_1Zu_2,V} + A^{u_1Zu_2,A}$$
$$= D_1^{u_1Zu_2} + D_2^{u_1Zu_2} + D_3^{u_1Zu_2} + D_4^{u_1Zu_2} + \text{crossed}$$

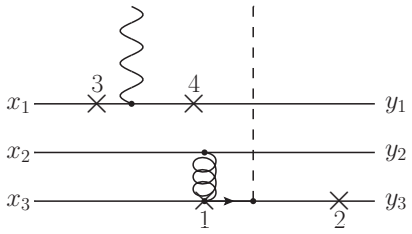

$$A^{u_1d_Z} = A^{u_1d_Z,V} + A^{u_1d_Z,A}$$
$$= D_1^{u_1d_Z} + D_2^{u_1d_Z} + D_3^{u_1d_Z} + D_4^{u_1d_Z} + \text{crossed}$$

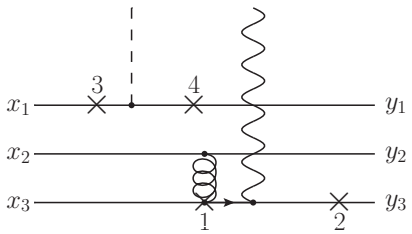

$$A^{u_1Zd} = A^{u_1Zd,V} + A^{u_1Zd,A}$$
$$= D_1^{u_1Zd} + D_2^{u_1Zd} + D_3^{u_1Zd} + D_4^{u_1Zd} + \text{crossed}$$

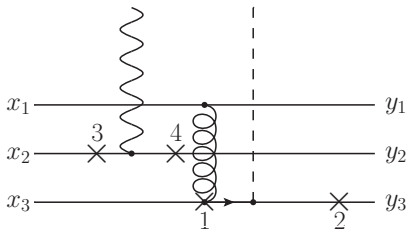

$$A^{u_2d_Z} = A^{u_2d_Z,V} + A^{u_2d_Z,A}$$
$$= D_1^{u_2d_Z} + D_2^{u_2d_Z} + D_3^{u_2d_Z} + D_4^{u_2d_Z} + \text{crossed}$$

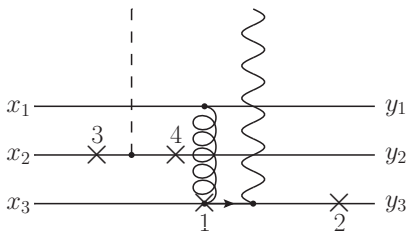

$$A^{u_2Zd} = A^{u_2Zd,V} + A^{u_2Zd,A}$$
$$= D_1^{u_2Zd} + D_2^{u_2Zd} + D_3^{u_2Zd} + D_4^{u_2Zd} + \text{crossed}$$

Table B.2: Diagrams contributing to the subprocess of γZ-exchange within the pQCD factorization approach. The $\times$'s indicate the possibilities to attach the gluon. The subscripts 1-4 of D_i refer to the gluon exchange as given in the Feynman diagrams.

Appendix C

Form Factor Parametrization

In this appendix the form factor parametrizations, which have been used in this thesis, are summarized.

C.1 Electromagnetic Nucleon Form Factors

Spacelike Models

Inverse polynomial model [107]:

$$G_E^i(Q^2),\ \frac{G_M^i(Q^2)}{\mu_p} \;=\; \left(1 + p_2\,Q^2 + p_4\,Q^4 + \cdots p_{2n}\,Q^{2n}\ \right)^{-1}, \tag{C.1}$$

where the parameter obtained from fits to the Rosenbluth data are

	p_2	p_4	p_6	p_8
G_E^n	3.226	1.508	-0.3773	0.611
G_M^n/μ_n	3.19	1.335	0.151	-0.0114

Friedrich-Walcher parametrization [108]:

$$\begin{aligned} G_E^i(Q^2),\ \frac{G_M^i(Q^2)}{\mu_p} &= G_s(Q^2) + a_b\,Q^2\,G_b(Q^2), \\ \text{with} \qquad G_s(Q^2) &= \frac{a_{10}}{\left(1+\frac{Q^2}{a_{11}}\right)^2} \;+\; \frac{a_{20}}{\left(1+\frac{Q^2}{a_{21}}\right)^2}, \\ G_b(Q^2) &= \mathrm{e}^{-\frac{1}{2}\left(\frac{(Q-Q_b)^2}{\sigma_b}\right)^2} \;+\; \mathrm{e}^{-\frac{1}{2}\left(\frac{(Q+Q_b)^2}{\sigma_b}\right)^2}, \end{aligned} \tag{C.2}$$

where the parameters have been obtained from fits to the form factors. In the case of the neutron form factor it has been found:

	a_{10}	a_{11}	a_{20}	a_{21}	a_b	Q_b	σ_b
G_E^n	1.04	1.73	-1.04	1.54	0.009	0.29	0.20
G_M^n/μ_n	1.012	0.770	-0.012	6.8	-0.011	0.33	0.14

VMD Models

In Ref. [48], a nucleon form factor model for both spacelike as well as timelike electromagnetic form factors has been presented.

The spacelike parametrizations are given by

$$\begin{aligned}
F_1^S(q^2) &= \frac{1}{2}\,g(q^2)\Big[(1-\beta_\omega-\beta_\phi)-\beta_\omega\frac{m_\omega^2}{q^2-m_\omega^2}-\beta_\phi\frac{m_\phi^2}{q^2-m_\phi^2}\Big],\\
F_1^V(q^2) &= \frac{1}{2}g(q^2)\Big[\;1-\beta_\rho-\beta_\rho\frac{m_\rho^2}{q^2-m_\rho^2}\Big],\\
F_2^S(q^2) &= \frac{1}{2}g(q^2)\Big[(0.12+\alpha_\phi)\frac{m_\omega^2}{q^2-m_\omega^2}-\alpha_\phi\frac{m_\phi^2}{q^2-m_\phi^2}\Big],\\
F_2^V(q^2) &= \frac{1}{2}g(q^2)\Big[-\;3.706\frac{m_\rho^2}{q^2-m_\rho^2}\Big],
\end{aligned} \tag{C.3}$$

with

$$g(Q^2) = \frac{1}{(1-\gamma q^2)^2}. \tag{C.4}$$

In order to take the non-negligible width of the ρ meson into account, the propagator has been replaced as

$$\frac{m_\rho^2}{q^2-m_\rho^2} \;\rightarrow\; \frac{m_\rho^2+8\Gamma_\rho m_\pi/\pi}{q^2-m_\rho^2+(q^2-4m_\pi^2)\Gamma_\rho\alpha(Q^2)/m_\pi}, \tag{C.5}$$

with

$$\alpha(Q^2) = \left(\frac{Q^2+4m_\pi^2}{Q^2}\right)\frac{2}{\pi}\log\left(\frac{\sqrt{Q^2+4m_\pi^2}+\sqrt{Q^2}}{2m_\pi}\right). \tag{C.6}$$

In the timelike region a phase has been introduced to the intrinsic form factors:

$$g(q^2) = \frac{1}{(1-e^{i\theta}\gamma q^2)^2}. \tag{C.7}$$

The pole of the ρ meson has been modified as

$$\frac{m_\rho^2}{q^2-m_\rho^2} \;\rightarrow\; \frac{m_\rho^2+8\Gamma_\rho m_\pi/\pi}{q^2-m_\rho^2+(q^2-4m_\pi^2)\Gamma_\rho\alpha(q^2)/m_\pi-\mathrm{i}\Gamma_\rho 4m_\pi\beta(q^2)}, \tag{C.8}$$

with

$$\begin{aligned}
\alpha(q^2) &= \left(\frac{q^2-4m_\pi^2}{q^2}\right)\frac{2}{\pi}\log\left(\frac{\sqrt{q^2-4m_\pi^2}+\sqrt{q^2}}{2m_\pi}\right),\\
\beta(q^2) &= \left(\frac{q^2}{4m_\pi^2}-1\right)^{3/2}\left(\frac{q^2}{4m_\pi^2}\right)^{-1/2}\Theta\left(q^2-4m_\pi^2\right).
\end{aligned} \tag{C.9}$$

The free parameters are obtained by fitting the spacelike data, the phase from a fit to the timelike data

$$\begin{aligned}
&\beta_\omega = 1.102, \quad \beta_\phi = 0.112, \quad \beta_\rho = 0.672, \quad \alpha_\phi = -0.052,\\
&\gamma = 0.25\ \mathrm{GeV}^{-2}, \quad \theta = 53^\circ.
\end{aligned} \tag{C.10}$$

Timelike Models

QCD-inspired form factor model:

$$|G_{E,M}| = \frac{\mathcal{B}}{q^4 \left(\ln^2 \frac{q^2}{\Lambda^2} + \pi^2 \right)}, \tag{C.11}$$

where $\mathcal{B}$ is a free fit parameter.

Improved fit of F_2/F_1 including logarithmic corrections to the power law fall off as expected from QCD [79]:

$$\frac{F_2}{F_1} = \kappa_p \frac{1 + \left(Q^2/0.791 \text{ GeV}^2\right)^2 \ln^{7.1}\left(1 + Q^2/4m_\pi^2\right)}{1 + \left(Q^2/0.38 \text{ GeV}^2\right)^3 \ln^{5.1}\left(1 + Q^2/4m_\pi^2\right)}. \tag{C.12}$$

C.2 Axial Nucleon Form Factor

The axial form factor in the spacelike region has been parametrized through a dipole form:

$$G_A(Q^2) = \frac{g_A}{\left(1 + \frac{Q^2}{m_A^2}\right)^2}, \tag{C.13}$$

with $g_A = 1.27$ and $m_A = 1.026$ GeV [84]. In addition, this dipole parametrization has been used in order to express the timelike axial form factor with $Q^2 \to -q^2$.

List of Acronyms

2γ	two-photon
DA	Distribution Amplitude
FAIR	Facility for Antiproton and Ion Research
Fermilab	Fermi National Accelerator Laboratory
GDA	Generalized Distribution Amplitude
GPD	Generalized Parton Distribution
JLab	Thomas Jefferson National Accelerator Facility
LEAR	Low Energy Antiproton Ring
MAMI	Mainz Microtron
MESA	Mainz Energy-Recovering Superconducting Accelerator
PANDA	Antiproton Annihilation at Darmstadt
pQCD	perturbative QCD
PV	parity-violating
QCD	Quantum Chromodynamics
QED	Quantum Electrodynamics
SLAC	Stanford Linear Accelerator Center
SSA	single spin asymmetry
TBE	two-boson exchange
VMD	vector meson dominance

Bibliography

[1] R. Frisch and O. Stern, Z. Phys **85**, 4 (1933).

[2] G. Aad *et al.* (ATLAS Collaboration), Phys. Lett. **B716**, 1 (2012).

[3] S. Chatrchyan *et al.* (CMS Collaboration), Phys. Lett. **B716**, 30 (2012).

[4] D. Gross and F. Wilczek, Phys. Rev. Lett. **30**, 1343 (1973).

[5] H. D. Politzer, Phys. Rev. Lett. **30**, 1346 (1973).

[6] K. G. Wilson, Phys. Rev. **D10**, 2445 (1974).

[7] R. Hofstadter, Ann. Rev. Nucl. Part. Sci. **7**, 231 (1957).

[8] M. Breidenbach, J. I. Friedman, H. W. Kendall, E. D. Bloom, D. Coward, *et al.*, Phys. Rev. Lett. **23**, 935 (1969).

[9] M. K. Jones *et al.* (Jefferson Lab Hall A), Phys. Rev. Lett. **84**, 1398 (2000).

[10] R. Walker, B. Filippone, J. Jourdan, R. Milner, R. McKeown, *et al.*, Phys. Rev. **D49**, 5671 (1994).

[11] O. Gayou *et al.* (Jefferson Lab Hall A), Phys. Rev. Lett. **88**, 092301 (2002).

[12] J. Guttmann, N. Kivel, M. Meziane, and M. Vanderhaeghen, Eur. Phys. J. **A47**, 77 (2011).

[13] J. Guttmann, N. Kivel, and M. Vanderhaeghen, Phys. Rev. **D83**, 094021 (2011).

[14] J. Guttmann and M. Vanderhaeghen, Phys. Lett. **B719**, 136 (2013).

[15] S. J. Brodsky and G. R. Farrar, Phys. Rev. **D11**, 1309 (1975).

[16] M. N. Rosenbluth, Phys. Rev. **79**, 615 (1950).

[17] C. Perdrisat, V. Punjabi, and M. Vanderhaeghen, Prog. Part. Nucl. Phys. **59**, 694 (2007).

[18] A. Puckett, E. Brash, M. Jones, W. Luo, M. Meziane, *et al.*, Phys. Rev. Lett. **104**, 242301 (2010).

[19] J. Arrington, Phys. Rev. **C68**, 034325 (2003).

[20] I. Qattan, J. Arrington, R. Segel, X. Zheng, K. Aniol, *et al.*, Phys. Rev. Lett. **94**, 142301 (2005).

[21] Y.-S. Tsai, Phys. Rev. **122**, 1898 (1961).

[22] L. W. Mo and Y.-S. Tsai, Rev. Mod. Phys. **41**, 205 (1969).

[23] L. Maximon and J. Tjon, Phys. Rev. **C62**, 054320 (2000).

[24] M. Vanderhaeghen, J. Friedrich, D. Lhuillier, D. Marchand, L. Van Hoorebeke, *et al.*, Phys. Rev. **C62**, 025501 (2000).

[25] R. Ent, B. Filippone, N. Makins, R. Milner, T. O'Neill, *et al.*, Phys. Rev. **C64**, 054610 (2001).

[26] F. Weissbach, K. Hencken, D. Trautmann, and I. Sick, Phys. Rev. **C80**, 064605 (2009).

[27] P. A. M. Guichon and M. Vanderhaeghen, Phys. Rev. Lett. **91**, 142303 (2003).

[28] M. Sudol, M. Mora Espi, E. Becheva, J. Boucher, T. Hennino, *et al.*, Eur. Phys. J. **A44**, 373 (2010).

[29] G. Bardin, G. Burgun, R. Calabrese, G. Capon, R. Carlin, *et al.*, Nucl. Phys. **B411**, 3 (1994).

[30] B. Aubert *et al.* (BABAR Collaboration), Phys. Rev. **D73**, 012005 (2006).

[31] J. Lees *et al.* (BaBar Collaboration), Phys. Rev. **D 87**, 092005 (2013).

[32] M. Lutz *et al.* (PANDA Collaboration)(2009), arXiv:0903.3905 [hep-ex].

[33] W. Bartel, F. Busser, W. Dix, R. Felst, D. Harms, *et al.*, Nucl. Phys. **B58**, 429 (1973).

[34] K. Hanson, J. Dunning, M. Goitein, T. Kirk, L. Price, *et al.*, Phys. Rev. **D8**, 753 (1973).

[35] F. Borkowski, P. Peuser, G. Simon, V. Walther, and R. Wendling, Nucl. Phys. **B93**, 461 (1975).

[36] A. Sill, R. Arnold, P. E. Bosted, C. Chang, J. Gomez, *et al.*, Phys. Rev. **D48**, 29 (1993).

[37] P. E. Bosted, L. Clogher, A. Lung, L. Stuart, J. Alster, *et al.*, Phys. Rev. Lett. **68**, 3841 (1992).

[38] M. Christy *et al.* (E94110 Collaboration), Phys. Rev. **C70**, 015206 (2004).

[39] T. Armstrong *et al.* (E760 Collaboration), Phys. Rev. Lett. **70**, 1212 (1993).

[40] M. Andreotti, S. Bagnasco, W. Baldini, D. Bettoni, G. Borreani, *et al.*, Phys. Lett. **B559**, 20 (2003).

[41] M. Ambrogiani *et al.* (E835 Collaboration), Phys. Rev. **D60**, 032002 (1999).

[42] A. Antonelli, R. Baldini, P. Benasi, M. Bertani, M. Biagini, *et al.*, Nucl. Phys. **B517**, 3 (1998).

[43] D. Bisello, S. Limentani, M. Nigro, L. Pescara, M. Posocco, *et al.*, Nucl. Phys. **B224**, 379 (1983).

[44] M. Ablikim *et al.* (BES Collaboration), Phys. Lett. **B630**, 14 (2005).

[45] A. Dubnickova, S. Dubnicka, and M. Rekalo, Z. Phys. **C70**, 473 (1996).

[46] H. Fonvieille and V. Karmanov, Eur. Phys. J. **A42**, 287 (2009).

[47] F. Iachello, A. D. Jackson, and A. Lande, Phys. Lett. **B43**, 191 (1973).

[48] F. Iachello and Q. Wan, Phys. Rev. **C69**, 055204 (2004).

[49] E. Tomasi-Gustafsson, F. Lacroix, C. Duterte, and G. Gakh, Eur. Phys. J. **A24**, 419 (2005).

[50] M. Meziane *et al.* (GEp2gamma Collaboration), Phys. Rev. Lett. **106**, 132501 (2011).

[51] P. Blunden, W. Melnitchouk, and J. Tjon, Phys. Rev. **C72**, 034612 (2005).

[52] P. G. Blunden, W. Melnitchouk, and J. A. Tjon, Phys. Rev. Lett. **91**, 142304 (2003).

[53] S. Kondratyuk, P. Blunden, W. Melnitchouk, and J. Tjon, Phys. Rev. Lett. **95**, 172503 (2005).

[54] S. Kondratyuk and P. Blunden, Phys. Rev. **C75**, 038201 (2007).

[55] Y. Chen, A. Afanasev, S. Brodsky, C. Carlson, and M. Vanderhaeghen, Phys. Rev. Lett. **93**, 122301 (2004).

[56] A. V. Afanasev, S. J. Brodsky, C. E. Carlson, Y.-C. Chen, and M. Vanderhaeghen, Phys. Rev. **D72**, 013008 (2005).

[57] N. Kivel and M. Vanderhaeghen, Phys. Rev. Lett. **103**, 092004 (2009).

[58] D. Borisyuk and A. Kobushkin, Phys. Rev. **D79**, 034001 (2009).

[59] M. Belushkin, H.-W. Hammer, and U.-G. Meissner, Phys. Lett. **B658**, 138 (2008).

[60] D. Borisyuk and A. Kobushkin, Phys. Rev. **C78**, 025208 (2008).

[61] M. Kohl, AIP Conf. Proc. **1160**, 19 (2009).

[62] JLab experiment E-05-007.

[63] J. Arrington, V. Dmitriev, R. Holt, D. Nikolenko, I. Rachek, *et al.*(2004), arXiv:nucl-ex/0408020 [nucl-ex].

[64] A. Gramolin, J. Arrington, L. Barkov, V. Dmitriev, V. Gauzshtein, *et al.*, Nucl. Phys. Proc. Suppl. **225-227**, 216 (2012).

[65] M. Gorchtein, P. A. Guichon, and M. Vanderhaeghen, Nucl. Phys. **A741**, 234 (2004).

[66] Y. Bystritskiy, E. Kuraev, and E. Tomasi-Gustafsson, Phys. Rev. **C75**, 015207 (2007).

[67] V. Punjabi *et al.*, Phys. Rev. **C71**, 055202 (2005).

[68] JLab experiment E-05-017, spokesperson J. Arrington.

[69] M. P. Rekalo and E. Tomasi-Gustafsson, Eur. Phys. J. **A22**, 331 (2004).

[70] E. Tomasi-Gustafsson, E. Kuraev, S. Bakmaev, and S. Pacetti, Phys. Lett. **B659**, 197 (2008).

[71] G. Gakh and E. Tomasi-Gustafsson, Nucl. Phys. **A761**, 120 (2005).

[72] D. Chen, H. Zhou, and Y. Dong, Phys. Rev. **C78**, 045208 (2008).

[73] G. P. Lepage and S. J. Brodsky, Phys. Rev. **D22**, 2157 (1980).

[74] V. Braun, R. J. Fries, N. Mahnke, and E. Stein, Nucl. Phys. **B589**, 381 (2000).

[75] A. Radyushkin, JINR Rapid Commun. **78**, 96 (1996).

[76] V. L. Chernyak, A. A. Ogloblin, and I. R. Zhitnitsky, Z. Phys. **C42**, 569 (1989).

[77] V. M. Braun, A. Lenz, and M. Wittmann, Phys. Rev. **D73**, 094019 (2006).

[78] M. Gockeler *et al.*, Phys. Rev. Lett. **101**, 112002 (2008).

[79] S. J. Brodsky, C. E. Carlson, J. R. Hiller, and D. S. Hwang, Phys. Rev. **D69**, 054022 (2004).

[80] M. Diehl, P. Kroll, and C. Vogt, Eur. Phys. J. **C26**, 567 (2003).

[81] P. Kroll and A. Schafer, Eur. Phys. J. **A26**, 89 (2005).

[82] R. Brown, K. Mikaelian, V. Cung, and E. Paschos, Phys. Lett. **B43**, 403 (1973).

[83] I. Khriplovich, Yad. Fiz. **17**, 576 (1973).

[84] V. Bernard, L. Elouadrhiri, and U. Meissner, J. Phys. **G28**, R1 (2002).

[85] C.-C. Kuo *et al.* (Belle Collaboration), Phys. Lett. **B621**, 41 (2005).

[86] J. Beringer *et al.* (Particle Data Group), Phys. Rev. **D86**, 010001 (2012).

[87] D. Armstrong, A. Asaturyan, T. Averett, J. Benesch, J. Birchall, *et al.*(2012), arXiv:1202.1255.

[88] D. Spayde *et al.* (SAMPLE Collaboration), Phys. Rev. Lett. **84**, 1106 (2000).

[89] E. Beise, M. Pitt, and D. Spayde, Prog. Part. Nucl. Phys. **54**, 289 (2005).

[90] K. Aniol *et al.* (HAPPEX Collaboration), Phys. Rev. **C69**, 065501 (2004).

[91] K. Aniol *et al.* (HAPPEX Collaboration), Phys. Lett. **B635**, 275 (2006).

[92] A. Acha *et al.* (HAPPEX collaboration), Phys. Rev. Lett. **98**, 032301 (2007).

[93] Z. Ahmed *et al.* (HAPPEX collaboration), Phys. Rev. Lett. **108**, 102001 (2012).

[94] F. Maas *et al.* (A4 Collaboration), Phys. Rev. Lett. **93**, 022002 (2004).

[95] F. Maas, K. Aulenbacher, S. Baunack, L. Capozza, J. Diefenbach, *et al.*, Phys. Rev. Lett. **94**, 152001 (2005).

[96] S. Baunack, K. Aulenbacher, D. Balaguer Rios, L. Capozza, J. Diefenbach, *et al.*, Phys. Rev. Lett. **102**, 151803 (2009).

[97] D. Armstrong *et al.* (G0 Collaboration), Phys. Rev. Lett. **95**, 092001 (2005).

[98] D. Androic *et al.* (G0 Collaboration), Phys. Rev. Lett. **104**, 012001 (2010).

[99] A. V. Afanasev and C. E. Carlson, Phys. Rev. Lett. **94**, 212301 (2005).

[100] Y. C. Chen, C. W. Kao, and M. Vanderhaeghen(2009).

[101] H. Q. Zhou, C. W. Kao, and S. N. Yang, Phys. Rev. Lett. **99**, 262001 (2007).

[102] J. Tjon, P. Blunden, and W. Melnitchouk, Phys. Rev. **C79**, 055201 (2009).

[103] M. Gorchtein and C. Horowitz, Phys. Rev. Lett. **102**, 091806 (2009).

[104] A. Sibirtsev, P. Blunden, W. Melnitchouk, and A. Thomas, Phys. Rev. **D82**, 013011 (2010).

[105] B. C. Rislow and C. E. Carlson, Phys. Rev. **D83**, 113007 (2011).

[106] M. Gorchtein, C. Horowitz, and M. J. Ramsey-Musolf, Phys. Rev. **C84**, 015502 (2011).

[107] J. Arrington, Phys. Rev. **C69**, 022201 (2004).

[108] J. Friedrich and T. Walcher, Eur. Phys. J. **A17**, 607 (2003).

[109] C. Adamuscin, E. Kuraev, E. Tomasi-Gustafsson, and F. Maas, Phys. Rev. **C75**, 045205 (2007).

[110] J. Boucher, Ph.D. thesis, Universite Paris Sud XI, Orsay, and Johannes Gutenberg University, Mainz(2011).

[111] J. Lansberg, B. Pire, and L. Szymanowski, Phys. Rev. **D76**, 111502 (2007).

[112] J. Lansberg, B. Pire, K. Semenov-Tian-Shansky, and L. Szymanowski, Phys.Rev. **D86**, 114033 (2012).

[113] T. Armstrong *et al.* (Fermilab E760 Collaboration), Phys. Rev. **D56**, 2509 (1997).

[114] T. Regge, Nuovo Cim. **14**, 951 (1959).

[115] P. Collins, Cambridge University Press, Cambridge(1977).

[116] J. Storrow, Phys. Rept. **103**, 317 (1984).

[117] M. Guidal, J. Laget, and M. Vanderhaeghen, Nucl. Phys. **A627**, 645 (1997).

[118] M. Vanderhaeghen, M. Guidal, and J. Laget, Phys. Rev. **C57**, 1454 (1998).

[119] H. Blok *et al.* (Jefferson Lab), Phys. Rev. **C78**, 045202 (2008).

[120] M. Coman *et al.* (Jefferson Lab Hall A Collaboration), Phys. Rev. **C81**, 052201 (2010).

[121] V. Pascalutsa, M. Vanderhaeghen, and S. N. Yang, Phys. Rept. **437**, 125 (2007).

[122] L. Tiator, D. Drechsel, S. Kamalov, and M. Vanderhaeghen, Eur. Phys. J. ST **198**, 141 (2011).

[123] V. Pascalutsa and M. Vanderhaeghen, Phys. Rev. **D76**, 111501 (2007).